

RHEOLOGY, STRUCTURE AND TRANSPORT PROPERTIES OF HYBRID
HAIRY NANOPARTICLES AND THEIR APPLICATIONS

A Dissertation

Presented to the Faculty of the Graduate School

of Cornell University

In Partial Fulfillment of the Requirements for the Degree of

Doctor of Philosophy

By

Akanksha Agrawal

August 2016

© 2016 Akanksha Agrawal

RHEOLOGY, STRUCTURE AND TRANSPORT PROPERTIES OF HYBRID
HAIRY NANOPARTICLES AND THEIR APPLICATIONS

Akanksha Agrawal, Ph. D.

Cornell University 2016

Polymer grafted nanoparticles have been of increasing scientific interest due to their potential applications in numerous fields. They have emerged as model systems to understand the structure, dynamics and phase stability of molecular and atomic liquids. One such class of polymer-tethered nanoparticles are the self-suspended hairy nanoparticles created by covalent attachment of polymer chains to inorganic nanostructures without any dispersing medium. The work reported in this thesis examines the flow, structural and dynamical properties of these self-suspended hybrid hairy nanoparticles with a particular emphasis on understanding the roles played by interactions between tethered chains on material structure and dynamics. By means of Small Angle X-ray Scattering (SAXS), rheology, and dielectric relaxation experiments coupled with theoretical studies, it is shown that interpenetration of the grafted polymer chains under the action of temperature, enthalpic attraction of tethered polymer chains, nanoparticle curvature size and the requirement that tethered chains must fill the inter-particle space; has a profound effect on structural, mechanical, dynamic, and transport properties of the materials. With the help of these findings the present work provides new insights into a variety of heretofore poorly understood phenomena in self-suspended materials, including observation of a stress overshoot

during start-up of steady shear flow, thermal jamming, and dramatic slowing down of polymer chain dynamics. Additionally, it is shown that armed with these physical phenomena one can easily manipulate the design variables (e.g. size distribution of the core particles, polydispersity in the corona molecular weight, dispersity in corona grafting density and chemistry of the corona chains) to create novel materials with unusual property profiles. Research reported in this thesis shows, for example, that a blend of self-suspended hairy particles comprised of bi-disperse core sizes exhibits multiple yielding transitions, jamming to unjamming state transitions, and facilitates fast transport of ions in bulk electrolytes and at electrochemical interfaces. Extending these ideas to create self-suspended nanoparticle blends in which hairy particles comprised of chemically dissimilar corona, but the same core, are shown to enable even more unusual materials designs that facilitate fundamental studies of interactions across tethered polymer interfaces from high signal-to-noise bulk experiments.

BIOGRAPHICAL SKETCH

Akanksha Agrawal was born and brought up in Noida, Uttar Pradesh; which is the National Capital Region of India. As a child, she was always interested in subjects of science and mathematics, and thus she chose the science stream in her high school. After graduating from Cambridge School Noida, she cleared the Joint Entrance Examination in 2008 and joined Indian Institute of Technology (IIT), Roorkee. Her four years of undergraduate studies were an unforgettable experience; where she gathered knowledge not only about science and research, but also formed bonds of everlasting friendships, for which she will always be grateful to Roorkee. As an undergrad she was first introduced to emulsions and colloidal science, and she worked extensively then on probing the rheology and structure of single-phase emulsions. After obtaining her degree in Bachelor of Technology (B.Tech.) in Chemical Engineering with honors, she applied for a Ph.D. in Chemical Engineering at Cornell University in 2012. Having been exposed to colloidal science in her undergraduate, the research done in Archer group greatly fascinated her. Since then she has worked with Prof. Lynden Archer on analyzing the fundamental properties of polymer-grafted nanoparticles and using them as electrolytes in rechargeable lithium metal batteries. Her four years at Cornell have been an extremely pleasant experience, which have been made even more beautiful by her friends and her advisor. She will always be indebted to Cornell for everything that it has given her; it has greatly influenced and matured her as a researcher and also as a person.

Dedicated to my parents, my brother and to all those who love science

ACKNOWLEDGMENTS

“I feel a very unusual sensation – if it is not indigestion, I think it must be gratitude.”

-Benjamin Disraeli

I would like to start by asking for an apology, as my words will not be able to do justice to the people and the organizations that I wish to thank for supporting me in my Ph.D. journey or in my life. I would like to firstly express my immense gratitude to my advisor Prof. Lynden Archer. His knowledge and wisdom, his enthusiasm for science and his dedication towards research has influenced and inspired me greatly. His counsel in matters of research and otherwise has always been of great help, and I cannot express my gratefulness to him enough. Thank you Professor for making me a better researcher and a better person!

I greatly appreciate the help from my committee members Prof. Donald Koch and Prof. Ulrich Wiesner. The discussions with Prof. Koch about the theoretical DFT framework of my experiments have been extremely valuable. I am extremely thankful to Prof. Wiesner for his insights about my research and for giving me valuable guidance. I really appreciate their patience with me.

Huge thanks to all the former and present Archer Group members. To Rajesh, who was my first mentor in the lab, to Samanvaya for teaching me synthesis and characterization, and to Jennifer and Sung for their helpful suggestions. I cannot express enough gratitude to Snehashis who has worked very closely with me on the synthesis and application side of hybrid hairy nanoparticles. His research acumen, his advice in matters of science and otherwise are much appreciated. He has become a very dear friend over the years and I hope he keeps up his spirit towards research and continues making people laugh! I am also grateful to Rahul and Ric for their suggestions and advice. I am really grateful to Emily, who helped me with my experimental work. I would also like to thank the other members of Archer group -

Shuya, who gave me suggestions about using hybrid hairy nanoparticles in batteries; Mukul, Pooja, Lin, Zhengyuan, Sampson, Wajdi, and Mun Sek.

I greatly appreciate the help that I received from Hsiu-Yu over the years. Her patience with me in explaining the structure factor theory for NOHMs is immeasurable. I really appreciate her commitment to research, and even though we worked remotely together through emails and Skype, she made everything so easy and smooth for me. I would also like to thank Brandon from Ober group for teaching me ATRP synthesis and for making it seem so easy. I am really thankful to Anubhab from Koch group for being so helpful in explaining the theoretical aspects of NOHMs so clearly to me.

Most of my X-ray scattering work was performed at Argonne National Laboratory and at Cornell High Energy Synchrotron Source (CHESS). I am really thankful to Dr. Suresh Narayanan at Argonne for his guidance in X-ray Photon Correlation Spectroscopy measurements. I wish to acknowledge Dr. Xiaobing Zuo and Dr. Jan Ilavsky at Argonne National lab for their guidance with SAXS measurements. I appreciate the help that I received at CHESS from Dr. Detlef Smilgies and Dr. Ruipeng Li.

I also appreciate the help and support from the staff at CCMR and KAUST-CU/CNET center with a special mention to Brenda Fisher for providing me with technical support for my experiments.

I would like to thank Prof. Stroock and Prof. Lucks for making my experience as a TA for Heat and Mass Transfer very valuable.

I consider myself lucky to have found some really awesome people at Ithaca and Cornell, who have made my stay here extremely memorable. Snehashis, Himanshu, Anubhab, and Senjuti- thanks for being such a strong support here. A very big thanks to Neeraj, Pooja, Ritesh, Binit, Rajesh, Ravi, Rahul, Neetu, Jade, Jiali, Misook, Ankit, Prashanth, Aritro, Mukul, Zhenia, Ghazal, Lingfeng, and my TA training team for

making Cornell such an enjoyable experience for me. I am thankful to Shruti and Manisha for being ever so helpful and understanding, even though we are in opposite corners of the world.

Lastly, and very importantly, I wish to thank Adi, without whom the journey would not have been half as wonderful and exciting. Thank you so much for being so supportive and for being there, always! To my parents and my brother, their love and sacrifice cannot be described by any words in any language. Whatever I am, and will be, will always be because of you.

TABLE OF CONTENTS

Abstract	iii
Biographical Sketch	v
Dedication	vi
Acknowledgements	vii
CHAPTER 1: INTRODUCTION	1
1.1 POLYMER-GRAFTED NANOPARTICLES	2
1.2 SELF-SUSPENDED HAIRY NANOPARTICLES	4
1.3 GOALS AND METHODS	6
1.3.1 <i>Flow and Structural Properties of Self-Suspended Hairy Nanoparticles</i>	7
1.3.2 <i>Application of Hybrid Hairy Nanoparticles</i>	8
1.4 OUTLINE	9
REFERENCES	12
CHAPTER 2: SELF-SUSPENDED SUSPENSIONS OF COVALENTLY GRAFTED HAIRY NANOPARTICLES	19
2.1 ABSTRACT	20
2.2 INTRODUCTION	20
2.3 EXPERIMENTAL SECTION	22
2.3.1 <i>Synthesis of self-suspended covalently grafted nanoparticles</i>	22
2.3.2 <i>Characterization</i>	23
2.3.3 <i>Small Angle X-ray Scattering measurements</i>	24
2.3.4 <i>Rheology measurements</i>	25
2.4 RESULTS AND DISCUSSION	25
2.5 CONCLUSIONS.....	41
ACKNOWLEDGEMENTS	42
REFERENCES	43
APPENDIX	48
CHAPTER 3: DYNAMICS AND YIELDING OF BINARY SOFT COLLOIDS	56
3.1 ABSTRACT	57
3.2 INTRODUCTION	57
3.3 EXPERIMENTAL METHODOLOGY	59
3.3.1 <i>Material and Synthesis</i>	59
3.3.2 <i>Small Angle X-ray Scattering measurements</i>	61
3.3.3 <i>X-ray Photon Correlation Spectroscopy measurements</i>	61
3.3.4 <i>Rheology measurements</i>	62
3.4 RESULTS AND DISCUSSION	63

3.5 CONCLUSIONS.....	80
ACKNOWLEDGEMENTS	81
REFERERENCES	82
APPENDIX	89
CHAPTER 4: A HIGHLY CONDUCTIVE, NON-FLAMMABLE POLYMER-NANOPARTICLE HYBRID ELECTROLYTE	95
4.1 ABSTRACT	96
4.2 INTRODUCTION	97
4.3 MATERIALS AND METHODS	100
4.3.1 <i>Synthesis</i>	100
4.3.2 <i>Characterization</i>	101
4.3.3 <i>Electrochemical measurements</i>	101
4.3.4 <i>Characterizing Flammability</i>	102
4.4 RESULTS AND DISCUSSION	102
4.5 CONCLUSIONS.....	113
ACKNOWLEDGEMENTS	116
REFERERENCES	117
APPENDIX	122
CHAPTER 5: HYBRID HAIRY NANOPARTICLE ELECTROLYTES STABILIZING LITHIUM METAL BATTERIES	125
5.1 ABSTRACT	126
5.2 INTRODUCTION	126
5.3 MATERIALS AND METHODS	130
5.3.1 <i>Synthesis</i>	130
5.3.2 <i>Characterization</i>	131
5.3.3 <i>Electrochemical measurements</i>	131
5.3.4 <i>Analyzing the Columbic Efficiency</i>	132
5.3.5 <i>Cell lifetime study</i>	133
5.4 RESULTS AND DISCUSSION	133
5.5 CONCLUSIONS.....	150
ACKNOWLEDGEMENTS	151
REFERERENCES	152
APPENDIX	158
CHAPTER 6: MOLECULAR ORIGINS OF TEMPERATURE INDUCED JAMMING IN SELF- SUSPENDED HAIRY NANOPARTICLES	164
6.1 ABSTRACT	165
6.2 INTRODUCTION	165
6.3 EXPERIMENTAL METHODS	169
6.3.1 <i>Synthesis</i>	169

6.3.2 <i>Small Angle X-ray Scattering (SAXS) measurements</i>	170
6.3.3 <i>Rheology measurements</i>	170
6.4 RESULTS AND DISCUSSION	171
6.5 CONCLUSIONS.....	191
ACKNOWLEDGEMENTS	193
REFERENCES	194
APPENDIX	198
CHAPTER 7: INTERACTIONS, STRUCTURE AND DYNAMICS OF POLYMER-TETHERED NANOPARTICLE BLENDS.....	201
7.1 ABSTRACT	202
7.2 INTRODUCTION	203
7.3 EXPERIMENTAL METHODS	206
7.3.1 <i>Synthesis</i>	206
7.3.2 <i>Rheology measurements</i>	207
7.3.3 <i>Small Angle X-ray Scattering</i>	208
7.3.4 <i>Differential Scanning Calorimetry (DSC) and Dielectric Spectroscopy</i> ..	208
7.4 RESULTS AND DISCUSSION	209
7.5 CONCLUSION	227
ACKNOWLEDGEMENTS	229
REFERENCES	230
APPENDIX	235

LIST OF FIGURES

1.1 Schematic showing self-suspended hairy nanoparticles	5
2.1 a) Reaction schematic for synthesizing the functionalized PEO and then tethering it to silica. b) Upturned vial showing liquid-like behavior of solvent-less covalently grafted nanoparticles. c) Typical transmission electron microscopy (TEM) image of the covalently grafted hairy nanoparticles.	26
2.2 a) FT-IR spectra of tethered PEO chain, free PEO and 3-(Triethoxysilyl) propyl isocyanate. b) ^1H NMR spectra with structural assignments of functionalized PEO. c) DSC thermograms of free PEO and tethered PEO chains.....	28
2.3 a) FT-IR spectra for tethered PEO chains with different grafting densities and for free PEO chain. b) Intensity ratios between helix and zigzag structures of tethered and free PEO chains c) Intensity ratio between gauche and trans conformations of C-C bonds of tethered and free PEO chain.	30
2.4 Experimental structure factor $S(q)$ comparison with DFT predictions and Hard Sphere calculations for a) $\Sigma \sim 1.18$ chains/nm ² b) $\Sigma \sim 1.03$ chains/nm ² c) $\Sigma \sim 0.703$ chains/nm ² and d) $\Sigma \sim 0.576$ chains/nm ²	32
2.5 a) Inter-particle distance, d_{p-p} extracted from the experimental $S(q)$ compared with theoretical d_{p-p} . b) The height of first peak of $S(q)$ and c) $S(0)$ values at different grafting densities compared with DFT and Hard sphere predictions	35
2.6 a) The height of normalized loss maximum as a function of strain at different temperatures. b) Structure factor variation with the scaled wave-vector at different temperatures. c) Loss tangent, $\tan\delta$ decreases with temperature.....	37
2.7 a) G' in the linear viscoelastic regime decreases with increase in grafting density. b) cage size, R estimated from G' and SAXS. c) Linear viscoelastic loss tangent, $\tan\delta_{\gamma \rightarrow 0}$	40
3.1 Transmission electron micrograph for binary systems with a) $r = 0.4$ b) $r = 0.2$, c) $r = 0.125$ and d) $r = 0.05$ at $x_L = 0.2$. e) Scaled intensities, $I(q)$ from SAXS experiments as a function of wave vectors	64
3.2 a) Structure factor $S(q)$ vs q for systems with different x_L . Comparison of b) $S(q)$ at $q \sim 0.22\text{nm}^{-1}$ and c) $S(0)$ with HS calculations at different x_L	67
3.3 a) Intensity auto-correlation function $g_2(q,t)$ at $q = 0.22\text{nm}^{-1}$ with stretched exponential fits. b) and c) Relaxation time τ as a function of wave vector q at different x_L . d) Variation of τ with x_L at $q \sim 0.22\text{nm}^{-1}$	69
3.4 a) Comparison of G' and G'' between a monodisperse ($x_L = 0$) and a binary system ($x_L = 0.2$) at $r = 0.4$. b) Normalized loss modulus, $G''/G''_{\gamma \rightarrow 0}$ at $\omega = 10\text{rad/s}$ with lognormal fits at $r = 0.4$. Energy dissipated in breaking the cage, U_d calculated from the normalized loss modulus for c) $r = 0.4$ and d) $r = 0.2$	73
3.5 Amplitude sweep measurements of storage modulus, G' and loss modulus, G'' at ω	

=10rad/s for size ratios a) $r = 0.125$ b) $r = 0.05$ and c) $r = 0.027$	75
3.6 Comparison of loss tangent, $\tan(\delta)$ at zero strain with increase in x_L at different size ratios a) $r = 0.2$ and $r = 0.4$, and b) $r = 0.125$, $r = 0.05$ and $r = 0.027$. Plateau modulus normalized with energy density and normalized complex viscosity measured at $\omega=1\text{rad/s}$ for c) $r = 0.2$ and $r = 0.4$, and d) $r = 0.125$, $r = 0.05$ and $r = 0.027$	77
3.7 Experimental state diagram for x_L vs. size ratio, r . For smaller size ratios, increase in x_L leads to a weakening of glass, while for larger size ratios increase in x_L results in a transition from a soft glass to liquid and then again to an arrested glass.	79
4.1 Physical Characterization- a) Schematic of hairy nanoparticle synthesis. b) TEM image of binary hairy nanoparticle composite with $x_L=0.5$. c) Intensity ($I(q)$) as a function of wave vector (q) for $x_L=0.5$ at different Φ , obtained from SAXS measurements. d) Pictorial representation of a battery with binary hairy nanoparticle composite electrolyte.....	103
4.2 Electrochemical properties- Conductivity as a function of inverse of temperature for different core volume fraction (Φ) at various fractions of bigger nanoparticles in the binary composite electrolyte indicated by x_L , as, a) $x_L=0$; b) $x_L=0.25$; c) $x_L=0.5$; d) $x_L=0.75$; e) $x_L=1$	105
4.3 Analysis of ion transport- a) Conductivity as a function of x_L at 30°C at different Φ ; b) Activation energy landscape at different x_L values and corresponding Φ ; c) Reduced conductivity given by the ratio of actual conductivity to that of the organic content, as a function of x_L at 30°C d) Tortuosity given as, $\tau=[S_o(1-\Phi)]/S$, versus x_L	108
4.4 Rheological properties- a) Evolution of storage modulus, G' and loss modulus, G'' as a function of amplitude strain, γ with particle volume fraction, Φ at $x_L=0,0.5$ and 1 . b) Variation of Loss Tangent, $\tan(\delta)=G''/G'$ obtained at $\gamma \rightarrow 0$ as a function of x_L at $\Phi=0.5$. c) Storage modulus at $\gamma \rightarrow 0$ varying as a function of Φ at different x_L values.	112
4.5 Flammability Test- Electrolyte samples with different particle volume fraction a) before ignition i.e. $t<0$. b) At ignition time i.e. $t=0$ c) after ignition i.e. at $t=4\text{s}$ d) At the extinguishing time.	114
5.1 Physical Characterization: a) Variation in ionic diffusivity, D as calculated from Nernst-Einstein equation, and glass transition temperature, T_g with fraction of larger particles, x_L . b) Intensity, $I(q)$ as a function of wave vector q at $\phi=0.3$, as obtained from SAXS measurements for different values of x_L . c) TEM for bi-disperse hybrid electrolytes at $\phi=0.3$ for $x_L=0.25,0.5$ and 0.75	136
5.2 Structure Factor: a) Evolution of Structure factor, $S(q)$ with the wave vector q for different volume fractions, $\phi=0.2, 0.3$ and 0.4 at $x_L=0.5$. b) Surface-to-surface distances, h_{11}, h_{12} and h_{22} for the same volume fractions as a function of x_L	139
5.3 Electrochemical Characterization: Impedance spectra for electrolytes with core volume fractions a) $\phi=0.2$, b) 0.3 , and c) 0.4 measured at different fractions of larger particles added, x_L . d) Bulk resistance, R_b and e) Interfacial resistance, R_{int} measured at	

different core volume fractions as a function of x_L	141
5.4 Surface Characterization: a) Scanning Electron Micrographs (SEM) for lithium electrode surface after the symmetric cell was cycled for 10 cycles at $0.03\text{mA}/\text{cm}^2$ with the bi-disperse hybrid electrolyte. b) Electrical double layer, λ and electrochemical capacitance per unit area, C_d for $\phi=0.3$ as a function of x_L	143
5.5 Electrochemical Stability: a) Initial impedance spectra for a symmetric cell with hybrid particle electrolyte at $\phi=0.3$ and $x_L=0.5$ compared with the spectra at $t=1440$ hours. b) Variation in faradic current density, J as a function of voltage as measured from Linear sweep voltammetry measurements for $x_L=0.5$ compared for $\phi=0.3$ and $\phi=0.4$. c) Leak current measured as a function of time for different steps of voltage as measured in a floating point test.	146
5.6 Galvanostatic performance: a) Comparison of columbic efficiency as a function of cycle number for neat PC electrolyte and hybrid particle electrolyte with $\phi=0.3$ and $x_L=0.5$ for Li electrolyte Stainless Steel configuration. b) Charge-discharge profiles for Li/LFP half-cell containing hybrid particle electrolyte with $\phi=0.3$ and $x_L=0.5$ at a fixed rate of $C/3$ in the initial, 10^{th} and 50^{th} cycle.	149
6.1 a) The maximum in normalized loss modulus, $G''/G''_{\gamma=0}$ (closed symbols) increases with increase in temperature. b) Energy dissipated per unit volume, U_d , in yielding the material, as calculated from area under the loss modulus peak. c) Illustration of localization length, ξ between two interacting hairy nanoparticles. ξ is shown to decrease with an increase in temperature. Inset shows the variation in plateau storage modulus, G_e with temperature, which is used to obtain ξ	174
6.2 a) Evolution of structure factor $S(q)$ as a function of the wave vector, q at different temperatures. b) $S(q)$ as obtained from the prediction of DFT theory, assuming a Lennard-Jones potential interaction between the corona chains, is compared with the result from HS theory. c) The peak height of the first peak in structure factor, $S(q_{\text{peak}})$ is seen to increase significantly with an increase in temperature. d) Comparisons of $S(q_{\text{peak}})$ and root mean-square distance between the chain center of mass and the core, $\langle R_{\text{cc}}^2 \rangle^{1/2}$ with scaled temperature T^* . e) Illustration showing the effect on the corona chains with temperature.	179
6.3 a) Relaxation modulus, $G(t)$ measured as a function of time for different temperatures, ranging from 70°C to 120°C . b) The material relaxation time, τ as obtained from the stretched exponential fits to $G(t)$ is seen to increase with an increase in temperature.	182
6.4 a) Characteristic overshoot recovery experiment, which measures the variation in the peak of stress overshoot, σ_{peak} with different delay times between successive measurements. Variation in σ_{peak} as a function of delay time for b) 70°C & 80°C , and c) 90°C & 100°C . e) The network strand dis-entanglement time, τ_e and the stress relaxation time of the material, τ_d , increase with temperature.	184
6.5 a) Normalized shear stress vs strain values obtained experimentally at shear rate= 0.01s^{-1} . b) Simulation results from prediction of the constitutive model on physically associating crosslinked gels, exhibiting qualitatively similar features as	

experiments.	189
7.1 Evolution of the loss maximum normalized with the zero strain value i.e. $G''/G''_{\gamma \rightarrow 0}$ as a function of the imposed oscillatory strain for a) $\phi_{PMMA}=0$ to 0.47 and b) $\phi_{PMMA}=0.57$ to 1. c) Energy dissipated per unit volume, U_d in yielding the hybrid particles as a function of ϕ_{PMMA} at different temperatures. d) The plateau modulus, G_e as obtained from the zero shear strain values of storage modulus from oscillatory shear measurements as a function of ϕ_{PMMA}	211
7.2 a) Experimental structure factor $S(q)$ as obtained from SAXS measurements for different compositions at 120°C, fitted with theoretical predictions from DFT analysis. b) Comparison of experimental inter-particle distance d_{p-p} (red closed circles) with theoretical d_{p-p} (black open squares) as obtained from DFT analysis. c) Variation in the surface-to-surface distance h and the number of monomers assumed to be a part of the core, n_m as a function of ϕ_{PMMA} . d) The first peak height in $S(q)$ given as $S(q_{peak})$ follows a non-monotonic variation with ϕ_{PMMA} , which is consistent with the observations made from surface-to-surface distance.	215
7.3 a) Variation in $1/T_m - 1/T_m^0$ as a function of ϕ_{PMMA}^2/T_m for untethered polymer chains fitted with Nishi-Wang equation. b) Heating of mixing ΔH_m obtained as a function of ϕ_{PMMA} at 120°C. c) Critical interaction parameter χ as obtained from equations 5a), 5b) and 5c) for the grafted polymer chains. d) Critical heat of mixing $\Delta H_{m(c)}$ as a function of ϕ_{PMMA} at 120°C, obtained for polymer chains grafted to particles.	219
7.4 Dielectric spectra of the loss modulus as a function of frequency at 120°C for a) untethered polymer chains, and b) tethered polymer chains for different compositions. Variation in $\ln(\tau)$ as obtained from H-N fitting as a function of temperature for c) $\phi_{PMMA}=0.06$ to 0.47, and d) $\phi_{PMMA}=0.57$ to 1.	223
7.5 a) Ratio of relaxation time of tethered to untethered polymer chains as a function of ϕ_{PMMA} b) Activation energy E_a as obtained from the Arrhenius fit to relaxation times increases with an increase in the fraction of PMMA for both the tethered and untethered chains. b) The dielectric strength $\Delta\epsilon$ however, follows a non-monotonic variation with ϕ_{PMMA} for both the tethered and untethered polymer chains.	226

LIST OF TABLES

2.1 Polydispersity in grafting densities as calculated from DFT	34
2.2 VFT fit parameters for noise temperature X for systems with different grafting densities.	38
6.1 VFT fit parameters for different relaxation time scales	185
6.2 Fit parameters for the crosslinked gel constitutive model	190

Chapter 1

Introduction

1.1 Polymer-Grafted Nanoparticles

It is well accepted now that addition of nanoparticles to a polymer melt, known as a polymer nanocomposite, can lead to a significant improvement in the mechanical, thermal, optical, and electrical properties of the materials.¹⁻¹¹ This unique combination which utilizes the properties of both the nanoscale inorganic fillers and the polymer matrix, makes the polymer nanocomposites a promising candidate to be used in variety of applications such as electronics, data storage, sustainable energy and environment, biomedicine etc.¹²⁻²² One of the main requirements for using these nanoparticles in various applications has been to design a well-dispersed state of the particles in the polymer host such that they do not aggregate.^{12,23-25} The nanometer length scales of the particles though provides them a high surface area to volume ratio, which results in large interfaces, however such small sizes also lead to strong van Der Waals forces of attraction which leads to the formation of irreversible aggregates.^{24,26-28} In addition to the van Der Waals attractive forces between the particles, the excluded volume interaction and depletion attraction forces experienced by the polymer hosts induces a strong particle-particle aggregation, which makes the controlled dispersion of nanoparticles in polymer hosts an extremely challenging task.²⁹⁻³¹

One of the obvious solutions to this problem has been to screen these attractive forces by grafting the surfaces of nanoparticles with long enough polymer chains, such that they sterically stabilize the particles and prevent their irreversible aggregation. Numerous experimental and theoretical studies have now advanced our understanding of controlling the dispersion of polymer grafted nanoparticles in a host matrix.³⁰⁻³³ Broadly, the tethered polymer chains when interpenetrated by the host matrix chains, which is referred to as the

“wetting” of the polymer brush, the overall configurational space of both the polymers increases which facilitates a uniform dispersion.^{34–36} Specifically, for spherical nanoparticles, the conformational space for the tethered polymer chains increases in proportion to the distance from the center of the sphere, due to the strong curvature of spherical nanoparticles, and hence favors dispersion.^{37–48} A significant amount of research has been devoted to understanding the phase stability for these nanocomposites as a function of polymer size, polymer chemistry and grafting densities. Some recent studies have shown that irrespective of particle size or chemistry, for high enough grafting density and same polymer architecture, a phase separation is observed when the ratio of P/N is greater than 5, such that P is the degree of polymerization of the host polymer and N is the degree of polymerization of the grafted chains.^{39,48–50} Since the chemistry of both the grafted and host matrix chains is same, the immiscibility of the longer polymer matrix chains is entropic and is attributed to “brush autophobicity”.^{33,41,51–}

56

To overcome these barriers, recent studies have emerged which have produced stable particle dispersion for even higher host molecular weights by utilizing enthalpic attraction between the grafted and the host polymer chains.^{57–59} However, since the phase stability of the polymer grafted nanoparticles in a host matrix is largely dependent on the molecular weights of both the grafted and host chains, we provide a different platform that avoids this issue of miscibility between the polymer chains and prevent particle aggregation. These polymer grafted nanoparticles referred to as Nanoscale Organic Hybrid Materials (NOHMs), have long enough polymer chains grafted on the surface of the particles but are not dispersed in any solvent.^{60–62}

1.2 Self-Suspended Hairy Nanoparticles

The solvent-less hairy nanoparticles, also called as the self-suspended hairy nanoparticles, can be thought of as a single component nanocomposite, where the host polymer matrix is chemically attached to the surface on the nanoparticles. Figure 1.1 a) shows a schematic of these solvent-less hairy nanoparticles. Since the suspended phase and the suspending medium are essentially the same for these particles, they are referred to as the self-suspended nanoparticles. Even in the absence of a solvent, the particles always exhibit a stable dispersion phase, as the grafted polymer chains not only provide steric stabilization to the particles but also play the role of the solvent for the particles, which allows them to be well-dispersed.^{62,63} The physical properties of these particles can be tuned by varying the core size, the molecular weight of the grafted corona chains, their grafting density, corona chemistry etc.⁶⁴⁻⁶⁷ These varied degrees of freedom allows us to alter the design of these solvent-less hairy nanoparticles such that they can be used to achieve a unique combination of optimized properties of the inorganic fillers and the organic polymer corona.

Since, the absence of a suspending medium implies that the grafted corona chains have to play the role of the solvent for the nanoparticles, this imposes a “space-filling” constraint on the grafted polymer chains. The core-core interactions are mediated by the grafted corona chains, and under the constraint of filling the space as a solvent for the particles, the grafted corona chains tend to uniformly suspend the particles.^{63,68} Density functional theory and simulation studies in fact show that the materials are analogous to incompressible molecular fluids, wherein each nanoparticle core carries a share of fluid with itself, excluding exactly one neighboring particle. This results in suppression of long

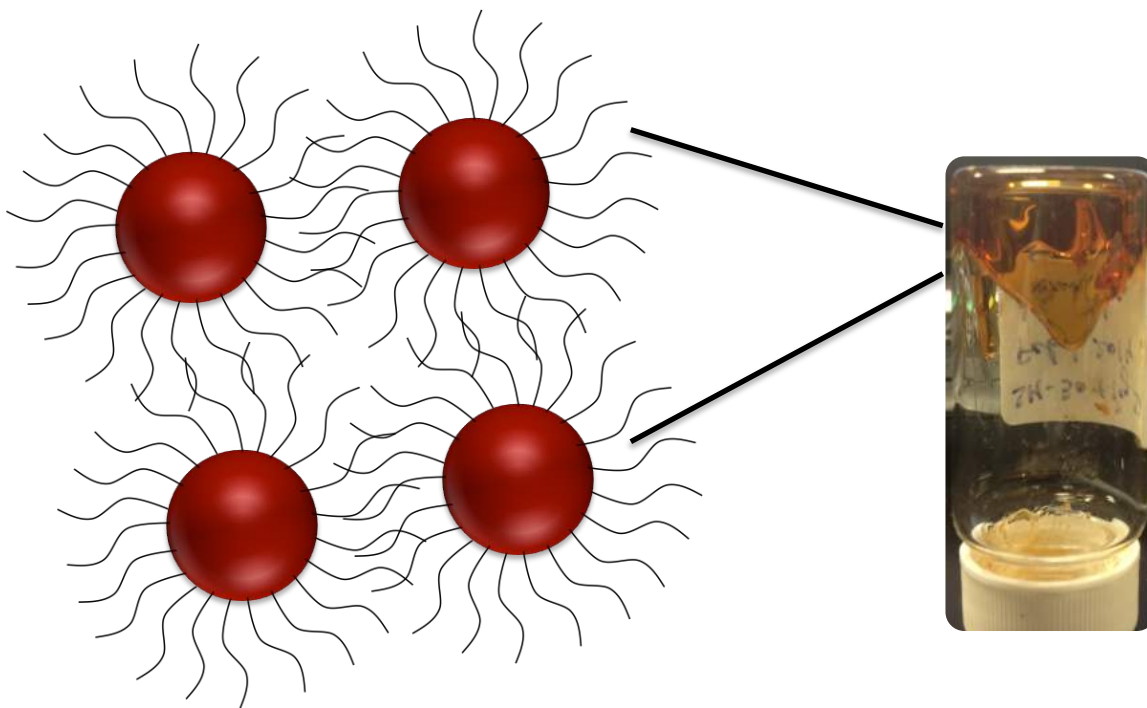


Figure 1.1 Schematic showing self-suspended hairy nanoparticles. Polymer chains are grafted to silica nanoparticles with no other suspending medium. The image shows liquid-like flow properties of these materials when high molecular weight chains are grafted.

wavelength density fluctuations in a monodisperse suspension of these particles, which drives a uniform dispersion of particles.^{63,68,69}

A recent body of work has been devoted to understanding the structure, rheology and dynamical properties of these materials.^{64,65,67,70-72} Specifically working with silica nanoparticles, a significant feature of these particles has been that they exhibit a characteristic soft-glassy behavior as seen in bulk rheology measurements.^{62,64,67} Furthermore, since the dispersing medium and the dispersed phase are the same, any complications arising due to enthalpic interactions can be minimalized and thus thermal properties of these materials can be investigated over a wide range of temperatures. These particles have emerged as model materials for understanding the structure and dynamics of a well-dispersed system of polymer grafted nanoparticles.

1.3 Goals and Methods

The present work aims to understand the fundamental physical properties of solvent-less hairy nanoparticles, and to utilize them to develop high ionic conducting electrolytes for applications in rechargeable lithium metal batteries. While in the previously studied self-suspended nanoparticles, the polymer chains were grafted ionically to the surface of the nanoparticles, the present work focuses on covalently grafted hairy nanoparticles. The most widely studied examples of these materials utilized an ionic linkage between the amine group of the polymer chain and silica particles functionalized with the sulfonic acid group. However, recent studies have shown that electrostatic interactions between an ionically linked particle core and corona can lead to complex layering of the charged core and corona.^{73,74} In particular, these authors found that the diffusivity of the grafted

polymeric chains does not correlate with the hard-sphere-like diffusivity of the core and instead point out that the exchange of polymers between a bilayer of chains tethered to the particles creates a dynamic interface between the particle core and polymer corona.⁷⁴ In a model self-suspended system of nanoparticles, this exchange is undesirable. The present work studies physical properties of covalently grafted hairy nanoparticles, where the ends of the amine terminated polymer chain is modified to silane chemistry which is known to form a strong covalent bond with silica.

In self-suspended hairy nanoparticles the dynamics of polymer chains is coupled with the dynamics of the core, which is again governed by the interactions mediated by the grafted corona chains. The goal of the present study is to understand the flow and structural properties, and in turn the interaction forces between the core and the corona chains. We perform rheological, dynamical and structural studies on particles of various core sizes, corona grafting densities, and corona chemistries. An underlying observation that emerges from these studies is that the degree of interaction of the corona chains from neighboring particles affects the mechanical and structural properties of these materials. We focus on ways to tune this degree of interaction by creating blends of particles with different core sizes and corona chemistries.

1.3.1 Flow and Structural Properties of Self-Suspended Hairy Nanoparticles

Though the self-suspended nanoparticles appear physically similar to a star polymer or a soft colloidal suspension, preliminary studies analyzing their dynamical and rheological properties have revealed that these analogies are merely superficial. For instance, while rheological measurements on NOHMs reveal a Newtonian flow behavior^{62,75} and show an intermediate relaxation time scale for the grafted chains like a star polymer^{65,66},

however the viscosity of the materials decreases with an increase in the molecular weight of the chains⁷⁵ or the relaxation time of the chains decreases with an increase in their molecular weight, which is in clear contrast to star polymers.^{66,76} Also, unlike typical colloidal suspensions increase in temperature leads to an enhanced jamming or solid-like behavior in NOHMs.⁶⁴

In the present study we explore these properties in detail and investigate how the changes in core sizes, corona grafting density, corona chemistry and temperature can influence the jamming and yielding behavior of these materials. We study the flow properties through conventional oscillatory and linear rheology measurements, while detailed information about the structural changes of these particles is obtained through Small Angle X-ray Scattering (SAXS) measurements when they are compared with the predictions from the theory developed by Yu and Koch.^{63,69} While the entropic contribution from the corona chains is altered by changing the core size and grafting density, effect of enthalpic contribution is also studied by blending particles with favorably interacting polymer chains.

1.3.2 Application of Hybrid Hairy Nanoparticles

Self-suspended hybrid materials can be tailored to utilize in a variety of applications. As the corona is covalently linked to the nanoparticle core, one is no longer constrained by chemistry that may favor phase separation. Tunability of corona chemistry has been utilized in certain studies to selectively capture CO₂⁷⁷⁻⁸⁰, while the changes in core chemistry can make materials that are magnetically or optically responsive⁸¹, or can work as efficient dry lubricants.^{82,83} Self-suspended nanocomposites based on densely grafted

ionic liquids^{84,85} and those with both oligomeric chains and molecular species have also been demonstrated as attractive candidates for electrolytes.^{17,25}

Numerous studies have focused on utilizing nanocomposites as electrolytes in rechargeable lithium metal batteries to make them portable, leakage free and non-flammable.^{22,86-90} The high modulus of inorganic fillers also suppresses uneven electrodeposition.⁹¹ Grafting polyethylene glycol (PEG) or ionic liquid to these nanoparticles not only provides a well-dispersed state for the particles, but they also facilitate ion transport through ion-hopping mechanism.^{17,20,25} Thus the mobility of the grafted chains plays a significant role in enhancing ion transport, and thus the conductivity of the electrolytes. In the present work, we utilize bi-dispersity in core size to increase the corona chain mobility. One of the major advantages of using a bi-disperse mixture is that it helps to design a hybrid electrolyte that has MPa elastic modulus and mS cm^{-1} ionic conductivities even at room temperature. In addition to this, these bi-disperse hybrid electrolytes exhibit exceptionally high voltage stability (>7 V) over extended times; protect Li metal anodes by forming a particle-rich coating on the electrode that allows stable, long-term cycling of the anode at high coulombic efficiency; and manifest low bulk and interfacial resistance at room temperature.

1.4 Outline

In the present work, we study the rheology, structural and dynamical properties of covalently grafted self-suspended nanoparticles in detail and explore the application of hybrid hairy nanoparticles as electrolytes in rechargeable lithium metal batteries. In Chapter 2, we discuss the synthesis and physical properties of covalently grafted solvent-

less silica nanoparticles. We investigate the conformational stability of the grafted polymer chains at various grafting densities using Fourier Transform Infrared Spectroscopy (FTIR) and Differential Scanning Calorimetry. The mesoscopic stability and homogeneity of the self-suspended hairy nanoparticles is examined in conjunction with bulk scale rheology measurements, which reveal a soft glassy fluid-like behavior for these materials. We find that contrary to star polymers or usual suspensions of polymer-grafted nanoparticles, reduction in grafting density leads to a higher degree of stretching of the grafted chains, which we propose arises due to increased entropic penalty on the corona chains to fill the interstitial space between the cores.

Chapter 3 discusses the role of bi-dispersity of core size in influencing the flow and dynamical properties of the self-suspended hairy nanoparticles. Using rheology and X-ray Photon Correlation Spectroscopy (XPCS) measurements, insights about the correlation between particle dynamics and the bulk mechanical properties of the materials are discussed. We discuss our findings in terms of ligand-mediated jamming and unjamming of hairy particle suspensions.

In Chapter 4, we utilize the understanding about the yielding behavior of a bi-disperse suspension and use it to enhance ion transport properties of the hybrid materials. We discuss about the enhanced mobility of grafted polymer chains, which mediate an increased ionic transport of lithium ions when bi-disperse hybrid particles are used as electrolytes by dispersing in an aprotic liquid host. We find that bi-dispersity allows these materials to have high ionic conductivities and higher modulus values at room temperature. They also exhibit low or no flammability which makes these materials promising candidates to be used as electrolytes for rechargeable lithium metal batteries.

Chapter 5 further discusses the use of bi-disperse suspensions of hybrid particles in improving the stability of a lithium metal battery. Bi-dispersity in core size helps in reducing interfacial and bulk resistance of the electrolytes; they protect the Li metal electrode by forming a particle rich coating on the surface which allows a stable, long-term cycling of the lithium anode with high columbic efficiency.

In Chapter 6 we discuss the phenomena of *thermal jamming* in self-suspended hairy nanoparticles, where we find that increase in temperature invokes enhanced jamming or more solid-like behavior in these materials. We utilize structural, dynamical and rheological studies to understand the molecular origins of this behavior. A theoretical comparison with physically associating polymer solutions or a physically cross-linked network is used to explain higher degree of stretching of corona chains which in turn leads to enhanced inter-digitation of the grafted chains with increase in temperature.

Chapter 7 discusses the effect of favorable enthalpic interactions between grafted polymer chains which lead to strong mechanical and structural response in the self-suspended particles. The corona chemistry is changed such that the polymers chains grafted on particles form a thermodynamically stable blend, and this increased enthalpic attraction between the polymer chains is used to mediate the interaction of the particles and influence their dynamics.

REFERENCES

- (1) Bockstaller, M. R.; Mickiewicz, R. A.; Thomas, E. L. *Adv. Mater.* **2005**, *17* (11), 1331–1349.
- (2) Krishnamoorti, R.; Vaia, R. A.; Giannelis, E. P. *Chem. Mater.* **1996**, *8*, 1728–1734.
- (3) Lebaron, P. C.; Wang, Z.; Pinnavaia, T. J. *Appl. Clay Sci.* **1999**, *15* (1-2), 11–29.
- (4) Krishnamoorti, R. *MRS Bull.* **2007**, *32* (April).
- (5) Lin, Y.; Boker, A.; He, J.; Sill, K.; Xiang, H. *Nature* **2005**, *404*, 55–59.
- (6) Mohammad, M.; Winey, K. I. *Macromolecules* **2006**, *39* (16), 5194–5205.
- (7) Oberdisse, J. *Soft Matter* **2006**, *2* (1), 29–36.
- (8) Vaia, R. A.; Maguire, J. F. *Chem. Mater.* **2007**, *19* (11), 2736–2751.
- (9) Winey, K. I.; Vaia, R. A. *Mrs Bull.* **2007**, *VOLUME 32* (APRIL), 314–358.
- (10) Payne, A. R. *J. Appl.* **1965**, *9*, 2273–2284.
- (11) Zhu, Z.; Thompson, T.; Wang, S.; von Meerwall, E. D.; Halasa, A. *Macromolecules* **2005**, *38* (21), 8816–8824.
- (12) Balazs, A. C.; Emrick, T.; Russell, T. P. *Science (80)*. **2006**, *314* (5802), 1107–1110.
- (13) Chapman, R.; Mulvaney, P. *Chem. Phys. Lett.* **2001**, *349* (5-6), 358–362.
- (14) Evans, L. *Annu. Rev. Mater. Res.* **2001**, *32*, 347–375.
- (15) Hussain, F.; Hojjati, M.; Okamoto, M.; Gorga, R. E. *J. Compos. Mater.* **2006**, *40* (17), 1511–1575.

- (16) Yoon, P. J.; Fornes, T. D.; Paul, D. R. *Polymer (Guildf)*. **2002**, *43* (25), 6727–6741.
- (17) Schaefer, J. L.; Moganty, S. S.; Yanga, D. A.; Archer, L. A. *J. Mater. Chem.* **2011**, *21* (27), 10094–10102.
- (18) Moganty, S. S.; Jayaprakash, N.; Nugent, J. L.; Shen, J.; Archer, L. A. *Angew. Chemie* **2010**, *122* (48), 9344–9347.
- (19) Choudhury, S.; Mangal, R.; Agrawal, A.; Archer, L. A. *Nat. Commun.* **2015**, *6*:10101, 1–9.
- (20) Agrawal, A.; Choudhury, S.; Archer, L. A. *RSC Adv.* **2015**, *5*, 20800–20809.
- (21) Choudhury, S.; Agrawal, A.; Wei, S.; Jeng, E.; Archer, L. A. *Chem. Mater.* **2016**, *28*, 2147–2157.
- (22) Srivastava, S.; Schaefer, J. L.; Yang, Z.; Tu, Z.; Archer, L. A. *Adv. Mater.* **2014**, *26* (2), 201–234.
- (23) Hussain, F. *J. Compos. Mater.* **2006**, *40* (17), 1511–1575.
- (24) Zhang, Q.; Archer, L. A. *Langmuir* **2002**, *18* (26), 10435–10442.
- (25) Nugent, J. L.; Moganty, S. S.; Archer, L. A. *Adv. Mater.* **2010**, *22* (33), 3677–3680.
- (26) Hooper, J. B.; Schweizer, K. S. *Macromolecules* **2005**, *38* (21), 8858–8869.
- (27) Hooper, J. B.; Schweizer, K. S. *Macromolecules* **2006**, *39* (15), 5133–5142.
- (28) Napper, D. H. *Ind. Eng. Chem. Prod. Res. Dev.* **1970**, *9* (4), 467–477.
- (29) Feigin, R. I.; Napper, D. H. *J. Colloid Interface Sci.* **1980**, *75* (2), 525–541.
- (30) Napper, D. H. *Polymeric stabilization of colloidal dispersions*; Academic Press: London, 1984.

- (31) Napper, D. H.; Netschey, A. *J. Colloid Interface Sci.* **1971**, *37* (3), 528–535.
- (32) Vincent, B. *Adv. Colloid Interface Sci.* **1974**, *4* (2-3), 193–277.
- (33) Sunday, D.; Ilavsky, J.; Green, D. L. *Macromolecules* **2012**, *45* (9), 4007–4011.
- (34) de Gennes, P. G. *Macromolecules* **1980**, *13* (19), 1069–1075.
- (35) Ferreira, P. G.; Ajdari, A.; Leibler, L. *Macromolecules* **1998**, *31* (12), 3994–4003.
- (36) Milner, S.; Witten, T.; Cates, M. *Macromolecules* **1988**, *21* (10), 2610–2619.
- (37) Akcora, P.; Liu, H.; Kumar, S. K.; Moll, J.; Li, Y.; Benicewicz, B. C.; Schadler, L. S.; Acehan, D.; Panagiotopoulos, A. Z.; Pryamitsyn, V.; Ganesan, V.; Ilavsky, J.; Thiagarajan, P.; Colby, R. H.; Douglas, J. F. *Nat. Mater.* **2009**, *8* (4), 354–359.
- (38) Green, D. L.; Mewis, J. *Langmuir* **2006**, *22* (18), 9546–9553.
- (39) Chevigny, C.; Dalmas, F.; Di Cola, E.; Gigmès, D.; Bertin, D.; Boué, F.; Jestin, J. *Macromolecules* **2011**, *44* (1), 122–133.
- (40) Oh, H.; Green, P. F. *Nat. Mater.* **2009**, *8* (2), 139–143.
- (41) Xu, C.; Ohno, K.; Ladmiral, V.; Composto, R. J. *Polymer (Guildf)*. **2008**, *49* (16), 3568–3577.
- (42) McEwan, M. E.; Egorov, S. A.; Ilavsky, J.; Green, D. L.; Yang, Y. *Soft Matter* **2011**, *7* (6), 2725.
- (43) Wang, X.; Foltz, V. J.; Rackaitis, M.; Böhm, G. G. A. *Polymer (Guildf)*. **2008**, *49* (26), 5683–5691.
- (44) Fischer, S.; Salcher, A.; Kornowski, A.; Weller, H.; Förster, S. *Angew. Chemie - Int. Ed.* **2011**, *50* (34), 7811–7814.
- (45) Inoubli, R.; Dagréou, S.; Lapp, A.; Billon, L.; Peyrelasse, J. *Langmuir* **2006**, *22* (15), 6683–6689.

- (46) Robbes, A. S.; Cousin, F.; Meneau, F.; Dalmas, F.; Schweins, R.; Gigmes, D.; Jestina, J. *Macromolecules* **2012**, *45* (22), 9220–9231.
- (47) Ndong, R. S.; Russel, W. B. *J. Rheol. (N. Y. N. Y.)* **2011**, *55* (2), 331.
- (48) Srivastava, S.; Agarwal, P.; Archer, L. A. *Langmuir* **2012**, *28* (15), 6276–6281.
- (49) Chevigny, C.; Jestin, J.; Gigmes, D.; Schweins, R.; Di-Cola, E.; Dalmas, F.; Bertin, D.; Boué, F. *Macromolecules* **2010**, *43* (11), 4833–4837.
- (50) Kumar, S. K.; Jouault, N.; Benicewicz, B.; Neely, T. *Macromolecules* **2013**, *46* (9), 3199–3214.
- (51) Iacovella, C. R.; Horsch, M. A.; Glotzer, S. C. *J. Chem. Phys.* **2008**, *129* (4).
- (52) Meli, L.; Arceo, A.; Green, P. F. *Soft Matter* **2009**, *5* (3), 533–537.
- (53) Zhao, L.; Li, Y.-G.; Zhong, C. *J. Chem. Phys.* **2007**, *126* (1), 014906.
- (54) Schadler, L. S.; Kumar, S. K.; Benicewicz, B. C.; Lewis, S. L.; Harton, S. E. *MRS Bull.* **2007**, *32* (04), 335–340.
- (55) Harton, S. E.; Kumar, S. K. *J. Polym. Sci. Part B Polym. Phys.* **2008**, *46*, 351–358.
- (56) Matsen, M. W.; Gardiner, J. M. *J. Chem. Phys.* **2001**, *115* (6), 2794–2804.
- (57) Mangal, R.; Srivastava, S.; Archer, L. A. *Nat. Commun.* **2015**, *6*:7198, 1–9.
- (58) Borukhov, I.; Leibler, L. *Macromolecules* **2002**, *35* (13), 5171–5182.
- (59) Borukhov, I.; Leibler, L. *Phys. Rev. E* **2000**, *62* (1), 41–44.
- (60) Bourlinos, A. B.; Ray Chowdhury, S.; Herrera, R.; Jiang, D. D.; Zhang, Q.; Archer, L. A.; Giannelis, E. P. *Adv. Funct. Mater.* **2005**, *15* (8), 1285–1290.
- (61) Bourlinos, A. B.; Herrera, R.; Chalkias, N.; Jiang, D. D.; Zhang, Q.; Archer, L. A.; Giannelis, E. P. *Adv. Mater.* **2005**, *17* (2), 234–237.
- (62) Agarwal, P.; Qi, H.; Archer, L. A. *Nano Lett.* **2010**, *10* (1), 111–115.

- (63) Yu, H.-Y.; Koch, D. L. *Langmuir* **2010**, *26* (22), 16801–16811.
- (64) Agarwal, P.; Srivastava, S.; Archer, L. A. *Phys. Rev. Lett.* **2011**, *107* (26), 268302–1 – 5.
- (65) Agarwal, P.; Kim, S. A.; Archer, L. A. *Phys. Rev. Lett.* **2012**, *109* (25), 258301–1 – 4.
- (66) Kim, S. A.; Mangal, R.; Archer, L. A. *Macromolecules* **2015**, *48* (17), 6280–6293.
- (67) Choudhury, S.; Agrawal, A.; Kim, S. A.; Archer, L. A. *Langmuir* **2015**, *31*, 3222–3231.
- (68) Chremos, A.; Panagiotopoulos, A. Z.; Yu, H.-Y.; Koch, D. L. *J. Chem. Phys.* **2011**, *135* (11), 114901.
- (69) Yu, H.-Y.; Srivastava, S.; Archer, L. A.; Koch, D. L. *Soft Matter* **2014**, *10* (45), 9120–9135.
- (70) Agarwal, P.; Archer, L. A. *Phys. Rev. E* **2011**, *83* (4), 041402–1 – 5.
- (71) Kim, S. A.; Archer, L. A. *Macromolecules* **2014**, *47*, 687–694.
- (72) Agrawal, A.; Yu, H.-Y.; Srivastava, S.; Choudhury, S.; Narayanan, S.; Archer, L. A. *Soft Matter* **2015**, *11*, 5224–5234.
- (73) Fernandes, N. J.; Wallin, T. J.; Vaia, R. A.; Koerner, H.; Giannelis, E. P. *Chem. Mater.* **2013**, *26*, 84–96.
- (74) Jespersen, M. L.; Mirau, P. A.; Meerwall, E.; Vaia, R. A.; Rodriguez, R.; K, E. P. *G.* **2010**, *4* (7), 3735–3742.
- (75) Srivastava, S.; Agarwal, P.; Mangal, R.; Koch, D. L.; Narayanan, S.; Archer, L. A. *ACS Macro Lett.* **2015**, *4* (10), 1149–1153.
- (76) Doi, M.; Kuzuu, N. *J. Polym. Sci. B Polym. Lett. Ed.* **1980**, *18* (12), 775–780.

- (77) Petit, C.; Park, Y.; Lin, K. Y. A.; Park, A. H. A. *J. Phys. Chem. C* **2012**, *116* (1), 516–525.
- (78) Lin, K. Y. A.; Park, A. H. A. *Environ. Sci. Technol.* **2011**, *45* (15), 6633–6639.
- (79) Park, Y.; Decatur, J.; Lin, K.-Y. A.; Park, A.-H. A. *Phys. Chem. Chem. Phys.* **2011**, *13* (40), 18115.
- (80) Park, Y.; Shin, D.; Jang, Y. N.; Park, A. H. A. *J. Chem. Eng. Data* **2012**, *57* (1), 40–45.
- (81) Bhattacharjee, R. R.; Li, R.; Estevez, L.; Smilgies, D.-M.; Amassian, A.; Giannelis, E. P. *J. Mater. Chem.* **2009**, *19*, 8728.
- (82) Kim, D.; Archer, L. *Langmuir* **2011**, 3083–3094.
- (83) Zhang, Y.; Gu, S.; Yan, B.; Ren, J. *J. Mater. Chem.* **2012**, *22* (30), 14843.
- (84) Lu, Y.; Korf, K.; Kambe, Y.; Tu, Z.; Archer, L. A. *Angew. Chemie* **2014**, *126* (2), 498–502.
- (85) Lu, Y.; Das, S. K.; Moganty, S. S.; Archer, L. A. *Adv. Mater.* **2012**, *24* (32), 4430–4435.
- (86) Croce, F.; Sacchetti, S.; Scrosati, B. *J. Power Sources* **2006**, *162* (1), 685–689.
- (87) Bruce, P. G.; Scrosati, B.; Tarascon, J.-M. *Angew. Chem. Int. Ed. Engl.* **2008**, *47* (16), 2930–2946.
- (88) Croce, F.; Appetecchi, G. B.; Persi, L.; Scrosati, B. **1998**, *394* (July), 456–458.
- (89) Kashiwagi, T.; Du, F.; Douglas, J. F.; Winey, K. I.; Harris, R. H.; Shields, J. R. *Nat. Mater.* **2005**, *4* (12), 928–933.
- (90) Tang, C.; Hackenberg, K.; Fu, Q.; Ajayan, P. M.; Ardebili, H. **2012**, 1152–1156.

- (91) Gurevitch, I.; Buonsanti, R.; Teran, A. A.; Gludovatz, B.; Ritchie, R. O.; Cabana, J.; Balsara, N. P. *J. Electrochem. Soc.* **2013**, *160* (9), A1611–A1617.

Chapter 2

Self-Suspended Suspensions of Covalently Grafted Hairy Nanoparticles¹

Reproduced with permission from
Snehashis Choudhury*, Akanksha Agrawal*, Sung A Kim, Lynden A. Archer, Self-suspended
suspensions of covalently grafted hairy nanoparticles, *Langmuir*, 2015, 31(10), 3222-3231.
Copyright © 2015, American Chemical Society

¹ S. Choudhury and A. Agrawal contributed equally to this work

2.1 Abstract

Dispersions of small particles in liquids have been studied continuously for almost two centuries for their ability to simultaneously advance understanding of physical properties of fluids and their widespread use in applications. In both settings, the suspending (liquid) and suspended (particle) phases are normally distinct and uncoupled on long length and time-scales. In this study, we report on the synthesis and physical properties of a novel family of covalently grafted nanoparticles that exist as self-suspended suspensions with high particle loadings. In such suspensions, we find that the grafted polymer chains exhibit unusual, multiscale structural transitions and enhanced conformational stability at sub-nanometer and nanometer length scales. On mesoscopic length-scales, the suspensions exhibit exceptional homogeneity and colloidal stability, which we attribute to steric repulsions between grafted chains, which prevent close contact, and a space filling constraint on the tethered chains, which inhibits phase segregation. On macroscopic length scales, the suspensions exist as neat fluids, which exhibit soft glassy rheology and, counter-intuitively, display enhanced elasticity upon increasing temperature. This feature is discussed in terms of increased interpenetration of the grafted chains and jamming of the nanoparticles.

2.2 Introduction

Dispersions of small particles in simple liquids have been studied for at least a century to understand their interaction forces and dynamics¹⁻⁴. In recent years interest in suspensions of particles with nanometer-sized dimensions has grown in response to their exceptional promise for applications in multiple fields of technology. In medicine, they are receiving increasing attention as therapeutics^{5,6} and for biomedical imaging⁷⁻¹⁰. In

energy harvesting and storage, nanosize particles have been reported to provide attractive attributes when used as tunable components in the anode, cathode, or electrolyte¹¹⁻²⁴. Because of the small size of the particles, surface forces dominate and the difficulty in preparing dispersions of un-aggregated nanoparticles is well known and extensively studied. This challenge has nevertheless hindered fundamental studies of the materials and delayed progress in understanding their colloidal science²⁵⁻²⁷. A variety of approaches have been reported in the literature for controlling phase stability of large and small particles. Only two are regarded as sufficiently versatile to be employed in practice: electrostatic stabilization^{28,29} using charges physically adsorbed to the particle surface in solution; and steric stabilization using physically/chemically attached polymers³⁰⁻³⁵. Recently, the concept of solvent-less nanoparticle fluids has been proposed, which structurally resemble block copolymers micelles and multi-arm star polymers³⁶⁻⁴². These nanoparticle fluids are comprised of polymer chains grafted to nanoparticles at such high coverage that the particles exhibit remarkable phase stability and fluidity in the absence of a solvent^{25,43,44}. Theoretical studies show that the exceptional colloidal stability of such *self-suspended suspensions* arise from two sources, steric forces between the tethered polymer chains and by the space filling constraints these chains experience in the absence of any suspending medium^{45,46}. Density functional theoretical and molecular simulation studies further show that each nanoparticle in a self-suspended material carries its own share of the suspending fluid (the tethered polymer) on its back such that exactly one neighboring core is excluded by each hairy nanoparticle. This feature of the materials simultaneously make them analogous to incompressible, single-component fluids comprised of molecular units and leads to a vanishing structure factor $S(q \rightarrow 0) = 0$ ^{45,46}

and good model systems for understanding interactions, structure, and dynamics of soft colloids⁴⁵⁻⁴⁹.

A fundamental question that arises in the context of using self-suspended materials as model systems for soft colloids arises from the fidelity of the ligand coupling³⁴⁻³⁵ possible with the ionic sulfonic acid – amine bond most commonly used for creating the most widely studied materials^{25,43,50}. Additionally, recent work by Fernandez et al. show that electrostatic interactions between ionically linked core and corona can lead to leading to complex layering of the charged core and corona⁵¹. In particular, these authors found that the diffusivity of the grafted polymeric chains do not correlate with the hard sphere like diffusivity of the core^{51,52} and contended that exchange of polymers between a bilayer of chains tethered to the particles creates a dynamic interface between the core and polymer^{51,52}. In a model self-suspended system of nanoparticles, this exchange is undesirable. Herein we report a synthesis strategy for creating truly self-suspended suspensions of nanoparticles in which polymeric ligands are covalently grafted to nanoparticles at coverage where the system spontaneously exhibits a homogeneous fluid state in the absence of any solvent. The materials open new opportunities for both fundamental studies and for applications where the particles must be exposed to high-dielectric constant, polar solvents that may dissociate the polymer-particle linkages in their ionic counterparts. We show by means of scattering experiments and rheology that the materials are self-suspended, exhibit hierarchical structure, and soft glassy fluid rheology.

2.3 Experimental Section

2.3.1 Synthesis of self-suspended covalently grafted nanoparticles

Figure 2.1(a) shows the reaction scheme used for the synthesis. Briefly these covalently grafted hairy nanoparticles are synthesized in a two-step process in which the polymer is first functionalized with a silane group, after which it is grafted to the silica nanoparticle surface. In the first step of reaction, the Polymer (in this case Polyethylene Oxide,) was attached to a Silane group, by the reacting the isocyanate group in 3-(Triethoxysilyl) propyl isocyanate (purchased from Sigma Aldrich) to the amine group present in Amino-Polyethylene Oxide (MW~5000Da, PDI~1.1, purchased from Polymer Source) in stoichiometric ratio, creating a stable urethane bond between the core and corona. In the next step, the silanized PEO is reacted to the hydroxyl groups on the surface of silica nanoparticle(SM-30, Sigma Aldrich), with diameter $10\text{nm}\pm 2\text{nm}$ (see supplementary figure 2.1) The excess polymer chains were removed from the system by repeated centrifugation in a chloroform-hexane mixture. This is an important step, in order to make sure that there are no extra polymeric chains other than what is carried by the nanoparticles. The inorganic content of these hairy nanoparticles was analyzed after each centrifuge cycle using Thermo-gravimetric Analysis (TGA) on TGA Q1000 (TA Instruments). The inorganic content was found to reduce with successive cycles, finally reaching a constant value. The TGA for different samples revealed an inorganic content of 16.97%, 26.03%, 37.21% and 42% corresponding to grafting density of approximately 1.18 chains/nm^2 , 1.03 chains/nm^2 , 0.703 chains/nm^2 and 0.576 chains/nm^2 , respectively.

2.3.2 Characterization

The sample for Transmission Electron Micrograph(TEM) was prepared by solvent casting method. Dilute suspensions of the nanoparticles in chloroform were dropped on

copper grids, which were subsequently annealed at 65°C for 24 hrs to ensure complete evaporation of chloroform and uniform particle dispersion.

¹H NMR (Nuclear Magnetic Resonance) spectra were collected on NOVA 600 MHz NMR operating at 599.50 MHz at 25°C to confirm the formation of covalent bond. The chemical shifts were referenced to CDCl₃ as standards. 2D ¹H-¹³C short-range correlation spectra were recorded through edited HSQC (Heteronuclear Single Quantum Correlation) using HSQCAD sequence in CDCl₃. HMBC (Heteronuclear Multiple Bond Correlation) experiment was performed with gradient HMBCAD sequence in CDCl₃ for long-range correlation. Melting temperature of tethered and free PEO chains were studied using Differential Scanning Calorimetry on a DSC Q2000 (TA Instruments).

Further analysis of chain conformations was done using Attenuated Total Reflectance-Fourier Transform Infrared Spectroscopy (ATR FT-IR) on a Nicolet iS10 FTIR spectrometer (Thermo Fisher Scientific) equipped with deuterated triglycine sulfate (DTGS) detector and SMART iTR diamond ATR accessory.

2.3.3 Small Angle X-ray Scattering measurements

Small Angle X-ray Scattering (SAXS) measurements were performed at Station D1 of Cornell High Energy Synchrotron Source (CHESS) using a point collimated X-ray beam. Samples were smeared on a thermal sample cell and the measurements were performed at different temperatures above melting temperature of PEO. The measured scattering intensity, $I(q)$ depends on wave vector q and particle volume fraction φ as:

$$I(q, \varphi) = P(q)S(q, \varphi) \quad (1)$$

Where, $P(q)$, and $S(q, \varphi)$ represent the particle form factor and the inter-particle structure factor. Since in the limit of infinite dilution $S(q, \varphi \rightarrow 0) \sim 1$, the particle form factor can thus

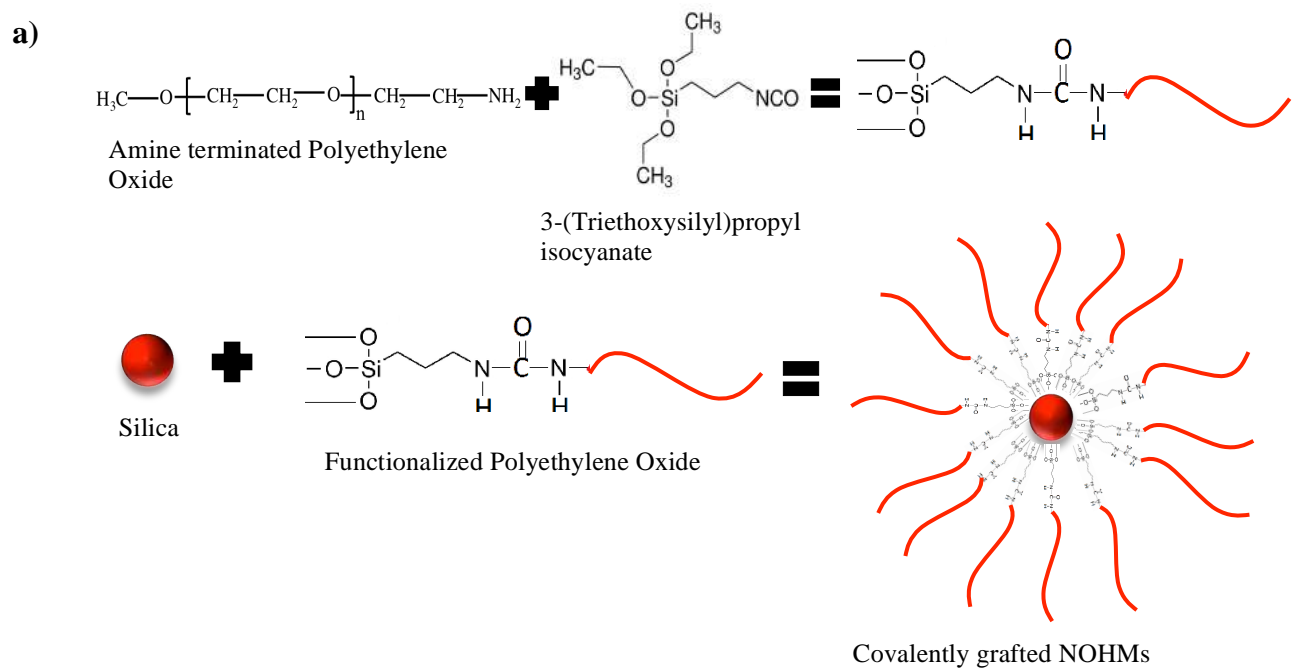
be obtained from the scattering intensities of dilute aqueous suspensions of particle. The structure factor can then be obtained by normalizing the scattered intensity with the form factor.

2.3.4 Rheology measurements

Oscillatory Shear Measurements were performed on an MCR501 (Anton Paar) Rheometer using a 10mm cone and plate fixture at temperatures ranging from 70°C to 150°C. All the suspensions were presheared to erase any strain history. Variable amplitude oscillatory measurements were performed at a fixed angular frequency of $\omega=10$ rad/s.

2.4 Results and Discussion

On macroscopic length scales, these materials exhibit liquid-like behavior, even in the absence of a solvent as evident from Figure 2.1(b), while at nano-scale, as observed from the Transmission Electron Micrograph (TEM) for these systems, shown in Figure 2.1(c), each nanoparticle is uniformly dispersed and well segregated from each other. It is remarkable that there is no aggregation or phase separation in the sea of nanoparticles. The formation of covalent bond is mapped using FTIR and NMR techniques. Figure 2.2(a) shows the Infra-red Spectra for Monoamine terminated Polyethylene oxide, Silane Propyl Isocyanate and the Silane terminated PEO. It is clearly observed that the $-NCO$ peak (2270cm^{-1}) present in the Silane Propyl Isocyanate is consumed, while in the Silane terminated PEO, there is evidence of the formation of the urethane bond indicated by the $-NH$ bond (3350cm^{-1}) and $-C=O$ bond (1640cm^{-1})⁵³. Also, to further confirm the reaction step, two-dimensional HSQC and HMBC NMR experiments were performed on



b)

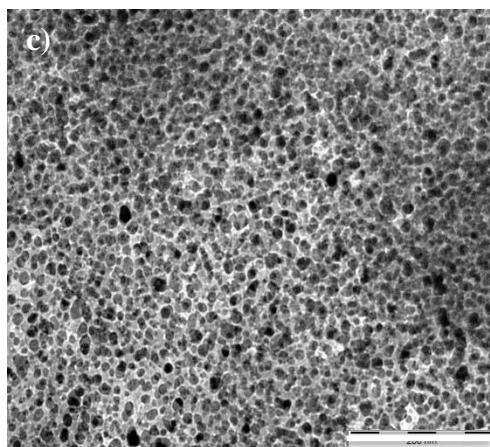


Figure 2.1 **a)** Reaction schematic for synthesizing the functionalized PEO and then tethering it to silica. **b)** Upright vial showing liquid-like behavior of solvent-less covalently grafted nanoparticles. **c)** Typical transmission electron microscopy (TEM) image of the covalently grafted hairy nanoparticles. The scale for the TEM image is 200nm.

Silanized PEO (see Supplementary figure 2.2). Figure 2.2(b), shows the ^1H NMR spectrum with structural assignments of the functionalized PEO. All the chemical species and bonds in the expected structure of the Silanized PEO are observed in the NMR spectrum. This confirms the formation of a covalent bond between silane isocyanate and the PEO chain.

The stability of these covalently grafted particles is contrasted with their ionic counterparts using ultracentrifuge at 10000 rpm for one hour in water. Supplementary figure 2.3 (a,b) in shows the inorganic content of the ionic and covalently grafted hairy nanoparticles before and after ultracentrifugation in water. Owing to the ionic linkage and dissociation of ions in a high-dielectric constant medium, there is a noticeable loss of polymer chains in the ionically grafted materials under a high centrifugal force in the presence of water. This can be contrasted with the covalently grafted materials where the net polymer content is essentially completely preserved after ultracentrifugation under the same conditions! Further, it is shown in Supplementary figure 2.3(c), that the amplitude sweep curves obtained from rheological measurements overlap for samples before and after ultracentrifugation. It has been previously reported that an untethered PEO has three melting peaks owing to three types of crystallites while there is just one melting peak (single crystallite) present in tethered PEO polymer⁵⁴. Figure 2.2(c) indeed shows the reduction of melting modes from three to one in the DSC thermogram of PEO after the above steps, again confirming the absence of free chains and covalent linkage of the PEO onto silica particles. The reduction of the degrees of freedom in polymer chains by surface confinement has been previously reported to lead to stable conformations^{54,55}. Figure 2.3(a) reports results from FTIR measurements on covalent SiO_2 -PEO systems

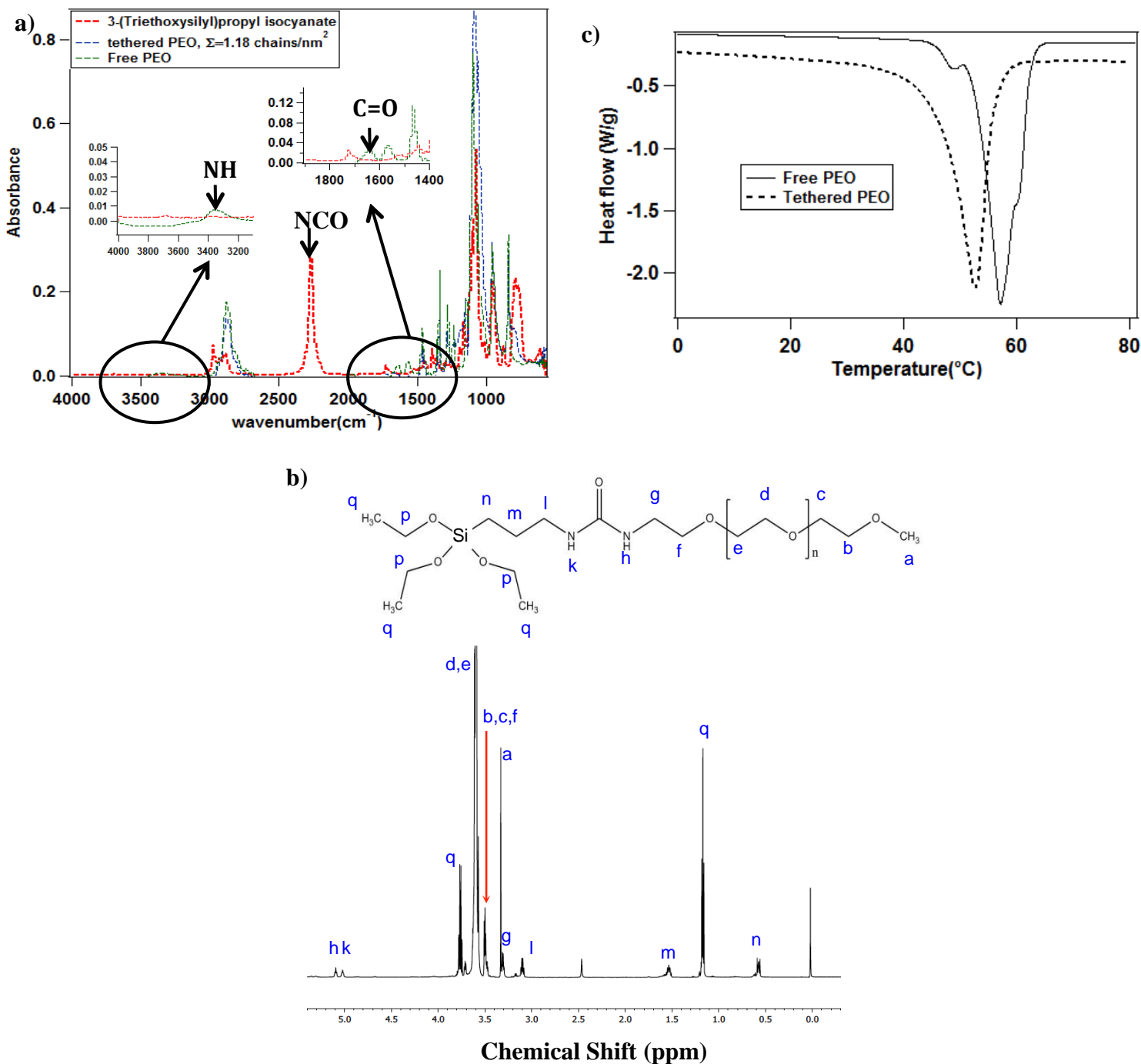


Figure 2.2 a) FT-IR spectra of tethered PEO chain, free PEO and 3-(Triethoxysilyl)propyl isocyanate. b) ^1H NMR spectra with structural assignments of functionalized PEO. c) DSC thermograms of free PEO (solid line) and tethered PEO chains (dashed lines). Free PEO chains have three types of crystallite structures-extended, once folded and twice folded- as seen on going from high to low temperature corresponding to the three peaks while the tethered chains have just the extended type crystallite structure and thus only one peak in the DSC.

with different grafting densities. For a PEO polymer, the chain conformations can be determined using the relative intensities of the FTIR peaks^{18,54,56,57}. It has been previously reported that the most stable conformation in a PEO strand is trans-trans-gauche, followed by trans-trans-trans in (-O-CH₂-CH₂) which, ultimately form the building blocks for helix-like and zigzag unit cells, respectively^{18,54,56,57}. These hairy nanoparticles can be characterized using only C-C trans and gauche conformation modes of the CH₂ (1342-1360cm⁻¹) (shown in Supplementary Table 2.1). The relative FTIR intensities were measured exactly by de-convolution the peak using Gaussian function (shown in Supplementary figure 2.4). Figure 2.3(b) and 2.3(c) show relative conformational abundance in angstrom scale and nanometer scale respectively. The tethered PEO chains are shown to have higher abundance of gauche conformations at lower grafting density (shown in Figure 3(b)). It is known that the gauche state has lower energy compared to the trans state in a C-C bond^{18,54}. Thus, it can be concluded that at the molecular level the PEO chains are more thermodynamically stable when tethered at a lower grafting density. At the mesoscale, the helix and zigzag type unit cells were counted by adding up the intensities at each assigned peak, as given in Supplementary Table 2.1. Figure 2.3(c) shows the proportion of these two types of structures at various grafting densities (Σ). Again, the PEO chains in lower grafting densities are seen to have higher stability owing to the fact that the helix unit cell is more stable than the zigzag type^{18,54}.

Small Angle X-ray Scattering (SAXS) measurements were employed to study structural changes in the materials as the grafting density of tethered chains is varied. The scattering intensities shown in Supplementary figure 2.5, show the absence of an upturn in low q region⁵⁸, which indicates that the particles are well-dispersed with no aggregation or

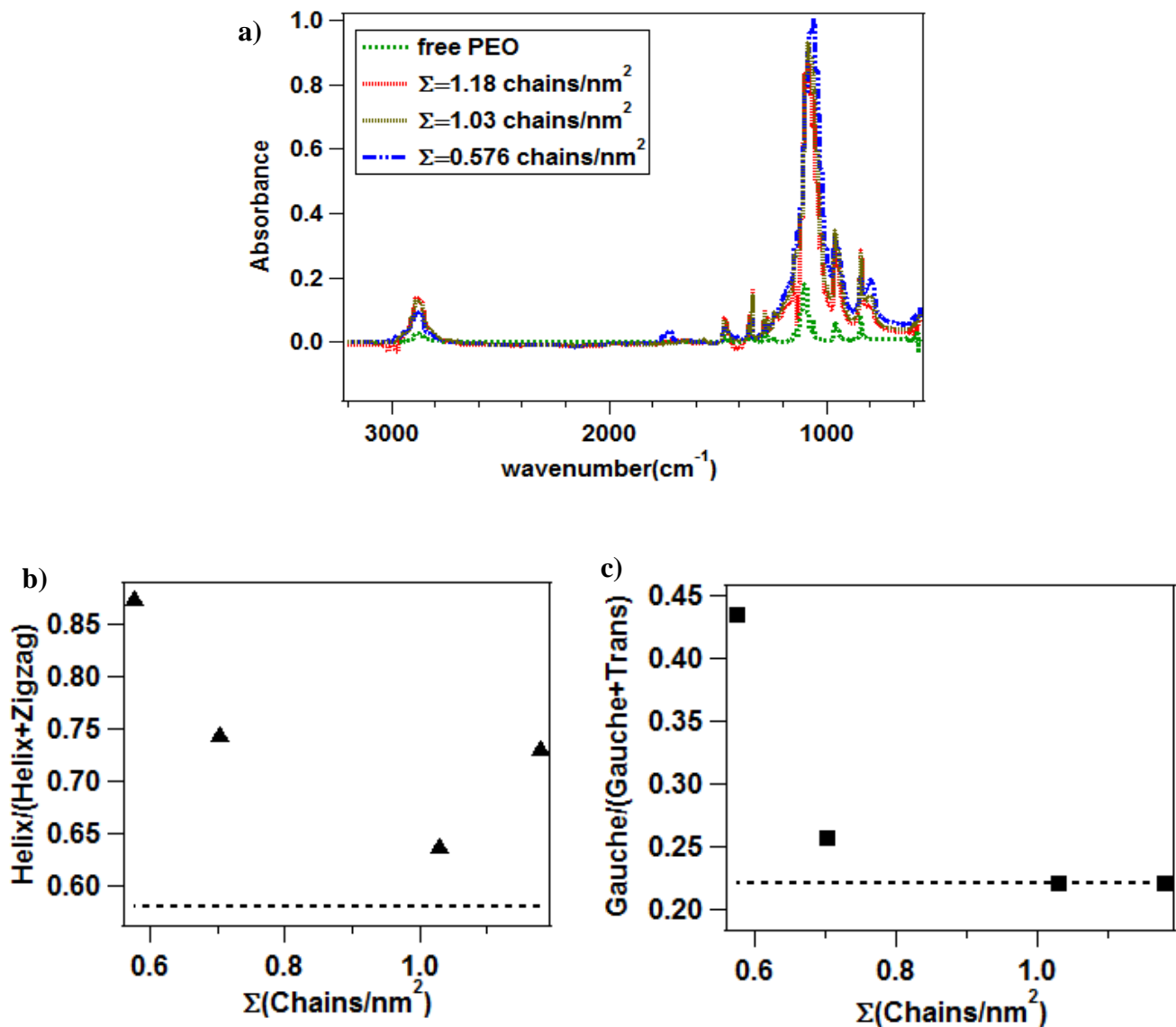


Figure 2.3 a) FT-IR spectra for tethered PEO chains with different grafting densities and for free PEO chain. b) Intensity ratios as obtained from the Gaussian fitting between helix and zigzag structures of tethered (squares) and free (dashed line) PEO chains c) Intensity ratio between gauche (wavenumber ≈ 1357 cm⁻¹) and trans (wavenumber ≈ 1342 cm⁻¹) conformations of C-C bonds of tethered (triangles) and free (dashed line) PEO chain. Decrease in grafting density leads to increased helix and gauche conformations for the tethered chains, indicating enhanced stability.

phase separation. Figure 2.4 reports the structure factor $S(q)$ for different grafting densities (Σ) as a function of the wave vector q non-dimensionalised with the particle core radius a . The structure factors determined from experiment are compared with the predictions from DFT theory for self-suspended NOHMs^{45,59}, and with reference hard-sphere systems. It is evident from Figure 2.4 that both the experiment and DFT theory show stronger peaks in $S(q)$ than the corresponding hard-sphere suspensions, which indicate an enhanced particle-particle correlation. Also, the first peak is shifted to a smaller q value, which implies a larger inter-particle separation due to steric repulsion from the chains, and lower $S(q)$ values in the low q region is a direct manifestation of the entropic penalty imposed on the tethered chains to uniformly fill the spaces between the cores.⁴⁵ A notable feature of the self-suspended covalently grafted nanoparticles is the presence of a stronger first peak than the second peak in $S(q)$. The first peak is now understood to be an indication of the steric repulsion of the chains while the second peak is a reflection of entropic attraction between the chains. In contrast to previous observations in ionically grafted particles,⁵⁹ where the first peak was found to be weaker for densely grafted systems, the stronger first peak observed for the present systems even at higher grafting densities is a consequence of the permanent bond between the chains and the particle surface. Remarkably, this observation of a weaker second peak has also been observed in computer simulations of self-suspended particles⁴⁷. It was postulated that this trend reflects the fact that chains in covalently grafted hairy nanoparticles are directly tethered to the surface of the core as opposed to previous studies where electrostatic interactions between the positively charged core with negatively charged corona^{52,59} produced stronger $S(q)$ peaks at higher q . The recently developed DFT

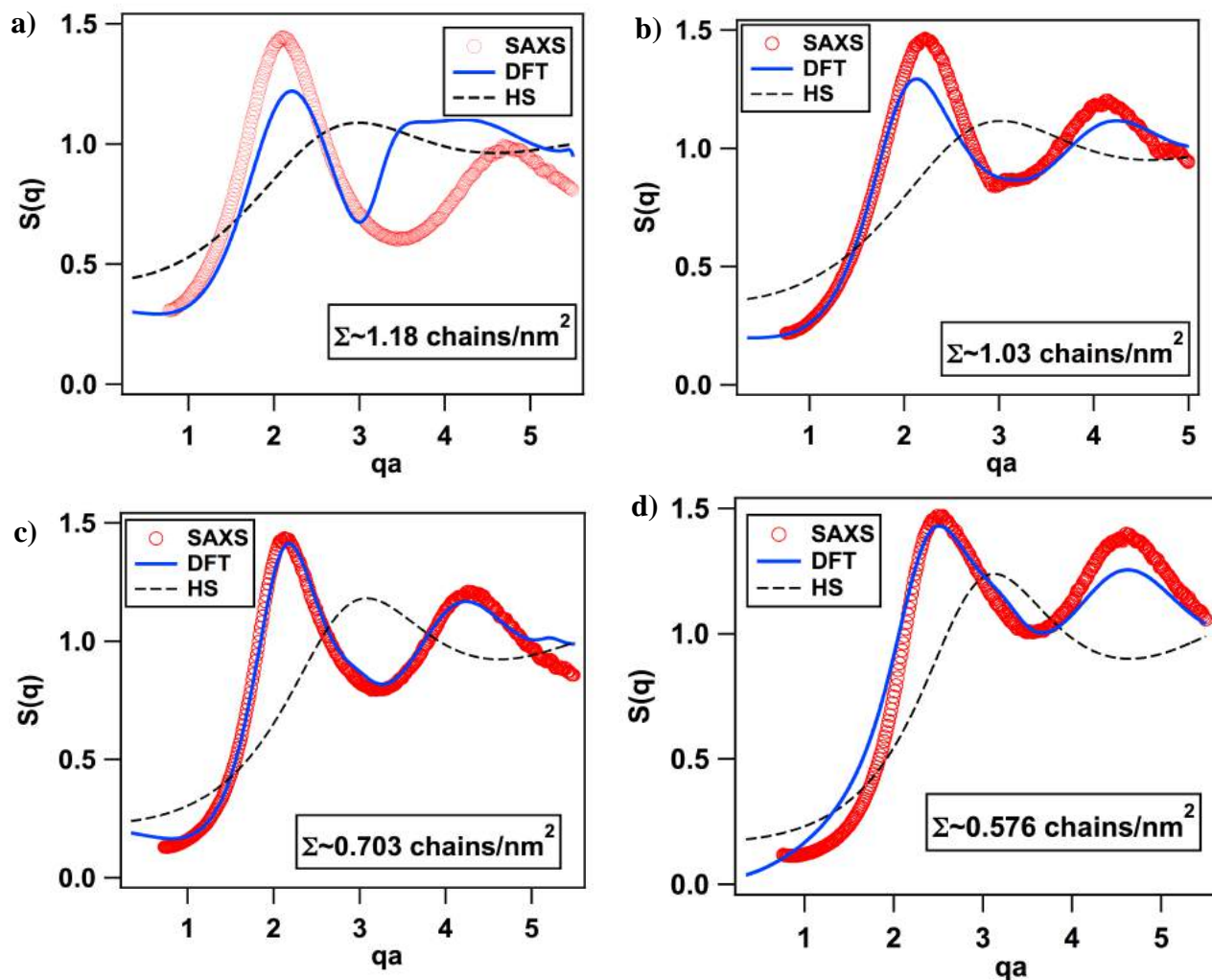


Figure 2.4 Structure factor, $S(q)$ varies with the wave vector non-dimensionalized with the core radius, qa for **a)** $\Sigma \sim 1.18$ chains/nm² **b)** $\Sigma \sim 1.03$ chains/nm² **c)** $\Sigma \sim 0.703$ chains/nm² and **d)** $\Sigma \sim 0.576$ chains/nm². The red circles are for experimental values, the blue solid lines represent DFT fit and the dotted black lines are for hard-sphere calculations.

theory⁵⁹ predicts polydispersities in core size and grafting densities to fit the experimental data. Supplementary figure 2.1 shows the polydispersity in core size, as extracted from Gaussian fitting of a dilute suspension of the silica nanoparticles. It shows an average size of $10\pm 2\text{nm}$, which corresponds to a polydispersity of 20% in core size. On assuming a polydispersity of 20% in core size, as extracted from Gaussian fitting of the dilute suspension of silica nanoparticles (Supplementary figure 2.1), we obtain the polydispersities in grafting density for different systems from DFT, as reported in Table 2.1. It can be noted that with increasing Σ , or decreasing particle volume fraction, the polydispersity in grafting density increases. This suggests that the stronger entropic constraints on the chains at lower volume fraction can be released more efficiently by introducing more polydispersity in the grafting density. Figure 2.5a) compares the inter-particle distance, d_{p-p} extracted from the first peak position of $S(q)$ with Σ . It can be seen that the inter-particle distance increases with Σ which is not surprising as higher grafting density means that the tethered chains are more effective in keeping the cores apart, and thus exhibit an effectively higher steric repulsion as compared to systems with lower grafting density. The experimental d_{p-p} is found to be roughly consistent with the theoretical estimate of $d_{p-p}=2a(0.63/\phi)^{1/3}$, where ϕ is particle volume fraction. A similar trend is manifested in the decrease of peak height of first peak $S(q_{peak})$ (Figure 2.5(b)) with increasing grafting density. Since densely tethered cores are able to push each other more due to stronger steric repulsion by the tethered chains, this results in a decrease of correlation amongst the nearest neighbors as opposed to the sparsely tethered cores where the chains are not able to stretch out as much and thus the particles are much closer, and the correlation is hence much enhanced. A potentially even more interesting feature is the

Table 2.1. Polydispersity in grafting densities as calculated from DFT.

Grafting density (chains/nm²)	Polydispersity in grafting density(%)
1.18	42%
1.03	35%
0.703	20%
0.576	5%

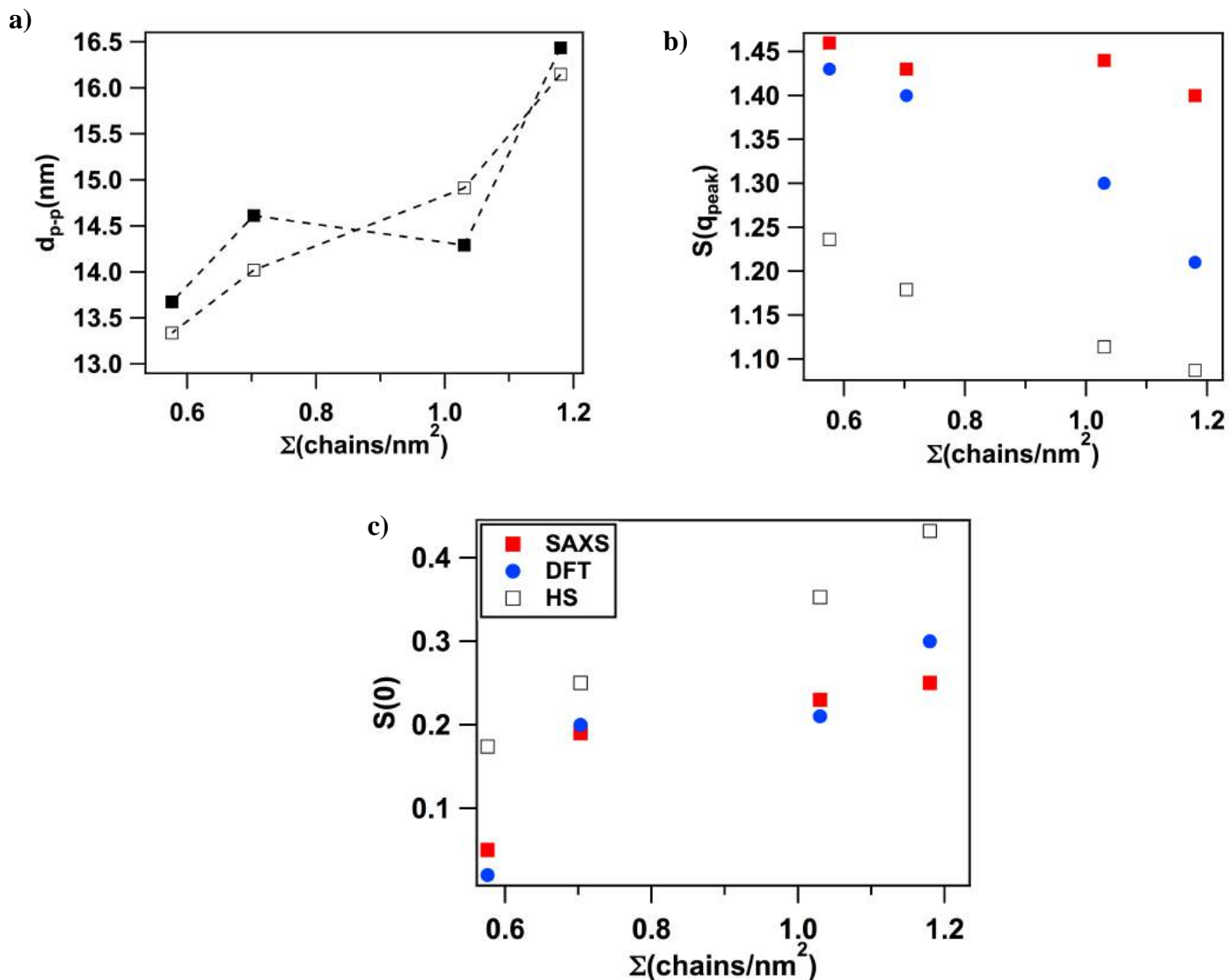


Figure 2.5 a) Inter-particle distance, d_{p-p} extracted from the experimental $S(q)$ (closed symbols) increases with grafting density. A similar trend is observed for theoretical d_{p-p} (open symbols). The dashed lines are guide to the eye. b) The height of first peak of $S(q)$ decreases while the c) $S(0)$ values increases with increase in grafting density. The experimental values agree well with DFT, while the HS $S(0)$ are seen to be higher.

increasing $S(q)$ value at low $q \rightarrow 0$ with the increase in Σ , as shown in Figure 2.5(c). A lower $S(0)$ value at lower grafting densities indicates a more uniform distribution for particles than at higher grafting densities. The $S(0)$ value for experimental systems was extracted by performing a quadratic fit for $S(q)$ in the low q region ($qa < 1.5$) and was then extrapolated to $q=0$. It is noteworthy, that the $S(0)$ values for experiment are comparable to theory and are much lower than the hard sphere values, which is strong evidence of a more uniform distribution for self-suspended particles as opposed to hard spheres.

We performed oscillatory shear experiments at variable shear strain to investigate the properties of these self-suspended nanoparticles on macroscopic length scale. The observed material response (inset of Figure 2.6(a)) is typical of a soft glass^{43,60,61} wherein the storage modulus G' dominates the loss modulus G'' at low strain values and on further increasing the strain a prominent maximum is observed in G'' which is now understood to be associated with breaking of the cages neighboring particles exert on each other. Figure 2.6(a) reports the effect of temperature on the strain-dependent rheological response of the materials. We observe that the loss maximum increases with temperature, indicating enhanced jamming because the height of G'' is a reflection of the degree of jamming in the system. This conclusion is confirmed by a clear decrease in the loss tangent, $\tan\delta (=G''/G')$ with increasing temperature (Figure 2.6(c)), indicative of an enhancement in jamming with increasing temperature. As previously seen in ionically grafted silica nanoparticles⁵⁰, the measurement temperature has no noticeable effect on the location of the first peak in $S(q)$ (Figure 2.6b)) for the covalently grafted self-suspended nanoparticles. This implies that changing the temperature does not alter the interparticle spacing but rather the increase in temperature appears to lead to enhanced

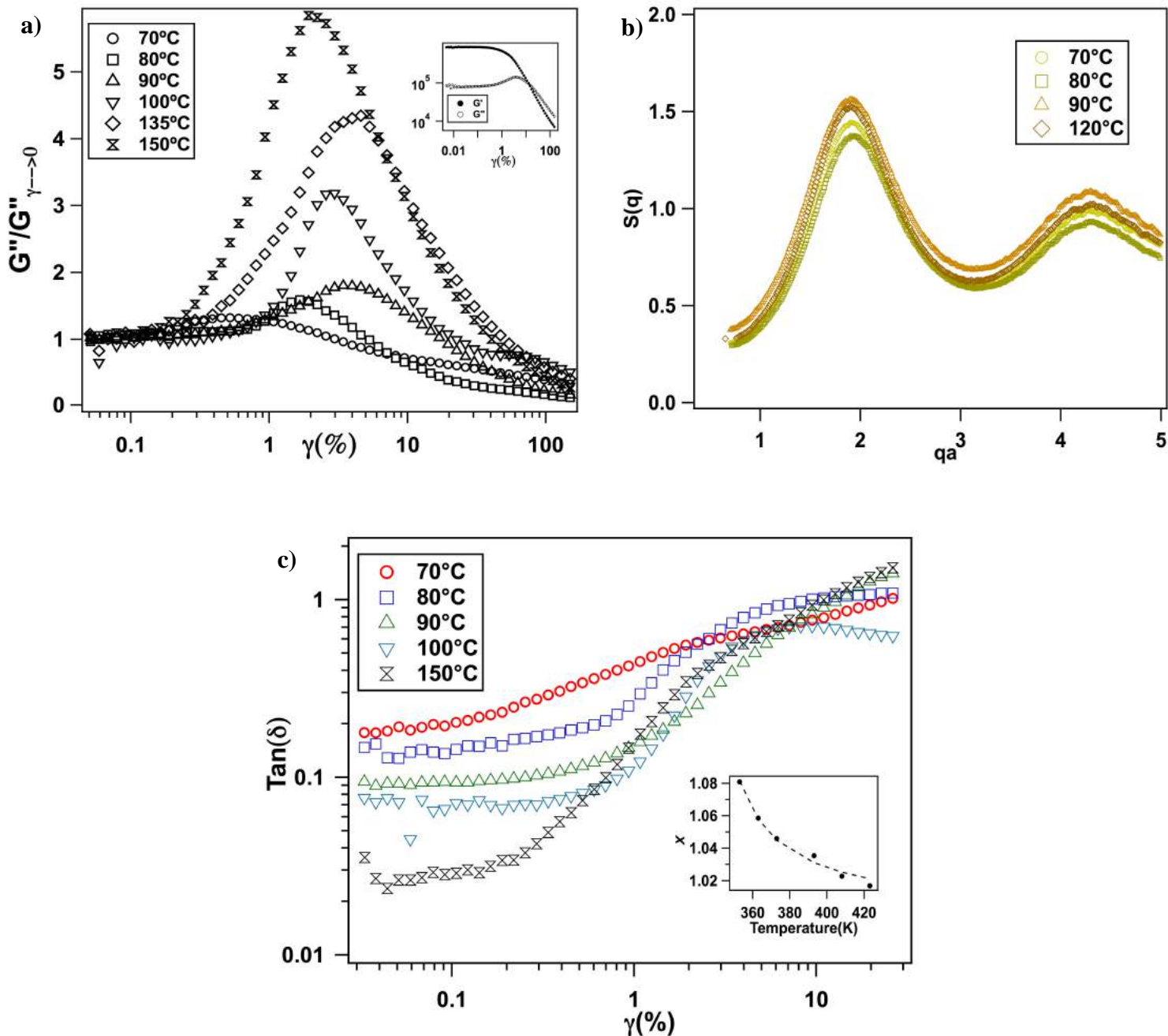


Figure 2.6 a) The height of normalized loss maximum, $G''/G''_{\gamma \rightarrow 0}$ increases with temperature. The inset shows typical soft glassy response of the material. All the measurements are performed at $\omega=10\text{rad/s}$. b) The inter-particle distance does not change with temperature as observed from the variation of the first peak of structure factor $S(q)$ with wave vector q at different temperatures for system. c) loss tangent, $\text{tan}\delta$ decreases with temperature. All the results are for $\Sigma \sim 1.18\text{chains/nm}^2$. The inset shows decrease in noise temperature, X with temperature. The dashed line is VFT fit to data.

Table 2.2. VFT fit parameters for noise temperature X for systems with different grafting densities.

Grafting density (chains/nm²)	A	B	T*(K)
1.18	1.0	2.006	327.42
0.703	1.029	0.967	323
0.576	1.004	2.537	323

corona interpenetration and thereby to tighter cages and enhanced jamming. This temperature-induced jamming of the system can be quantified using a parameter referred to as noise temperature, X which has been described in the soft glassy rheology (SGR) model^{61,62} as an indication of the amount of energy available for each particle to hop out of its potential energy well in the energy landscape. The noise temperature can be related to loss tangent as: $X = 1 + \frac{2}{\pi} \delta$ ^{42,52}. The inset of Figure 2.6c) shows a decreasing trend for X with increase in temperature for $\Sigma \sim 1.18$ chains/nm², which implies that the particles have lesser energy available for hopping at higher temperatures, thus leading to jamming of the system with increase in temperature. Similar behavior with temperature is seen at lower grafting densities of 0.703 and 0.576 chains/nm² as shown in the supplementary information. It is also striking that the dependence of X on T follows the Vogel- Fulcher- Tammann (VFT) fit⁶³: $X = A \exp(\frac{B}{T - T^*})$, where A is the high temperature value of X , B is the activation energy and T^* is the Vogel temperature. T^* values for all of the materials studied are listed in Table 2.2. It is remarkable that, irrespective of the grafting density, T^* is close to the melting point of PEG, indicating that the tethered chains play a crucial role in determine the dependence of X on T . It is also notable that the value of A is always close to unity, indicating that the colloidal glass transition occurs at high temperature. The thermal jamming observed here is reminiscent of thermal vitrification that is observed in star polymers.^{64,65} In those systems, the star polymers form clusters due to improved solvent quality on heating. For the current materials, the space-filling constraint imposed on the tethered chains and absence of a solvent prevent the formation

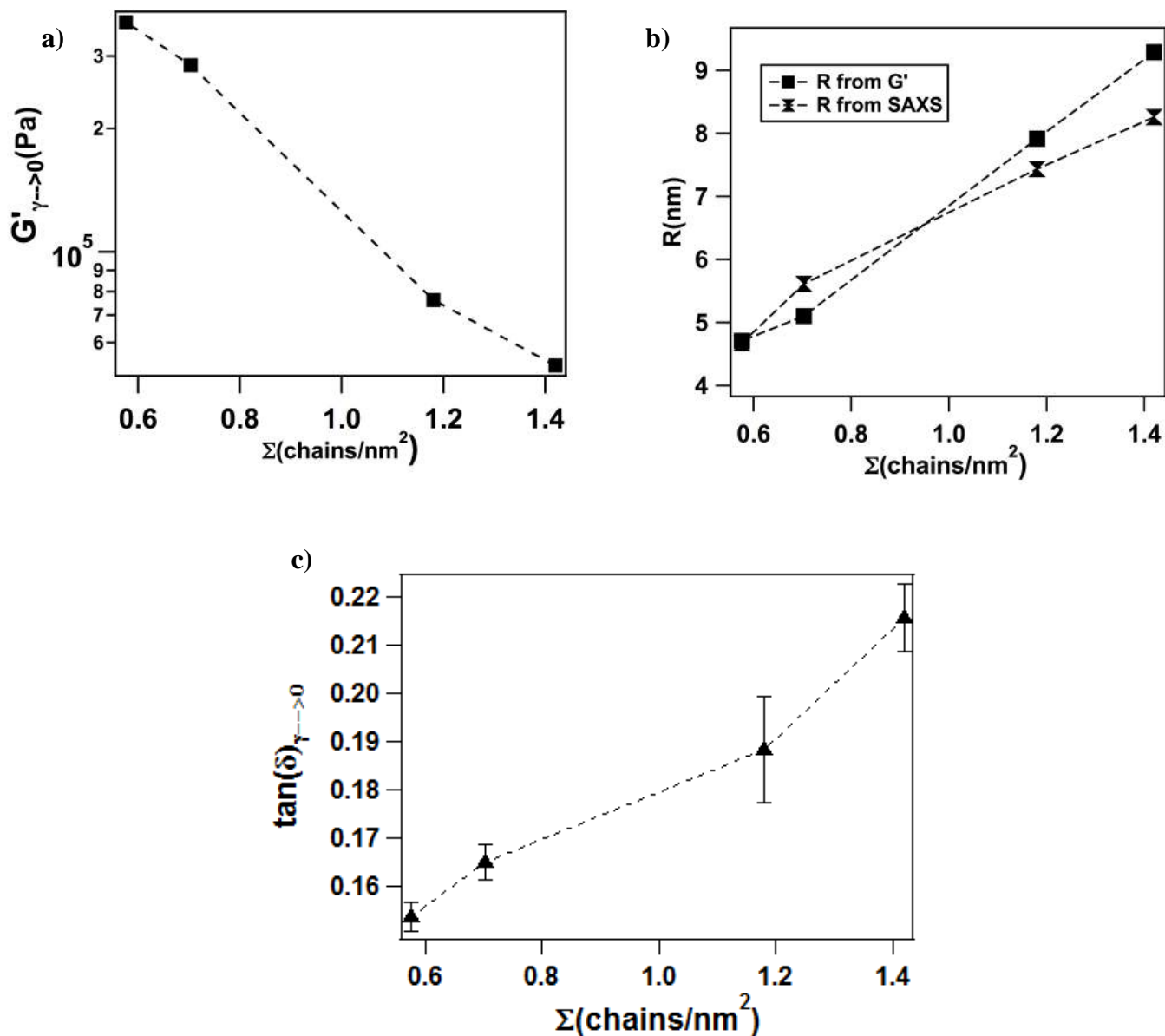


Figure 2.7 a) G' in the linear viscoelastic regime decreases with increase in grafting density while b) the cage size, R estimated from G' and SAXS, and c) Linear viscoelastic loss tangent, $\tan\delta_{\gamma \rightarrow 0}$ increases while with increase in grafting density. The lines are guide to eye.

of clusters, implying that thermal jamming has an entirely entropic origin. The effect of variation of grafting density (Σ) on cage strength can also be deduced from the rheological data. In particular, from Figure 2.7(a) it is apparent that the value of G' in the linear viscoelastic regime decreases with increasing Σ . Previous studies have shown that G' varies as $\sim kT/r_{loc}^2 D$, where r_{loc} is the particle localization length within the cage and D is the particle diameter, maximum distance which can be moved by the particle inside the cage.^{66,67} In the present systems, the cage is determined both by the interactions of the tethered chains and the particles to which they are attached. The cage dimension can thus be estimated using the following simple formula $G' \approx kT/R^3$ where $2R$ is the effective cage size. The cage size estimated from G' is close to the value obtained from SAXS as $2R = d_{p-p} - 2a$ (Figure 2.7b)) and is seen to increase with an increase in Σ , implying that the materials become less jammed on increasing the grafting density. This behavior is consistent with the result obtained by plotting $\tan \delta$ as a function of Σ (Figure 2.7c)). The increase in $\tan \delta$ with Σ indicates unjamming of the system on adding more chains to the particles, which clearly indicates that the cage strength is lowered by an increase in grafting density.

2.5 Conclusions

We report a facile synthesis route for creating self-suspended nanoparticles in which each particle permanently carries its own share of liquid in the form of covalently tethered polymer chains. The materials are found to exhibit outstanding phase stability in absence of any solvent; they are among the first example of a nanoparticle-polymer composite in which each and every building block is itself a nanoparticle-polymer composite. On nanometer length scales, the materials show the dominance of thermodynamically stable

conformational modes in the polymer strands compared to free polymer. On mesoscopic length-scales, we observe that these systems exhibit less heterogeneity as opposed to their ionic counterparts and have stronger steric repulsions due to the absence of any electrostatic interactions between the core and corona conforming to the observations from DFT results. On macroscopic length scales, dynamic rheology measurements firmly place the materials in the universality class of soft glasses, but we find that temperature can enhance jamming in the systems, an unexpected result for a true soft glass where the cage energy is considered substantially higher than kT .

Acknowledgements

This work was supported by the National Science Foundation, Award No. DMR-1006323 and by Award No. KUS-C1-018-02, made by King Abdullah University of Science and Technology (KAUST). Use of the Cornell High Energy Synchrotron Source was supported by the U.S. DOE under Contract No. DE-AC02-06CH11357. This work made use of the Cornell Center for Materials Research Shared Facilities, which are supported through the NSF MRSEC program (DMR-1120296). We thank Dr. Rajesh Mallavajula for his insights and ideas. We also acknowledge Dr. Ivan Keresztes for the help with the NMR experiment. We would also like to thank Adithya Sagar Gurram for his help with DFT calculations.

REFERENCES

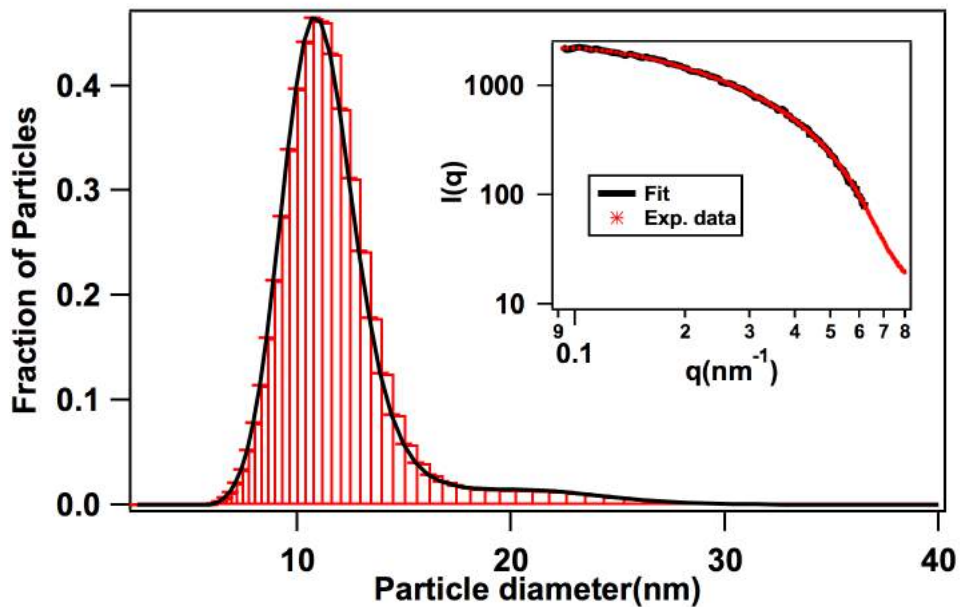
- (1) Einstein, A. *Ann. d. Phys* **1906**, *19*, 371–381.
- (2) Batchelor, G. K. *J. Fluid Mech.* **1972**, *52* (02), 245–268.
- (3) Batchelor, G. K. *J. Fluid Mech.* **1976**, *74* (01), 1–29.
- (4) Batchelor, G. K. *J. Fluid Mech.* **1977**, *83* (01), 97–117.
- (5) Davis, M. E.; Chen, Z. G.; Shin, D. M. *Nat. Rev. Drug Discov.* **2008**, *7* (9), 771–782.
- (6) Salata, O. **2004**, *6*, 1–6.
- (7) Phillips, E.; Penate-Medina, O.; Zanzonico, P. B.; Carvajal, R. D.; Mohan, P.; Ye, Y.; Humm, J.; Gonen, M.; Kalaigian, H.; Schoder, H.; Strauss, H. W.; Larson, S. M.; Wiesner, U.; Bradbury, M. S. *Sci. Transl. Med.* **2014**, *6* (260), 260ra149–ra260ra149.
- (8) Kim, Y.; Lobatto, M. E.; Kawahara, T.; Lee Chung, B.; Mieszawska, A. J.; Sanchez-Gaytan, B. L.; Fay, F.; Senders, M. L.; Calcagno, C.; Becraft, J.; Tun Saung, M.; Gordon, R. E.; Stroes, E. S. G.; Ma, M.; Farokhzad, O. C.; Fayad, Z. a; Mulder, W. J. M.; Langer, R. *Proc. Natl. Acad. Sci. U. S. A.* **2014**, *111* (3), 1078–1083.
- (9) Rocco, M. a; Kim, J.-Y.; Burns, A.; KostECKI, J.; Doody, A.; Wiesner, U.; DeLisa, M. P. *Bioconjug. Chem.* **2009**, *20* (8), 1482–1489.
- (10) Bradbury, M. S.; Phillips, E.; Montero, P. H.; Cheal, S. M.; Stambuk, H.; Durack, J. C.; Sofocleous, C. T.; Meester, R. J. C.; Wiesner, U.; Patel, S. *Integr. Biol. (Camb)*. **2013**, *5* (1), 74–86.
- (11) Liu, S.; Wang, H.; Imanishi, N.; Zhang, T.; Hirano, A.; Takeda, Y.; Yamamoto, O.; Yang, J. *J. Power Sources* **2011**, *196* (18), 7681–7686.

- (12) Lu, Y.; Korf, K.; Kambe, Y.; Tu, Z.; Archer, L. A. *Angew. Chemie* **2014**, *126* (2), 498–502.
- (13) Schaefer, J. L.; Moganty, S. S.; Yanga, D. A.; Archer, L. A. *J. Mater. Chem.* **2011**, *21* (27), 10094–10102.
- (14) Croce, F.; Appetecchi, G. B.; Persi, L.; Scrosati, B. **1998**, *394* (July), 456–458.
- (15) Bruce, P. G.; Scrosati, B.; Tarascon, J.-M. *Angew. Chem. Int. Ed. Engl.* **2008**, *47* (16), 2930–2946.
- (16) Gurevitch, I.; Buonsanti, R.; Teran, A. A.; Gludovatz, B.; Ritchie, R. O.; Cabana, J.; Balsara, N. P. *J. Electrochem. Soc.* **2013**, *160* (9), A1611–A1617.
- (17) Moganty, S. S.; Srivastava, S.; Lu, Y.; Schaefer, J. L.; Rizvi, S. A.; Archer, L. A. *Chem. Mater.* **2012**, *24* (7), 1386–1392.
- (18) Chrissopoulou, K.; Andrikopoulos, K. S.; Fotiadou, S.; Bollas, S.; Karageorgaki, C.; Los, D. C.; Voyiatzis, G. A.; Anastasiadis, S. H. **2011**, 9710–9722.
- (19) Zheng, G.; Lee, S. W.; Liang, Z.; Lee, H.-W.; Yan, K.; Yao, H.; Wang, H.; Li, W.; Chu, S.; Cui, Y. *Nat. Nanotechnol.* **2014**, *9* (8), 618–623.
- (20) Liu, S.; Imanishi, N.; Zhang, T.; Hirano, A.; Takeda, Y.; Yamamoto, O.; Yang, J. *J. Power Sources* **2010**, *195* (19), 6847–6853.
- (21) Lu, Y.; Das, S. K.; Moganty, S. S.; Archer, L. A. *Adv. Mater.* **2012**, *24* (32), 4430–4435.
- (22) Baker, G. L.; Colsons, S. **1994**, No. 2, 2359–2363.
- (23) Srivastava, S.; Schaefer, J. L.; Yang, Z.; Tu, Z.; Archer, L. A. *Adv. Mater.* **2014**, *26* (2), 201–234.
- (24) Agrawal, A.; Choudhury, S.; Archer, L. A. *RSC Adv.* **2015**, *5*, 20800–20809.

- (25) Srivastava, S.; Agarwal, P.; Archer, L. A. *Langmuir* **2012**, 28 (15), 6276–6281.
- (26) Balazs, A. C.; Emrick, T.; Russell, T. P. *Science* **2006**, 314 (5802), 1107–1110.
- (27) Krishnamoorti, R. *MRS Bull.* **2007**, 32 (April).
- (28) Park, B. J.; Vermant, J.; Furst, E. M. *Soft Matter* **2010**, 6 (21), 5327.
- (29) Fritz, G.; Scha, V.; Willenbacher, N.; Wagner, N. J. **2002**, No. 8, 6381–6390.
- (30) Zhulina, E. B.; Borisov, O.; Priamitsyn, V. A. *J. Colloid Interface Sci.* **1990**, 137 (2), 495–511.
- (31) Smith, G. D.; Bedrov, D. *Langmuir* **2009**, 25 (19), 11239–11243.
- (32) Kalb, J.; Dukes, D.; Kumar, S. K.; Hoy, R. S.; Grest, G. S. *Soft Matter* **2011**, 7 (4), 1418.
- (33) Chevigny, C.; Jestin, J.; Gigmes, D.; Schweins, R.; Di-Cola, E.; Dalmas, F.; Bertin, D.; Boué, F. *Macromolecules* **2010**, 43 (11), 4833–4837.
- (34) Green, D. L.; Mewis, J. *Langmuir* **2006**, 22 (18), 9546–9553.
- (35) Hasegawa, R.; Aoki, Y.; Doi, M. **1996**, 9297 (96), 6656–6662.
- (36) Roovers, J.; Paul, L. Z.; Zwan, M. Van Der; Iatrou, H.; Hadjichristidisi, N. *Macromolecules* **1993**, 4324–4331.
- (37) Watanabe, H.; Yao, M.; Sato, T.; Osaki, K. *Macromolecules* **1997**, 9297 (96), 5905–5912.
- (38) Watanabe, H. *J. Nonnewton. Fluid Mech.* **1999**, 82 (2-3), 315–329.
- (39) Sato, T.; Watanabe, H.; Osaki, K. *Macromolecules* **1996**, 9297 (part 2), 3881–3889.
- (40) Willner, L.; Richter, J. J. D.; Roovers, J.; Z, L.; Festkörperforschung, I.; Gmbh, F. *J. Macromolecules* **1994**, 3821–3829.

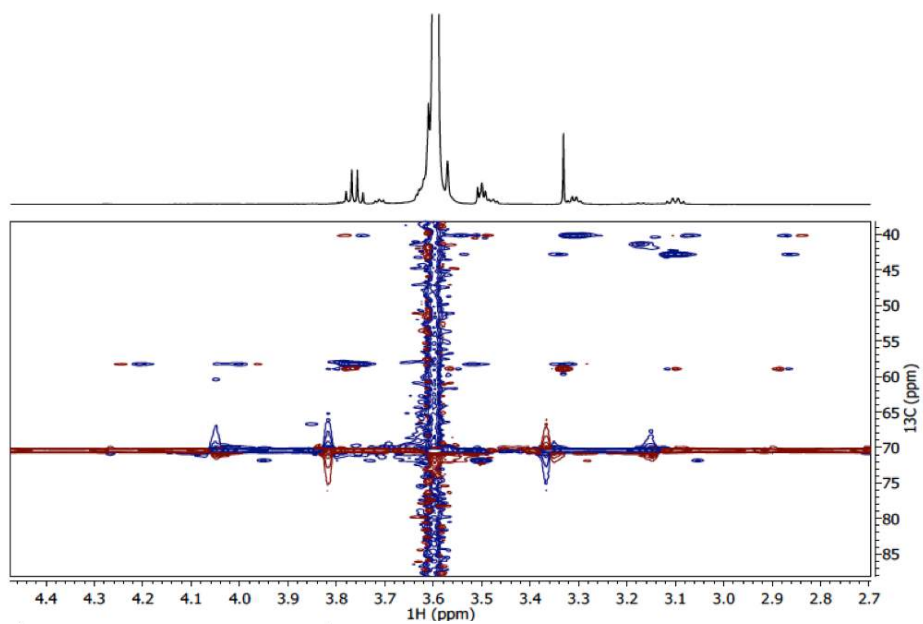
- (41) Adams, J. L.; Graessley, W. W. *Macromolecules* **1994**, No. 27, 6026–6032.
- (42) Fetters, L. J.; Andrea, D. K.; J, D. S. P.; Quack, G. F.; Vitus, F. J. *Macromolecules* **1993**, No. 26, 647–654.
- (43) Agarwal, P.; Qi, H.; Archer, L. A. *Nano Lett.* **2010**, *10* (1), 111–115.
- (44) Fernandes, N. J.; Akbarzadeh, J.; Peterlik, H.; Giannelis, E. P. **2013**, No. 2, 1265–1271.
- (45) Yu, H.-Y.; Koch, D. L. *Langmuir* **2010**, *26* (22), 16801–16811.
- (46) Chremos, A.; Panagiotopoulos, A. Z.; Yu, H.-Y.; Koch, D. L. *J. Chem. Phys.* **2011**, *135* (11), 114901.
- (47) Hong, B.; Chremos, A.; Panagiotopoulos, A. Z. *Faraday Discuss.* **2012**, *154*, 29.
- (48) Chremos, A.; Panagiotopoulos, A. Z.; Koch, D. L. *J. Chem. Phys.* **2012**, *136* (4), 044902.
- (49) Goyal, S.; Escobedo, F. A. *J. Chem. Phys.* **2011**, *135* (18), 184902.
- (50) Agarwal, P.; Srivastava, S.; Archer, L. A. *Phys. Rev. Lett.* **2011**, *107* (26), 268302–1 – 5.
- (51) Jespersen, M. L.; Mirau, P. A.; Meerwall, E.; Vaia, R. A.; Rodriguez, R.; K, E. P. *G.* **2010**, *4* (7), 3735–3742.
- (52) Fernandes, N. J.; Wallin, T. J.; Vaia, R. A.; Koerner, H.; Giannelis, E. P. *Chem. Mater.* **2013**, *26*, 84–96.
- (53) Coleman, M. M.; Skrovanek, D. J.; Hu, J.; Painter, P. C. *Macromolecules* **1988**, *21* (1), 59–65.
- (54) Kim, S. A.; Archer, L. A. *Macromolecules* **2014**, *47*, 687–694.

- (55) Agarwal, P.; Kim, S. A.; Archer, L. A. *Phys. Rev. Lett.* **2012**, *109* (25), 258301–1–4.
- (56) Matsuura, H.; Fukuhara, K. **1986**, *24*, 1383–1400.
- (57) Deng, Y.; Dixon, J. B.; White, G. N. *Colloid Polym. Sci.* **2005**, *284* (4), 347–356.
- (58) Glatter, O.; Kratky, O. *Small Angle X-ray Scattering*, United Sta.; Academic Press: New York, 1982.
- (59) Yu, H.-Y.; Srivastava, S.; Archer, L. A.; Koch, D. L. *Soft Matter* **2014**, *10* (45), 9120–9135.
- (60) Mason, T. G.; Weitz, D. A. *Phys. Rev. Lett.* **1995**, *75* (14), 2770–2773.
- (61) Sollich, P.; Lequeux, F.; Hébraud, P.; Cates, M. *Phys. Rev. Lett.* **1997**, *78* (10), 2020–2023.
- (62) Sollich, P. *Phys. Rev. E* **1998**, *58* (1), 738–759.
- (63) Angell, C. A.; Ngai, K. L.; McKenna, G. B.; McMillan, P. F.; Martin, S. W. *J. Appl. Phys.* **2000**, *88* (6), 3113.
- (64) Kapnistos, M.; Vlassopoulos, D.; Fytas, G.; Mortensen, K.; Fleischer, G.; Roovers, J. *Phys. Rev. Lett.* **2000**, *85* (19), 4072–4075.
- (65) Loppinet, B.; Stiakakis, E.; Vlassopoulos, D.; Fytas, G.; Roovers, J. **2001**, No. about 270, 8216–8223.
- (66) Mason, T. G. *Rheol. Acta* **2000**, *39*, 371–378.
- (67) Shah, S. A.; Chen, Y.-L.; Schweizer, K. S.; Zukoski, C. F. *J. Chem. Phys.* **2003**, *119* (16), 8747.

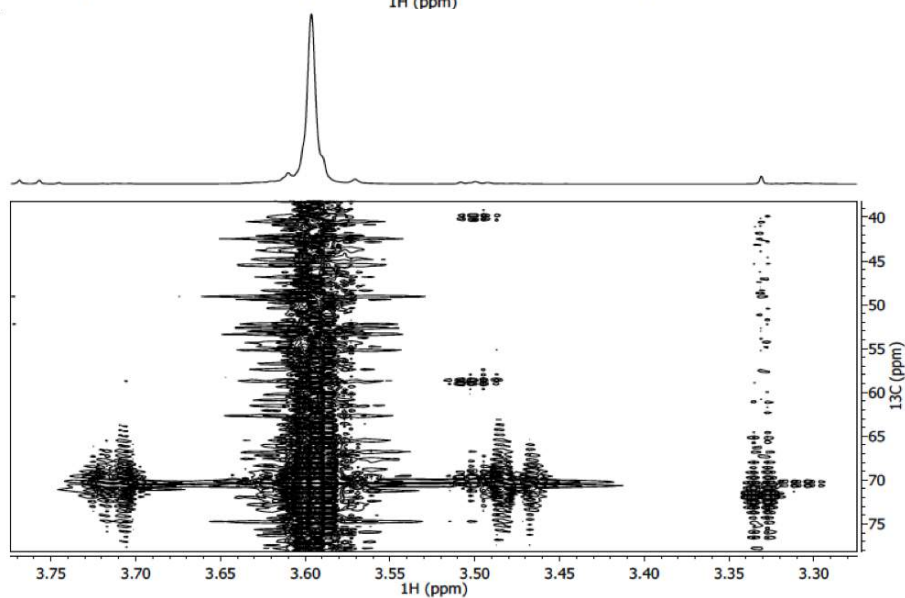


Supplementary figure 2.1 Size distribution of Silica nanoparticles as determined from SAXS analysis. The solid line denoted Gaussian fits to the data. Inset: Experimental scattering intensity for Silica nanoparticles (red dots) and the fit to data (Black line).

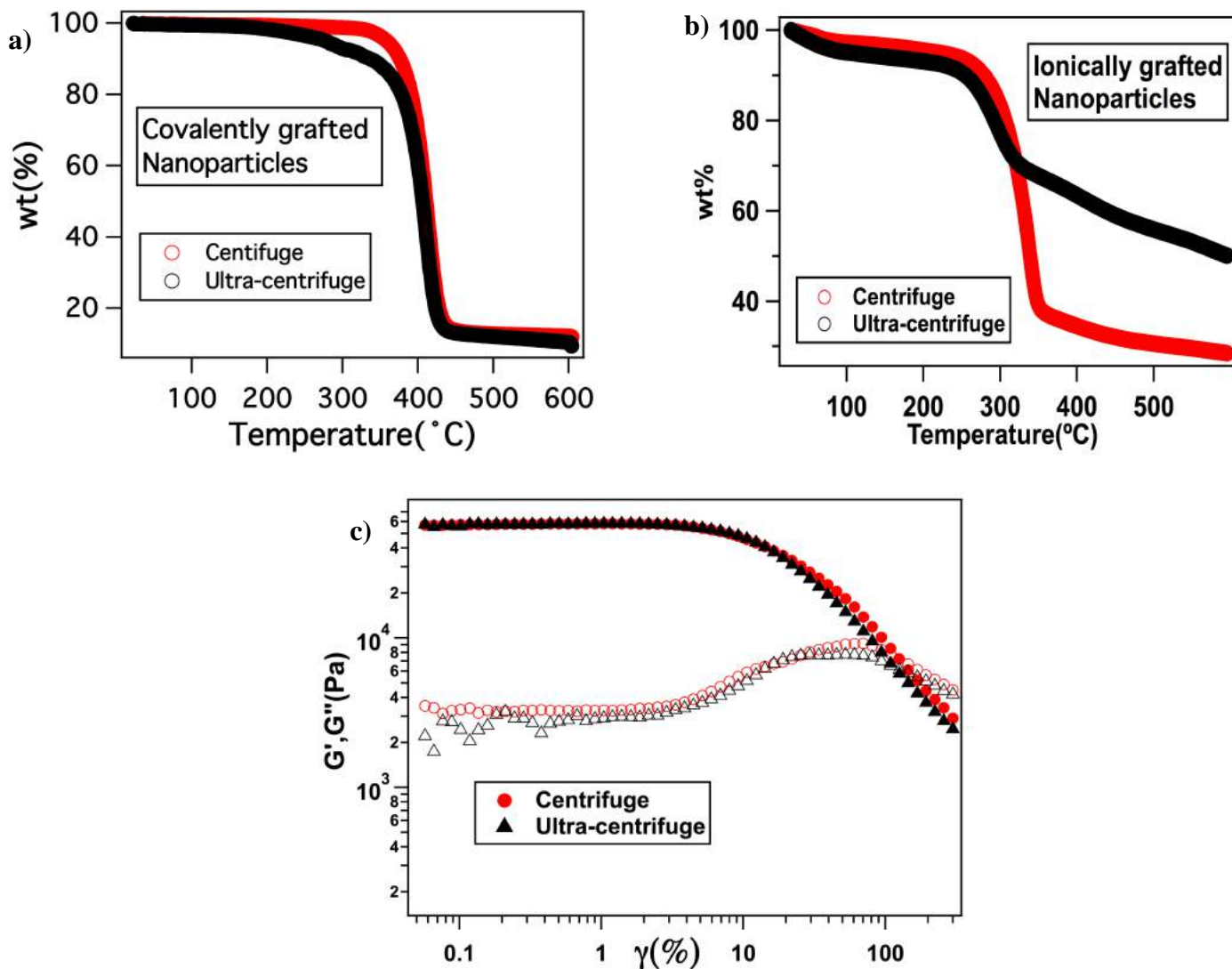
a)



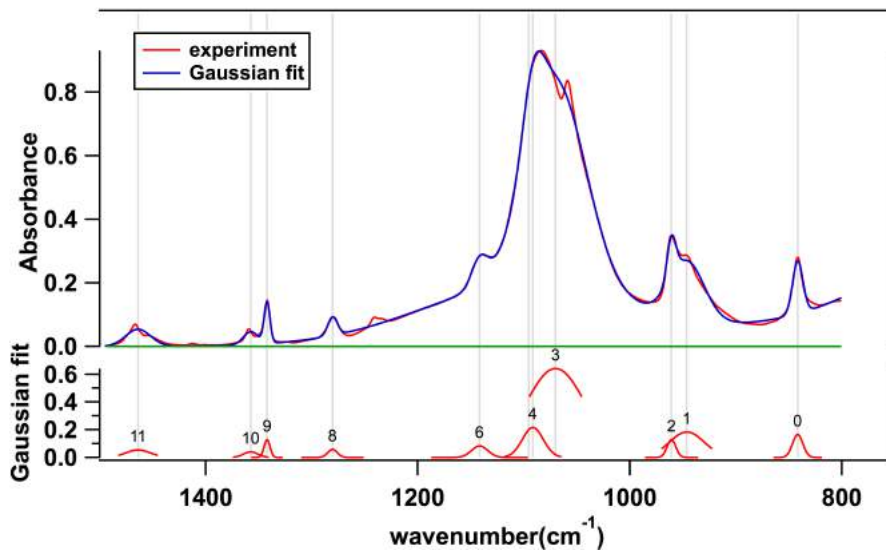
b)



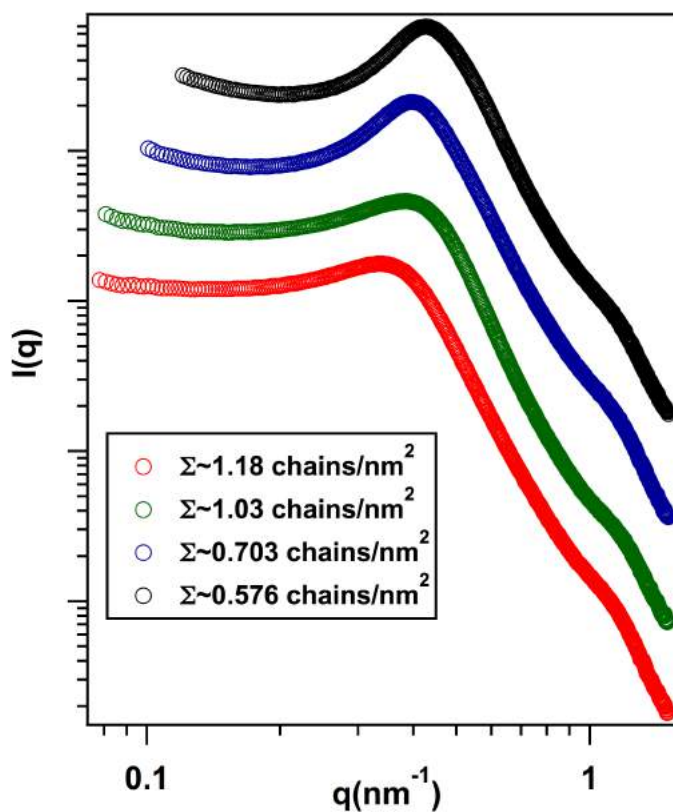
Supplementary figure 2.2 a) HSQC ^1H - ^{13}C in CDCl_3 at 25°C . b) HMBC ^1H - ^{13}C in CDCl_3 at 25°C



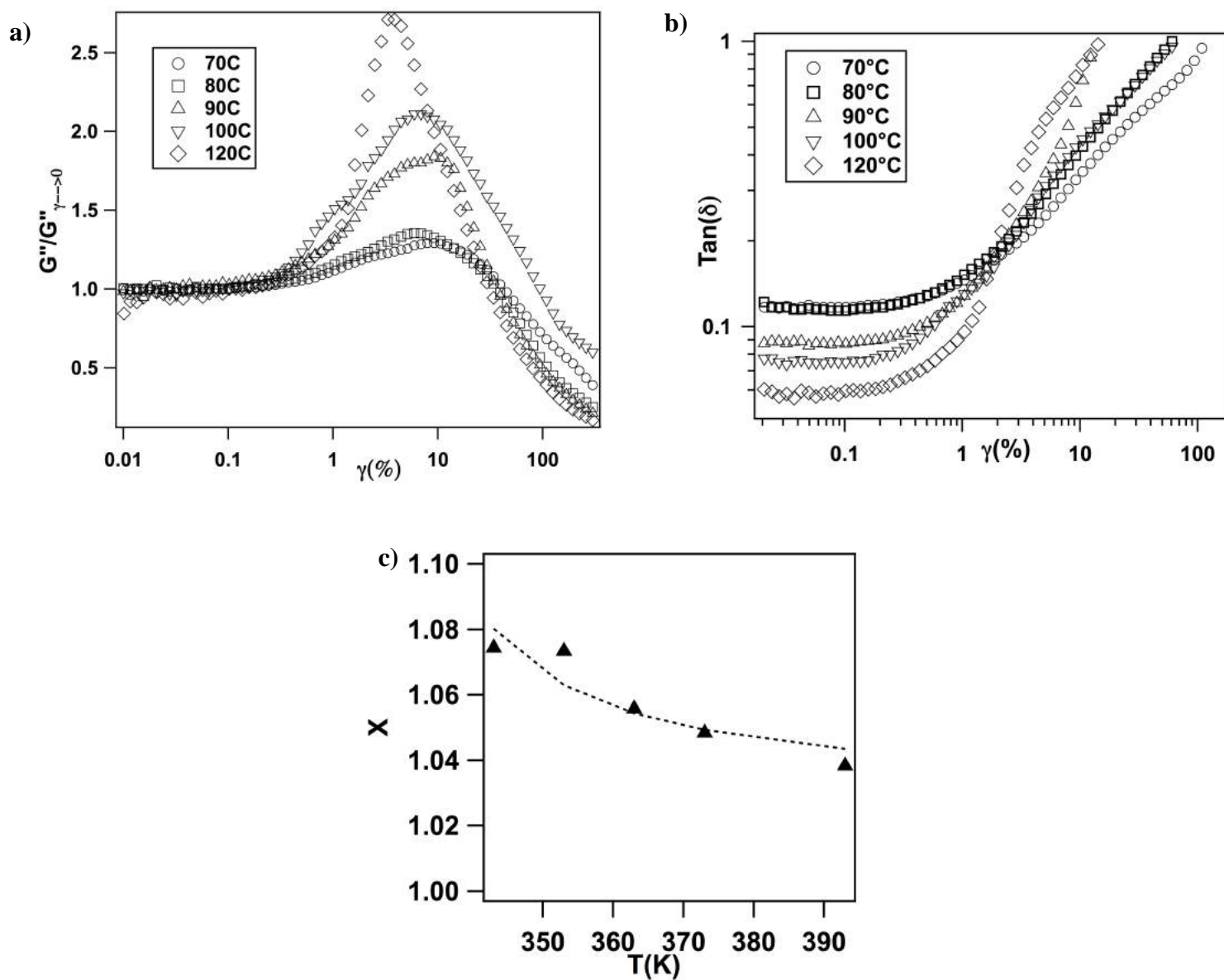
Supplementary figure 2.3 Comparison of centrifuge and ultra-centrifuge for **a)** covalently grafted nanoparticles and **b)** Ionically grafted nanoparticles. It can be observed that the resultant weight % for the covalent system is the same from both the methods while for the ionic system the weight fraction of silica goes on decreasing when ultra-centrifuged. **c)** Amplitude sweep measurement of the covalently grafted sample for normal centrifuge and after ultra-centrifuge. The two measurements can be seen to overlap.



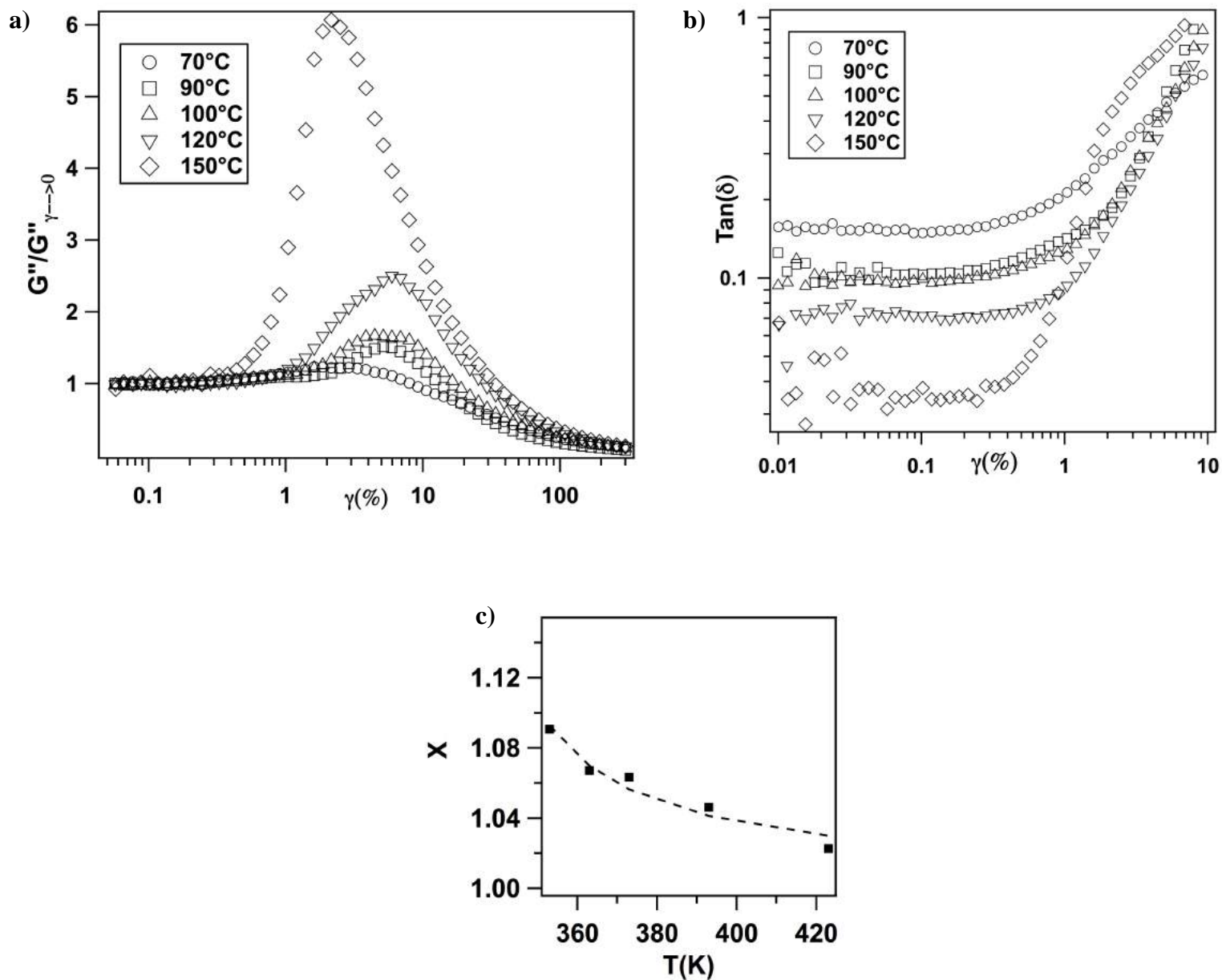
Supplementary figure 2.4. Gaussian fitting of the FT-IR peaks for tethered PEO chains of grafting density, $\Sigma \sim 1.03$ chains/nm².



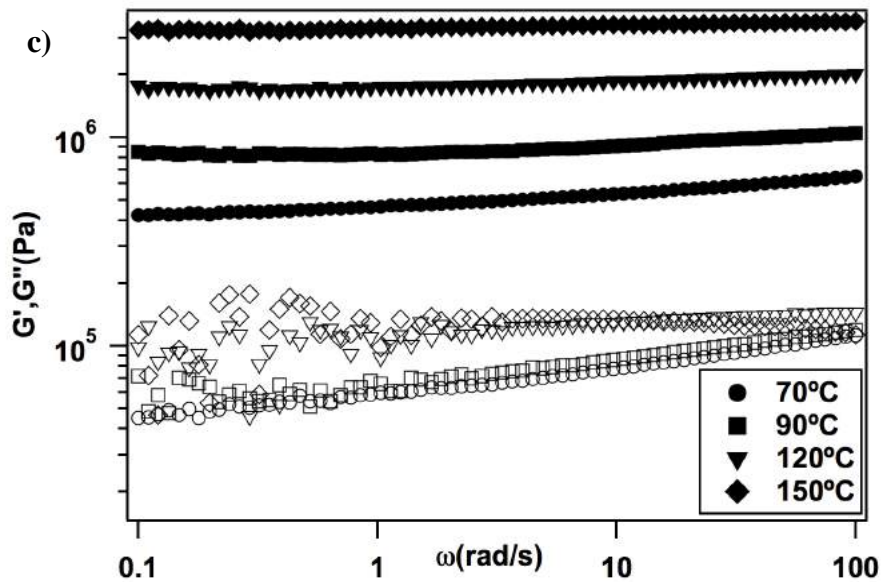
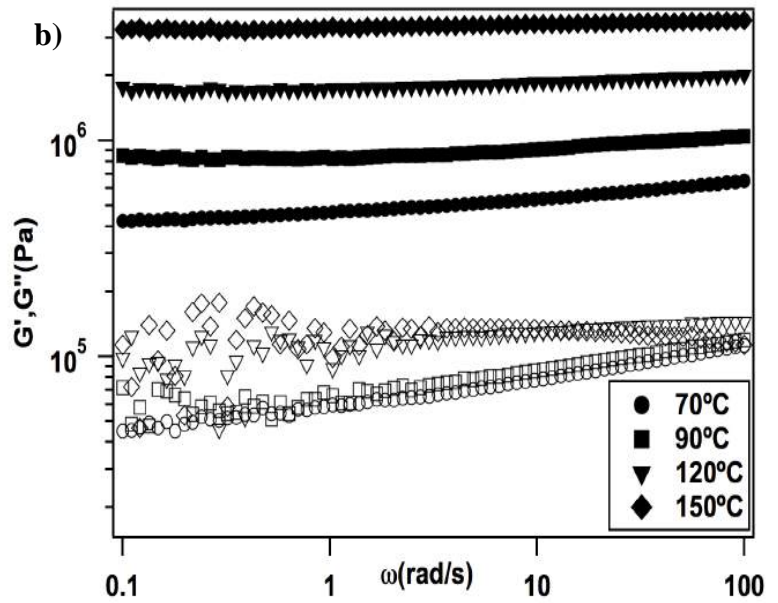
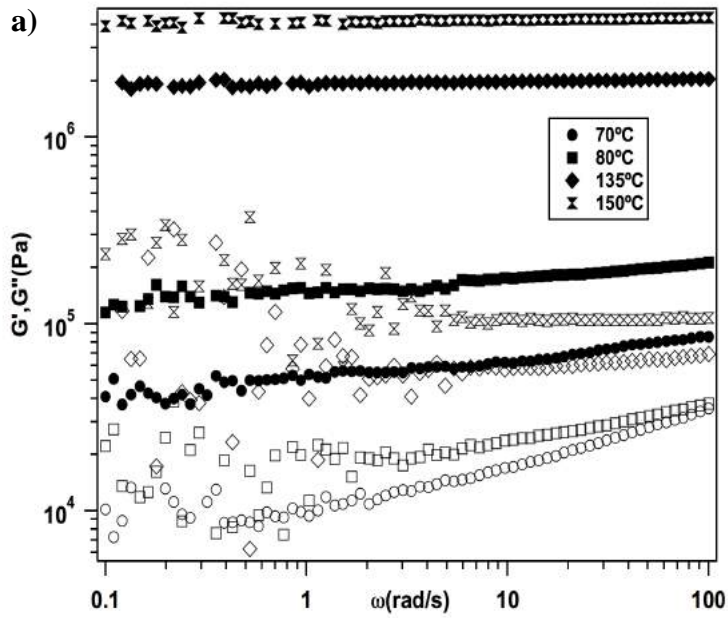
Supplementary figure 2.5 Variation of intensity ($I(q)$) as measured from SAXS experiments with q at different grafting densities.



Supplementary figure 2.6 a) Variation of normalised loss modulus $G''/G''_{\gamma \rightarrow 0}$ and b) $\tan(\delta)$ with strain amplitude at different temperatures. All the measurements are performed at $\omega=10$ rad/s c) Similar trends are seen in noise temperature X variation with temperature. The results are for system with $\Sigma \sim 0.703$ chains/nm²



Supplementary figure 2.7 a) Variation of normalised loss modulus $G''/G''_{\gamma \rightarrow 0}$ and b) $\tan(\delta)$ with strain amplitude at different temperatures and at $\omega=10\text{rad/s}$ c) Similar trends are seen in noise temperature X variation with temperature. The results are for system with $\Sigma \sim 0.576$ chains/nm²



Supplementary figure 2.8 Frequency sweep measurements at $\gamma=0.1\%$ at different temperatures for a) $\Sigma \sim 1.18$ chains/nm² b) $\Sigma \sim 0.703$ chains/nm² and c) $\Sigma \sim 0.576$ chains/nm². Storage Modulus, G' (closed symbols) is found to be always greater than the loss modulus, G'' (open symbols)

Supplementary Table 2.1. Assignment of FTIR peaks for free and tethered chains to the corresponding conformations and structure of crystal unit cell

Free PEO peak position(cm^{-1})	Tethered PEO(1.18chains/nm^2) peak position(cm^{-1})	Vibrational assignment	conformations	Crystal unit cell
842	841	C-O stretch, CH_2 rock	mostly C-C gauche	helix
949	950	C-O stretch, CH_2 rock	C-C gauche, C-O trans	helix
961	961	C-O stretch, CH_2 rock		zigzag
1060	1064	C-O stretch, C-C stretch CH_2 rock		helix
1098	1094	C-O stretch, C-C stretch		
1146	1150	C-O stretch, C-C stretch		
1238	1238	CH_2 twist (anti-symmetric)	C-O trans	helix
1279	1280	CH_2 twist (symmetric)	C-O gauche	helix
1341	1342	CH_2 wag (anti-symmetric)	C-C trans	zigzag
1358	1357	CH_2 wag (anti-symmetric)	C-C gauche	helix
1466	1464	CH_2 scissor		zigzag

Chapter 3

Dynamics and Yielding of Binary Self-Suspended Soft Colloids

Akanksha Agrawal, Hsiu-Yu Yu, Samanvaya Srivastava, Snehashis Choudhury, Suresh Narayanan, Lynden A. Archer, Dynamics and Yielding of Binary Self-Suspended Soft Colloids, *Soft Matter*, 2015, 11, 5224-5234.

Reproduced by permission of The Royal Society of Chemistry

3.1 Abstract

Yielding and flow transitions in bi-disperse suspensions of particles are studied using a model system comprised of self-suspended spherical nanoparticles. An important feature of the materials is that the nanoparticles are uniformly dispersed in the absence of a solvent. Addition of larger particles to a suspension of smaller ones is found to soften the suspensions, and in the limit of large size disparities, completely fluidizes the material. We show that these behaviors coincide with a speeding-up of de-correlation dynamics of all particles in the suspensions and are accompanied by a reduction in the energy dissipated at the yielding transition. We discuss our findings in terms of ligand-mediated jamming and un-jamming of hairy particle suspensions.

3.2 Introduction

Dispersions of small particles in simple liquids have been studied for at least a century to understand their interaction forces and dynamics¹⁻⁴. In recent years interest in suspensions of particles with nanometer-sized dimensions has grown in response to their exceptional promise for applications in multiple fields of technology. In medicine, they are receiving increasing attention as therapeutics^{5,6} and for biomedical imaging⁷⁻¹⁰. In energy harvesting and storage, nanosize particles have been reported to provide attractive attributes when used as tunable components in the anode, cathode, or electrolyte¹¹⁻²⁴. Because of the small size of the particles, surface forces dominate and the difficulty in preparing dispersions of un-aggregated nanoparticles is well known and extensively studied. This challenge has nevertheless hindered fundamental studies of the materials and delayed progress in understanding their colloidal science²⁵⁻²⁷. A variety of

approaches have been reported in the literature for controlling phase stability of large and small particles. Only two are regarded as sufficiently versatile to be employed in practice: electrostatic stabilization^{28,29} using charges physically adsorbed to the particle surface in solution; and steric stabilization using physically/chemically attached polymers^{30–35}.

Recently, the concept of solvent-less nanoparticle fluids has been proposed, which structurally resemble block copolymers micelles and multi-arm star polymers^{36–42}. These nanoparticle fluids are comprised of polymer chains grafted to nanoparticles at such high coverage that the particles exhibit remarkable phase stability and fluidity in the absence of a solvent^{25,43,44}. Theoretical studies show that the exceptional colloidal stability of such *self-suspended suspensions* arise from two sources, steric forces between the tethered polymer chains and by the space filling constraints these chains experience in the absence of any suspending medium^{45,46}. Density functional theoretical and molecular simulation studies further show that each nanoparticle in a self-suspended material carries its own share of the suspending fluid (the tethered polymer) on its back such that exactly one neighboring core is excluded by each hairy nanoparticle. This feature of the materials simultaneously make them analogous to incompressible, single-component fluids comprised of molecular units and leads to a vanishing structure factor $S(q \rightarrow 0) = 0$ ^{45,46} and good model systems for understanding interactions, structure, and dynamics of soft colloids^{45–49}.

A fundamental question that arises in the context of using self-suspended materials as model systems for soft colloids arises from the fidelity of the ligand coupling^{34–35} possible with the ionic sulfonic acid – amine bond most commonly used for creating the most widely studied materials^{25,43,50}. Additionally, recent work by Fernandez et al. show that

electrostatic interactions between ionically linked core and corona can lead to leading to complex layering of the charged core and corona⁵¹. In particular, these authors found that the diffusivity of the grafted polymeric chains do not correlate with the hard sphere like diffusivity of the core^{51,52} and contended that exchange of polymers between a bilayer of chains tethered to the particles creates a dynamic interface between the core and polymer^{51,52}. In a model self-suspended system of nanoparticles, this exchange is undesirable. Herein we report a synthesis strategy for creating truly self-suspended suspensions of nanoparticles in which polymeric ligands are covalently grafted to nanoparticles at coverage where the system spontaneously exhibits a homogeneous fluid state in the absence of any solvent. The materials open new opportunities for both fundamental studies and for applications where the particles must be exposed to high-dielectric constant, polar solvents that may dissociate the polymer-particle linkages in their ionic counterparts. We show by means of scattering experiments and rheology that the materials are self-suspended, exhibit hierarchical structure, and soft glassy fluid rheology.

3.3 Experimental Methodology

3.3.1 Material and Synthesis

Silica nanoparticles with diameters $10\pm 2\text{nm}$ (Ludox SM-30, Sigma Aldrich), $25\pm 3\text{nm}$ (Ludox TM-50, Sigma Aldrich), $50\pm 1.5\text{nm}$ (Nanocomposix Inc), $80\pm 1\text{nm}$ (Nanocomposix Inc), $200\pm 2\text{nm}$ (Nanocomposix Inc), and $360\pm 4\text{nm}$ (Stöber synthesis⁴²) were grafted by covalent attachment of polyethylene glycol(PEG, MW~5000 g mol^{-1} , Polymer Source) using a previously described synthesis procedure.⁴³ The polydispersities in the particle sizes is estimated from maximum entropy method using

IRENA package⁴⁴, as shown in Supplementary figure 3.1. The grafting densities of the chains on the silica cores, computed from analysis of the residual inorganic content using thermal gravimetric analysis (TGA, TA instruments Q500) were found to be 1.4 chains/nm², 2.1 chains/nm², 1.8 chains/nm², 1.2 chains/nm², 2.0 chains/nm² and 1.2 chains/nm², respectively. The suspensions can be characterized using two parameters:(i) The particle size ratio, $r = D_s / D_L$, where D_s and D_L are, respectively, the diameter of the smaller and larger SiO₂ core particles; and(ii) The fraction, $x_L = \phi_L / (\phi_s + \phi_L)$, of the larger SiO₂ particles in the suspension. Here ϕ_L and ϕ_s are the respective volume fractions of large and smaller particles. Silica particles tethered with PEG are first dissolved in chloroform, which is a good solvent for silica and PEG. Particles of different sizes were mixed with 10nm size particles in different x_L fractions, while continuously stirring the solution. Chloroform was evaporated by keeping the sample vial on a hot plate and continuously stirring it to ensure uniform particle mixing. The sample was subsequently kept under vacuum for two days, to ensure complete solvent evaporation and to remove any residual strain in the system. For the systems studied here, $D_s=10\text{nm}$, while D_L is varied such that $r=0.4, 0.2, 0.125, 0.05$ and 0.027 . The fraction of larger particles, x_L ranges from 0 to 1 with total core volume fraction, ϕ is around 0.12-0.15 for all the systems (Supplementary figure 2.2). The total core volume fraction can be given as-

$$\phi = \frac{\left(\frac{w_s}{\rho_s}\right)}{\left(w_s\left(\frac{1}{\rho_s} - \frac{1}{\rho_p}\right) + \frac{1}{\rho_p}\right)}$$

Where, ρ_s and ρ_p are the densities of silica and PEG respectively and w_s is the weight fraction of silica as determined from TGA.

The dispersion state of the materials with different size ratios was observed using Transmission Electron Microscopy (TEM). The samples for TEM were prepared by solvent casting method. Dilute suspensions of the nanoparticles in chloroform were dropped on copper grids, which were subsequently annealed at 65°C for 24 hrs to ensure complete evaporation of chloroform and uniform particle dispersion.

3.3.2 Small Angle X-ray Scattering (SAXS) measurements

Small angle X-ray scattering (SAXS) measurements were performed on the binary systems with size ratio $r=0.4$ at Sector-12-ID-B of Advanced Photon Source(APS) at Argonne National Laboratory using a point collimated X-ray beam. All the samples were smeared on a thermal sample cell and the measurements were performed at 90°C, which is above the melting point of PEG. The measured scattering intensity $I(q)$ as a function of wave vector q , can be divided into contributions from the individual particles and from inter-particle correlations as $I(q, R_S, R_L, x_L, \phi_L) = P(q, R_S, R_L, x_L)S(q, R_S, R_L, x_L, \phi_L)$, with P and S denoting the form and the structure factors, respectively. In the limit of infinite dilution, $S(q, R_S, R_L, \phi_S \rightarrow 0, \phi_L \rightarrow 0) \sim 1$, and the form factors can be conveniently estimated from the scattering intensities. SAXS measurements on dilute aqueous binary suspensions(1% volume fraction) of charge stabilized silica nanoparticles at different x_L values were performed to obtain the form factor. The measured form factor \bar{P} for each binary suspension diluted in water is in good agreement with expectations based upon the mole fraction-weighted form factors for the pure species (Supplementary figure 2.3).⁴⁵⁻⁴⁷ Thus, S could be facilely obtained as $S = I / \bar{P}$, and provides a means for evaluating particle correlations in the binary systems.^{45,48}

3.3.3 X-ray Photon Correlation Spectroscopy (XPCS) measurements

X-ray photon correlation spectroscopy (XPCS) measurements were performed on binary systems with $r=0.4$ in sector-8-ID-I of Advanced Photon Source at Argonne National Laboratory across a range of wave vector q at an x-ray photon energy of 7.35keV. All the samples were kept in vacuum and the measurements were carried out by precisely controlling the temperature at 90°C to eliminate any external fluctuations.⁴⁹ XPCS measures the intensity auto-correlation function, which is defined as:

$$g_2(q,t) = \frac{\langle I(q,t')I(q,t'+t) \rangle}{\langle I(q,t') \rangle^2} \quad (1)$$

Here $I(q,t')$ is the intensity measured at wave vector q at time t' .⁵⁰⁻⁵² $g_2(q,t)$ is related to the normalized intermediate scattering function (ISF, $f(q,t)$) through the Siegert relation:

$$g_2(q,t) = 1 + b|f(q,t)|^2 \quad (2)$$

Here b is the instrument optical contrast. Previous studies^{49,50,53} have shown that the ISF and subsequently the $g_2(q,t)$ can be fitted using a stretched exponential form:

$$f(q,t) = \exp[-(t/\tau)^\beta] \quad (3)$$

Where τ and β are the characteristic relaxation time and stretching exponent of the ISF.

3.3.4 Rheology measurements

Dynamic rheological properties were studied using frequency- and strain-dependent oscillatory shear measurements at 90°C. A MCR501 (Anton Paar) mechanical rheometer equipped with a 10mm diameter, 2° cone-and-plate fixtures was used for these experiments. Prior to data collection, all the suspensions were pre-sheared by applying a variable shear strain ranging from 0.1% to 100% at a frequency of 10rad/s. This was done

until the data was reproducible and the measurements were taken immediately after pre-shearing. Variable amplitude oscillatory shear measurements were performed at a fixed angular frequency of $\omega=10$ rad/s and frequency-dependent oscillatory measurements were performed at a fixed shear strain of $\gamma = 0.5\%$, chosen to fall well within the linear viscoelastic regime for all the materials studied. The time sweep measurements to observe any aging in the system were done at a strain of $\gamma = 0.5\%$ and an angular frequency of $\omega=10$ rad/s, with the time of measurement as long as 6×10^4 s.

3.4 Results and Discussion

Figure 3.1a)-d) reports typical transmission electron micrographs for bi-disperse hairy particle suspensions with different size ratios at $x_L = 0.2$. It is apparent from Figures 3.1a) and b) that for moderate size ratios of $r = 0.4$ and 0.2 , both the small and big particles are well-dispersed. At the same time, Figures 3.1c) and 3.1d) indicate that on progressing towards lower size ratios, the bigger particles tend to form clusters, consistent with the presence of depletion attraction between the larger particles induced by the smaller particles.³¹

The well-dispersed state of bi-disperse systems with $r = 0.4$ is further confirmed from SAXS experiments. It can be observed from Figure 3.1e) that the scattering intensities $I(q)$ are at most weakly dependent on the wave vector at low q values, and exhibit a q^{-4}

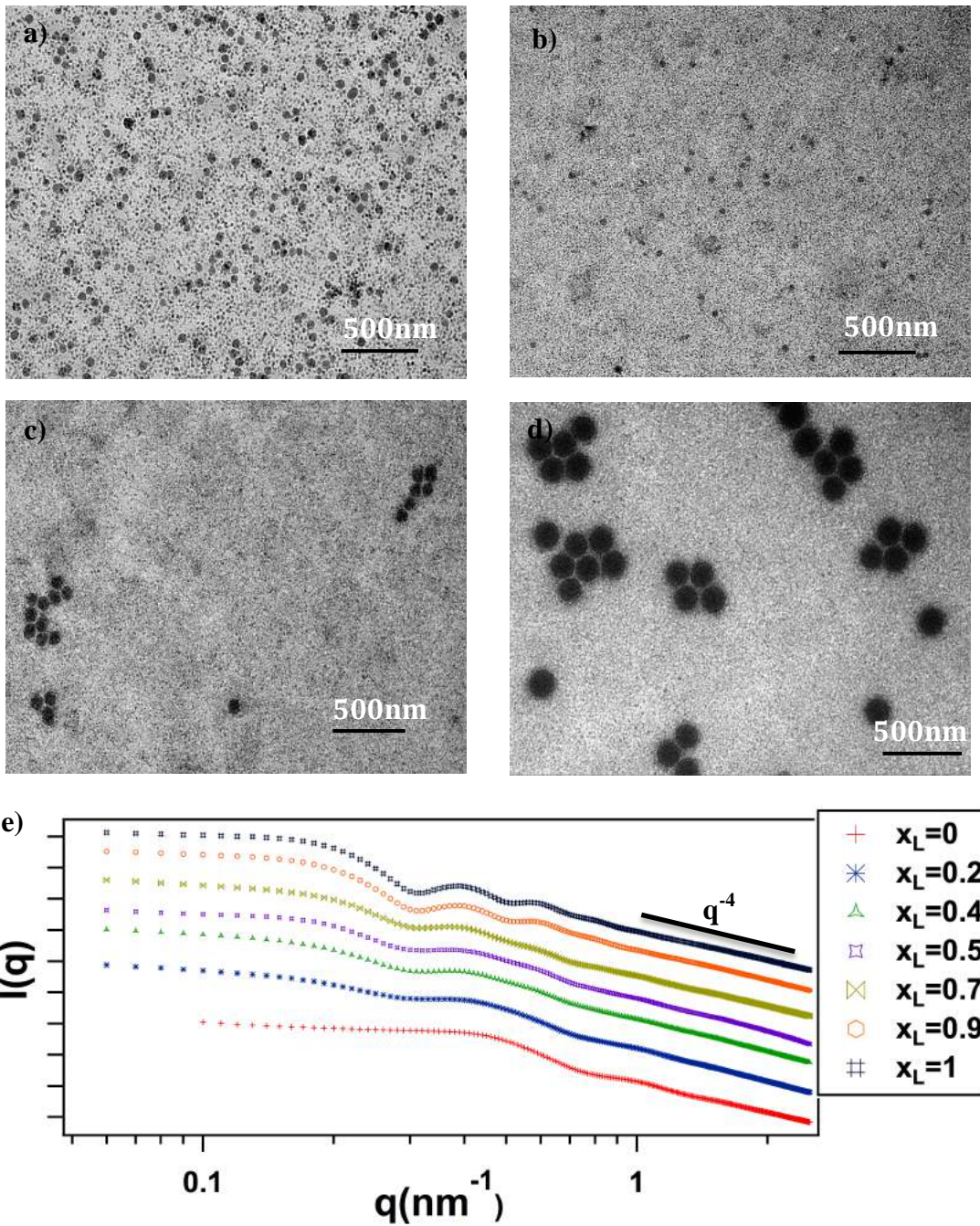


Figure 3.1 Transmission electron micrograph for binary systems with **a)** $r = 0.4$ **b)** $r = 0.2$, **c)** $r = 0.125$ and **d)** $r = 0.05$ at $x_L = 0.2$. **e)** Scaled intensities, $I(q)$ from SAXS experiments as a function of wave vectors on a log-log scale, from $x_L = 0$ to 1, bottom to top for $r = 0.4$.

scaling at high q values, both of which are characteristics of well-dispersed spherical nanoparticles.^{54,55} Figure 3.2a) reports the static structure factor for a range of x_L values at fixed $\phi \sim 0.15$ for $r = 0.4$. The position of the first maximum in S is largely insensitive to x_L and remains fixed at $q \sim 0.46 \text{ nm}^{-1}$ for $x_L \leq 0.25$ and at $q \sim 0.22 \text{ nm}^{-1}$ for $x_L \geq 0.4$, which correspond to the inter-particle correlation lengths for self-suspended suspensions of the pure small and big particles, respectively. Remarkably, these trends are mirrored in $S(q)$ computed for semi-dilute bi-disperse hard sphere suspensions using the Percus-Yevick approximation.⁵⁶ The location of the first peak of the calculated S is seen to transition from $q \sim 0.5 \text{ nm}^{-1}$ to $q \sim 0.25 \text{ nm}^{-1}$ on increasing x_L over the same range.

The latter results can be understood by resolving the HS structure factor into three components (Supplementary figure 2.4) — S_{11} , S_{12} and S_{22} , where the subscripts 1 and 2 denote small and large particles, respectively. At high volume fractions of the smaller particles, i.e. $x_L < 0.3$, S_{11} dominates, while S_{22} contributes the most to the overall S as the volume fraction of bigger particles approaches unity. It is also noted that the contribution from S_{12} is always dwarfed by S_{11} or S_{22} and the first maximum in S is therefore predominantly determined by either S_{11} or S_{22} . Therefore, the similarity between the variation of the first maximum in $S(q)$ for our self-suspended systems and hard spheres reflects the dominant structural contributions from the silica nanocores.

The space filling constraints imposed on the tethered ligands that suspend the particles has been noted previously to produce a more uniform particle dispersion than achieved with hard spheres, which manifest as unique features in the structure factor.^{57,58} In particular, the strong chain mediated correlations among the core particles lead to higher primary peaks, while the space filling constraint suppresses concentration fluctuations

and results in a more rapid decay and lower S values in the low q regime. These features are conveniently captured in the S value at $q = 0.22\text{nm}^{-1}$ (Figure 3.2b)). For large particle dominated systems ($x_L \geq 0.7$), $q = 0.22\text{nm}^{-1}$ corresponds to the position of the primary correlation peak in S , and the $S_{q=0.22\text{nm}^{-1}}$ values deviates positively from the corresponding hard sphere values, characterizing a stronger chain-mediated inter-particle correlation.

Meanwhile, for $x_L \leq 0.7$, $S_{q=0.22\text{nm}^{-1}}$ corresponds to the low- q regime where $qR < 1.5$ with R being the average core radius, and the $S_{q=0.22\text{nm}^{-1}}$ values deviate negatively from the corresponding hard sphere values, denoting the suppression of system density fluctuations by the space-filling oligomers. Figure 3.2c) illustrates this result more clearly by comparing $S(q>0)$ for the hairy particle blends with the calculated values for hard sphere suspensions. The $S(0)$ values for the experimental systems were obtained by fitting the measured $S(q)$ to a quadratic function and extrapolating to $q=0$. It is apparent that $S(0)$ for the self-suspended hairy nanoparticles is always lower than for the corresponding binary hard sphere suspensions, which means that the self-suspended particles indeed have a more uniform dispersion than a suspension of hard spheres due to the space-filling constraint on the tethered ligands. In either case, however, increasing polydispersity leads to larger concentration fluctuations and therefore higher $S(0)$ values. Thus, we conclude that the inherent physical characteristics of the individual particles used for the experiments (a hard core and soft corona) are preserved in the structure of the bi-disperse suspensions. We may also conclude that the polymers tethered to the nanocores not only play a very significant role in dispersion of these particles, but because of the requirement that they fill the inter-particle space, may also contribute to unique system dynamics.

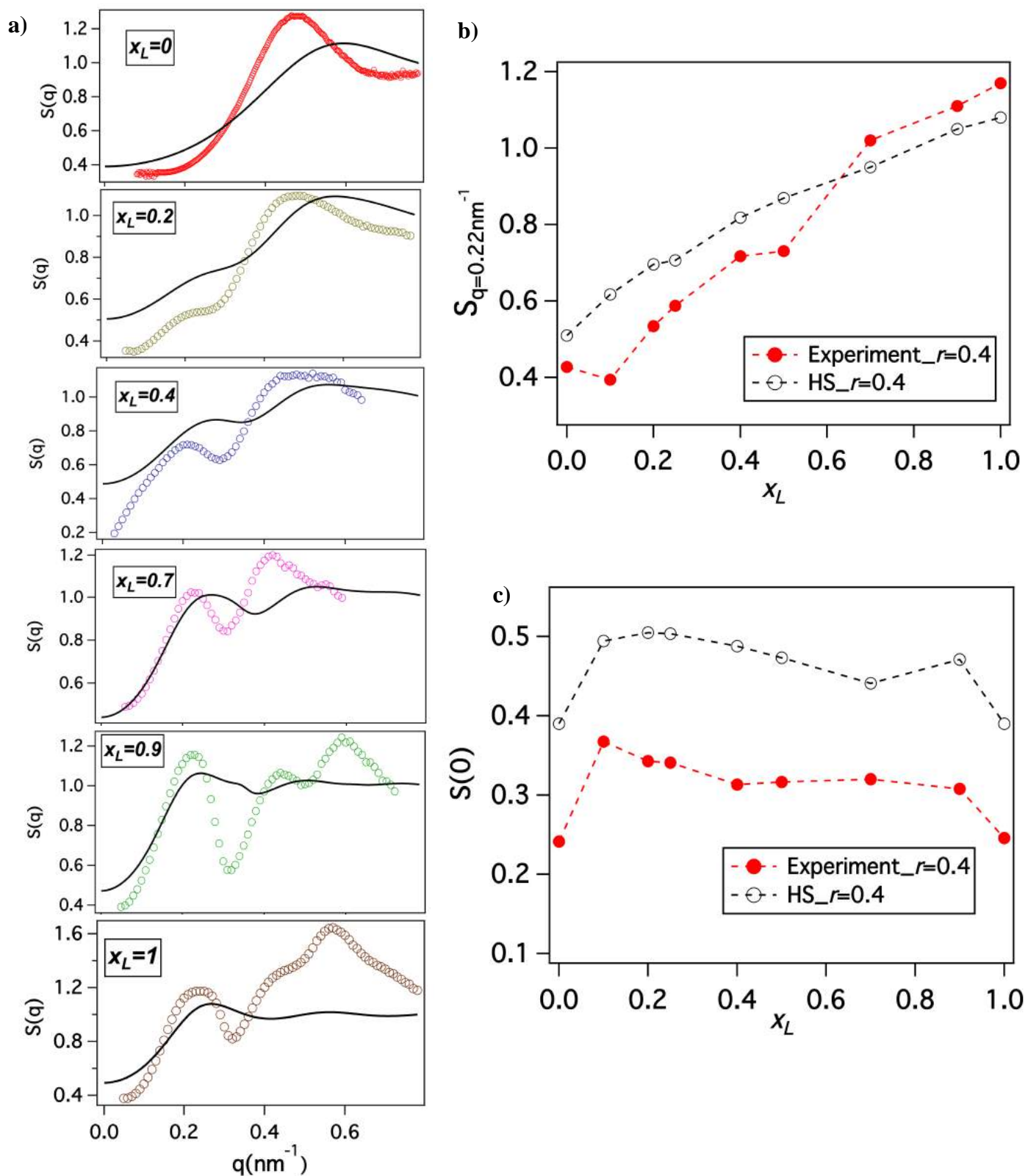


Figure 3.2 a) Structure factor $S(q)$ vs q for systems with different x_L . The circles represent experimental result and lines are for HS calculations. Comparison of b) $S(q)$ at $q \sim 0.22\text{nm}^{-1}$ and c) $S(0)$ with HS calculations at different x_L .

To further examine the effect of polydispersity on particle-particle correlations, we probed the dynamics of fluctuations in particle correlations using X-ray photon correlation spectroscopy (XPCS). Supplementary figure 3.5a) shows that the loss and storage moduli show a very weak dependence on time, implying that the materials used for the study show negligible aging.⁵⁹ This is also confirmed by negligible variation in $g_2(q,t)$ over a time span of 3600s (Supplementary figure 3.5b)) which is higher than the time span of XPCS measurement for a system. Figure 3.3a) shows the evolution of the auto-correlation function, $g_2(q,t)$ for different binary particle mixtures. A terminal relaxation regime ($g_2(q,t) \sim 1$ at large time) is observed in every case, which is unusual for jammed colloidal suspensions comprising of soft spheres.¹⁷ However, as reported earlier, the suspensions of densely-grafted hairy nanoparticles are able to reach an equilibrium state^{39,60} and our observations therefore concurs with the absence of aging in these systems discussed above.

All particle blends also consistently exhibit a $\tau \sim q^{-1}$ relationship (Figure 3.3b) and c)), with $\beta \sim 1.5$ (Supplementary figure 3.6). This finding is in agreement with previous observations that the single-component self-suspended particles are jammed and exhibit slow, hyper-diffusive dynamics.^{16,50,61} τ values for different systems were extracted at a fixed wave vector, $q \sim 0.22\text{nm}^{-1}$, which corresponds to the inter-particle distance for large particles, and are reported in Figure 3.3d) as a function of x_L . It can be seen that the de-correlation time decreases with increasing x_L until $x_L \approx 0.7$ and then rises again. This means that addition of either smaller or larger particles to a system of pure larger or smaller particles, respectively, leads to faster dynamics. Since the particles are well-dispersed and un-aggregated, this speeding-up of dynamics cannot be a result of

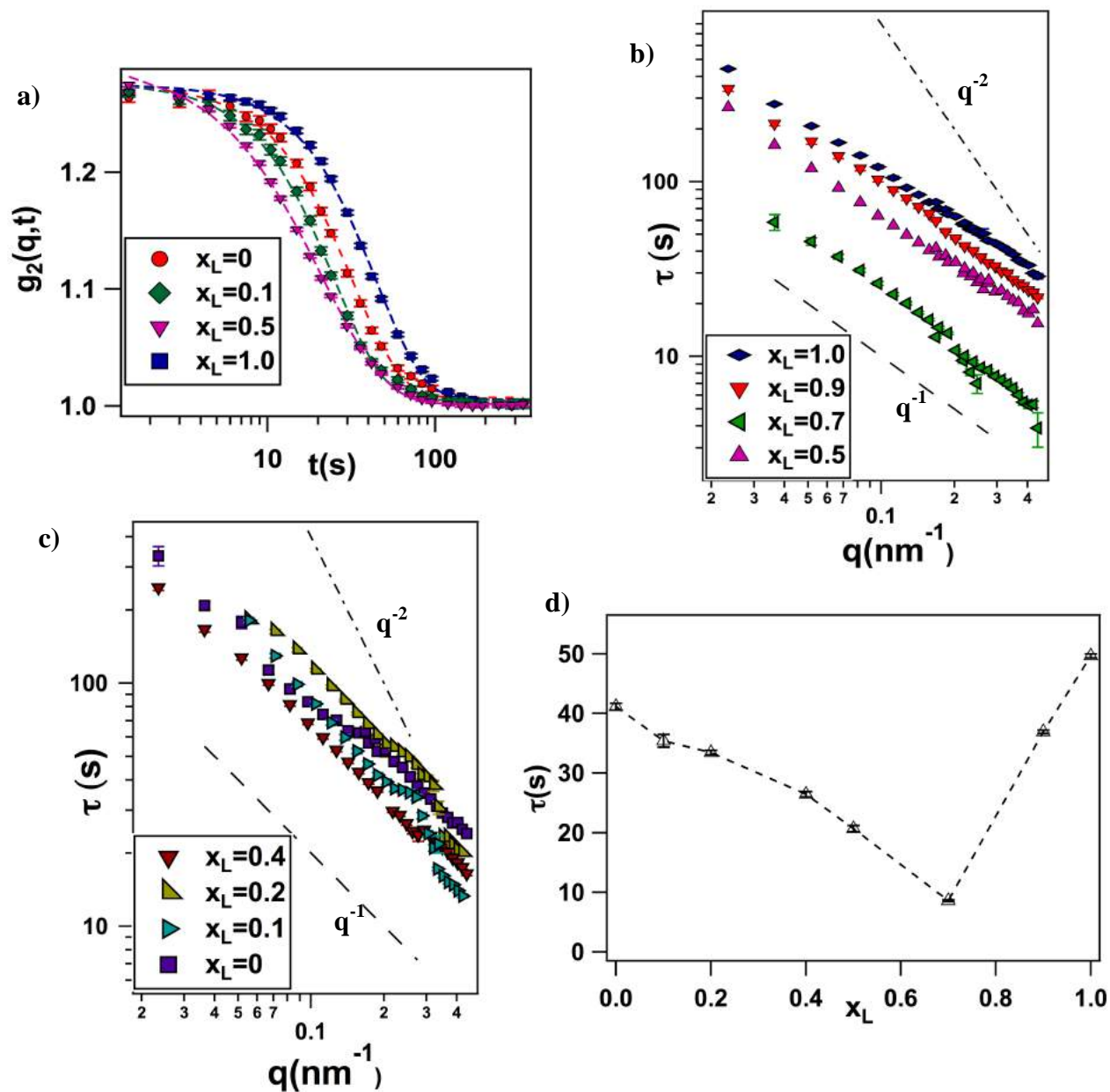


Figure 3.3 **a)** Intensity auto-correlation function $g_2(q,t)$ at $q = 0.22\text{nm}^{-1}$ with stretched exponential fits. **b)** and **c)** Relaxation time τ as a function of wave vector q at different x_L . The dashed line denotes $\tau \propto 1/q$ scaling, and the dashed-dotted line denotes $\tau \propto 1/q^2$ scaling. **d)** Variation of τ with x_L at $q \sim 0.22\text{nm}^{-1}$. It can be seen that addition of either species first reduces the de-correlation time and then increases it.

depletion induced interaction as reported previously.³² The faster particle dynamics observed upon initial addition of either species is more likely the result of reduced correlations among particles. This increased entropy in bi-dispersed particle systems appears to be a consequence of the heterogeneity introduced due to polydispersity in size and variation in the oligomer volume carried by the smaller/bigger particles in the mixtures. Specifically, we propose that since the larger and smaller particles are defined by differences in curvature and the number of oligomers they carry per unit volume, addition of a different sized hairy particle to a pure self-suspended suspension of particles of another size increases heterogeneity and relaxes the space filling constraints on ligands tethered to their large/smaller cohorts. Since it is the ligand mediated interactions between the particles that lead to jamming at the low particle volume fractions studied here, the faster dynamics can be interpreted as a ligand-induced softening of the suspensions.

We expect these dynamical effects to have consequences on the rheological properties of the materials. Oscillatory shear rheology is an established method for studying the mechanical properties and jamming behavior of suspensions and other soft glassy materials. Supplementary figure 3.7a) shows the frequency-dependent dynamic moduli for a bi-disperse system with $r = 0.4$. The observed response is typical of any soft glass, with $G' \gg G''$ and a distinct minimum in G'' , which is a reflection of structural relaxations inside the cage.^{4,35} Also, it is noteworthy that the minimum in G'' , occurs at an angular frequency of $\omega = 10 \text{ rad/s}$ for all the x_L values. Hence, the large amplitude oscillatory shear measurements for the systems were performed at this frequency. At larger strain amplitudes, the measurements can be used to obtain more detailed

information about the strength and longevity of cage constraints. Figure 3.4a) reports a typical response to shear strain for the pure self-suspended suspension as well as for a typical bi-disperse material. It can be observed that the pure species show a single maximum in G'' , which is associated with a single-step yielding transition in a soft glass^{4,33,34,62–65} and has been attributed to strain-induced breakage of the “cage” which constraints the motion of particles in the material. In contrast, the bi-disperse suspensions show a characteristic two-step yielding transition, indicating that the cage landscape is more complex.

Similar two-step yielding has been observed for attractive glasses and gels^{33,35} and it has been attributed to the breaking of inter-particle bonds followed by cage escape. A weak stress-strain response reminiscent of two-step yielding has also been reported for a binary mixture of hard spheres in a solvent,⁶⁶ but in that case the observations were limited to one x_L value. Figure 3.4b) reports the loss modulus normalized by its zero strain value, $G''/G''_{\gamma \rightarrow 0}$ as a function of shear strain. It is evident that a clear and distinct two-step yielding transition is seen over a wide range of x_L , which implies that there are two cage environments in the bi-disperse hairy particle mixtures over a wide composition range. We propose that the first, lower strain, yielding event reflects the release of cage constraints for smaller particles as it occurs at strains similar to those where the pure small-particle suspensions show a clear one-step yielding transition. The second yielding event is attributed to release of constraints on bigger particles and thus occurs at a higher strain value.

From the loss modulus one can estimate the energy dissipated per unit volume, U_d , in each cage-breaking event, after removing the contribution from the background

dissipation by subtracting dissipation measured in the low amplitude linear viscoelastic regime. Specifically, we de-convolute the two peaks in G'' using a lognormal fit, (shown by dotted lines in Figure 3.4b), which allows U_d to be estimated using the formula:⁶⁷

$$U_d = \int \sigma(t) \dot{\gamma}(t) dt \sim \int \sigma d\gamma \sim \int G''(\gamma) \gamma d\gamma . \quad (1)$$

Figure 3.4c) reports U_d as a function of x_L for $r = 0.4$. The closed symbols represent energy dissipated in breaking the first cage while the open symbols reflect the second cage breakage event. Since, the first peak in the normalized G'' (Figure 3.4b)) is attributed to relaxation of constraints for smaller, more tightly jammed particles, it is apparent that even a minute fraction of large particles relaxes cage constraints on smaller ones and markedly lowers the energy dissipated upon cage breakage. Similarly, introduction of smaller particles to pure larger particles leads to a reduction in dissipated energy associated with the breaking of the second cage, attributed to release of cage constraints on the bigger particles. Increasing the content of bigger particles added to the pure smaller-particle system eventually leads to an increase in U_d for both cages.

The observation of a minimum of U_d at $x_L \sim 0.5$ is consistent with the appearance of a minimum in τ observed in Figure 3.3d). We hypothesize that both observations reflect heterogeneity of corona interactions between larger and smaller particles. In our solvent-free self-suspended systems, the oligomers have to uniformly fill the interstitial space. Even for equal molecular weight corona molecules, differences in grafting density and/or curvature of the particles to which the molecules are grafted will produce differences in the ease/difficulty with which the tethered fluid is able to fill the inter-particle space. These changes are anticipated to manifest as different degrees of chain stretching among

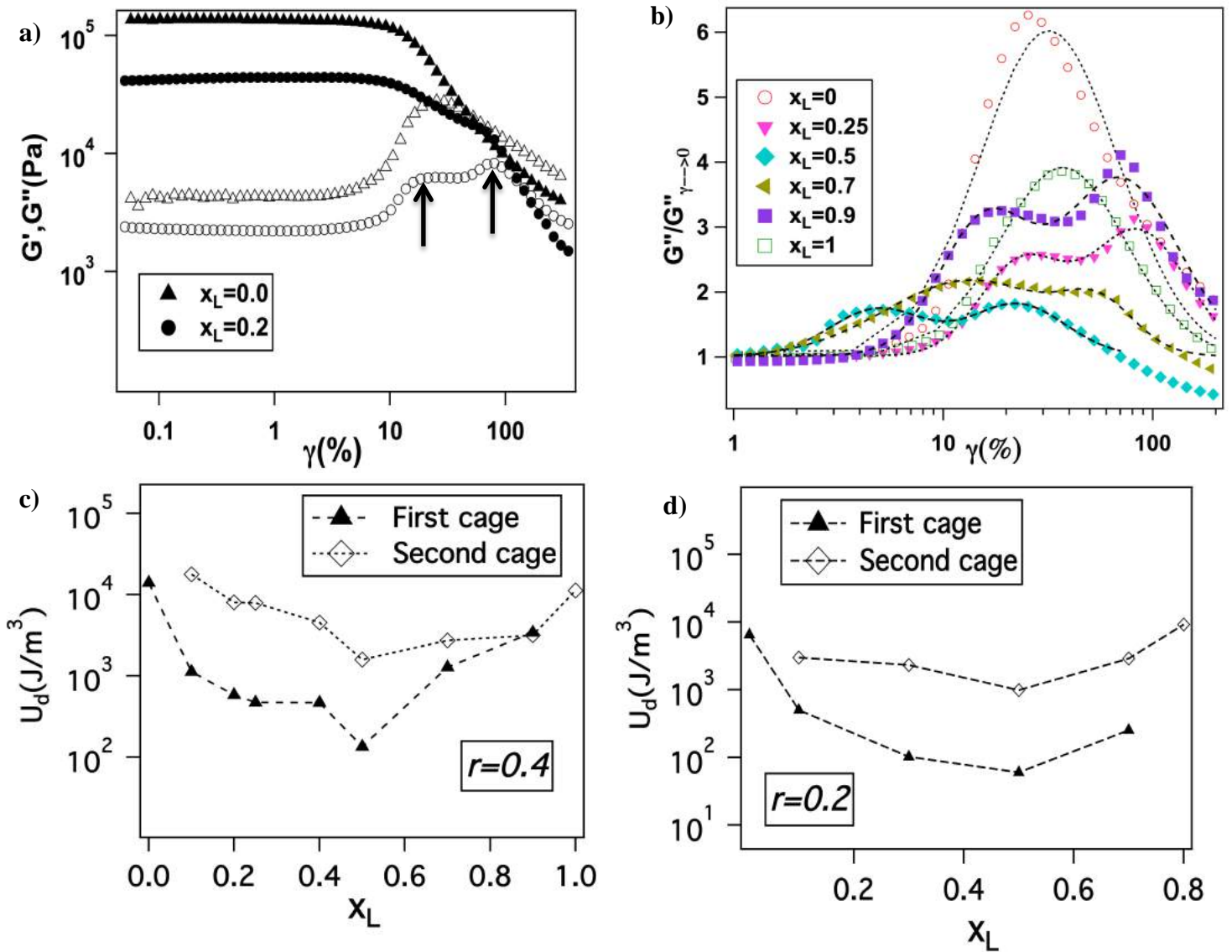


Figure 3.4 **a)** Comparison of G' (closed symbols) and G'' (open symbols) between a monodisperse ($x_L = 0$) and a binary system ($x_L = 0.2$) at $r = 0.4$. **b)** Normalized loss modulus, $G''/G''_{\gamma \rightarrow 0}$ at $\omega = 10 \text{ rad/s}$ with lognormal fits (dotted lines) at $r = 0.4$. Energy dissipated in breaking the cage, U_d calculated from the normalized loss modulus for **c)** $r = 0.4$ and **d)** $r = 0.2$. The first cage corresponds to the constraints on the smaller particles while the second cage corresponds to the constraints set on larger particles.

chains tethered to pure smaller, pure larger, and bi-disperse mixtures of the particles. The heterogeneity in corona structure in the bi-disperse mixtures should therefore lead to an effective disordering of the tethered ligands and a softening of the cage constraints. A correlation between the faster particle de-correlation dynamics and the energy dissipated upon cage breakage is then unsurprising. Our observation that addition of larger particles to a bi-disperse blend can reduce the extent of jamming is, nevertheless, quite different from previous reports, where adding larger particles to a suspension of smaller ones is typically found to facilitate vitrification due to arrest of both the particles in their cages.³⁶ We test our hypothesis by looking at the trends in rheological behavior for different size ratios. At $r = 0.2$ we see similar trends as observed above, as shown in Supplementary figure 3.7b) and Supplementary figure 3.8. Figure 3.4d) shows the energy dissipated in breaking the cage for $r = 0.2$. We find again that addition of bigger particles leads to a dramatic decrease in the dissipated energy for the smaller ones. It is noteworthy that the dissipated energies for $r = 0.2$ are much lower than $r = 0.4$, as the bigger particles bring in more oligomer volume and thus leads to a stronger relaxation of the cage constraints on the smaller ones. On progressing towards lower size ratios, we find that the systems progressively move towards a liquid phase. As seen from Figure 3.5a) at $r = 0.125$, addition of just a small fraction of larger particles leads to a transition to a liquid phase with $G'' > G'$. Further addition of larger particles leads to a transition back to a jammed soft glassy behavior. A similar progression to liquid phase is observed for $r = 0.05$ (Figure 3.5b)) and $r = 0.027$ (Figure 3.5c)).

An important parameter which can be used to quantify this behavior is the loss tangent, $\tan(\delta) = G''/G'$. Since it is the ratio of loss modulus to storage modulus, it is an

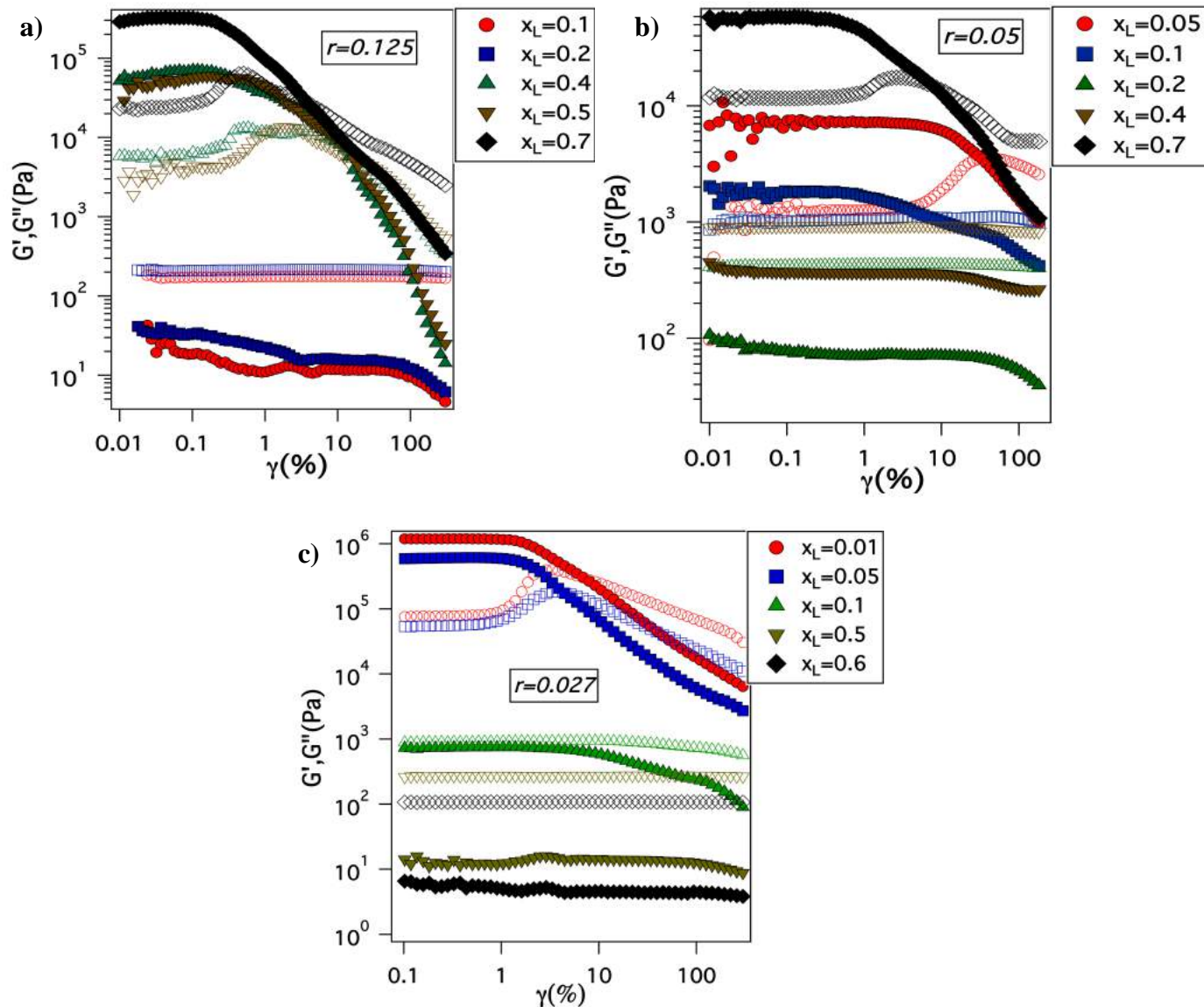


Figure 3.5 Amplitude sweep measurements of storage modulus, G' (closed symbols) and loss modulus, G'' (open symbols) at $\omega = 10 \text{ rad/s}$ for size ratios **a)** $r = 0.125$ **b)** $r = 0.05$ and **c)** $r = 0.027$. At $r = 0.125$ and $r = 0.05$, addition of bigger particles first leads to melting of glass, after which further increase in x_L leads to a transition to soft glassy behavior. While for $r = 0.027$, increase in x_L leads to complete melting of glass.

indication of the extent of elasticity of the system and a loss tangent value greater than unity can be loosely used to identify a transition to liquid phase. Figure 3.6a) and b) report loss tangent values obtained in the linear viscoelastic regime at a fixed angular frequency, $\omega = 10\text{rad/s}$. Consistent with our observations from XPCS experiments and dissipated energy calculations, we find that for larger size ratios, addition of bigger particles to a suspension of pure jammed smaller particles weakens the suspension and further introduction of bigger particles retrieves the jammed state. However, for smaller size ratios, we observe that addition of bigger particles leads to an increase in $\tan(\delta)$ well beyond unity, indicating a transition to a liquid-like regime. Further addition of bigger particles results in a decrease in the loss tangent. Thus, in contrast to previous studies on binary hard spheres,^{66,68} we find that the effect of jamming/un-jamming produced by addition of larger particles to smaller ones in a bi-disperse blend is more sustained and distinct, even at moderate x_L values. This result is believed to be a direct manifestation of the change in the space filling constraint for the tethered oligomeric fluid with the introduction smaller/bigger particles to a mono-disperse system. These loss tangent results are complemented by the trends observed in plateau modulus and complex viscosity as a function of x_L for various size ratios. Figures 3.6c) and 3.6d) show the plateau modulus normalized with energy density, which is given as $k_B T / \langle R^3 \rangle$, where k_B is the Boltzmann constant, T is the temperature and $\langle R^3 \rangle$ is the average of the cube of particle radius⁶⁶; and the rescaled complex viscosity at $\omega=1\text{rad/s}$ measured from frequency sweep measurements. We observe that for larger size ratios of $r=0.4$ and 0.2 , addition of bigger particles leads to a weaker storage modulus, and a decrease in complex viscosity, replicating the results obtained from dissipated energy and loss tangent. While

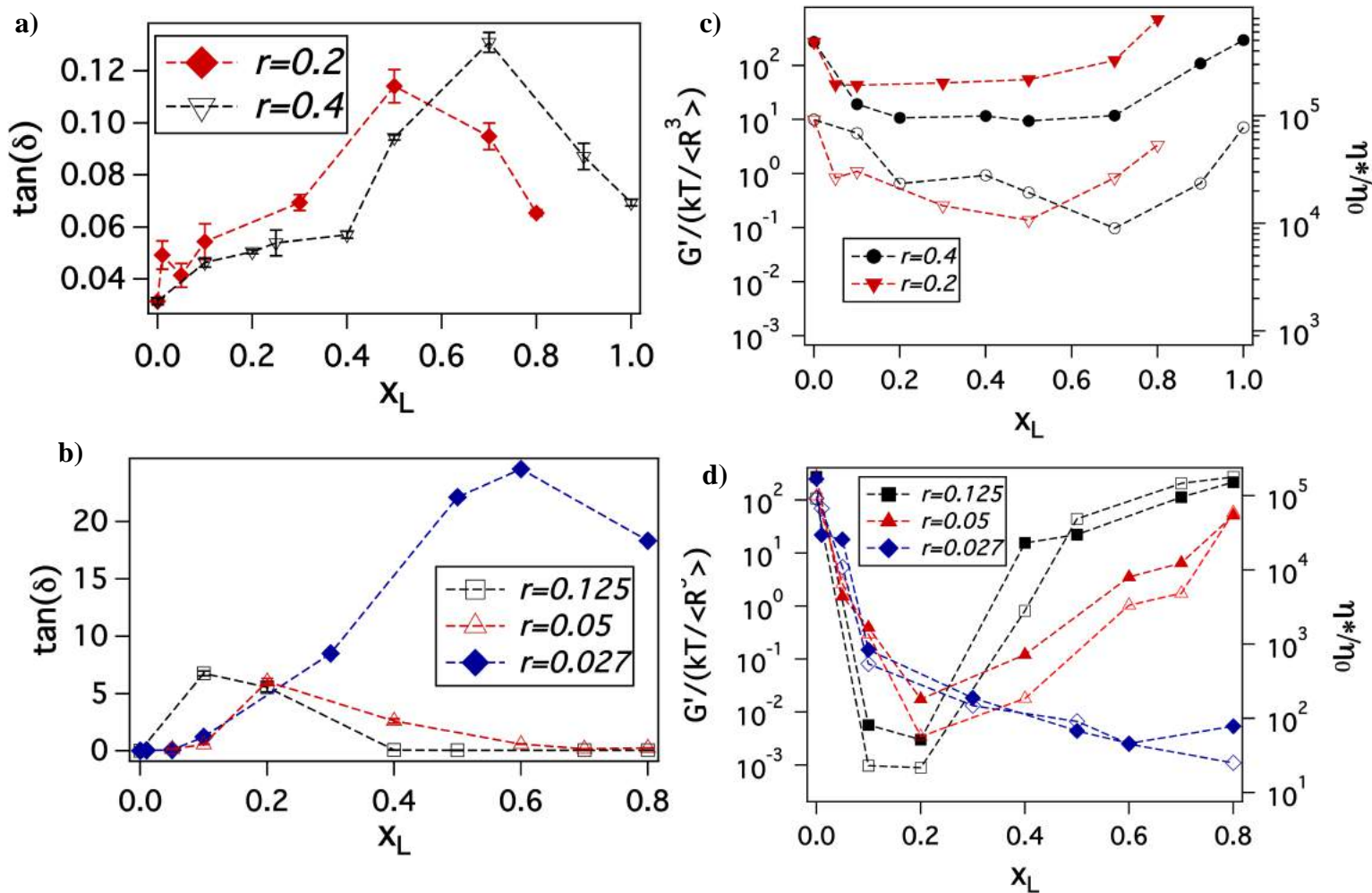


Figure 3.6 Comparison of loss tangent, $\tan(\delta)$ at zero strain with increase in x_L at different size ratios **a)** $r = 0.2$ and $r = 0.4$, and **b)** $r = 0.125$, $r = 0.05$ and $r = 0.027$. Addition of bigger particles first leads to an increase in $\tan(\delta)$, indicating particle unjamming and then a decrease in loss tangent. While for smaller size ratios of $r = 0.125$, $r = 0.05$ and $r = 0.027$, the loss tangent is greater than unity, indicating transition to liquid state. Plateau modulus normalized with energy density (closed symbols) and normalized complex viscosity (open symbol) measured at $\omega=1\text{rad/s}$ for **c)** $r = 0.2$ and $r = 0.4$, and **d)** $r = 0.125$, $r = 0.05$ and $r = 0.027$. η_0 corresponds to the complex viscosity to PEG (MW~5000g/mol) melt. The trends in normalized plateau modulus and complex viscosity confirm to the trends seen in loss tangent.

for smaller size ratios, addition of larger particles, decrease the plateau modulus to below unity which indicates that the energy due to thermal motion of the particles is much higher and hence implies a transition to liquid regime. Similar trends are observed in normalized complex viscosity, where addition of larger particles leads to a drastic decrease in the viscosity values, and further addition leads to a transition to jammed state. An experimental state diagram (Figure 3.7) can be constructed based on the observations from the rheological responses in Figure 3.6. At larger particle size ratios, an increase in x_L first weakens a suspension of pure smaller particles and, at higher x_L , leads to a transition back to a jammed state. On progressing towards smaller size ratios, an increase in x_L leads to a transition from a soft glass to liquid and then back to a jammed glass. The state diagram observed here is much similar to that of the binary soft spheres^{36,37} however the, the size ratios at which this transition from glass to a liquid regime is seen are much smaller, and the transition to the liquid regime occurs at increasingly smaller x_L values. This is a consequence of the increasingly high heterogeneity in oligomer volume that is introduced as the particle size increases, and hence the quantity of the bigger particles required to relax the smaller particles becomes lesser. Previous studies on binary hard spheres have shown that for $r < 0.1$, smaller particles produce depletion induced interactions between the bigger particles, which in turn enable access of the smaller particles to a larger bulk volume, with the result that the system transitions to a liquid phase.³¹ However, the absence of a solvent in our self-suspended materials means that the increased volume available to the smaller particles increases the extent to which tethered chains must stretch to fill the inter-particle space. The bigger particles bring more oligomeric fluid volume, and thus relax constraints on the smaller ones considerably,

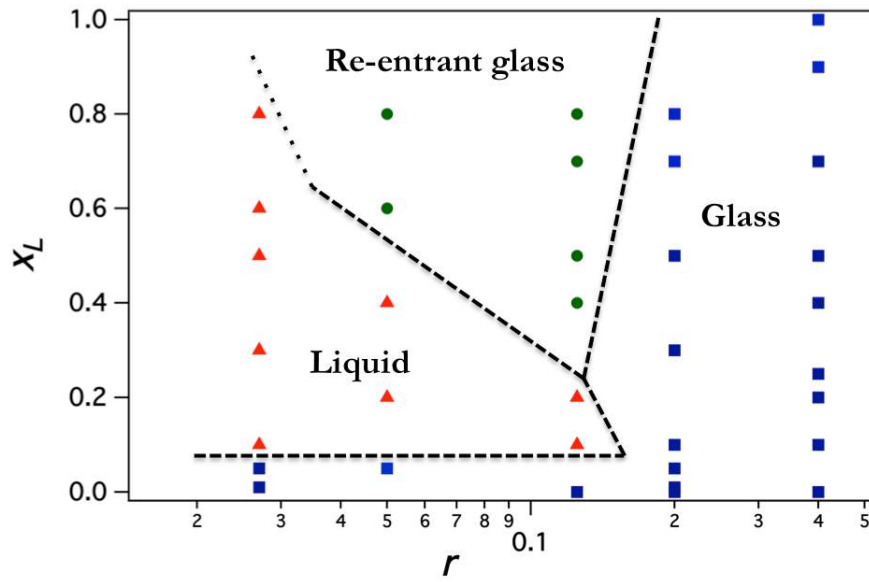


Figure 3.7 Experimental state diagram for x_L vs. size ratio, r . For smaller size ratios, increase in x_L leads to a weakening of glass, while for larger size ratios increase in x_L results in a transition from a soft glass to liquid and then again to an arrested glass.

resulting in a transition to a liquid state. The re-entrant glassy state observed here is again a double glass with dominant large particles as evident from the two-step yielding observed for $r = 0.125$ and 0.05 for the x_L values in this regime. A very unique aspect of these systems is that we are able to capture these state transitions for different size ratios at dilute concentrations of cores, which is much different from previous studies on binary hard spheres, where the studies were carried out at glass transition volume fraction of the system as high as 0.58 . A practical consequence, wherein the binary hybrid nanoparticles have been used as highly conducting electrolytes, have recently been reported.²⁵

3.5 Conclusions

In conclusion, we have studied the structure, dynamics, and rheology of bi-disperse suspensions of solvent-free polymer-functionalized, soft nanoparticles. We find that dispersity in particle size has significant and unexpected effects on both the dynamics and rheology of the suspensions. Specifically, for moderate size ratio, $r = 0.4$ and $r = 0.2$, adding bigger particles to a system of pure jammed smaller particle first weakens the glass, beyond which further increase in the concentration of bigger particles in the binary suspensions leads to jamming. In contrast, for extremely small size ratios, we find that even a small fraction of large particles can completely unjam a suspension of smaller ones.

These findings are confirmed by XPCS and rheology measurements, where addition of bigger particles speeds up de-correlation dynamics of the system. They are further supported by calculations of the energy dissipated at the jamming transition, where it is seen that the energy dissipated in releasing cage constraints on bigger and smaller particles is lower in bi-disperse blends than in monodisperse soft particle suspensions.

Significantly, all of these features are observed at an effective particle volume fraction of 0.12-0.15, which is much lower than the hard sphere glass transition volume fraction. This indicates that the tethered polymer chains play a major role in particle dispersion and their soft glassy behavior. We argue that interactions between these chains, dictated by the space filling constraint in a solvent-free self-suspended material, are responsible for the observed, large effects of particle size polydispersity on structure, dynamics, and rheology of bi-disperse suspensions of soft particles.

Acknowledgements

This work was supported by the National Science Foundation, Award No. DMR-1006323 and by Award No. KUS-C1-018-02, made by King Abdullah University of Science and Technology (KAUST). Use of the Advanced Photon Source, operated by Argonne National Laboratory, was supported by the U.S. DOE under Contract No. DE-AC02-06CH11357. We acknowledge Prof. D. L. Koch for helpful discussions.

REFERENCES

- (1) P. N. Pusey and W. V. Megen, *Phys. Rev. Lett.*, 1987, **59**, 2083–2086.
- (2) P. N. Pusey and W. V. Megen, *Lett. to Nat.*, 1986, **320**, 340–342.
- (3) P. N. Pusey, W. C. K. Poon, S. M. Ilett and B. P., *J. Phys. Condens. Matter*, 1994, **6**, A29–A36.
- (4) T. G. Mason and D. A. Weitz, *Phys. Rev. Lett.*, 1995, **75**, 2770–2773.
- (5) V. Trappe, V. Prasad, L. Cipelletti, P. N. Segre and D. a Weitz, *Nature*, 2001, **411**, 772–5.
- (6) J. Mattsson, H. M. Wyss, A. Fernandez-Nieves, K. Miyazaki, Z. Hu, D. R. Reichman and D. a Weitz, *Nature*, 2009, **462**, 83–6.
- (7) C. S. O’Hern, L. E. Silbert and S. R. Nagel, *Phys. Rev. E*, 2003, **68**, 011306–1–19.
- (8) A. J. Liu and S. R. Nagel, *Nature*, 1998, **396**, 21–22.
- (9) B. P. Tighe, E. Woldhuis, J. J. C. Remmers, W. van Saarloos and M. van Hecke, *Phys. Rev. Lett.*, 2010, **105**, 088303–1–4.
- (10) E. Stiakakis, D. Vlassopoulos and J. Roovers, *Langmuir*, 2003, **19**, 6645–6649.
- (11) D. Bonn, S. Tanase, B. Abou, H. Tanaka and J. Meunier, *Phys. Rev. Lett.*, 2002, **89**, 015701–1–4.

- (12) B. Abou, D. Bonn and J. Meunier, *Phys. Rev. E*, 2001, **64**, 021510–1–6.
- (13) S. P. Meeker, W. C. K. Poon, J. Crain and E. M. Terentjev, *Phys. Rev. E*, 2000, **61**, 6083–6086.
- (14) T. Zykova-Timan, J. Horbach and K. Binder, *J. Chem. Phys.*, 2010, **133**, 014705–1–10.
- (15) P. Levitz, E. Lecolier, A. Mourchid, A. Delville and S. Lyonnard, *Europhys. Lett.*, 2000, **49**, 672–677.
- (16) S. Srivastava, L. A. Archer and S. Narayanan, *Phys. Rev. Lett.*, 2013, **110**, 148302–1–5.
- (17) Z. Zhang, N. Xu, D. T. N. Chen, P. Yunker, A. M. Alsayed, K. B. Aptowicz, P. Habdas, A. J. Liu, S. R. Nagel and A. G. Yodh, *Nature*, 2009, **459**, 230–3.
- (18) X. Cheng, *Soft Matter*, 2010, **6**, 2931–2934.
- (19) X. Cheng, *Phys. Rev. E*, 2010, **81**, 031301–1–12.
- (20) A. Scala, F. W. Starr, E. La Nave, F. Sciortino and H. E. Stanley, *Lett. to Nat.*, 2000, **406**, 166–169.
- (21) J. R. Errington and P. G. Debenedetti, *Lett. to Nat.*, 2001, **409**, 1–4.
- (22) F. Sciortino, A. Geiger and H. E. Stanley, *Lett. to Nat.*, 1991, **354**, 218–221.

- (23) J. L. Schaefer, S. S. Moganty, D. A. Yanga and L. A. Archer, *J. Mater. Chem.*, 2011, **21**, 10094–10102.
- (24) J. L. Nugent, S. S. Moganty and L. A. Archer, *Adv. Mater.*, 2010, **22**, 3677–80.
- (25) A. Agrawal, S. Choudhury and L. A. Archer, *RSC Adv.*, 2015, **5**, 20800–20809.
- (26) M. Dijkstra, R. van Roij and R. Evans, *Phys. Rev. E. Stat. Phys. Plasmas. Fluids. Relat. Interdiscip. Topics*, 1999, **59**, 5744–71.
- (27) M. Dijkstra, R. van Roij and R. Evans, *Phys. Rev. Lett.*, 1998, **81**, 2268–2271.
- (28) R. Roth and S. Dietrich, *Phys. Rev. E*, 2000, **62**, 6926–6936.
- (29) T. Voigtmann, *EPL (Europhysics Lett.)*, 2011, **96**, 36006–p1–p6.
- (30) W. Götze and T. Voigtmann, *Phys. Rev. E*, 2003, **67**, 021502–1–14.
- (31) A. Imhof and J. K. G. Dhont, *Phys. Rev. Lett.*, 1995, **75**, 1662–1665.
- (32) M. Sikorski, A. R. Sandy and S. Narayanan, *Phys. Rev. Lett.*, 2011, **106**, 188301–1–4.
- (33) K. N. Pham, G. Petekidis, D. Vlassopoulos, S. U. Egelhaaf, W. C. K. Poon and P. N. Pusey, *J. Rheol. (N. Y. N. Y.)*, 2008, **52**, 649–676.
- (34) K. N. Pham, G. Petekidis, D. Vlassopoulos, S. U. Egelhaaf, P. N. Pusey and W. C. K. Poon, *Europhys. Lett.*, 2006, **75**, 624–630.

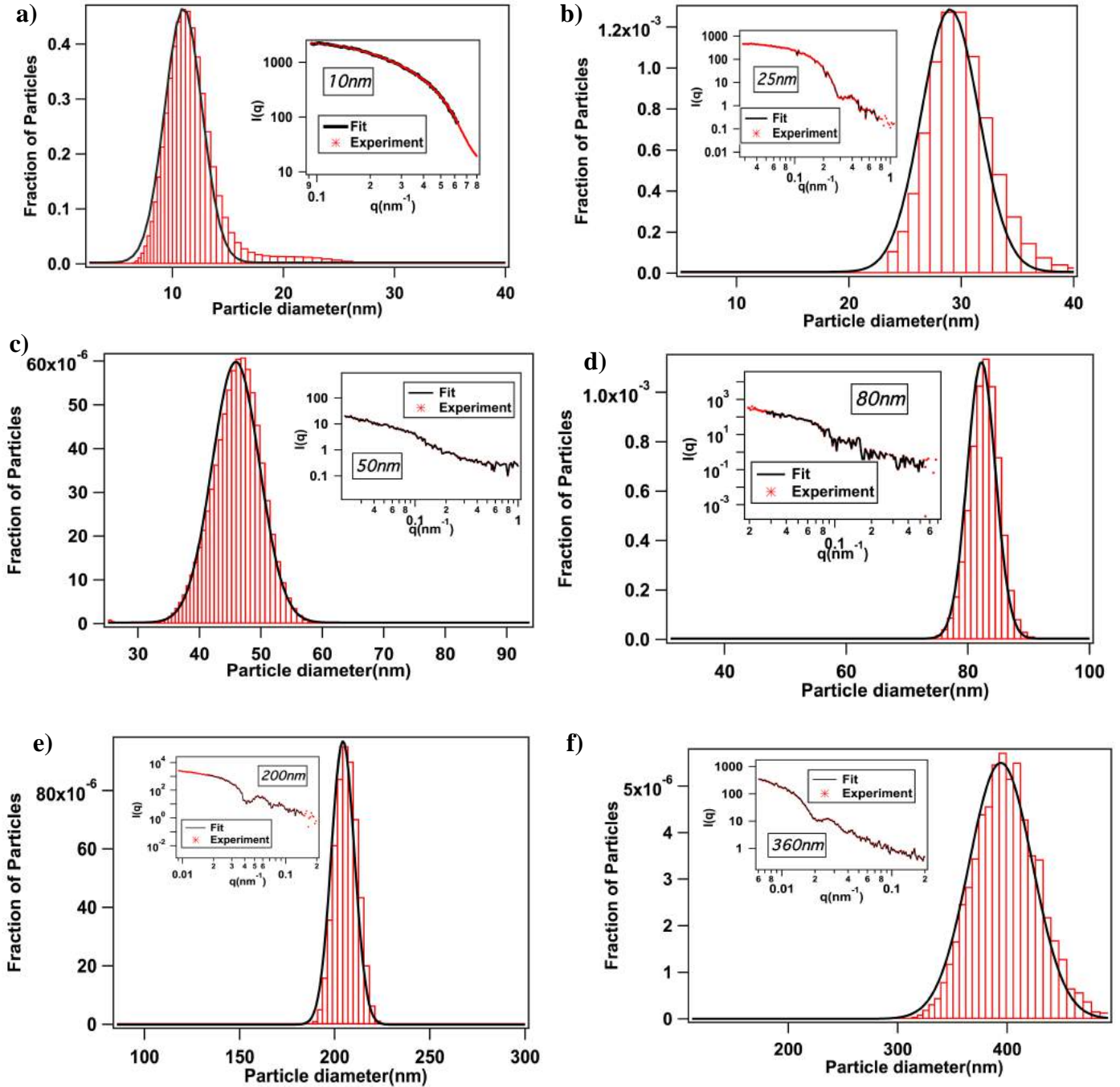
- (35) N. Koumakis and G. Petekidis, *Soft Matter*, 2011, **7**, 2456–2470.
- (36) E. Zaccarelli, C. Mayer, A. Asteriadi, C. Likos, F. Sciortino, J. Roovers, H. Iatrou, N. Hadjichristidis, P. Tartaglia, H. Löwen and D. Vlassopoulos, *Phys. Rev. Lett.*, 2005, **95**, 268301–1–4.
- (37) C. Mayer, E. Zaccarelli, E. Stiakakis, C. N. Likos, F. Sciortino, a Munam, M. Gauthier, N. Hadjichristidis, H. Iatrou, P. Tartaglia, H. Löwen and D. Vlassopoulos, *Nat. Mater.*, 2008, **7**, 780–4.
- (38) R. Rodriguez, R. Herrera, L. A. Archer and E. P. Giannelis, *Adv. Mater.*, 2008, **20**, 4353–4358.
- (39) P. Agarwal, H. Qi and L. A. Archer, *Nano Lett.*, 2010, **10**, 111–5.
- (40) A. Tuteja, P. Duxbury and M. Mackay, *Phys. Rev. Lett.*, 2008, **100**, 077801–1–4.
- (41) M. E. Mackay, A. Tuteja, P. M. Duxbury, C. J. Hawker, B. Van Horn, Z. Guan, G. Chen and R. S. Krishnan, *Science*, 2006, **311**, 1740–3.
- (42) G. H. Bogush, M. A. Tracy and C. F. Zukoski, *J. Non. Cryst. Solids*, 1988, **104**, 95–106.
- (43) S. Choudhury, A. Agrawal, S. A. Kim and L. A. Archer, *Langmuir*, 2015, **31**, 3222–3231.
- (44) J. Ilavsky and P. R. Jemian, *J. Appl. Crystallogr.*, 2009, **42**, 347–353.

- (45) B. D. Aguanno and R. Klein, *J.Chem.Soc.Faraday Trans.*, 1991, **87**, 379–390.
- (46) C. De Kruif and A. Vrij, *Colloid Polym. Sci.*, 1988, **1076**, 1068–1076.
- (47) B. Weyerich, J. Brunner-Popela and O. Glatter, *J. Appl. Crystallogr.*, 1999, **32**, 197–209.
- (48) R. Krause, B. D. Aguanno, J. M. Mendez-Alcaraz, G. Nagele, R. Klein and R. Weber, *J. Phys. Condens. Matter*, 1991, **3**, 4459–4475.
- (49) S. Mazoyer, L. Cipelletti and L. Ramos, *Phys. Rev. Lett.*, 2006, **97**, 238301–1–4.
- (50) R. L. Leheny, *Curr. Opin. Colloid Interface Sci.*, 2012, **17**, 3–12.
- (51) D. Lumma, L. B. Lurio, M. a. Borthwick, P. Falus and S. G. J. Mochrie, *Phys. Rev. E*, 2000, **62**, 8258–8269.
- (52) H. Guo, G. Bourret, M. K. Corbierre, S. Rucareanu, R. B. Lennox, K. Laaziri, L. Piche, M. Sutton, J. L. Harden and R. L. Leheny, *Phys. Rev. Lett.*, 2009, **102**, 075702–1–4.
- (53) A. Madsen, R. L. Leheny, H. Guo, M. Sprung and O. Czakkel, *New J. Phys.*, 2010, **12**, 055001.
- (54) O. Glatter and O. Kratky, *Small Angle X-ray Scattering*, Academic Press, New York, United Sta., 1982.
- (55) S. Srivastava, P. Agarwal and L. A. Archer, *Langmuir*, 2012, **28**, 6276–81.

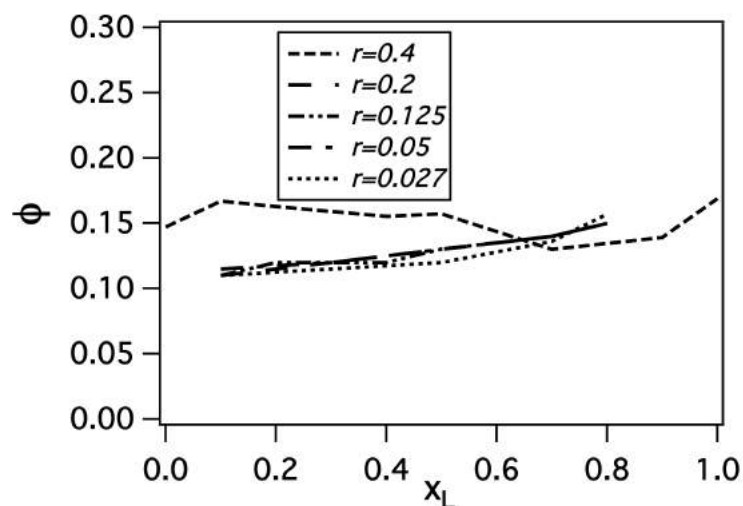
- (56) N. W. Ashcroft and D. C. Langreth, *Phys. Rev. Lett.*, 1967, **156**, 685–692.
- (57) H.-Y. Yu and D. L. Koch, *Langmuir*, 2010, **26**, 16801–11.
- (58) H.-Y. Yu, S. Srivastava, L. A. Archer and D. L. Koch, *Soft Matter*, 2014, **10**, 9120–35.
- (59) P. Agarwal and L. A. Archer, *Phys. Rev. E*, 2011, **83**, 041402–1–5.
- (60) S. Srivastava, J. H. Shin and L. A. Archer, *Soft Matter*, 2012, **8**, 4097–4108.
- (61) S. Narayanan, D. Lee, A. Hagman, X. Li and J. Wang, *Phys. Rev. Lett.*, 2007, **98**, 185506–1–4.
- (62) P. Sollich, F. Lequeux, P. Hébraud and M. Cates, *Phys. Rev. Lett.*, 1997, **78**, 2020–2023.
- (63) P. Agarwal, S. Srivastava and L. A. Archer, *Phys. Rev. Lett.*, 2011, **107**, 268302–1–5.
- (64) M. E. Helgeson, N. J. Wagner and D. Vlassopoulos, *J. Rheol. (N. Y. N. Y.)*, 2007, **51**, 297–316.
- (65) N. Koumakis, A. Pamvouxoglou, A. S. Poulos and G. Petekidis, *Soft Matter*, 2012, **8**, 4271–4284.
- (66) T. Sentjabrskaja, E. Babaliari, J. Hendricks, M. Laurati, G. Petekidis and S. U. Egelhaaf, *Soft Matter*, 2013, **9**, 4524–4533.

- (67) S. N. Ganeriwala and C. A. Rotz, *Polym. Eng. Sci.*, 1987, **27**, 165–178.
- (68) T. Sentjabrskaja, M. Hermes, W. C. K. Poon, C. D. Estrada, R. Castaneda-Priego, S. U. Egelhaaf and M. Laurati, *Soft Matter*, 2014, **10**, 6546–6555.

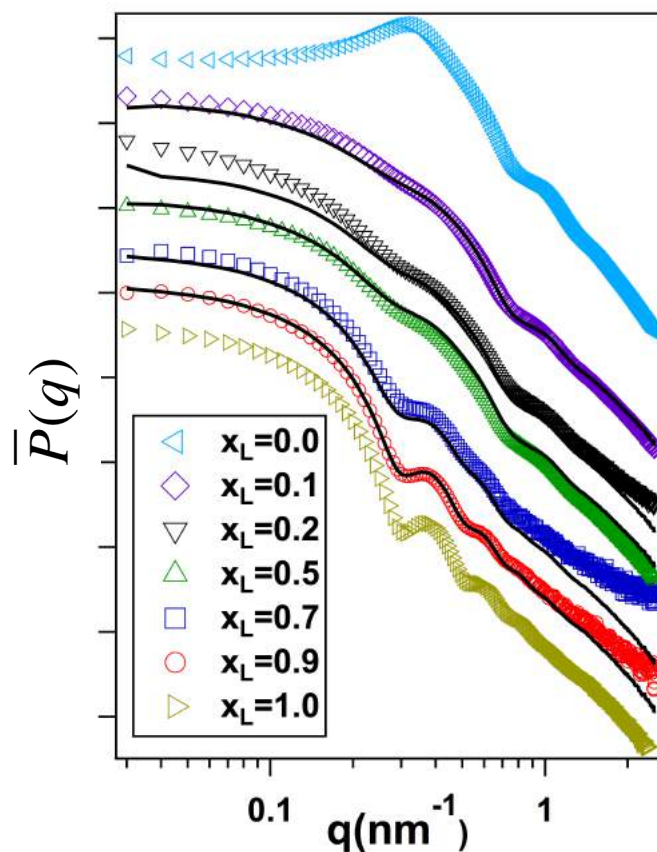
APPENDIX: Supplementary information for chapter 3



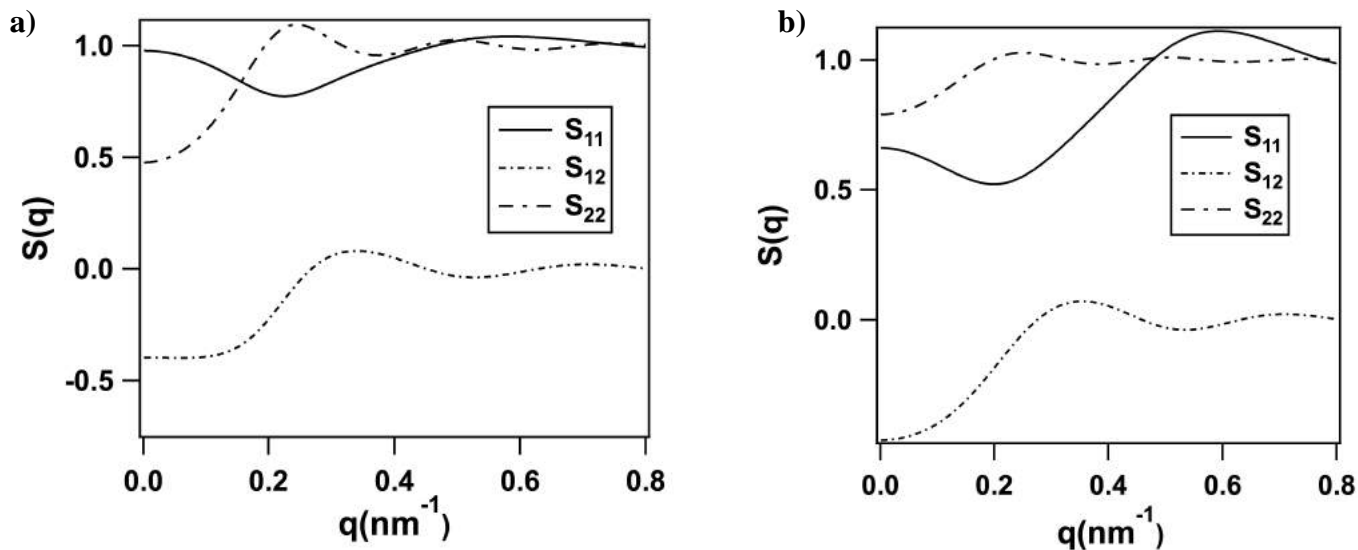
Supplementary figure 3.1 Size distribution of particles as determined from SAXS analysis for **a)** 10nm **b)** 25nm **c)** 50nm **d)** 80nm **e)** 200nm **f)** 360nm. The insets are the experimental scattering intensities (red dots) and the fit to data (black lines) for respective sizes.



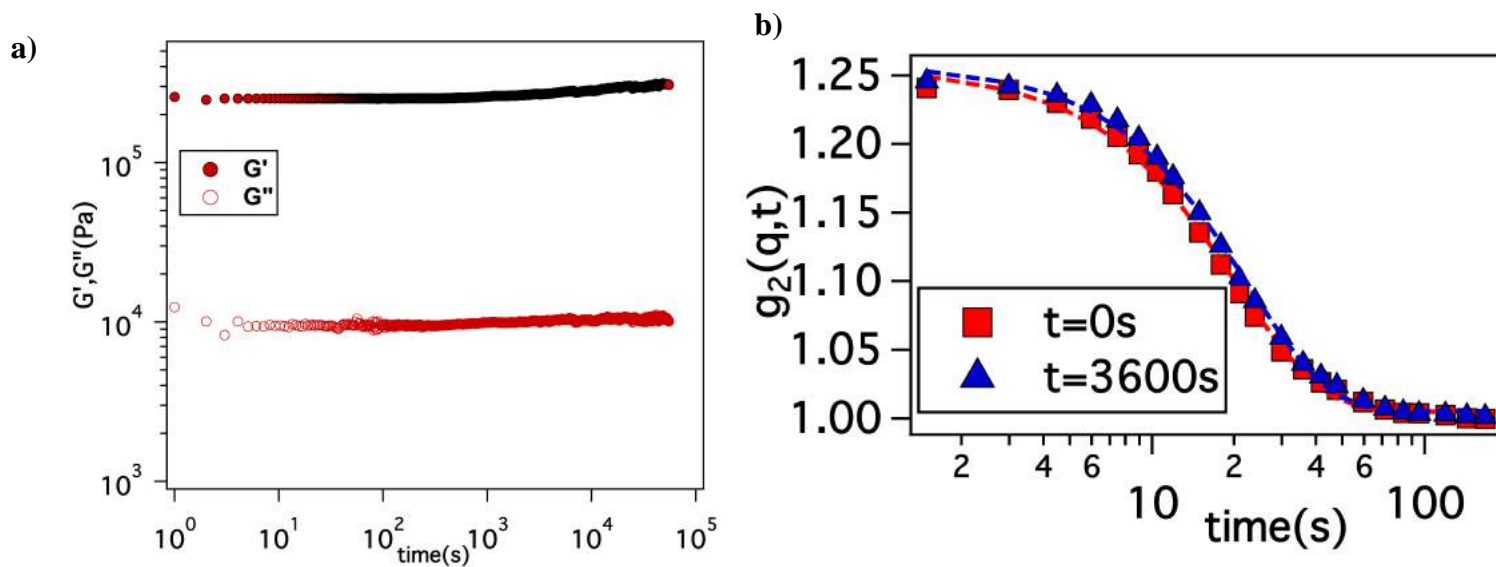
Supplementary figure 3.2 Variation of particle core volume fraction, Φ with x_L for different size ratios. The volume fraction is found to be around 0.10-0.15 for different systems.



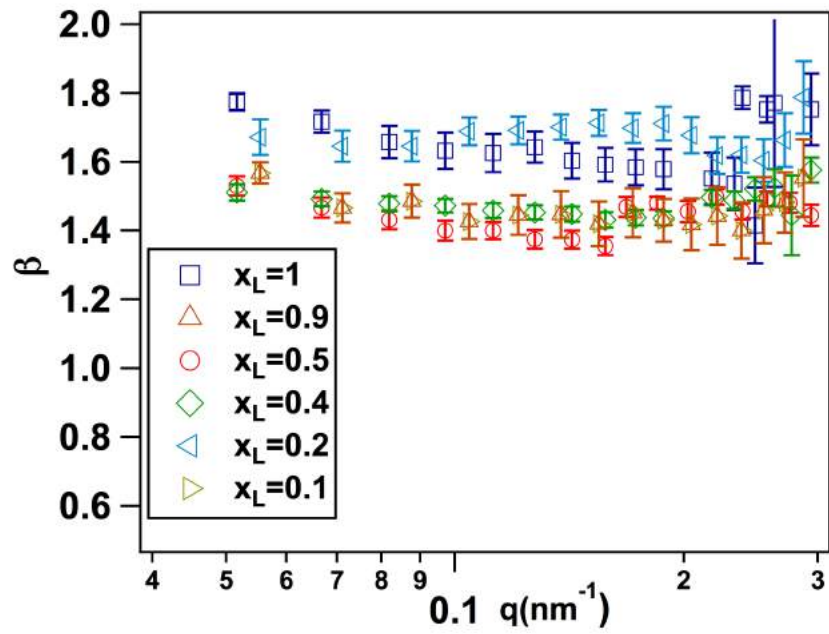
Supplementary figure 3.3 Form factors for different systems at $r = 0.4$ on a log-log plot. The open symbols are experimental values and the black lines are mole fraction-weighted averages of the measured form factors for the pure species as used in literature.^[45-47]



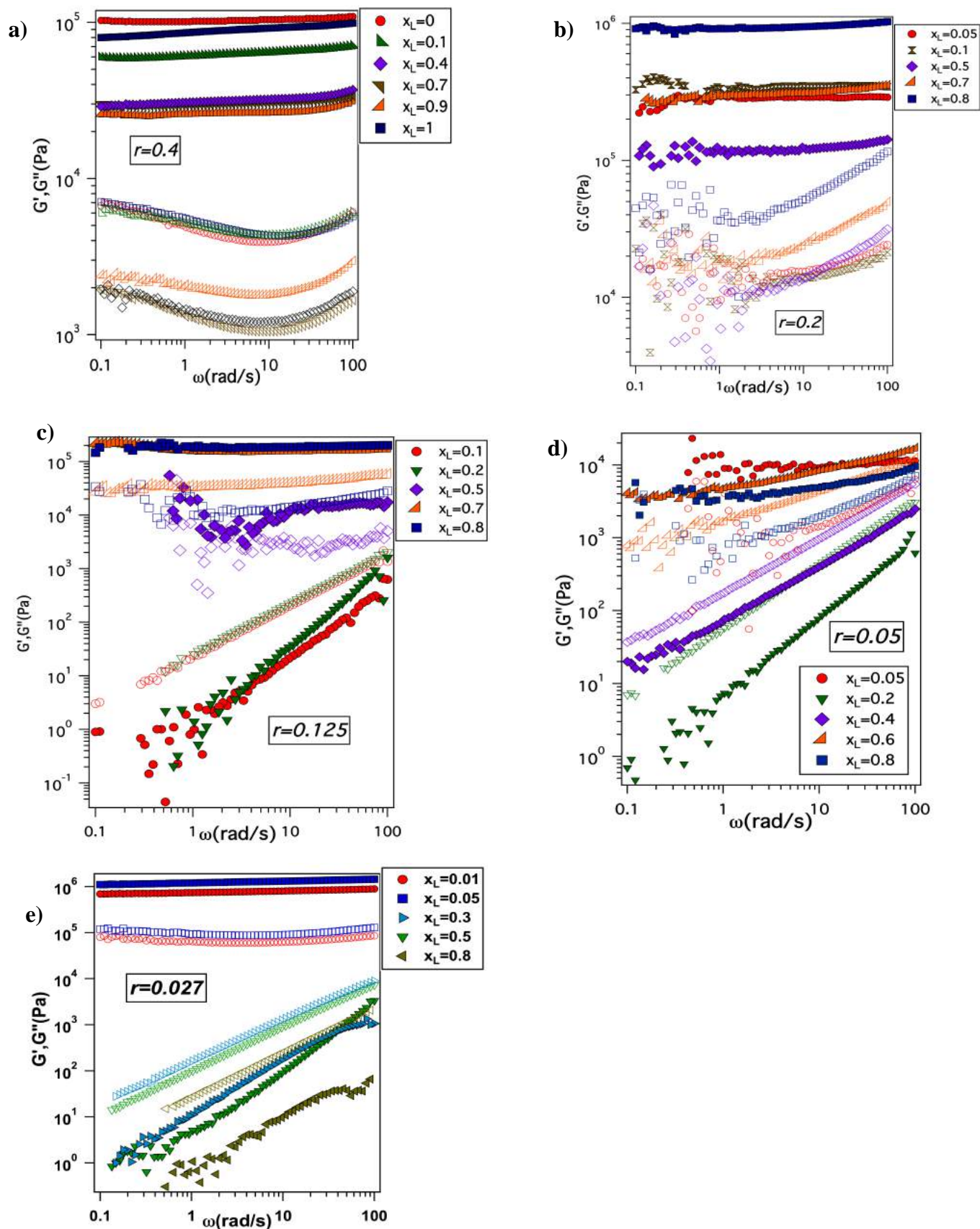
Supplementary figure 3.4. Comparison of S_{11} , S_{12} and S_{22} components of $S(q)$ for **a)** $x_L = 0.7$ and **b)** $x_L = 0.25$.



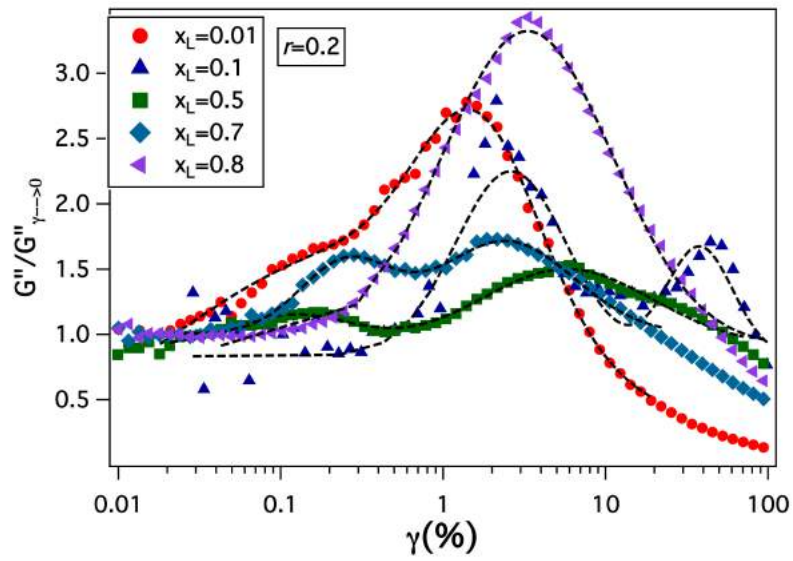
Supplementary figure 3.5 a) Variation of G' and G'' as a function of time after preshear by strain sweep. **b)** Comparison of $g_2(q,t)$ measured initially and after 3600s for $x_L=0.4$ at $q \sim 0.22 \text{ nm}^{-1}$. Since the moduli and the $g_2(q,t)$ do not change with time, it indicates absence of any aging in the system.



Supplementary figure 3.6 Variation of stretching exponent, β with wave vector q at different x_L values.



Supplementary figure 3.7 Storage modulus G' (filled symbols) and loss modulus G'' (open symbols) as a function of angular frequency ω at a strain of $\gamma = 0.5\%$ at different values of x_L for **a)** $r = 0.4$, **b)** $r = 0.2$, **c)** $r = 0.125$, **d)** $r = 0.05$ and **e)** $r = 0.027$.



Supplementary figure 3.8 Normalized loss modulus, $G''/G''_{\gamma \rightarrow 0}$ at $\omega = 10\text{rad/s}$ with lognormal fits (dotted lines) for $r = 0.2$.

Chapter 4

A highly conductive, non-flammable polymer-nanoparticle hybrid electrolyte²

Akanksha Agrawal*, Snehashis Choudhury*, Lynden A. Archer, A highly conductive, non-flammable polymer-nanoparticle hybrid electrolyte, *RSC Advances*, 2015, 5, 20800-20809

Reproduced by permission of The Royal Society of Chemistry

² A. Agrawal and S. Choudhury contributed equally to this work

4.1 Abstract

We report on physical properties of lithium-ion conducting nanoparticle-polymer hybrid electrolytes created by dispersing bidisperse mixtures of polyethylene glycol (PEG)-functionalized silica nanoparticles in an aprotic liquid host. At high particle contents, we find that the ionic conductivity is a non-monotonic function of the fraction of larger particles x_L in the mixtures, and that for the nearly symmetric case $x_L \approx 0.5$ (i.e. equal volume fraction of small and large particles), the room temperature ionic conductivity is nearly ten-times larger than in similar nanoparticle hybrid electrolytes comprised of the pure small ($x_L \approx 0$) or large ($x_L \approx 1$) particle components used in the mixtures. Complementary trends are seen in the activation energy for ion migration and effective tortuosity of the electrolytes, which both exhibit minima near $x_L \approx 0.5$. Characterization of the electrolytes by dynamic rheology reveals that the maximum conductivity coincides with a distinct transition in soft glassy properties from a jammed to partially jammed and back to jammed state, as the fraction of large particles is increased from 0 to 1. This implies that the conductivity enhancement arises from purely entropic loss of correlation between nanoparticle centers arising from particle size dispersity. As a consequence of these physics, it is now possible to create hybrid electrolytes with MPa elastic moduli and mS cm^{-1} ionic conductivity levels at room temperature using common aprotic liquid media as the electrolyte solvent. Remarkably, we also find that even in highly flammable liquid media, the bidisperse nanoparticle hybrid electrolytes can be formulated to exhibit low or no flammability without compromising their favorable room temperature ionic conductivity and mechanical properties.

4.2 Introduction

Significant research efforts have been devoted towards improving the portability, power, lifetime and safety of secondary batteries with extensive focus on battery electrolytes and ion conducting membranes¹⁻⁶. Polymer-nanoparticle composites have received particular attention because of their promise to create new electrolyte platforms that leverage the attractive transport properties, low flammability, and processability of polymers and the ability of nanostructures to disrupt polymer crystallization and facilitate ion transport in order to mitigate safety issues associated with conventional flammable liquid electrolytes⁴⁻⁸. These nanocomposite electrolytes have been shown to also improve portability of batteries by preventing electrolyte leakage and by eliminating the need for a physical separator⁹⁻¹⁵. The inorganic particles in such electrolytes also play an important role in ion transport mainly as passive fillers and sometimes as active fillers⁹. As a passive filler, they act as plasticizers for the polymers preventing crystallization, thus speeding up segmental dynamics and enhancing ion transport^{9,12,14-16}. However, specific particle surface chemistries and an optimum nanoparticle loading are required to ensure a well-dispersed state of the particles, such that the polymer viscosity remains reasonable and ion transport pathways are not disrupted, due to high particle concentration. Active fillers directly participate in the ion transfer process either by providing additional cations/anions or by surface reaction with mobile ions. They have been reported to improve the cation transference number, which ultimately results in significant increment in the cell-scale coulombic efficiency^{9,11,12,15,17,18}.

Perhaps the greatest benefit of nanocomposite electrolytes stems from the higher mechanical stability they provide to the entire battery design, which for example opens

the way to batteries in a much wider range of form factors than available today. It has also been previously reported that a high modulus electrolyte can be effective in preventing dendrite-induced short circuit in a Lithium metal battery, which provide opportunities for novel high-energy battery designs that take advantage of the factor of 10 or more improvement in anode capacity made possible by metallic lithium¹⁹⁻²⁵. Nanocomposite electrolyte-based batteries have shown encouraging results in this regard^{16,26-28}.

Despite this promise, a persistent and important challenge to application of nanocomposite electrolytes in practical rechargeable batteries has been their low ambient ionic conductivity and high interfacial resistance^{9,26,29,30}. Weston and Steele³¹ were the first to make improvements towards developing a decently ion conducting and highly mechanical stable electrolyte by adding ceramic fillers in low volume fractions to polyethylene oxide polymer. However, achieving practical conductivity at high particle loadings, where the mechanical strength is maximized, was not possible, and remains an unsolved problem despite almost two decades of focused research. More recent studies on hybrid electrolytes based on polymer-tethered nanoparticles have shown a significant promise towards this step³²⁻³⁴. These hybrid electrolytes based on hairy nanoparticles have good mechanical and electrochemical properties, and at the same time they provide enough room for nano-engineering to improve the current state of art even further. The polymer-grafted nanoparticles have been shown to exhibit interesting physical properties like viscoelasticity^{35,36}, thermal jamming³⁷, and star polymer like relaxation³⁸. Previously, studies on binary mixture of star polymers have gained significant attention by showing that addition of smaller star polymers to bigger ones leads to a transition from glassy state

to liquid state^{39,40}. Theoretical studies have shown that at the critical size ratio of 0.4, a transition from glassy to liquid state is observed in binary hard spheres⁴¹. Similar studies on the self-suspended binary mixtures of these hairy nanoparticles have demonstrated that addition of either small or bigger particles leads to un-jamming of the system⁴². Currently, we focus on this jamming transition observed in binary hairy nanoparticles in the context of an electrolyte and try to utilize it to build a better battery.

In this article we report on ionic conductivity, mechanical properties, and structure of hybrid electrolytes comprised of a bidisperse blend of SiO₂-PEG hairy nanoparticles dispersed in propylene carbonate (PC). The study focuses on silica particles with diameters of 10nm and 25nm (size ratio of 0.4) covalently functionalized with PEG oligomers. Also, on assuming a fcc packing arrangement for these particles we find that for large spheres of 25nm diameter, the interstitial space is estimated to be 10nm which is just sufficient to accommodate smaller particles. We thus propose that at this critical size ratio we can observe a transition from the jammed state of the material. Our specific interest is in understanding the effect of both the total particle volume fraction, Φ , and relative volume fraction of the bigger particles x_L – at a fixed Φ – on suspension structure and physical properties. We find that the additional degree of freedom provided by x_L allows the structure and transport properties of polymer-nanoparticle hybrid electrolytes to be tuned in novel ways to achieve both high ionic conductivity and good mechanical performance. To our knowledge, this is the first study to systematically investigate the effect of particle size dispersity on conductivity of nanoparticle-polymer hybrid electrolytes.

4.3 Materials and Methods

4.3.1 Synthesis

Silica nanoparticles (Ludox, SM-30 and TM-50; Sigma Aldrich) with diameters of 10nm and 25nm, respectively, were grafted by covalent attachment of a trimethoxysilane functionalized polyethylene glycol methyl ether (PEG, MW~500g/mol, Gelest chemicals) in aqueous solution using a previously reported silane chemistry^{43,44} (see schematic in Figure 4.1(a)). The grafting densities were computed from analysis of the residual inorganic content using thermal gravimetric analysis (TGA) to be $\Sigma \sim 1.3$ chains/nm² and $\Sigma \sim 1.5$ chains/nm² for 10nm and 25nm particles, respectively. Following synthesis, the hairy particles were purified using a two step process, first by dialysis using a snake skin membrane to remove any dissolved salts along with unattached free PEG chains; and second by repeated centrifugation at 8500rpm for 10 minutes using a chloroform (solvent)-hexane (non-solvent) mixture to completely remove any remaining unattached PEG oligomers. The particles were then subsequently dried in convection oven at 55°C overnight and at least for 12hrs under high vacuum. The dried sample was quickly transferred to Argon filled glove box for storage and subsequent modification. Electrolytes were prepared inside the glove box by suspending the hairy nanoparticles in the electrolyte solvent propylene carbonate (PC, Sigma Aldrich) at various core volume fractions, Φ ranging from 0.1 to 0.5. For each Φ , the relative fraction of bigger particles with respect to the overall particle volume fraction, i.e. $\Phi_L/\Phi = x_L$, in the SiO₂-PEG/PC suspensions was varied. The resulting solution of hybrid nanoparticles in PC was doped with bis(trifluoromethanesulfone imide) (LiTFSi, Sigma Aldrich) salt to create SiO₂-

PEG/PC hybrid electrolytes containing 1M LiTFSI based on the total organic content (i.e. PEG corona and PC electrolyte solvent).

4.3.2 Characterization

The particle weight fraction in the SiO₂-PEG/PC-LiTFSi hybrid electrolytes was determined from thermal gravimetric analysis (TGA) by heating the sample at 10 °C/min to 600 °C. The structure and dispersion state of the nanoparticles was characterized by angle-resolved Small Angle X-ray Scattering (SAXS) measurements at Station D1 of Cornell High Energy Synchrotron Source (CHESS) using a point collimated X-ray beam. All studied materials were smeared on a sample cell and the measurements were performed at 30 °C.

Dynamic rheological properties were studied using frequency- and strain-dependent oscillatory shear measurements at 30 °C on a MCR 301 rheometer outfitted with 10mm diameter, 2° cone and plate fixtures. The frequency sweep measurements were performed at a low strain, $\gamma=0.05\%$, which is within the linear viscoelastic regime for the materials. The strain-dependent oscillatory shear measurements were performed at a fixed angular frequency of $\omega=10\text{rad/s}$.

4.3.3 Electrochemical measurements

The ionic conductivity of the SiO₂-PEG/PC-LiTFSi hybrid electrolytes was measured as a function of temperature, ranging from 0°C to 105°C, using a Novocontrol Broadband Dielectric spectrometer. For each temperature, the frequency was varied from 0.1-3x10⁶ Hz. The DC conductivity at each temperature was obtained from the plot of real part of the conductivity with frequency using the procedure described by Jonscher⁴⁵. The $\text{Re}[\text{conductivity}]$ can be expressed as $\sigma'(\omega)=\sigma_{\text{DC}}+A\omega^s$; where A is a constant. The DC

conductivity can thus be estimated from the plateau value of the plot between $\text{Re}[\text{conductivity}]$ and ω .

4.3.4 Characterizing Flammability

The flammability of electrolytes containing the hairy SiO_2 -PEG nanoparticles was studied by suspending the particles in a more flammable electrolyte mixture, ethylene carbonate/diethyl carbonate (EC: DEC, Sigma Aldrich). This approach was necessary because the PC solvent used for the other studies is flammable only at very high temperatures. The samples used for this component of the study were doped with 1M of Lithium hexafluorophosphate (LiPF_6 , Sigma Aldrich). 0.2g of SiO_2 -PEG/EC:DEC/ LiPF_6 hybrid electrolytes at $x_L=0.5$ and various Φ were transferred to Aluminum pans. Material flammability was studied by igniting each electrolyte specimen with butane torch lighter and recording images at the time of ignition, 4s after ignition, and at the time the flame self-extinguished.

4.4 Results and Discussion

Figure 4.1(b) is a Transmission electron micrograph (TEM) of a SiO_2 -PEG/PC hybrid electrolyte with $\Phi=0.5$ and $x_L=0.5$. The particles are observed to be quite well dispersed in the PC host. Figure 4.1(c) reports the wavenumber (q)-dependent scattering intensity ($I(q)$) for SiO_2 -PEG/PC hybrid electrolyte obtained using SAXS measurements. The results are reported for a fixed value of $x_L=0.5$ at different Φ . It is evident that at any Φ , in the low q region, $I(q)$ is at best a very weak function of q , whereas in the high q region, $I(q)$ varies as q^{-4} . Both observations are characteristic of un-aggregated well-dispersed

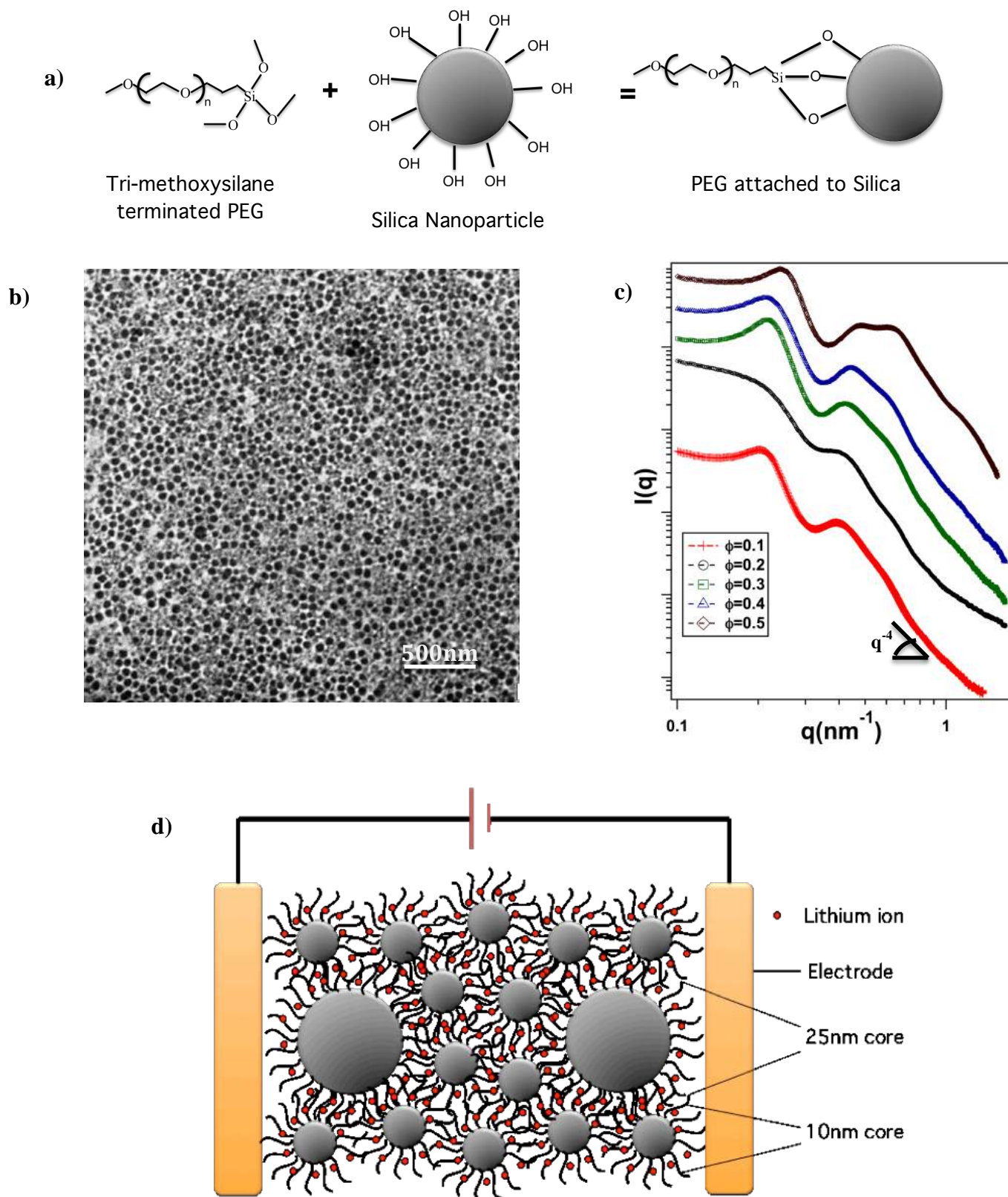


Figure 4.1: Physical Characterization- **a)** Schematic of hairy nanoparticle synthesis. **b)** Transmission Electron Micrograph (TEM) image of binary hairy nanoparticle composite with $x_L = 0.5$. **c)** Intensity ($I(q)$) as a function of wave vector (q) for $x_L = 0.5$ at different Φ , obtained from SAXS measurements. **d)** Pictorial representation of a battery with binary hairy nanoparticle composite electrolyte.

spherical nanoparticles confirming the good dispersion state of the materials inferred from the small-area TEM measurements^{46,47}.

Figure 4.2 shows the temperature dependent DC conductivity of SiO₂-PEG/PC-LiTFSi hybrid electrolytes at various particle volume fractions (Φ) and for a range of x_L values ($0 \leq x_L \leq 1$). The data is well described by the Vogel-Fulcher-Thamann (VFT) temperature dependent conductivity, $S(T) = A \exp(-E_a/k(T-T_0))$, over much of the temperature range and for all the electrolytes studied. Here the prefactor A , with units S/cm, is proportional to the number of mobile ions present in the electrolyte, E_a is the activation energy for ion mobility in kJ/mole, k is the gas constant in kJ/mole-K, and T_0 is the empirical reference Temperature in K⁴⁸ (see Supplementary table 4.1). The fact that conductivity for all electrolyte compositions studied are well described by the VFT relation over the entire range of temperature implies that there is no melting or crystallization transition, and that there is no phase separation.

In order to understand the effect of particle size dispersity on ionic conductivity, the DC conductivity measured at a fixed temperature $T=30^\circ\text{C}$ is plotted as a function of x_L at different Φ , in Figure 4.3(a). It can be observed that at $\Phi = 0.1$ and 0.2 , the conductivity does not vary much with changes in x_L . However, for $\Phi \geq 0.3$ conductivity for the bidisperse SiO₂-PEG/PC-LiTFSi hybrid electrolytes is noticeably than the conductivity of hybrid electrolytes comprised of the pure small ($x_L=0$) or big ($x_L=1$) SiO₂-PEG hairy nanoparticles. This effect is most pronounced at $\Phi=0.5$, where a clear maximum is seen near $x_L=0.5$. The conductivity is also plotted as a function of overall particle volume fraction for different x_L values in Supplementary figure 4.1. There is a greater drop in the conductivity on increasing the particle volume fraction for pure small ($x_L=0$) and big

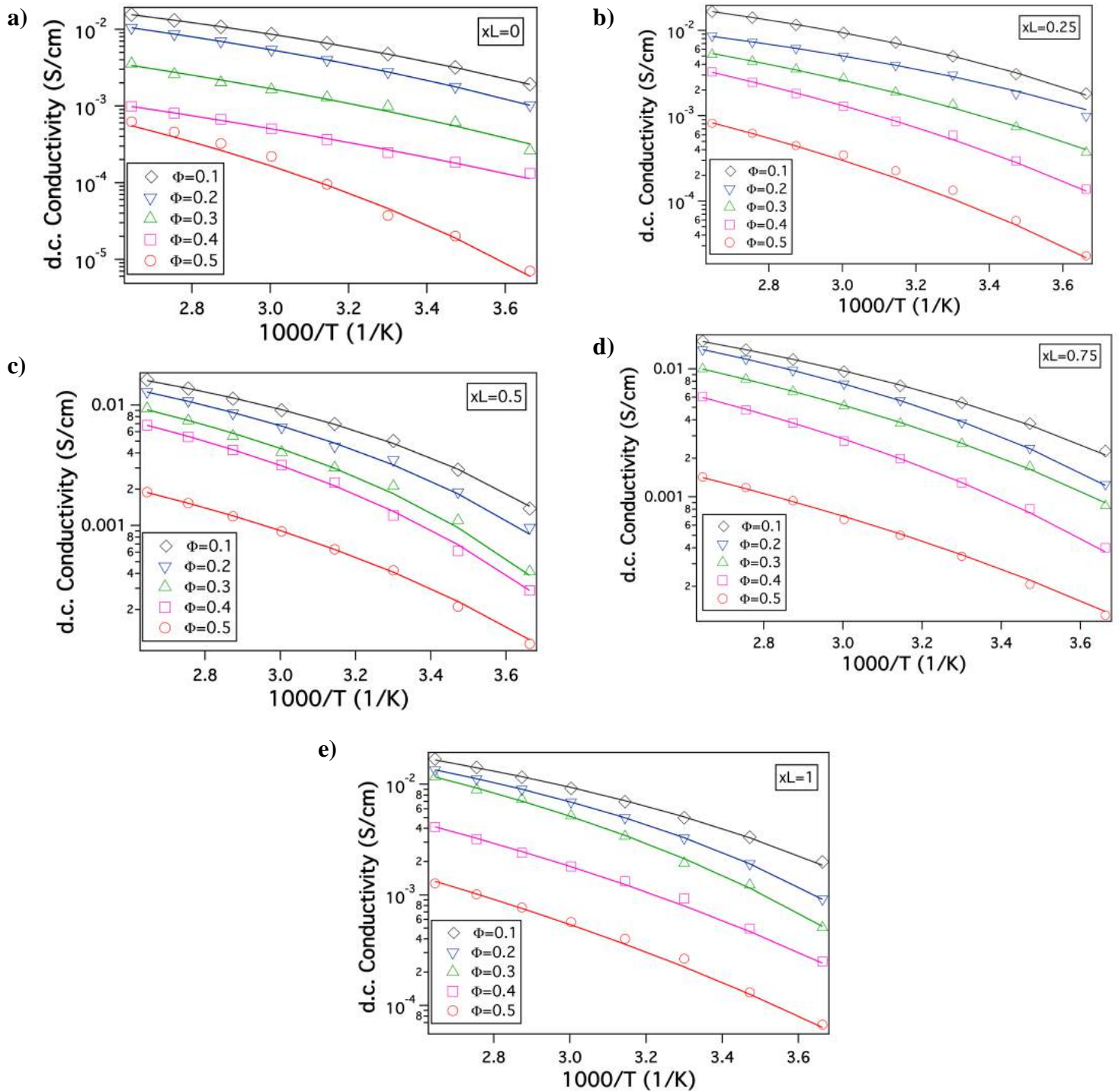


Figure 4.2: Electrochemical properties- Conductivity as a function of inverse of temperature for different core volume fraction (Φ) at various fractions of bigger nanoparticles in the binary composite electrolyte indicated by x_L , as, **a)** $x_L=0$; **b)** $x_L=0.25$; **c)** $x_L=0.5$; **d)** $x_L=0.75$; **e)** $x_L=1$

($x_L=1$) SiO₂-PEG/PC-LiTFSi hybrid electrolytes than for the bidisperse hybrid electrolytes; the effect being particularly visible in electrolytes with $x_L=0.5$ and 0.75 .

Activation energies computed from the VFT fits of temperature-dependent conductivity provides additional insights about the nature of ion transfer processes in electrolytes. It is known that for electrolytes with higher activation energy there is a significant change in conductivity associated with temperature, which is correlated with more practical risks, such as thermal runaway and fire in cells in which there are exothermic side reactions⁴⁹. Figure 4.3(b) reports the activation energy landscape obtained from VFT fits at different Φ and x_L . It is seen that for high Φ the activation energy is greatest for the pure small ($x_L=0$) or pure big ($x_L=1$) hybrid electrolyte and that it is minimum near $x_L \approx 0.5$ (see also, Supplementary figure Table 4.1). Consistent with the conductivity data, the effect becomes weaker as the overall particle volume fraction, Φ , in the electrolytes is reduced. Thus, the bidisperse system of nanocomposite electrolytes can find wide applications as electrolytes that can be used at ambient temperatures, while sustaining sudden thermal shocks.

We hypothesize that the observed enhancement in conductivity in bidisperse SiO₂-PEG/PC-LiTFSi hybrid electrolytes at high Φ and $x_L \approx 0.5$ may arise due to reduced correlation between particle-centers in the bidisperse materials. In particular at the high particle volume fractions, where bidispersity has the most noticeable effect on conductivity and activation energy, the positions of SiO₂-PEG nanospheres in a monodisperse suspension are more correlated than in the bidisperse case. The tethered PEG corona chains are hence more crowded and confined in electrolytes containing either pure small or pure large SiO₂-PEG particles. Such crowding of surface grafted chains has

already been reported to lead to dramatically slower chain reorientation dynamics for cis-1,4-polyisoprene tethered to SiO₂.³⁵ The motion of ions mediated by the confined PEG chains would therefore be expected to be correspondingly impaired and sluggish, which is consistent with the higher activation energy. In contrast, for a bidisperse suspension of SiO₂-PEG nanospheres, neighboring particles exert weaker constraints on each other because of the size dispersity. In other words, at high particle loadings, the system is less jammed due to the heterogeneities introduced by addition of a different sized species^{42,50,51}, thus loosening the packing of particles and reducing the confinement on tethered PEG chains, increasing their mobility and lowering the activation energy. This freedom would in turn increase the rate at which ions migrate in the electrolyte, reflected in a higher ionic conductivity. This hypothesis can also account for the weaker of particle size dispersity at lower Φ where the tethered PEG chains are not confined and ion motion is controlled more in coordination with the mobile PC phase.

Since, the organic phase in the SiO₂-PEG/PC-LiTFSi hybrid electrolytes is comprised of both PC and tethered PEG chains, it is useful to resolve the relative content of PEG and PC in different electrolytes to better understand the effect of bidispersity of the nanocores on electrolyte properties. The conductivity of PC/PEG-LiTFSi liquid electrolyte mixtures was measured as a function of composition and the results are reported in Figure S2. A straight-line fit of the data allows us to determine how the content of PC/PEG influences ionic conductivity in the absence of particles. Using this knowledge, the conductivity contribution (S_o) attributable to the organic content for each electrolyte shown in Figure 3(a) can be recovered. The relative PC content in each sample is tabulated in Supplementary Table 4.2. In order to isolate the contribution of the nanocores, we plot

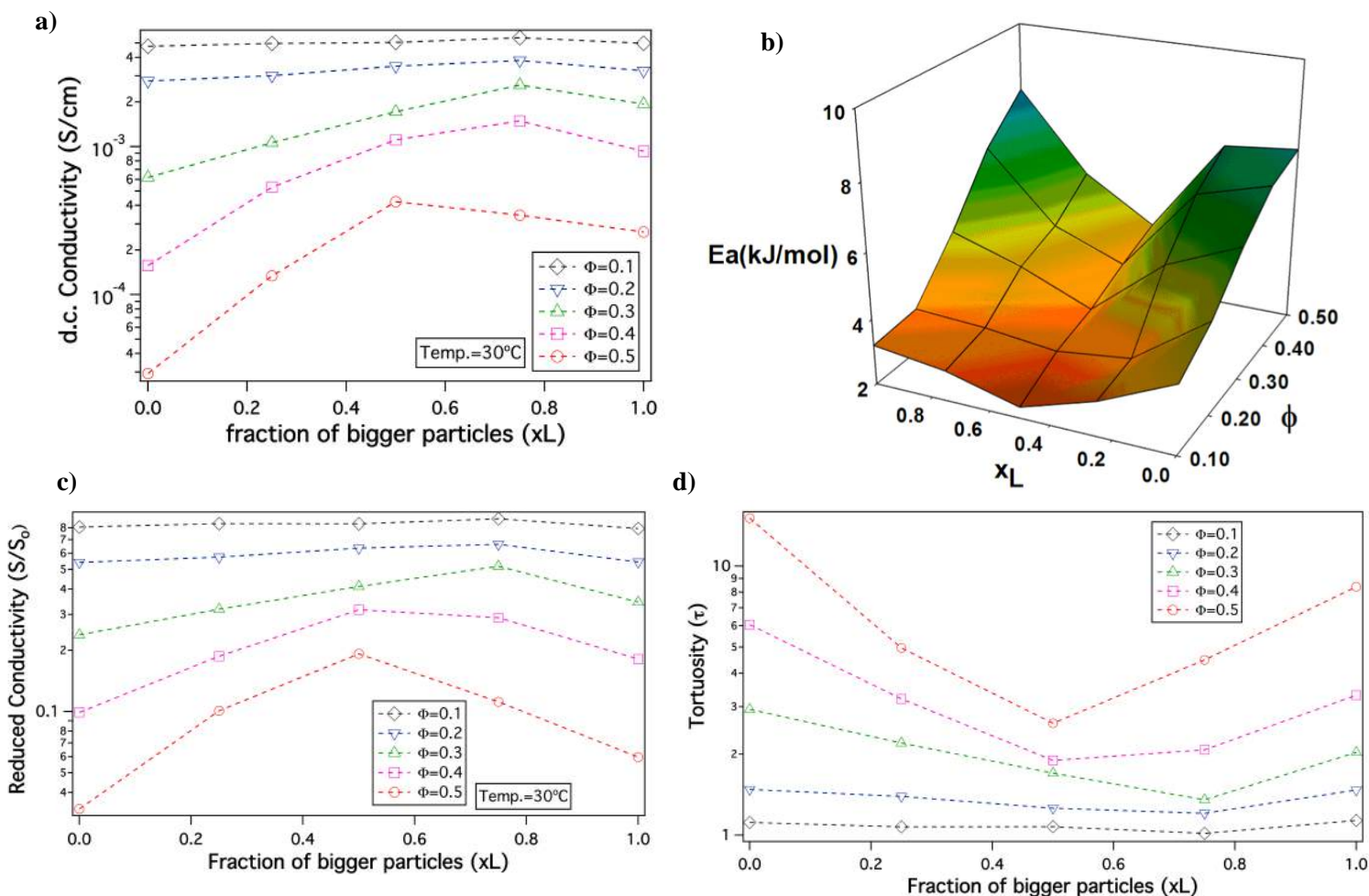


Figure 4.3: Analysis of ion transport- a) Conductivity as a function of x_L at 30°C at different Φ ; b) Activation energy landscape at different x_L values and corresponding Φ ; c) Reduced conductivity given by the ratio of actual conductivity to that of the organic content, shown as a function of x_L at 30°C d) Tortuosity given as, $\tau = [S_0(1 - \Phi)]/S$, versus x_L .

the reduced conductivity as S/S_0 versus the fraction of bigger particles (x_L) in Figure 4.3(c). The effect of particle size dispersity is now more profound, but again the maximum is most readily apparent for hybrids with the highest Φ and the maximum is clear. Hence, we conclude that the idea of unjamming a high volume fraction nanoparticle hybrid electrolyte by introducing bidispersity is not a function of the chemistry of the electrolyte solvent, making the concept a potentially powerful tool in other fields, such as ion exchange chromatography, desalination, and electroplating, where ion transport through complex media is relevant.

To understand the nature of the inter-particle spaces in the SiO₂-PEG/PC hybrid electrolytes, we look at the trends in ‘tortuosity’ of these materials, as previously proposed by Carman⁵². The conductivity of an electrolyte is a direct reflection of the tortuous nature of the conducting phase, where, tortuosity (τ) is defined as the ratio between the actual distance covered by the ions to travel across the bulk and the shortest distance between the two points. In the context of electrolytes, the conductivity of a neat electrolyte is suppressed by the addition of nanoparticles or other non-conducting entities depending upon the resulting porosity, which is equivalent to the volume fraction of the conductive phase in a suspension electrolyte. The experimental conductivity, S , is lower than that obtained empirically, $S_0(1 - \Phi)$, this discrepancy is quantified using the term effective tortuosity⁵³, $\tau = \frac{S_0(1 - \phi)}{S}$. Figure 3(d) reports tortuosity as a function of x_L for

different volume fractions for the binary hairy nanoparticle electrolytes. It is seen that for low volume fractions, there is little change across the range of x_L , and the tortuosity values remain close to unity. This is consistent with intuition that, at low particle volume fraction, the nature of the conducting pathway across the electrolyte is almost same as for

the particle-free electrolyte and size dispersity of the particulate phase has no obvious effect on conductivity. On increasing the particle volume fraction, the tortuosity of the pure small or pure big SiO₂-PEG/PC-LiTFSi electrolyte becomes greater than 10, however the bidisperse hybrid electrolytes are seen to have substantially lower effective tortuosity. This behavior can be attributed to the unjamming of densely packed SiO₂-PEG nanoparticles, facilitating nearly unimpeded transport of ions in the electrolyte. Although empirical models for tortuosity for different shaped randomly spaced particles exist,⁵³⁻⁵⁷ such models do not yet exist for the surface-functionalized particles used in this study, making it difficult at the present time to understand the significance of the experimentally determined values for τ .

The changes in ionic conductivity are associated with important changes in mechanical properties of the electrolytes. It can be seen from Figure 4.4(a) that for a given x_L value, on changing Φ from 0.2 to 0.5, the system undergoes a well-studied transition from a viscoelastic liquid in which the loss modulus, G'' , is larger than the storage modulus G' , to a soft glass, characterized by $G' \gg G''$ at low shear strains, and the tell tale maximum in G'' at higher strains associated with yielding and flow ($G'' > G'$) of the material^{58,59}. In particular, at low Φ and for $x_L = 0$ or 1, $G'' > G'$, indicating the electrolytes exhibit liquid-like behavior; remarkably, even under these conditions the bidisperse mixture with $x_L = 0.5$ shows soft glassy behavior. In concentrated particulate suspensions, soft glassy rheology is understood to result from crowding and trapping of particles in cages formed due to the presence of neighboring particles. Upon increasing the shear strain, these cages break producing the burst of dissipated energy as particles move relative to each other, which manifests as a maximum in G'' .^{60,61} This implies that in such suspensions high

shear strains can transform a jammed material to a less solid-like, processable form; removal of the strain causes the cage structure to reform and the solid-like jammed state is restored.

The degree of jamming in a soft glassy material can be quantified using the value of its loss tangent ($\tan\delta=G''/G'$), measured at low strains in the linear viscoelastic regime of oscillatory shear measurements. Figure 4.4(b) shows $\tan\delta$ value as a function of x_L , it is seen that addition of either the bigger or smaller particles to their pure cohorts leads to an increase in $\tan\delta$; implying that introduction of heterogeneity leads to less jamming of the system. Remarkably, at $\Phi = 0.5$, where the electrolyte exhibits soft glassy rheology over the entire range of x_L , $\tan\delta$ exhibits a clear maximum near $x_L=0.5$, i.e. exactly where the maximum in ionic conductivity and minimum in activation energy for the electrolytes is observed. This finding succinctly shows that the enhanced conductivity for the bidisperse SiO₂-PEG/PC hybrid electrolytes is a result of reduced jamming. Figure 4.4(c) shows the viscoelastic storage modulus (G') of these electrolytes as a function of volume fraction for various x_L . At high particle loading, these electrolytes display G' values around 5MPa (Supplementary Table 4.2), which is only modestly lower than the modulus of hybrid electrolytes created using the pure small or pure large particles at $\Phi = 0.5$.

The favorable ionic conductivity and mechanical properties of these bidisperse SiO₂-PEG/PC-LiTFSi hybrid electrolytes at relatively high nanoparticle concentrations is already attractive for the application related investigations outlined in the introduction. Since silica and PEG are both non- or poorly-flammable materials, it is possible that at the high particle loadings where size dispersity has the greatest effect on conductivity and rheology of the electrolytes, it may also have a positive effect on their safety. To explore

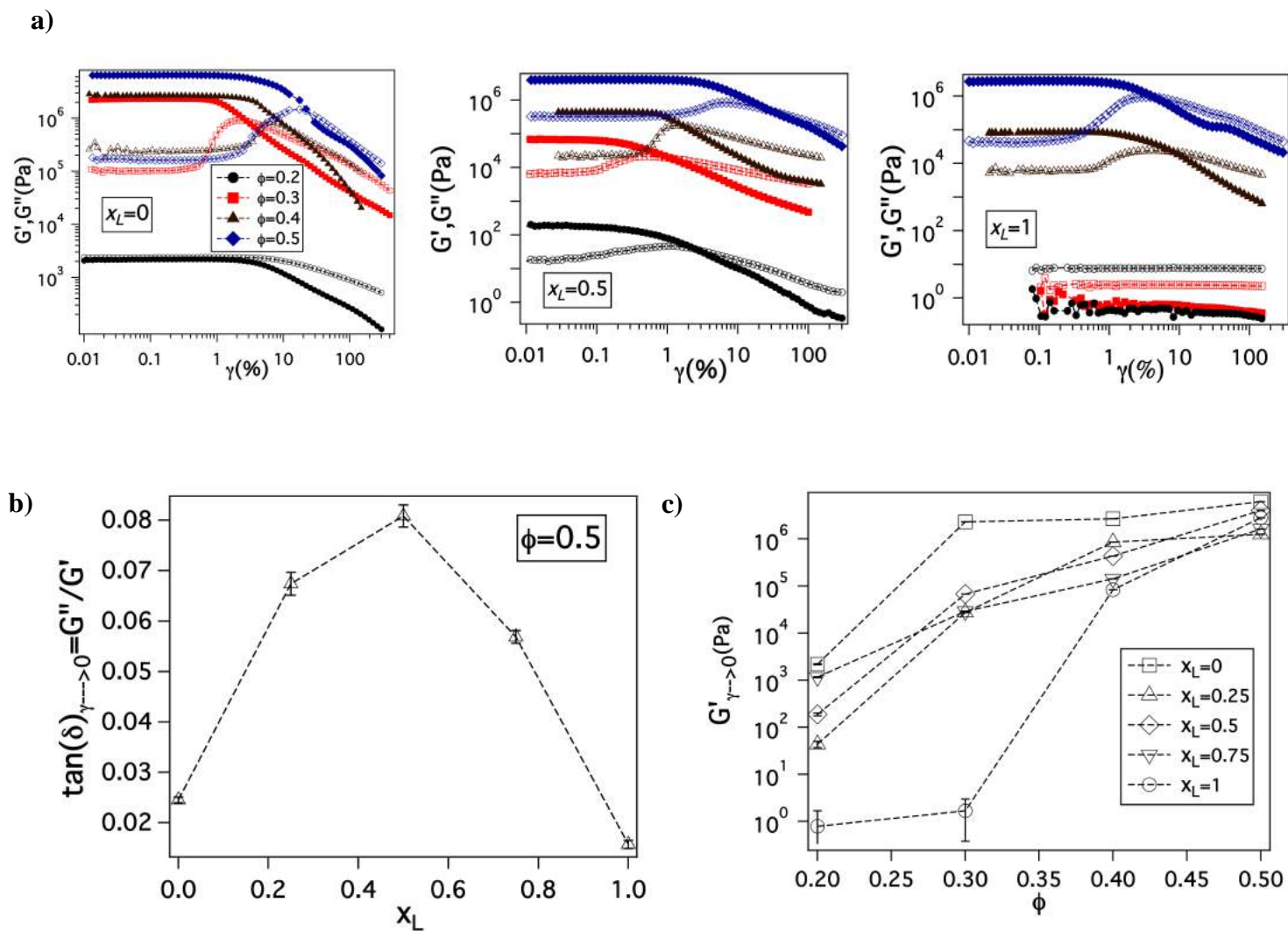


Figure 4.4: Rheological properties- **a)** Evolution of storage modulus, G' (closed symbol) and loss modulus, G'' (open symbol) as a function of amplitude strain, γ with particle volume fraction, Φ at $x_L = 0, 0.5$ and 1 on going from left to right. **b)** Variation of Loss Tangent, $\tan(\delta) = G''/G'$ obtained at $\gamma \rightarrow 0$ as a function of x_L at $\Phi = 0.5$. Since $\tan(\delta)$ is the ratio of loss modulus to storage modulus, the higher the loss tangent the more fluid-like or un-jammed the system is. It can be observed that addition of either small or big particles leads to increase in un-jamming of the particles as compared to the pure species. **c)** Storage modulus at $\gamma \rightarrow 0$ varying as a function of Φ at different x_L values. It can be seen that at high Φ , the modulus values are extremely high, more than 10⁶.

this aspect of the materials, we briefly studied their flammability using a previously disclosed protocol.¹³ The experiments are complicated by the fact that propylene carbonate, the electrolyte solvent used in the study so far, is only flammable at very high temperatures. In order to correctly assess the role of particles on flammability, we have created similar nanoparticle hybrid electrolytes in a more flammable electrolyte solvent (EC: DEC with 1M LiPF₆). Figure 5 reports the results from these experiments in the form of snapshots of an electrolyte with $x_L=0.5$, with varying nanoparticle contents at different times following ignition. Figure 4.5(a) shows the physical appearance of the electrolyte specimen at each volume fraction before ignition. Figure 4.5(b) shows the same materials at the time of ignition, i.e. at $t=0$. It can be seen that the electrolyte specimen with $\Phi=0.4$ initially catches fire, it is extinguished within one second of ignition; whereas the specimen with $\Phi=0.5$ is highly fire resistant. At the same time, the neat electrolyte without any particle or the samples with lower core volume fractions burn when ignited, as also seen in Figure 4.5(c). Figure 4.5(d) marks the time required for the fire to completely extinguish. Among the flammable samples, the particle-free electrolyte burns out the quickest, while the electrolytes with $\Phi=0.3$ take the longest to completely extinguish; implying that the degree of flammability decreases for higher volume fractions. The bidisperse hybrid electrolytes with $\Phi=0.4$ and 0.5 therefore appear to be good candidates for future applications-oriented studies.

4.5 Conclusions

In summary, we have synthesized nanoparticle hybrid electrolytes based on bidisperse mixtures of PEG-functionalized silica nanoparticles in aprotic electrolyte solvents. The nanoparticles are found to be well dispersed and un-aggregated in their liquid hosts, even

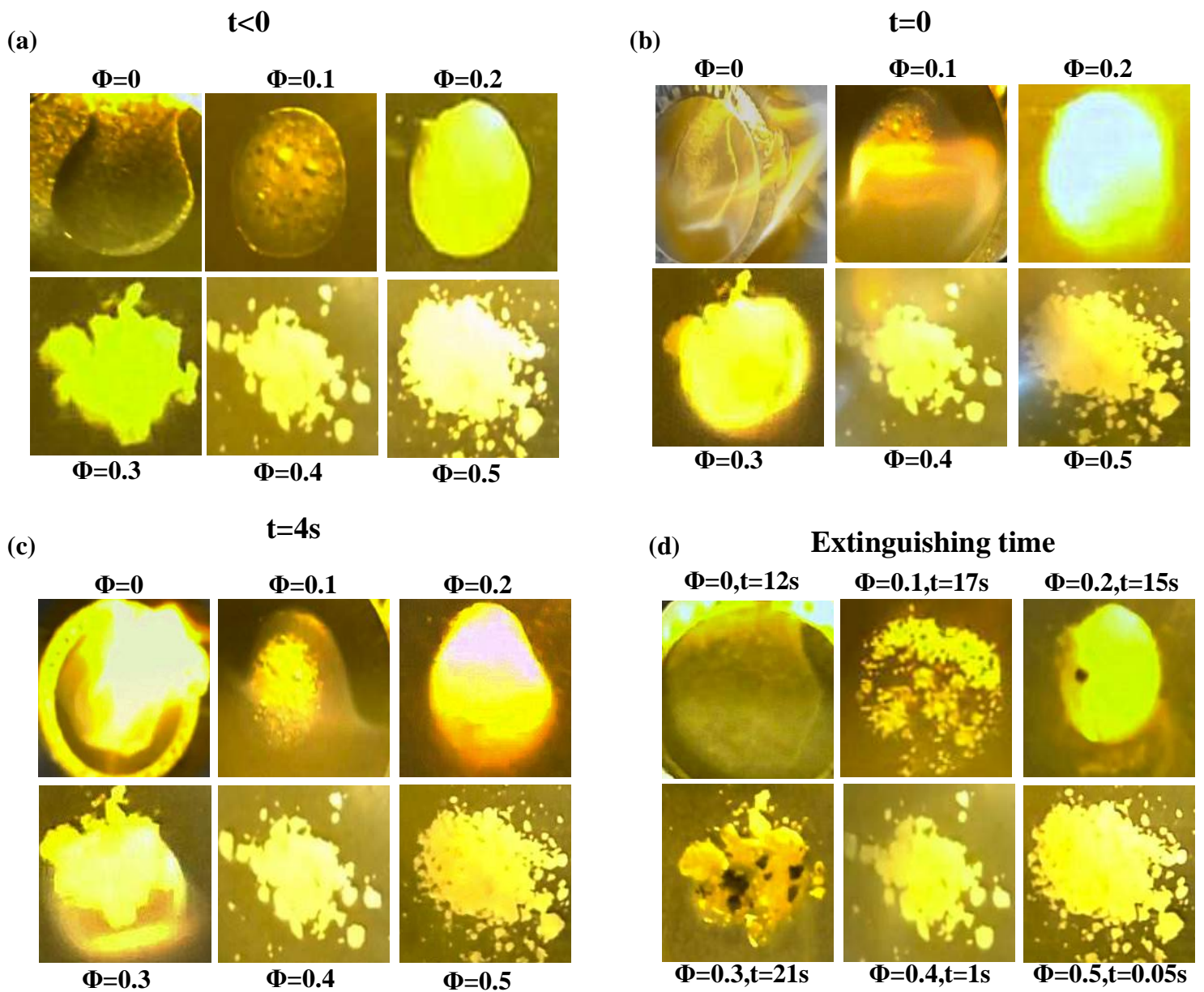


Figure 4.5: Flammability Test- Electrolyte samples with different particle volume fraction **a)** before ignition i.e. $t < 0$. **b)** At ignition time i.e. $t = 0$ **c)** after ignition i.e. at $t = 4s$ **d)** At the extinguishing time. The binary electrolyte sample used here corresponds to $x_L = 0.5$.

at high volume fractions. The conductivity of electrolytes containing nanoparticles with a bimodal size distribution is found to exhibit a pronounced maximum when the volume fraction of small and large particles are the same. This observation is attributed to the ability of large/small particles in a concentrated suspension of the opposite counterpart to produce disordering of the suspension by lowering correlation among the polydisperse particles. The tortuosity as well as activation energy values obtained from the measured conductivity show pronounced minima that correlate with the maximum conductivity, lending support to the idea that loose packing of the cores in a binary suspension is responsible for the observed enhancement in conductivity. Oscillatory shear rheology measurements show that the hybrid electrolytes transits from a jammed state to relatively unjammed and back to a jammed state when the fraction of bigger particles in the mixture is increased from 0 to 1. At high nanoparticle volume contents, where the effect of particle size dispersity on conductivity is greatest, little changes are seen in the elastic modulus of the materials. In particular, it is possible to create nanoparticle hybrid electrolytes with MPa mechanical modulus and mS cm^{-1} level ionic conductivity at room temperature. Preliminary studies of flammability show that even if the electrolyte solvent used in such bidisperse nanoparticle hybrid electrolytes is a high-flammability aprotic liquid, the electrolytes can be formulated to exhibit low flammability. Thus we conclude that nanoparticle hybrid electrolytes created using bidisperse mixtures of PEG-functionalized particles in conventional aprotic liquids provide an attractive platform for tuning multiple properties of contemporary interest for applications.

Acknowledgements

This work was supported by the National Science Foundation, Award No. DMR-1006323 and by Award No. KUS-C1-018-02, made by King Abdullah University of Science and Technology (KAUST).

REFERENCES

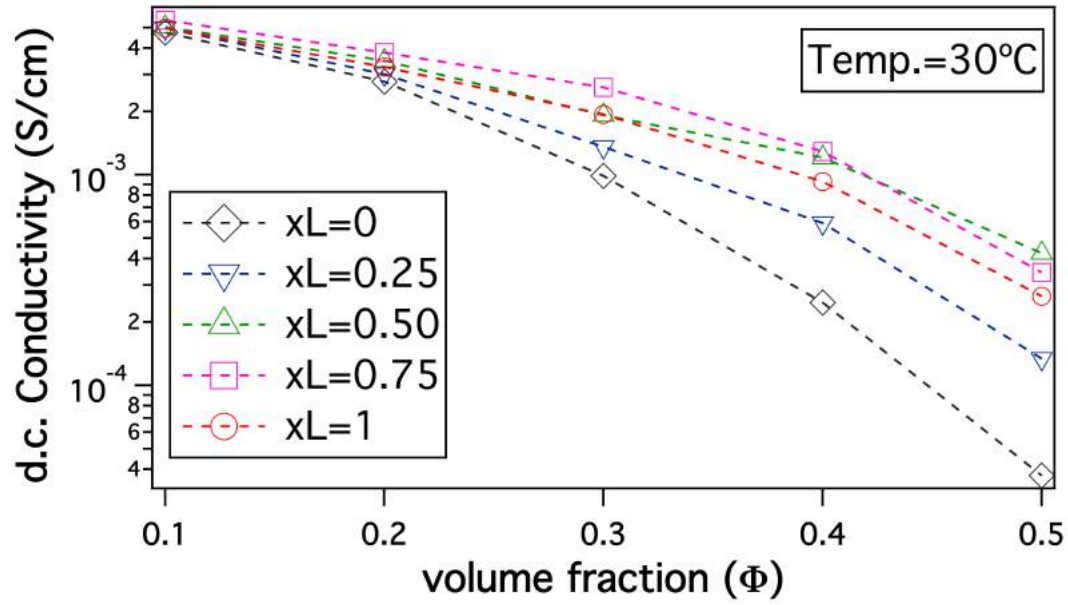
- (1) Dunn, B.; Kamath, H.; Tarascon, J.-M. *Science* **2011**, *334* (6058), 928–935.
- (2) Yang, P.; Tarascon, J.-M. *Nat. Mater.* **2012**, *11* (7), 560–563.
- (3) Bouchet, R.; Maria, S.; Meziane, R.; Aboulaich, A.; Lienafa, L.; Bonnet, J.; Phan, T. N. T.; Bertin, D.; Gigmes, D.; Devaux, D.; Denoyel, R.; Armand, M. *Nat. Mater.* **2013**, *12* (5), 452–457.
- (4) Tarascon, J. M.; Armand, M. *Nature* **2001**, *414* (6861), 359–367.
- (5) Dresselhaus, M. S.; Thomas, I. L. *Nature* **2001**, *414* (6861), 332–337.
- (6) Armand, M.; Tarascon, J.-M. *Nature* **2008**, *451* (7179), 652–657.
- (7) Zhou, M.; Cai, T.; Pu, F.; Chen, H.; Wang, Z.; Zhang, H.; Guan, S. *ACS Appl. Mater. Interfaces* **2013**, *5* (8), 3449–3455.
- (8) Goodenough, J. B.; Kim, Y. *Chem. Mater.* **2010**, *22* (3), 587–603.
- (9) Srivastava, S.; Schaefer, J. L.; Yang, Z.; Tu, Z.; Archer, L. A. *Adv. Mater.* **2014**, *26* (2), 201–234.
- (10) Croce, F.; Sacchetti, S.; Scrosati, B. *J. Power Sources* **2006**, *162* (1), 685–689.
- (11) Bruce, P. G.; Scrosati, B.; Tarascon, J.-M. *Angew. Chem. Int. Ed. Engl.* **2008**, *47* (16), 2930–2946.
- (12) Croce, F.; Appetecchi, G. B.; Persi, L.; Scrosati, B. **1998**, *394* (July), 456–458.
- (13) Kashiwagi, T.; Du, F.; Douglas, J. F.; Winey, K. I.; Harris, R. H.; Shields, J. R. *Nat. Mater.* **2005**, *4* (12), 928–933.
- (14) Tang, C.; Hackenberg, K.; Fu, Q.; Ajayan, P. M.; Ardebili, H. **2012**, 1152–1156.
- (15) Croce, F.; Scrosati, B. *Ann. N.Y. Acad. Sci.* **2003**, *984*, 207, 194–207.
- (16) Liu, S.; Imanishi, N.; Zhang, T.; Hirano, a.; Takeda, Y.; Yamamoto, O.; Yang, J.

- J. Power Sources* **2010**, *195* (19), 6847–6853.
- (17) Schaefer, J. L.; Yanga, D. A.; Archer, L. A. *Chem. Mater.* **2013**, *25* (6), 834–839.
- (18) Jung, S.; Kim, D. W.; Lee, S. D.; Cheong, M.; Nguyen, D. Q. **2009**, *30* (10).
- (19) Monroe, C.; Newman, J. J. *Electrochem. Soc.* **2004**, *151* (6), A880.
- (20) Monroe, C.; Newman, J. J. *Electrochem. Soc.* **2005**, *152* (2), A396.
- (21) Hallinan, D. T.; Mullin, S. a.; Stone, G. M.; Balsara, N. P. *J. Electrochem. Soc.* **2013**, *160* (3), A464–A470.
- (22) Tikekar, M. D.; Archer, L. a.; Koch, D. L. *J. Electrochem. Soc.* **2014**, *161* (6), A847–A855.
- (23) Tu, Z.; Kambe, Y.; Lu, Y.; Archer, L. A. *Adv. Energy Mater.* **2014**, *4* (2), 1300654(1–6).
- (24) Khurana, R.; Schaefer, J. L.; Archer, L. A.; Coates, G. W. *J. Am. Chem. Soc.* **2014**, *136* (20), 7395–7402.
- (25) Lu, Y.; Tu, Z.; Archer, L. A. *Nat. Mater.* **2014**, *13* (October), 961–969.
- (26) Stone, G. M.; Mullin, S. a.; Teran, a. a.; Hallinan, D. T.; Minor, a. M.; Hexemer, a.; Balsara, N. P. *J. Electrochem. Soc.* **2012**, *159* (3), A222–A227.
- (27) Gurevitch, I.; Buonsanti, R.; Teran, a. a.; Gludovatz, B.; Ritchie, R. O.; Cabana, J.; Balsara, N. P. *J. Electrochem. Soc.* **2013**, *160* (9), A1611–A1617.
- (28) Liu, S.; Wang, H.; Imanishi, N.; Zhang, T.; Hirano, a.; Takeda, Y.; Yamamoto, O.; Yang, J. *J. Power Sources* **2011**, *196* (18), 7681–7686.
- (29) Baker, G. L.; Colsons, S. **1994**, No. 2, 2359–2363.
- (30) Singh, M.; Odusanya, O.; Wilmes, G. M.; Eitouni, H. B.; Gomez, E. D.; Patel, A. J.; Chen, V. L.; Park, M. J.; Fragouli, P.; Iatrou, H.; Hadjichristidis, N.; Cookson,

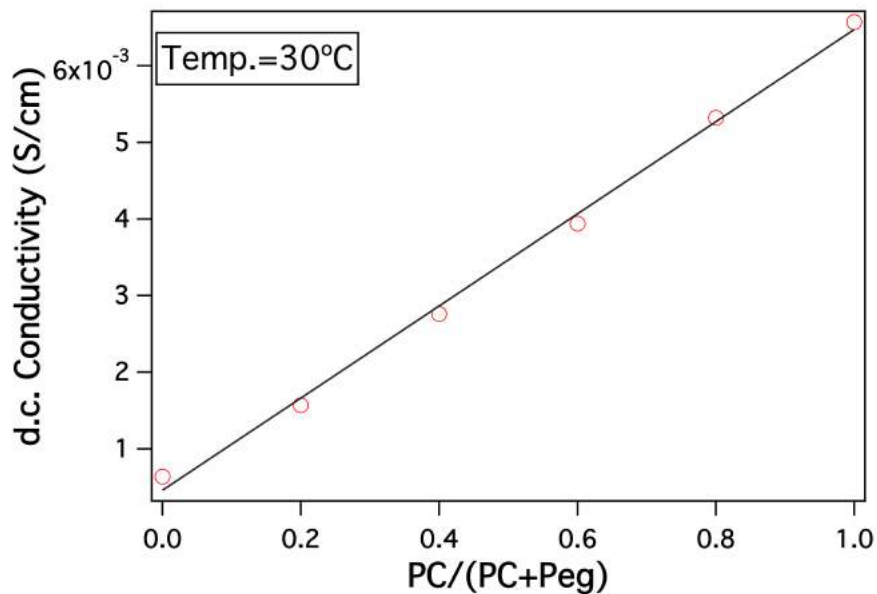
- D.; Sciences, M.; Di, V.; Berkeley, L. **2007**, 4578–4585.
- (31) Weston, J. E.; Steele, B. C. H. *Solid State Ionics* **1982**, *7*, 75–79.
- (32) Nugent, J. L.; Moganty, S. S.; Archer, L. A. *Adv. Mater.* **2010**, *22* (33), 3677–3680.
- (33) Schaefer, J. L.; Moganty, S. S.; Yanga, D. A.; Archer, L. A. *J. Mater. Chem.* **2011**, *21* (27), 10094–10102.
- (34) Gowdani, S.; Ramanjaneyulu, K.; Basak, P.; Division, P. C.; Technology, C.; Institutes, N.; Energy, S.; Pradesh, A. *ACS Nano* **2014**, *8* (11), 11409–11424.
- (35) Agarwal, P.; Qi, H.; Archer, L. A. *Nano Lett.* **2010**, *10* (1), 111–115.
- (36) Choudhury, S.; Agrawal, A.; Kim, S. A.; Archer, L. A. *submitted* 1–16.
- (37) Agarwal, P.; Srivastava, S.; Archer, L. A. *Phys. Rev. Lett.* **2011**, *107* (26), 268302–1 – 5.
- (38) Agarwal, P.; Kim, S. A.; Archer, L. A. *Phys. Rev. Lett.* **2012**, *109* (25), 258301–1 – 4.
- (39) Mayer, C.; Zaccarelli, E.; Stiakakis, E.; Likos, C. N.; Sciortino, F.; Munam, a; Gauthier, M.; Hadjichristidis, N.; Iatrou, H.; Tartaglia, P.; Löwen, H.; Vlassopoulos, D. *Nat. Mater.* **2008**, *7* (10), 780–784.
- (40) Zaccarelli, E.; Mayer, C.; Asteriadi, A.; Likos, C.; Sciortino, F.; Roovers, J.; Iatrou, H.; Hadjichristidis, N.; Tartaglia, P.; Löwen, H.; Vlassopoulos, D. *Phys. Rev. Lett.* **2005**, *95* (26), 268301(1–4).
- (41) Voigtmann, T. *EPL (Europhysics Lett.)* **2011**, *96* (3), 36006–p1 – p6.
- (42) Agrawal, A.; Yu, H.; Srivastava, S.; Narayanan, S.; Lynden, A. .
- (43) Zhang, Q.; Archer, L. A. *Langmuir* **2002**, *18* (26), 10435–10442.

- (44) Moganty, S. S.; Jayaprakash, N.; Nugent, J. L.; Shen, J.; Archer, L. A. *Angew. Chemie* **2010**, *122* (48), 9344–9347.
- (45) Jonscher, A. K. *Nature* **1977**, *267*, 673–679.
- (46) Glatter, O.; Kratky, O. *Small Angle X-ray Scattering*, United Sta.; Academic Press: New York, 1982.
- (47) Srivastava, S.; Agarwal, P.; Archer, L. A. *Langmuir* **2012**, *28* (15), 6276–6281.
- (48) Duclot, M.; Levy, M. **1996**, *85*, 149–157.
- (49) Wong, D. H. C.; Thelen, J. L.; Fu, Y.; Devaux, D.; Pandya, A. a; Battaglia, V. S.; Balsara, N. P.; DeSimone, J. M. *Proc. Natl. Acad. Sci. U. S. A.* **2014**, *111* (9), 3327–3331.
- (50) Sentjabrskaja, T.; Babaliari, E.; Hendricks, J.; Laurati, M.; Petekidis, G.; Egelhaaf, S. U. *Soft Matter* **2013**, *9* (17), 4524–4533.
- (51) Sentjabrskaja, T.; Hermes, M.; Poon, W. C. K.; Estrada, C. D.; Castaneda-Priego, R.; Egelhaaf, S. U.; Laurati, M. *Soft Matter* **2014**, *10*, 6546–6555.
- (52) Carman, P. C. *New York Acad. Press* **1956**.
- (53) Bouchet, R.; Phan, T. N. T.; Beaudoin, E.; Devaux, D.; Davidson, P.; Bertin, D.; Denoyel, R. **2014**.
- (54) Then, E. **1993**, *48*, 2173–2175.
- (55) Khirevich, S.; Höltzel, A.; Daneyko, A.; Seidel-Morgenstern, A.; Tallarek, U. *J. Chromatogr. A* **2011**, *1218* (37), 6489–6497.
- (56) Bouchet, R.; Denoyel, R. **2010**, *82* (7), 2668–2679.
- (57) Thorat, I. V.; Stephenson, D. E.; Zacharias, N. a.; Zaghbi, K.; Harb, J. N.; Wheeler, D. R. *J. Power Sources* **2009**, *188* (2), 592–600.

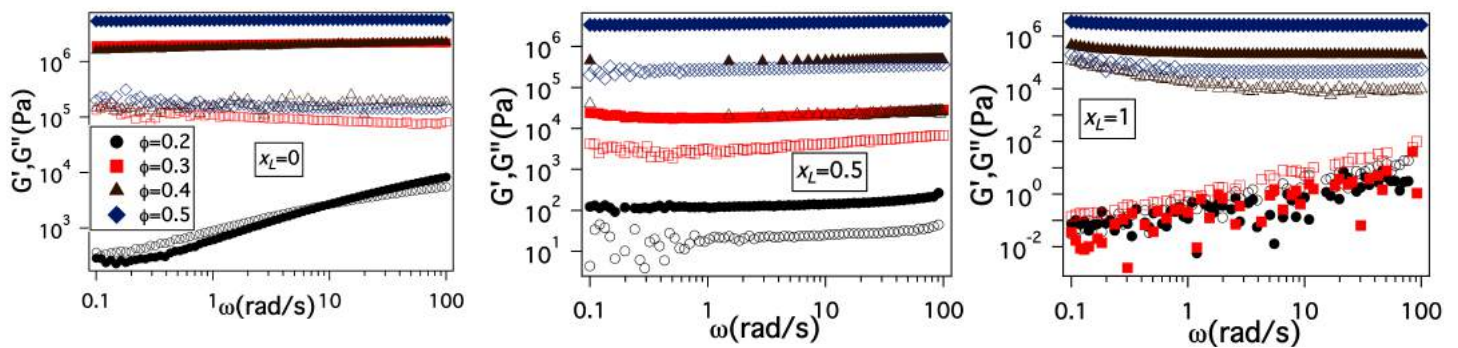
- (58) Frith, W. J.; Strivens, T. A.; Mewis, J. J. *Colloids Interface Sci.* **1990**, 139 (1).
- (59) Larson, R. G. *The structure and rheology of complex fluids*; 1999.
- (60) Sollich, P.; Lequeux, F.; Hébraud, P.; Cates, M. *Phys. Rev. Lett.* **1997**, 78 (10), 2020–2023.
- (61) Sollich, P. *Phys. Rev. E* **1998**, 58 (1), 738–759.



Supplementary figure 4.1: Conductivity as a function of volume fraction for different binary ratios, while the conductivity for pure samples decrease significantly, that of binary mixtures are not as low at particle loading



Supplementary figure 4.2: Conductivity as a function of volume fraction of PC in a mixture of PC and PEG. It is fitted to a linear regression. The conductivity values obtained from this line at different organic content are used to normalize the actual conductivity for the respective hybrid samples.



Supplementary figure 4.3: Variation of storage modulus, G' (closed symbols) and loss modulus, G'' (open symbols) with angular frequency, ω (rad/s) at different particle volume fraction, Φ for varying x_L values.

Supplementary table 4.1. VFT parameters: Pseudo-activation energy, E_a (kJ/mol), pre-factor A (S/cm), reference temperature, T_0 (K) and the error in fitting r^2 at different values of Φ with variation in x_L .

$\Phi=0.2$				
x_L	E_a (kJ/mol)	A (S/cm)	T_0 (K)	r^2 (goodness of fit)
0	4.83	0.143	155.30	8.63E-10
0.25	3.23	0.056	172.42	8.62E-08
0.50	2.95	0.092	197.19	2.51E-07
0.75	3.20	0.105	186.58	6.51E-09
1.0	3.32	0.113	190.10	1.32E-09
$\Phi=0.3$				
0	6.04	0.069	137.96	1.19E-07
0.25	5.07	0.088	159.78	6.48E-08
0.50	3.25	0.082	200.13	3.32E-07
0.75	4.17	0.109	168.55	1.98E-08
1.0	4.87	0.210	175.44	2.31E-07
$\Phi=0.4$				
0	7.33	0.041	173	1.58E-08
0.25	7.11	0.042	159.85	5.06E-09
0.50	4.18	0.023	178.91	1.01E-09
0.75	5.51	0.025	147.45	2.78E-09
1.0	7.93	0.068	136.45	7.92E-09
$\Phi=0.5$				
0	7.0	0.025	117.18	1.45E-09
0.25	6.37	0.106	158.37	8.24E-09
0.50	3.75	0.077	192.22	4.43E-08
0.75	4.61	0.087	171.488	2.44E-08
1.0	6.73	0.136	143.58	3.52E-08

Chapter 5

Hybrid Hairy Nanoparticle Electrolytes Stabilizing Lithium Metal Batteries³

Reproduced with permission from
Snehashis Choudhury*, Akanksha Agrawal*, Shuya Wei, Emily Jeng, Lynden A. Archer, Hybrid
Hairy Nanoparticle Electrolytes Stabilizing Lithium Metal Batteries, *Chemistry of Materials*,
2016, 28(7), 2147-2157.
Copyright © 2015, American Chemical Society

³ S. Choudhury and A. Agrawal contributed equally to this work

5.1 Abstract

Rechargeable batteries comprising an energetic metal (e.g. Li, Na, Al) at the anode provide unparalleled opportunities for increasing the energy stored in batteries either on a per unit mass or volume basis. A major problem that has hindered development of such batteries for the last four decades concerns the electrochemical and mechanical instability of the interface between energetic metals and ion conducting organic liquid electrolytes. This study reports that hybrid electrolytes created by blending low volatility liquids with a bi-disperse mixture of hairy nanoparticles provide multiple attractive attributes for engineering electrolytes that are stable in the presence of reactive metals and at high charge potentials. Specifically, we report that such hybrid electrolytes exhibit exceptionally high voltage stability ($> 7\text{V}$) over extended times; protect Li metal anodes by forming a particle-rich coating on the electrode that allows stable, long-term cycling of the anode at high columbic efficiency; and manifest low bulk and interfacial resistance at room temperature, which enables stable cycling of Li/LiFePO₄ half cells at a C/3 rate. We also investigate connections between particle curvature and ion transport in the bulk and at interfaces in such bi-disperse hybrid electrolytes.

5.2 Introduction

A rechargeable battery that uses metallic lithium as the anode is among the most sought-after technologies for portable storage of electrical energy. Such batteries are attractive for multiple reasons. First, lithium has the lowest redox potential (-3.04V vs. Standard Hydrogen Electrode (SHE)); Second, lithium has a low gravimetric density (0.534gm/cm^3) and high theoretical capacity (3860mAh/gm).¹⁻³ Third, because the anode

is lithium, the cathode in such lithium metal batteries (LMBs) can be an unlithiated material, such as sulfur, oxygen, or carbon dioxide/oxygen mixtures, which opens up opportunities for batteries with very high specific energies (SE), relative to today's Li-ion technology (e.g. $SE_{\text{Li-ion}} = 0.15\text{kWh/kg}$; $SE_{\text{Li-S}} = 2.5\text{kWh/kg}$; $SE_{\text{Li-O}_2/\text{CO}_2} = 10.5\text{kWh/kg}$). Four decades of focused research aimed at creating LMBs that live up to the promise of this technology has revealed multiple major problems associated with the reactivity of the metal with aprotic organic carbonate and ether-based liquid electrolytes in current use and with instability of Li electrodeposition at the anode during LMB recharge.

Under normal battery operation, exposed surfaces of a Li metal anode react with most organic liquid electrolytes to form a passivation layer loosely termed the solid electrolyte interface (SEI), which ideally would prevent further side reactions between the Li electrode and the electrolyte. In practice, the SEI formed on a Li metal surface breaks and reforms due to the expansion and compression of lithium during plating (charge) and stripping (discharge), resulting in continuous consumption of electrolyte.⁴ The lifetime and cyclability of a LMB is therefore now understood to depend on the ability to create a mechanically and electrochemically robust SEI layer, which also allows for relatively fast transport of Li-ions across the electrolyte/electrode interface. After extensive studies, Aurbach *et al.*⁵ in 2002 concluded that none of the aprotic organic electrolyte solvents in current use is compatible with a lithium metal anode because all react with Li to form unstable SEI layers at the high current densities required for practical battery operation. Researchers have pursued several approaches for stabilizing the SEI on a Li metal anode. Chemical electrolyte additives, such as vinylene carbonate (VC), thought to react preferentially with Li metal to form cross-linked polymers have been used as sacrificial

agents to create mechanically robust passivating layers on Li that also offer interfacial ionic conductivities comparable to a bulk liquid electrolyte.⁶⁻⁸ More recently, other electrolyte additives, including LiBOB⁹, LiNO₃¹⁰, LiF^{11,12}, and sultones^{13,14} have been shown to produce SEI compositions that not only limit contact between the electrolyte solvent and Li-metal, but which allow the SEI layer to retain its mechanical integrity over many cycles of charge and discharge. Methods for introducing such stabilizing components indirectly in the SEI using specific solvents, e.g. Fluoroethylene Carbonate¹⁵, or salts (e.g. binary LiTFSI-LiFSI¹⁶ or excess LiFSI¹) in the electrolyte have also been reported. In a recent departure from these approaches, Cui *et al.*⁴ showed that a thin film comprising of hollow carbon nanospheres on the lithium surface provides a robust artificial SEI layer that improved columbic efficiency of a Li metal anode to over 99%. Similar results have been observed with coatings of Boron Nitride¹⁷ and Polyacrylonitile¹⁸ on Li metal. Problems involving parasitic reaction between Li anodes and liquid electrolytes are exacerbated under conditions of uneven/dendritic electrodeposition of the metal during cell recharge because such deposition increases the contact surface area between the electrolyte and anode, promoting formation of new SEI after every charge cycle, which overtime depletes the electrolyte and causes the cell resistance to diverge. Modifying ion transport in the electrolyte via single ion conducting species^{19,20} or at the electrolyte/electrode interface by means of halide salts^{12,21} have been shown to prevent growth of dendritic structures during charging. Nanostructured separators with high modulus components have also been reported to yield flatter, more compact deposition of Li.^{7,12,22-25}

Weston and Steele²⁶ in 1982 were to our knowledge among the first to propose using nanocomposites, comprised of nanoparticle fillers in a liquid- or polymer-based ionic conducting material, as electrolytes in rechargeable batteries. Since then there have been a large number of studies that have established the benefits of such nanocomposite electrolytes for making portable, leakage-free, non-flammable batteries.^{24,27,28} High modulus inorganic fillers have also been successfully utilized in the past to suppress rough electrodeposition.²⁴ In this respect, surface modification of such fillers by special ionically associating species like PEO²⁹, anionic groups²⁰, ionic liquids (IL)^{30,31} have been illustrated as particularly effective in stabilizing electrodeposition of Li as a result of ion transport modifications. Korf *et al.*³², for example, recently used silica nano-fillers covalently grafted with the ionic liquid 1-methyl-1-propylpiperidinium bis(trifluoromethanesulfone) imide in a liquid propylene carbonate (PC) electrolyte in symmetric Li/Li cells and, interestingly, on postmortem analysis of the Li electrodes following several cycles of plating and stripping found that the regions where nanoparticles adsorb to the Li electrodes exhibited significantly smoother morphology compared to those where nanoparticles are absent. This finding is important because it is counter to what one would expect if the insulating SiO₂ particles are assumed to retard ion transport to the electrode it also opens up opportunities for more targeted use of nanocomposites as interfacial stabilizers and as building blocks for creating artificial SEI layers on battery electrodes.

Unfortunately, previous reports on nanocomposite electrolytes suggest that their ionic conductivity are too low at high particle volume fractions to realize these beneficial effects under ambient conditions.^{33,34} Very recently we showed that this difficulty can be

overcome by deliberately introducing size polydispersity to suspensions of hairy nanoparticles in liquid electrolyte hosts.²⁸ Herein, we build on these findings to create nanocomposite SEI layers on Li metal electrodes and to carry out an in-depth exploration of their transport and interfacial properties. We find that a SEI layer enriched with a polydisperse, nanoparticle-rich electrolyte imparts novel interfacial and transport behaviors at the electrode/electrolyte interface of a LMB and may also be used to enhance the high-voltage stability of aprotic liquid electrolytes.

5.3 Materials and Methods

5.3.1 Synthesis

Trimethoxysilane functionalized polyethylene glycol methyl ether (PEGME, MW~500g/mol, Gelest chemicals) were grafted to silica nanoparticles with size 10nm (Ludox, SM-30, Sigma Aldrich) and 25nm (Ludox, TM-50, Sigma Aldrich) using a previously described method.⁵⁶ The particles were purified by performing dialysis using a snake skin membrane to remove an unattached PEGME chains, followed by repeated centrifugation using ethanol-hexane as solvent-non-solvent to remove any residual PEGME from the material. The particles were then dried at 60°C for 24hours in a convection oven, followed by vacuum drying for 48 hours. Thermo Gravimetric Analysis (TGA) was used to estimate the residual inorganic content to compute the grafting densities (number of chains per unit surface area) which were evaluated to be $\Sigma \sim 1.3$ chains/nm² and $\Sigma \sim 1.5$ chains/nm² for 10nm and 25nm particles respectively. Hybrid electrolytes were prepared in Argon filled glove box by dispersing the hairy nanoparticles in propylene carbonate (PC, Sigma Aldrich) at various core volume fractions ϕ ranging from 0.2 to 0.4. At each ϕ , the relative fraction of larger particles added was varied which

is given by the parameter $x_L = \phi_L / \phi$. 1M of bis(trifluoromethanesulfoneimide) (LiTFSi, Sigma Aldrich) salt was added to the resultant solution of hybrid silica nanoparticles in PC to create SiO₂-PEGME/PC hybrid electrolytes.

5.3.2 Characterization

The dispersion and structure of hybrid particles was determined from Transmission Electron Microscopy (TEM) and Small Angle X-ray Scattering (SAXS) measurements. For TEM measurements, dilute suspensions of the hybrid electrolyte dissolved in chloroform were dropped on copper grids, with subsequent solvent evaporation and annealing at 70°C for 48 hours.

SAXS measurements were performed at D-1 beamline of Cornell High Energy Synchrotron Source (CHESS) using a point-collimated X-ray beam source. The scattered x-ray intensity from the hybrid electrolyte is measured with the variation in the wave-vector q and can be given as a function of particle form factor $P(q,D)$ and structure factor $S(q, \phi, D)$

$$I(q, \phi, D) = \Phi \Delta\rho_e V P(q, D) S(q, \phi, D)$$

Where, V and $\Delta\rho_e$ is the volume of a single particle core, and electron density contrast between the particle and the surrounding medium respectively. The form factor $P(q,D)$ gives the information about the size and shape of a single particle.

The glass transition temperature of the electrolytes was determined from Differential Scanning Calorimetric (DSC, Q2000 TA instruments) measurements.

5.3.3 Electrochemical Measurements

The ionic conductivities of the electrolytes were measured at room temperature using a Novocontrol Broadband Dielectric spectrometer with a frequency range of 0.1-3x10⁶ Hz.

The DC conductivities were obtained from the plateau of real part of the conductivity versus frequency curve.⁷³ The molar diffusivities were obtained using the Nernst-Einstein Equation:

$$D = \frac{\sigma k_B T}{C_0 q^2}$$

where, σ (S-m²/mol) is the D.C. molar ionic conductivity, k_B (J/K) is the Boltzmann constant, T (K) is the temperature, C_0 (#/m³) is the ion concentration and q (C) is the charge of the diffusing entity.

The AC impedance measurements were performed on a Solortron Electrochemical Impedance Spectrometer using a symmetric coin cell with lithium metal as the electrodes and SiO₂-PEGME/PC as the electrolyte at different ϕ and x_L at ambient temperature. The frequency was varied from 1MHz to 0.1Hz at amplitude of 50mV. Error bars in the final impedances were evaluated as deviations from running each measurement for 12 symmetric cells.

Electrochemical stability voltage window was determined by linear scan voltammetry measurements performed at a scan rate 1mV/s between -0.2V and 6.5V. The stability was further confirmed by performing floating-point test measurements where the voltage was stepped up to 7V, with each voltage step of 0.5V maintained for 5hours.

5.3.4 Analyzing the Columbic Efficiency

Li| electrolyte |Stainless steel 2032 type coin cells were assembled in an Argon-filled Glove Box. Control liquid electrolyte comprising 1M LiTFSi-PC with 1wt% Lithium Nitrate (LiNO₃) and 2vol% vinylene carbonate and a standard Celgrad separator were compared against hybrid nanoparticles dispersed in the same electrolyte with $\phi=0.3$ and $x_L=0.5$. In both cases, prior to the measurements, cells were conditioned by cycling them

between 0 to 0.5V for 10 cycles, to ensure the formation of a stable SEI layer on the electrodes as shown previously.⁷ To characterize the columbic efficiency, the conditioned cells were first discharged at a constant current density of 0.25mA/cm² for 2 hours to transfer an amount of lithium corresponding to 0.50mAh/cm² of charge from the Li electrode to the stainless steel electrode. The amount of charge recovered in the reverse cycle was then recorded where the cell was charged back to 0.5V at the same current density, and the fractional recovery between the two cycled was used to determine the columbic efficiency.

The lithium electrode surface was characterized using a similar procedure for hybrid electrolytes with $\phi=0.2$ and $x_L=0.5$ without any additives. The coin cells were disassembled inside the glove box and the lithium foil was repeatedly washed with pure PC to dissolve any excess of particles on the surface. Scanning Electron Microscopy (SEM) measurements were performed on the lithium foil to image the electrode surface.

5.3.5 Cell lifetime study

LiFePO₄ slurry was prepared by mixing the active material, super-P carbon and PVDF binder in 8:1:1 ratio in a ball-mill in presence of NMP solvent. The slurry was casted on an aluminium sheet using a doctor blade to prepared cathode sheets of 0.5mAh/cm² surface capacity. Half-cells were made in glovebox with Lithium foil as anode, Lithium Iron Phosphate as cathode and the hybrid binary nanocomposite as electrolyte. The batteries were cycled at constant current between the voltage limits of 2.5V and 3.8V

5.4 Results and Discussion

Physical Characterization and Ion Transport

Aggregation and phase separation are among the most important hurdles that have limited application of nanoparticle-polymer composites in many fields of technology.^{33,35-39} Surface functionalization of particles with short polymer chains is a widely practiced technique for creating uniform dispersion of particles in polymers and liquid hosts.⁴⁰⁻⁴⁸ Here we utilize previous chemistry to densely graft short polyethylene glycol methyl ether (PEGME, MW~500g/mol) chains to SiO₂ nanoparticles ($d_p = 10\text{nm}$ and 25nm) and dispersed these particles and their binary mixtures in Propylene Carbonate (PC)-based liquid electrolytes. The dispersion state of hairy nanoparticles in the resultant hybrid electrolytes was analyzed by observing their transmission electron micrographs (TEM). Figure 5.1(c) shows that irrespective of the volume ratio (x_L) of larger ($d_p = 25\text{nm}$) to smaller ($d_p = 10\text{nm}$) particles, the particles appear as well-dispersed objects in the hybrid electrolytes. This finding is confirmed by analyzing the variation in the scattered intensity $I(q)$ of X-rays from the bulk hybrid electrolytes using small-angle x-ray scattering (SAXS). Figure 5.1(b) reports typical $I(q)$ vs q data from SAXS measurements performed on a hybrid electrolyte with fixed volume fraction of nanoparticles ($\phi = 0.3$), but with varying fractions x_L of the larger particles. $I(q)$ is seen to exhibit a plateau for all x_L values in the low q region and a q^{-4} scaling in the high q region. Both of these features are known characteristics of uniformly dispersed, un-aggregated spheres.^{40,49}

Previous studies on bi-disperse suspensions of star polymers and hairy nanoparticles have shown that introduction of a larger species to a mono-disperse suspension comprised of smaller ones results in a transition from a highly jammed glass to a weakly jammed suspension, and, for large enough size ratios, ultimately to a liquid state.⁵⁰⁻⁵² This transition has also been reported in self-suspended suspensions of bi-disperse hairy

particles and is thought to reflect differences in the degree of inter-penetration of tethered oligomer chains produced by differences in curvature of the two different nanocore populations.⁵² As a consequence, tethered oligomer chains in a bi-disperse blend of hairy particles may acquire higher configurational entropy even at the same overall particle volume fraction. It has been observed previously that lithium-ion transport in electrolytes containing PEO occur predominantly by local diffusion of polymer chain segments and hopping of Li-ions between ether groups on PEO chains.^{33,34} Figure 5.1(a) reports the diffusivity of lithium ions obtained, via the Nernst-Einstein equation, from ionic conductivity data for a SiO₂-PEGME/PC hybrid electrolyte with $\phi=0.3$. The figure shows that the diffusivity is a maximum near $x_L = 0.75$. This higher diffusivity can be explained in terms of the lower interpenetration and hence higher mobility of PEGME chains in the binary hairy particle mixtures; the higher mobility of PEGME chains allows Li-ions in an electrolyte to migrate at a faster rate, which results in an increase in ionic conductivity and higher ionic diffusivity in the bi-disperse hybrid electrolytes. Figure 5.1(a) also reports the glass transition temperature, T_g , for SiO₂-PEGME/PC hybrid electrolytes as a function of x_L . Consistent with the explanation of the enhanced diffusivity at $x_L \approx 0.75$, it is seen that T_g exhibits a minimum at x_L close to where the maximum in diffusivity is observed. A reduced T_g for the bi-disperse suspension implies an increased free volume, which is consistent with our hypothesis that the tethered PEGME chains are less constrained in the bi-disperse hybrid electrolytes. Supplementary figure 5.1 presents results for electrolytes with $\phi=0.2$ and 0.4 , and shows that the observation of a maximum diffusivity at $x_L \approx 0.75$ and T_g minimum near this value is a generic feature of these materials.

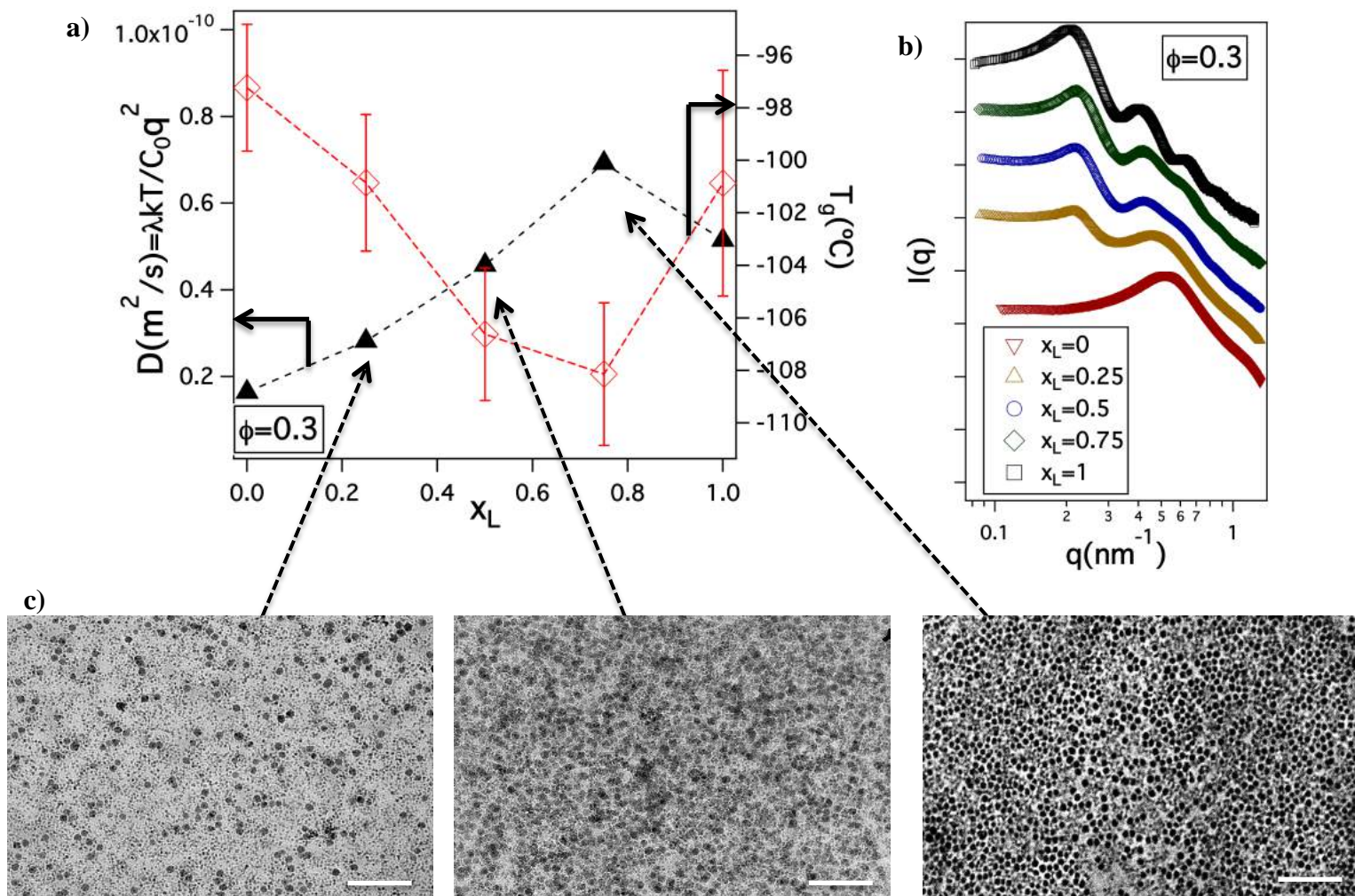


Figure 5.1 Physical Characterization: **a)** Variation in ionic diffusivity, D (triangles) as calculated from Nernst-Einstein equation, and glass transition temperature, T_g (diamonds) with fraction of larger particles, x_L . **b)** Intensity, $I(q)$ as a function of wave vector q at $\phi=0.3$, as obtained from SAXS measurements for different values of x_L , increasing from bottom to top. **c)** Transmission Electron Micrographs (TEM) for bi-disperse hybrid electrolytes at $\phi=0.3$ for $x_L=0.25, 0.5$ and 0.75 . The scale bar for all the images is 500nm.

Structural Factor analysis

Further insight about the structure of the SiO₂-PEGME/PC electrolytes and about the confinement of PEGME chains can be obtained by analyzing the SAXS structure factor $S(q)$ of the materials. Figure 5.2(a) compares the experimentally obtained $S(q)$ with the calculated structure factor for a binary hard sphere (HS) suspension using the Percus-Yevick (PY) approximation.⁵³ To account for the fact that a few PEGME chain segments nearest the anchor points on the particles are likely to be completely correlated with their particle substrate,⁴² the theoretical $S(q)$ approximate the particle size in terms of an effective radius, $a_{\text{eff},i} = a_i + n_{m,i} l_m \cos(\theta/2)$, such that a certain number of monomers, $n_{m,i}$, are assumed to be part of the core. Here $i=s,l$ for smaller particles and larger particles respectively, a_i is the original radius of the particle, $l_m=0.35\text{nm}$ which is the monomer length for PEO, and $\theta= 68^\circ$ which is the bond tetrahedral angle. In analyzing the experimental data using the PY approximation, $n_{m,i}$ was treated as an unknown variable and its value adjusted so that the peak positions of $S(q)$ computed for a binary HS suspension model coincide with those seen in the experimental $S(q)$. It can be observed from Figure 2(a) that whereas the $S(q)$ peak amplitudes and positions estimated from PY-HS analysis are in good agreement with the experimental values for electrolytes with low ϕ , the first $S(q)$ maxima are much higher than the predicted ones in electrolytes with high ϕ . A higher first-peak height for $S(q)$ implies a stronger inter-particle correlation, which results in the hybrid particles from enhanced interaction of tethered corona chains.⁵⁴⁻⁵⁶ Supplementary figure 5.2 reports the corresponding results for electrolytes with a range of particle size polydispersities, $x_L=0, 0.25, 0.75$ and 1. The discrepancy in the calculated and measured peak heights, especially the first peak, is clearly greatest in

systems with the largest asymmetry in nanoparticle size. The discrepancy is thought to reflect enhanced interaction between tethered oligomer chains in the hybrid particle electrolytes, which are not included in the PY-HS analysis.

Additional insights about the structure of the electrolytes can be obtained from the PY-HS predictions by resolving the structure factor into its three components- S_{11} , S_{12} and S_{22} where 1 and 2 denote smaller and larger particles respectively (see Supplementary figure 5.3). From the first peak positions of each of these components, three different inter-particle distances can be obtained viz., $d_{p-p,11}$, $d_{p-p,12}$ and $d_{p-p,22}$. Figure 5.2(b) show the variation in surface-to-surface distance for $\phi=0.2, 0.3$ and 0.4 , as a function of fraction of larger particles x_L . The surface-to-surface distance is calculated by subtracting the effective core diameter from the inter-particle distance i.e. $h_{ij}=d_{p-p,ij} - 2a_{eff,ij}$, where $i, j= 1$ and 2 and $i=j$ when analyzing the distance between the same species. It can be observed that for certain values of ϕ and x_L , h_{ij} is negative which implies that the corona chains overlap or inter-penetrate for those regions. It can be seen that as ϕ increases, as expected h_{ij} assumes higher negative values, implying higher degree of interpenetration and thereby confinement for tethered chains at higher volume fractions. For any core volume fraction ϕ , it can also be observed that initial addition of larger particles to a pure monodisperse suspension of smaller ones, first decreases the distance between the smaller particles after which the h_{11} value increases with further addition of larger particles. For the same x_L values, however, h_{22} is larger for a smaller fraction of large particles, and decreases with further increase in x_L . This implies that for smaller x_L values, the larger particles confine the smaller particles and increases the distance between themselves, and subsequent increase in x_L values leads to an increase in the average distance between

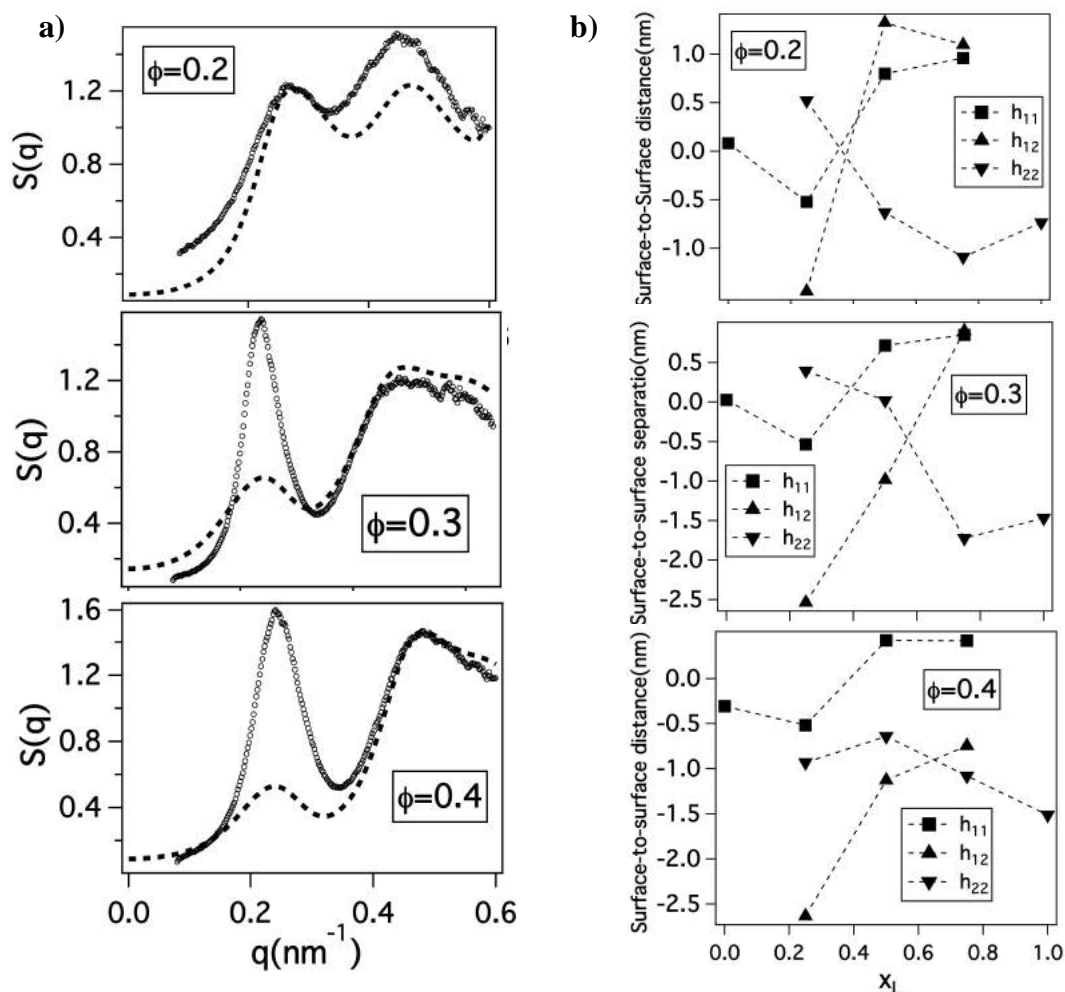
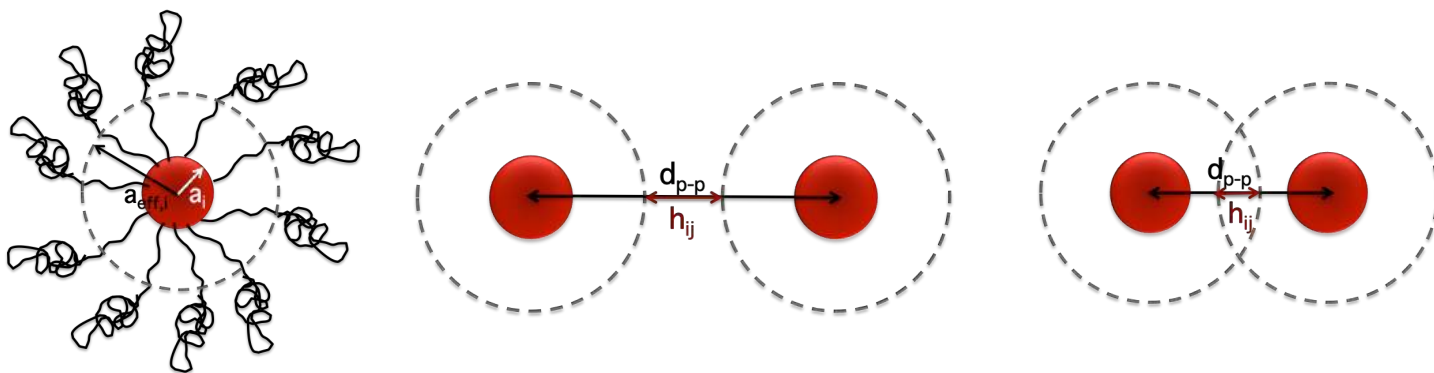


Figure 5.2 Structure Factor: a) Evolution of Structure factor, $S(q)$ with the wave vector q for different volume fractions, $\phi=0.2, 0.3$ and 0.4 at $x_L=0.5$. The open symbols are the experimentally obtained $S(q)$ values and the dashed lines are predictions from binary HS model for the same systems. The schematic above illustrates the effective particle radius, which includes some fraction of monomers as part of the core. b) Surface-to-surface distances, h_{11}, h_{12} and h_{22} for the same volume fractions as a function of x_L . The graphics illustrates the two scenarios for surface-surface distances which will be positive when there is no overlap and negative when the polymer chains have significant overlap.

smaller particles. This interpretation is confirmed from the h_{12} values, which always increase with increase in x_L , meaning that the distance between a smaller and a larger particle always increases. Also, for the pure mono-disperse suspensions of smaller and larger particles the h_{ij} values are either negative or close to zero, which implies that the tethered corona chains inter-penetrate much more in these suspensions, while h_{ij} values for bi-disperse suspensions are either positive or less negative than their mono-disperse counterparts, which indicates less interpenetration and hence reduced confinement of corona chain motions in bi-disperse suspension. This observation is in agreement with the trends seen in the diffusivity and T_g values, which confirms the hypothesis that in a bi-disperse suspension the tethered PEO chains are less confined or have higher mobility which subsequently leads to a higher ionic conductivity values for these hybrid electrolytes as observed previously.²⁸

Variation of interfacial resistance

Figure 5.3(a)-(c) report Nyquist plots obtained using electrochemical impedance spectroscopy measurements to evaluate the impedance in bulk electrolyte and at the electrode-electrolyte interface in symmetric Li/Li cells. The experimental plot is fitted using the circuit model shown schematically in Figure 5.3, where R_b corresponds to the resistance in bulk electrolyte, R_{int} represents interfacial resistance to ion migration at the electrode-electrolyte interface, CPE is the constant phase element capacitance near the electrode surface and W_d is the Warburg diffusion element.²³ Figure 5.3(d) and (e) summarize the magnitude of R_b and R_{int} as a function of x_L at different core volume fractions ϕ , respectively. While R_b does not show significant variation with x_L , R_{int} decreases significantly and exhibits similar trends to those discussed earlier for the ionic

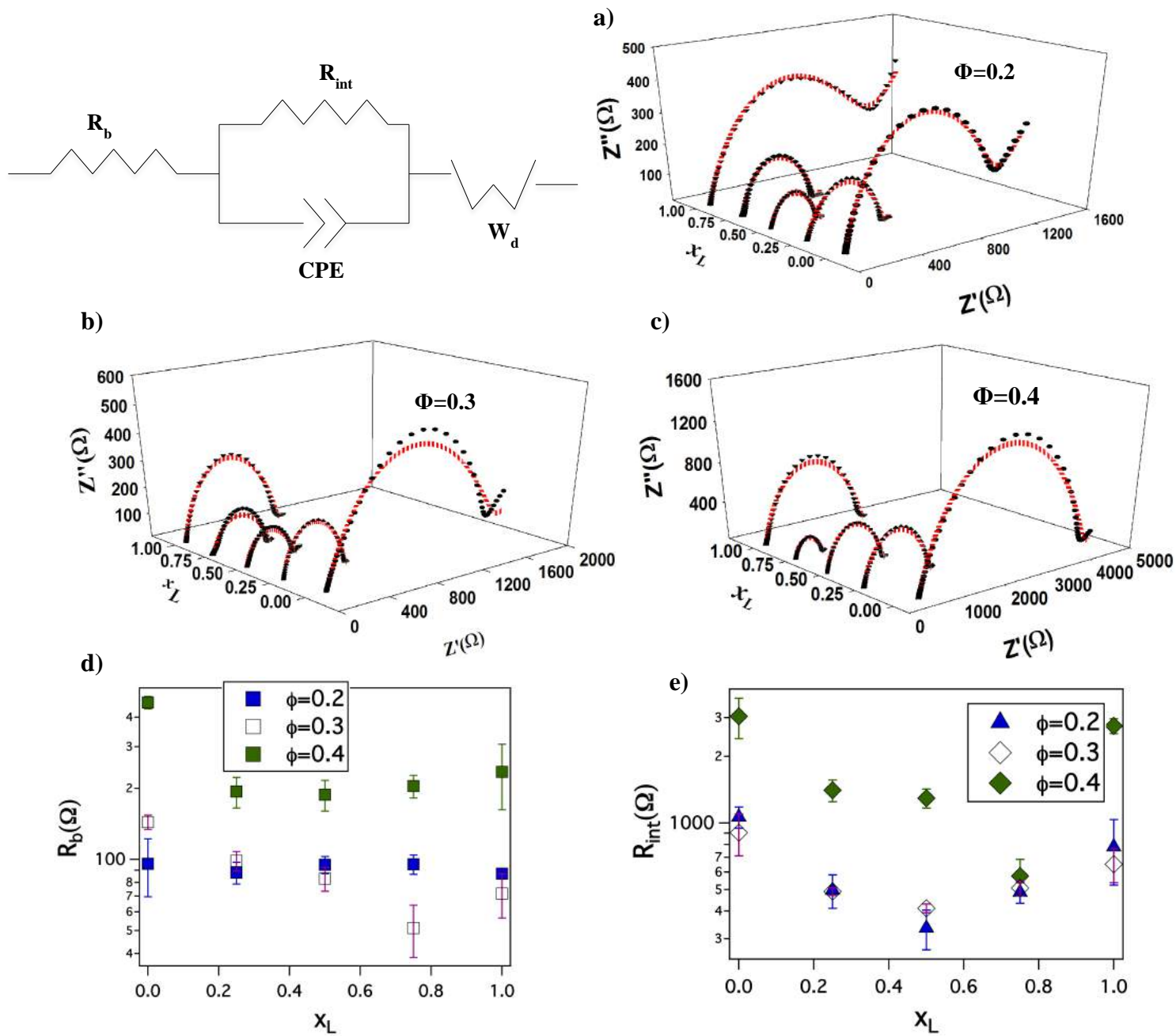


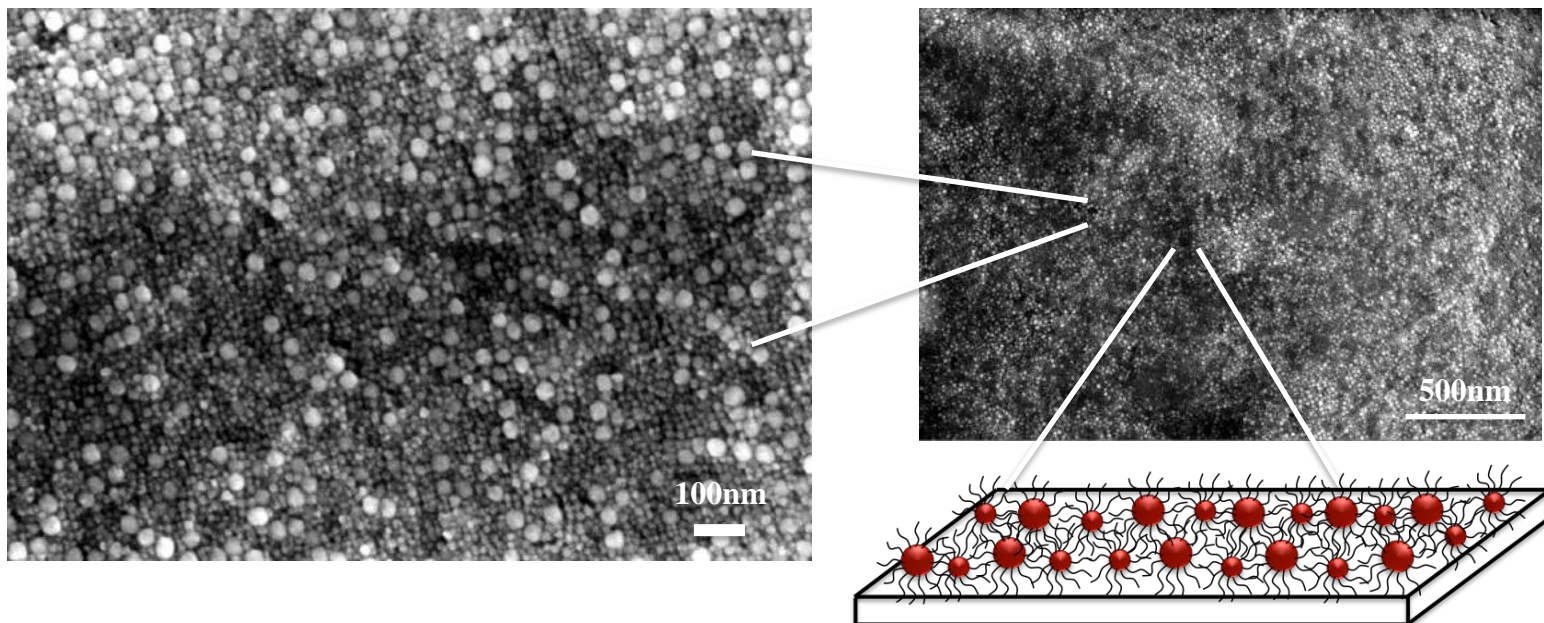
Figure 5.3 Electrochemical Characterization: Impedance spectra for electrolytes with core volume fractions **a)** $\phi=0.2$, **b)** 0.3, and **c)** 0.4 measured at different fractions of larger particles added, x_L . The black symbols are experimental data and the red lines are fit to the equivalent circuit model as shown. **d)** Bulk resistance, R_b and **e)** Interfacial resistance, R_{int} measured at different core volume fractions as a function of x_L .

diffusivity and T_g . We postulate that the relative invariance in R_b occurs because of adsorption of significant fraction of particles from the bulk electrolyte to the electrode surface, which results in bulk resistance values similar to those of liquid electrolytes with low nanoparticle loadings where ion transport is dominated by diffusion of electrolyte solvent-ion associates. This would then also lead to variations in interfacial resistance similar to trends seen in diffusivity due to the presence of particles.

Surface Characterization of Li anode

In order to evaluate the hypothesis that surface adsorption of SiO_2 -PEGME particles is the source of the weaker dependence of R_b and R_{int} on x_L , we performed Scanning Electron Microscopy (SEM) analysis of the lithium electrodes harvested from symmetric Li/Li cells following galvanostatic cycling at a low current density of $0.03\text{mA}/\text{cm}^2$ for 10 cycles. Prior to SEM analysis, the electrodes were vigorously washed with pure PC to remove any loosely bound material. Figure 5.4(a) shows a representative SEM image of the Li metal electrode for small and higher magnifications. It is apparent that a dense layer of bi-disperse particles of size 10nm and 25nm are adsorbed to the surface of the electrode. The hairy particles appear to form a continuous, protective film on the electrode surface. Supplementary figure 5.4 provides an image of pristine lithium electrode and with neat PC electrolyte after 10 cycles under the same conditions as mentioned above. It can be observed from the SEM that at such low current densities, the surface of lithium metal surface becomes rough when cycled without the particles, indicating uneven electrodeposition.

a)



b)

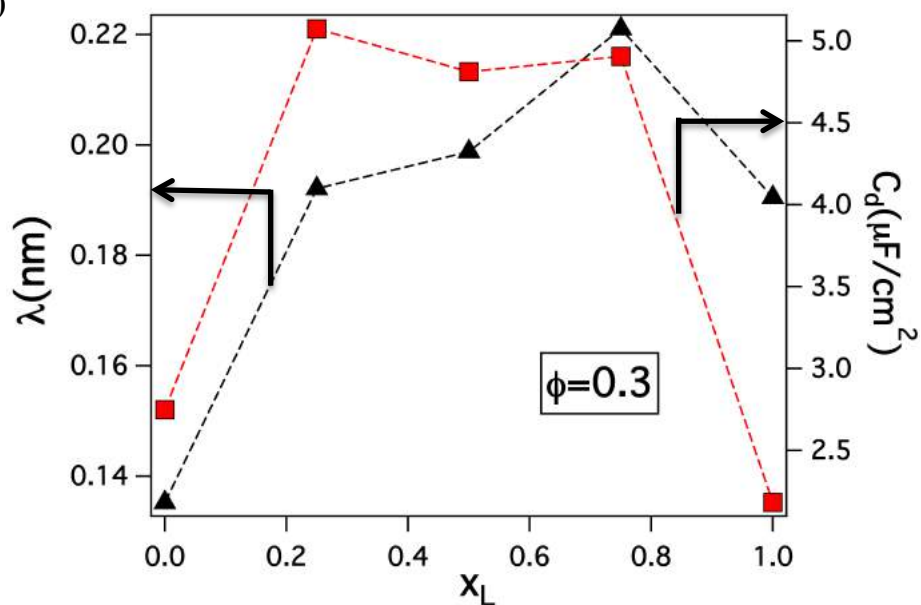


Figure 5.4 Surface Characterization: **a)** Scanning Electron Micrographs (SEM) for lithium electrode surface after the symmetric cell was cycled for 10 cycles at $0.03\text{mA}/\text{cm}^2$ with the bi-disperse hybrid electrolyte. The schematic illustrates the electrode surface as observed in SEM, where the particles form protective layer on the electrode surface. **b)** Electrical double layer, λ (triangles) and electrochemical capacitance per unit area, C_d (squares) for $\phi=0.3$ as a function of x_L .

It has been observed in a typical Lithium ion battery (LIB) that during charging or discharging, oppositely charged ions accumulate near the surface of respective electrodes.⁵⁷⁻⁵⁹ The electrochemical capacitance (EC) near the electrode surface can be determined from the relaxation frequency f_0 deduced from the Nyquist plot⁶⁰⁻⁶² and its relationship, $2\pi f_0 R_{\text{int}} C_d = 1$, to the interfacial resistance and capacitance.⁶³ The calculated capacitance can be written in terms of the dielectric constant at the interface as, $C_d = \epsilon \epsilon_0 A / l$ where, ϵ is the dielectric permittivity of the material at the interface, ϵ_0 is the vacuum permittivity, A is the surface area of the electrode and l is the thickness of the capacitive layer. Figure 5.4(b) shows the variation in the electrochemical capacitance C_d as a function of x_L for $\phi = 0.3$. It is apparent that hybrid electrolytes based on bi-disperse SiO₂-PEGME nanoparticles display higher interfacial capacitance than the mono-disperse particle suspension. This observation can be explained either in terms of an increase in the effective dielectric constant or a reduction in the SEI layer thickness as x_L increases. Based on the earlier observation that the particles form a stable, dense film on the Li anode, we conclude that l is likely to be a fixed number of the order of average particle diameter in the electrolytes. Inserting this value in the above formula, allows us to estimate ϵ and, from it, an apparent Debye screening length ($\lambda = \sqrt{\frac{\epsilon \epsilon_0 RT}{2F^2 C_0}}$), which is also shown as a function of x_L in Figure 5.4(b). Here F is Faraday's constant and C_0 is the molar concentration of salt in the electrolyte. For a pure PC electrolyte containing 1M salt, $\lambda \approx 0.26\text{nm}$, which is comparable to the highest values obtained in Figure 5.4(b), but somewhat larger than the values estimated for the electrolytes with $x_L = 0$ or $x_L = 1$, which is consistent with expectations for the factor of 5 to 10 difference in the reported dielectric constants for PEG and PC^{35,64-67}. One explanation of the high C_d and λ values

apparent at intermediate x_L is that they reflect greater access of PC to the SEI, which would increase ε . It is important to note however, that even the largest λ values are more than an order of magnitude lower than 1, meaning that the electric field gradients in the SEI layer formed by a hairy particle coating of Li are substantially smaller than in a pure electrolyte, which would lower both the diffusive and electro-convective flux of anions to the Li metal surface. The Li^+ transference number (t_{Li^+}) was determined by the Bruce-Scrosati method^{68,69} (see Supplementary Information) which was found to be approximately 0.32 for this electrolyte, in agreement with previously reported transference numbers for PEG based electrolytes.³⁴ The presence of particles in the SEI therefore does not influence the lithium ion transference number, which is consistent with expectations based on the theoretical predictions of Jacob⁷⁰, where it was found that the transference number has a strong dependence of the ratio of pore size to double layer thickness.

Enhanced electrochemical stability of nanocomposites

If the Li metal in a LMB is unprotected, the electrolyte continuously reacts with the anode to form insulating products, which increase the interfacial resistance of the battery with time. The interface stability in symmetric cells containing SiO_2 -PEGME/PC hybrid electrolyte with $\phi=0.3$ and $x_L=0.5$ were evaluated using impedance measurements as a function of time for a period of 2 months. It can be seen from Figure 5.5(a) that the time-resolved impedance plots overlay well onto each other, indicating that the particle-rich SEI layer imparts long-term enhanced chemical stability to Li-metal/electrolyte interface. This enhanced stability is consistent with the existence of a passivating particle film on the Li anode as deduced from the earlier SEM experiments. On comparing these results

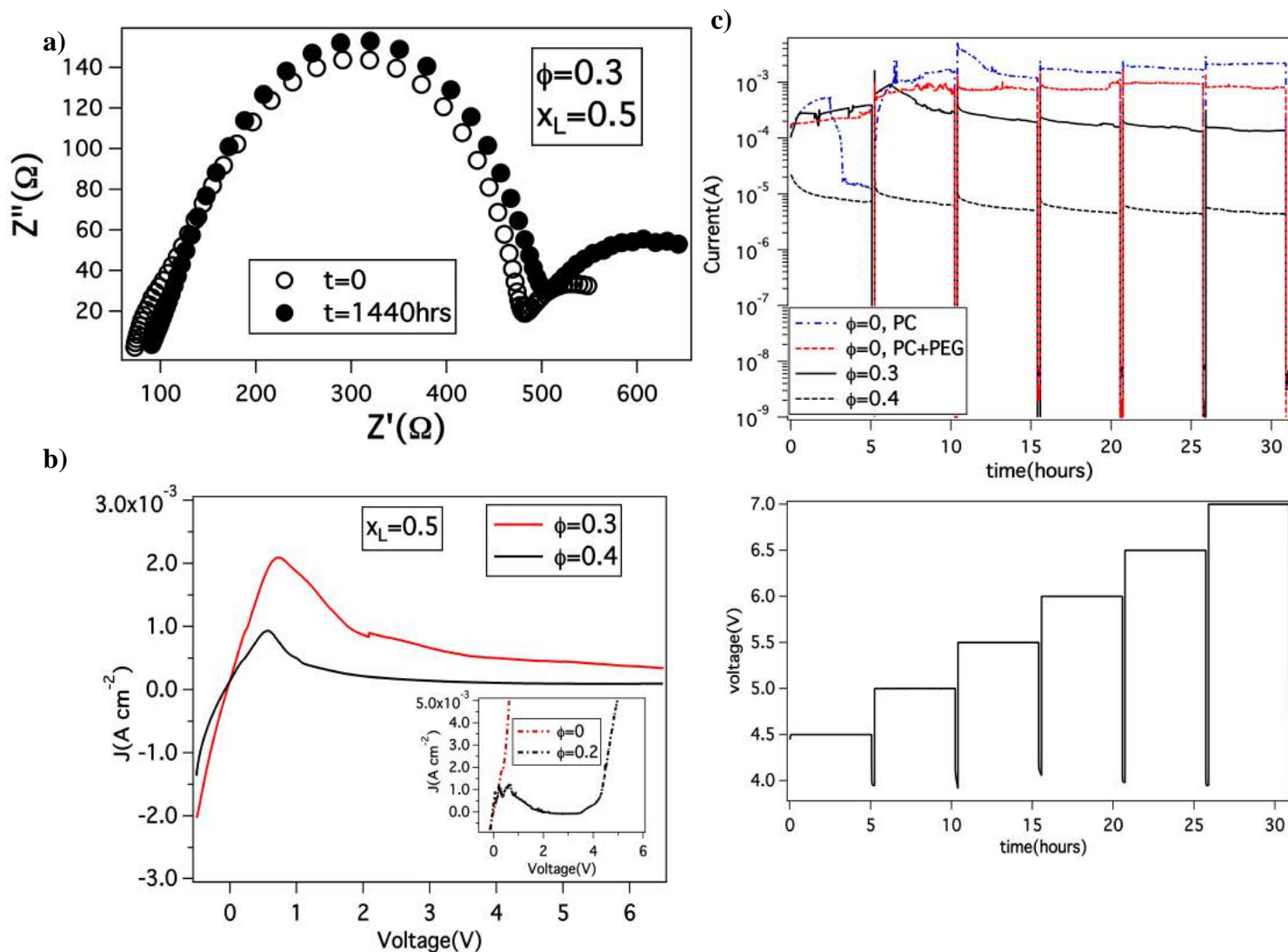


Figure 5.5 Electrochemical Stability: **a)** Initial impedance spectra (open symbols) for a symmetric cell with hybrid particle electrolyte at $\phi=0.3$ and $x_L=0.5$ compared with the spectra at $t=1440$ hours (closed symbols). **b)** Variation in faradic current density, J as a function of voltage as measured from Linear sweep voltammetry measurements for $x_L=0.5$ compared for $\phi=0.3$ (red line) and $\phi=0.4$ (black line). Inset shows the measurements for neat PC (red line) and $\phi=0.2$ (black line). **c)** Leak current measured as a function of time for different steps of voltage as measured in a floating point test. Profiles for symmetric cell with hybrid electrolyte at $\phi=0.3$ (black solid line) and $\phi=0.4$ (black dashed line) are compare against neat electrolytes with PC (blue line) and with PEG and PC (red line) blended in the same ratio as that for hybrid particle electrolyte with $\phi=0.3$.

with a neat PC electrolyte (Supplementary figure 5.7), it can be seen that the interfacial resistance quadruples over a timespan of just 72 hours, indicating that the particles indeed facilitate stabilization of the electrode. Figure 5.5(b) reports results from linear-sweep voltammetry and electrochemical floating point measurements on lithium cells containing the hybrid electrolytes. The linear sweep voltogram reveals that at higher particle volume fractions (e.g. $\phi=0.3$ and $\phi=0.4$) and for $x_L=0.5$ the hybrid electrolytes are stable up to 6.5V vs. Li/Li⁺. In contrast, electrolytes containing lower fractions $\phi=0.2$ of particles (inset of Figure 5.5(b)) become unstable at around 4V. The initial peak at 0.2V in all the measurements is the cathodic peak associated with the Li/Li⁺ reaction.^{7,12} Its presence for all of the materials studied means that this process is not compromised in the hybrid electrolytes. Similar trends were also observed in the floating-point tests in Figure 5.5(c), where hybrid electrolytes containing higher nanoparticle volume fractions are seen to manifest negligible leakage currents even after exposure to voltages as high as 7.5V for 5 hours. In contrast, the particle-free PC electrolyte or a blend of un-tethered PEG in PC already exhibits high leakage currents at 5V. Together, these results clearly show that SiO₂-PEGME/PC hybrid electrolytes with high SiO₂ are exceptionally stable, in agreement with previous reports.⁷¹

Analyzing galvanostatic performance

As a final assessment of the ability of a nanoparticle-rich SEI to stabilize Li metal anodes against reaction with liquid electrolytes, we analyzed the columbic efficiency obtained in galvanostatic measurements employing Li/stainless steel electrodes. In these experiments, a fixed amount of Li⁺ ions is stripped from lithium metal and deposited to the stainless steel substrate and plated back in successive runs. By measuring the capacity ratio for the

strip and plate segments of the cycle, the columbic efficiency (CE) of the cell can be quantified. It has been reported that PC-based electrolytes spontaneously form an insulating and unstable SEI layer on Li, yielding a low CE of ~70%.⁷² It has also been shown that the CE for PC can be improved by employing VC and LiNO₃ as electrolyte additives.^{6,7} To study the effect of particles on CE of Li metal electrodes, we utilized a PC-based electrolyte reinforced with 1% LiNO₃ and 2% VC as a control. It can be seen from Figure 5.6(a) that although both the control and hybrid PC electrolytes exhibit high CE, the control electrolyte is unable to maintain the improvements beyond ~25 cycles, implying that the VC and LiNO₃ are consumed. In contrast, the SiO₂-PEGME/PC hybrid electrolyte displays high CE for at least 80 cycles. In the control experiment, despite using additives, the neat PC electrolyte decomposes with each succeeding cycle due to its low stability window. Also, absence of a protective layer of particles on the electrode results in an uneven electrodeposition, which results in a higher exposed surface area of the electrode, accelerating this decomposition of neat electrolyte. On the other hand, as previously inferred from electrochemical stability tests and electron microscopy, the SiO₂-PEGME particles form a protective monolayer on the electrode surface that prevents constant exposure of liquid electrolyte to lithium surface and avoids the breakdown of additive rich SEI. This synergistic effect of the additives and SiO₂-PEGME particles helps in maintaining high columbic efficiency over large number of cycles. Figure 5.6(b) shows the room-temperature performance of the binary hybrid nanocomposite electrolytes in a Li/LiFePO₄ half-cell in which a SiO₂-PEGME/PC hybrid with $\phi = 0.3$ and $x_L = 0.5$ is employed. The figure reports the voltage profiles (voltage versus capacity) for the 1st, 10th and 50th cycles of charge and discharge. The low

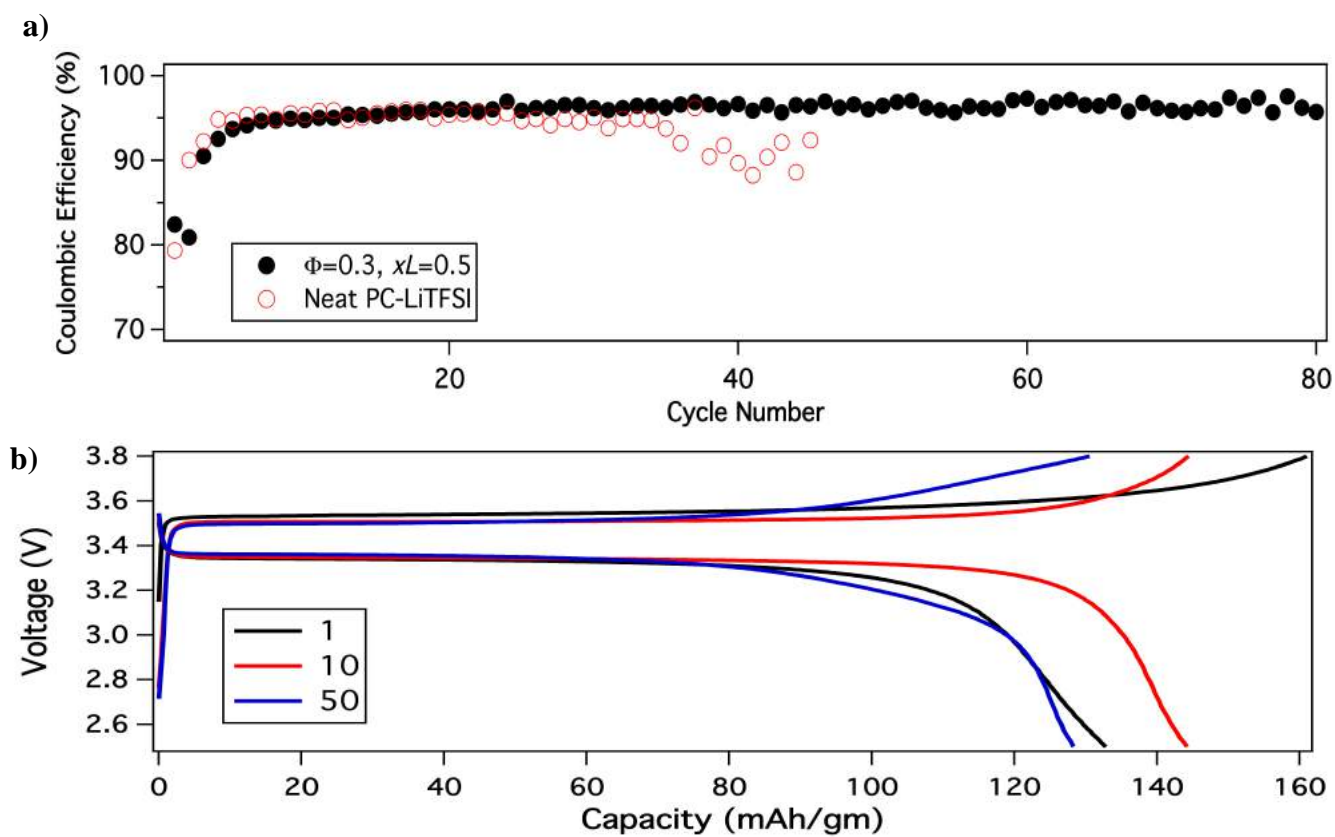


Figure 5.6 Galvanostatic performance: **a)** Comparison of coulombic efficiency as a function of cycle number for neat PC electrolyte and hybrid particle electrolyte with $\phi=0.3$ and $x_L=0.5$ for Li|electrolyte|Stainless Steel configuration. Measurements were performed at a current density of $0.25\text{mA}/\text{cm}^2$. **b)** Charge-discharge profiles for Li/LFP half-cell containing hybrid particle electrolyte with $\phi=0.3$ and $x_L=0.5$ at a fixed rate of $C/3$ in the initial, 10th and 50th cycle.

efficiency in the first cycle is associated with irreversible reactions that help in forming a stable passivation layer on the Li anode. The results in Figure 5.6(b) shows that even after 50 cycles the cells maintain a high discharge capacity of ~130mAh/gm at C/3 rate. Supplementary figure 5.8 shows that the columbic efficiency for the half-cell remains around 99% over 50 cycles.

5.5 Conclusions

In conclusion, we have studied hybrid electrolytes created by blending a low-volatility carbonate (PC) with a bi-disperse mixture of SiO₂-PEGME nanoparticles. We show that hybrid electrolytes based on bi-disperse hairy nanoparticles can be designed to provide multiple attractive features, including exceptional high voltage stability (> 7V) over extended times; protection of a Li metal anode that allows stable-long term cycling of the anode at high columbic efficiency; and low bulk and interfacial resistance at room temperature that enables stable cycling of Li/LiFePO₄ half cells at a C/3 rate.

The origin of the enhanced ion mobility in bi-disperse hybrid electrolytes is shown by means of DSC measurements, to be the reduction in T_g of the tethered PEGME chains and more fundamentally from SAXS analysis, to arise from an increase in mobility of tethered PEGME chains due to lower levels of chain interpenetration caused by differences in curvature of the larger and smaller particles in the bi-disperse electrolytes. By means of interfacial impedance measurements, it was further shown that the interfacial mobility of hybrid electrolytes at a Li metal electrode is a much stronger function of polydispersity than the bulk resistance. We hypothesize that this difference arises from the spontaneous adsorption of particles to the high energy Li metal electrode

to form a dense protective film. Post-mortem analysis of the Li electrode surface following galvanostatic cycling shows that a dense particle-rich film accumulates at the Li metal surface, which increases the interfacial capacitance and appears to be very effective in limiting access of liquid electrolyte to the Li metal surface without compromising interfacial transport of Li-ions. In contrast to control, particle-free electrolytes, hybrid electrolytes based on bi-disperse hairy nanoparticles are shown to enable Li/stainless steel cells with high coulombic efficiency for at least 80 cycles and Li/LiFePO₄ cells with high discharge capacity in extended cycling at room-temperature.

Acknowledgements

This work was supported by the National Science Foundation, Award No. DMR-1006323. Use of the Cornell High Energy Synchrotron Source (CHESS), was also supported NSF Award No. DMR-1006323.

REFERENCES

- (1) Qian, J.; Henderson, W. a; Xu, W.; Bhattacharya, P.; Engelhard, M.; Borodin, O.; Zhang, J.-G. *Nat. Commun.* **2015**, *6*:6362, 1–9.
- (2) Xu, W.; Wang, J.; Ding, F.; Chen, X.; Nasybulin, E.; Zhang, Y.; Zhang, J.-G. *Energy Environ. Sci.* **2014**, *7*, 513–537.
- (3) Tu, Z.; Nath, P.; Lu, Y.; Tikekar, M. D.; Archer, L. a. *Acc. Chem. Res.* **2015**, No. 48(11), 2947–2956.
- (4) Zheng, G.; Lee, S. W.; Liang, Z.; Lee, H.-W.; Yan, K.; Yao, H.; Wang, H.; Li, W.; Chu, S.; Cui, Y. *Nat. Nanotechnol.* **2014**, *9* (8), 618–623.
- (5) Aurbach, D.; Zinigrad, E.; Cohen, Y.; Teller, H. *Solid State Ionics* **2002**, *148* (3-4), 405–416.
- (6) Guo, J.; Wen, Z.; Wu, M.; Jin, J.; Liu, Y. *Electrochem. commun.* **2015**, *51*, 59–63.
- (7) Choudhury, S.; Mangal, R.; Agrawal, A.; Archer, L. A. *Nat. Commun.* **2015**, *6*:10101, 1–9.
- (8) Chen, L.; Wang, K.; Xie, X.; Xie, J. *J. Power Sources* **2007**, *174*, 538–543.
- (9) Xu, K.; Zhang, S.; Jow, T. R. *Electrochem. Solid-State Lett.* **2005**, *8*, A365–A368.
- (10) Li, W.; Yao, H.; Yan, K.; Zheng, G.; Liang, Z.; Chiang, Y.-M.; Cui, Y. *Nat. Commun.* **2015**, *6*:7436 (May), 1–8.
- (11) Choudhury, S.; Archer, L. A. *Adv. Electron. Mater.* **2015**, *2*, 1500246(1–6).
- (12) Lu, Y.; Tu, Z.; Archer, L. A. *Nat. Mater.* **2014**, *13* (October), 961–969.
- (13) Pires, J.; Timperman, L.; Castets, A.; Santos-pena, J.; Dumont, E.; Levasseur, S.;

- Dedryvere, R.; Tessier, C.; Anouti, M. *RSC Adv.* **2015**, *5*, 42088–42094.
- (14) Li, B.; Xu, M.; Li, T.; Li, W.; Hu, S. *Electrochem. commun.* **2012**, *17*, 92–95.
- (15) Etacheri, V.; Haik, O.; Goffer, Y.; Roberts, G. a.; Stefan, I. C.; Fasching, R.; Aurbach, D. *Langmuir* **2012**, *28* (1), 965–976.
- (16) Miao, R.; Yang, J.; Feng, X.; Jia, H.; Wang, J.; Nuli, Y. *J. Power Sources* **2014**, *271*, 291–297.
- (17) Luo, W.; Zhou, L.; Fu, K.; Yang, Z.; Wan, J.; Manno, M.; Yao, Y.; Zhu, H.; Yang, B.; Hu, L. *Nano Lett.* **2015**, *15*(9), 6149–6154.
- (18) Liang, Z.; Zheng, G.; Liu, C.; Liu, N.; Li, W.; Yan, K.; Yao, H.; Hsu, P.-C.; Chu, S.; Cui, Y. *Nano Lett.* **2015**, *15*(5), 2910–2916.
- (19) Lu, Y.; Tikekar, M.; Mohanty, R.; Hendrickson, K.; Ma, L.; Archer, L. A. *Adv. Energy Mater.* **2015**, *5* (9), 1402073(1–7).
- (20) Schaefer, J. L.; Yanga, D. A.; Archer, L. A. *Chem. Mater.* **2013**, *25* (6), 834–839.
- (21) Ozhabes, Y.; Gunceler, D.; Arias, T. A. *arXiv* **2015**, *1504.05799*, 1–7.
- (22) Khurana, R.; Schaefer, J. L.; Archer, L. A.; Coates, G. W. *J. Am. Chem. Soc.* **2014**, *136* (20), 7395–7402.
- (23) Tu, Z.; Kambe, Y.; Lu, Y.; Archer, L. A. *Adv. Energy Mater.* **2014**, *4* (2), 1300654(1–6).
- (24) Gurevitch, I.; Buonsanti, R.; Teran, a. a.; Gludovatz, B.; Ritchie, R. O.; Cabana, J.; Balsara, N. P. *J. Electrochem. Soc.* **2013**, *160* (9), A1611–A1617.
- (25) Bouchet, R.; Maria, S.; Meziane, R.; Aboulaich, A.; Lienafa, L.; Bonnet, J.; Phan,

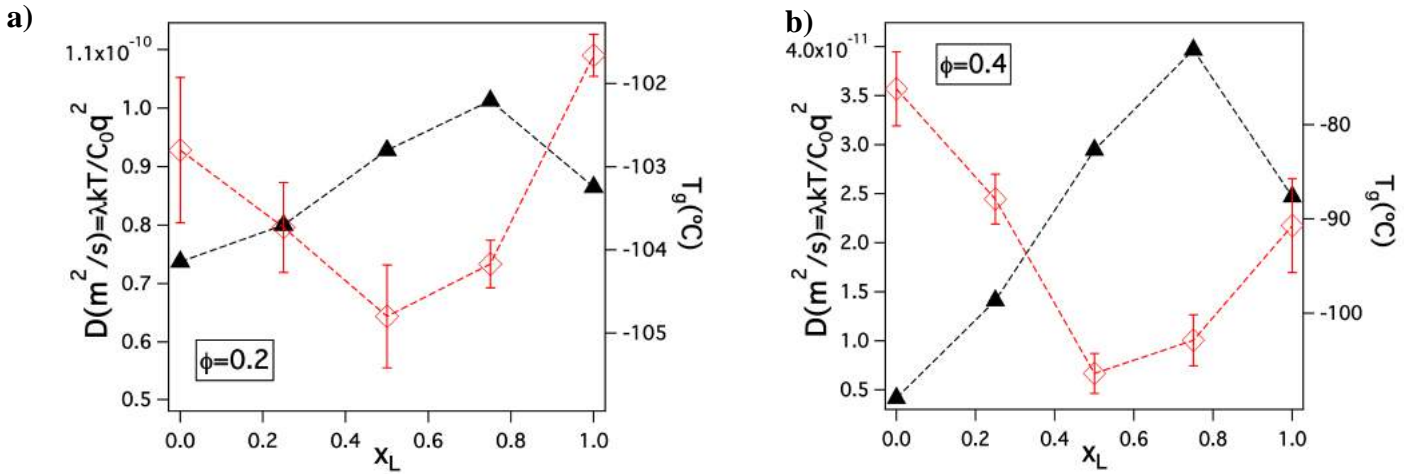
- T. N. T.; Bertin, D.; Gigmes, D.; Devaux, D.; Denoyel, R.; Armand, M. *Nat. Mater.* **2013**, *12* (5), 452–457.
- (26) Weston, J. E.; Steele, B. C. H. *Solid State Ionics* **1982**, *7*, 75–79.
- (27) Croce, F.; Scrosati, B. *Ann. N.Y. Acad. Sci.* **2003**, *984*, 194–207.
- (28) Agrawal, A.; Choudhury, S.; Archer, L. A. *RSC Adv.* **2015**, *5*, 20800–20809.
- (29) Srivastava, S.; Schaefer, J. L.; Yang, Z.; Tu, Z.; Archer, L. A. *Adv. Mater.* **2014**, *26* (2), 201–234.
- (30) Lu, Y.; Korf, K.; Kambe, Y.; Tu, Z.; Archer, L. A. *Angew. Chemie* **2014**, *126* (2), 498–502.
- (31) Lu, Y.; Das, S. K.; Moganty, S. S.; Archer, L. A. *Adv. Mater.* **2012**, *24* (32), 4430–4435.
- (32) Korf, K. S.; Lu, Y.; Kambe, Y.; Archer, L. A. *J. Mater. Chem. A* **2014**, *2* (30), 11866.
- (33) Nugent, J. L.; Moganty, S. S.; Archer, L. A. *Adv. Mater.* **2010**, *22* (33), 3677–3680.
- (34) Schaefer, J. L.; Moganty, S. S.; Yanga, D. A.; Archer, L. A. *J. Mater. Chem.* **2011**, *21* (27), 10094–10102.
- (35) Zhang, Q.; Archer, L. A. *Langmuir* **2002**, *18* (26), 10435–10442.
- (36) Moganty, S. S.; Jayaprakash, N.; Nugent, J. L.; Shen, J.; Archer, L. A. *Angew. Chemie* **2010**, *122* (48), 9344–9347.
- (37) Hussain, F. J. *Compos. Mater.* **2006**, *40* (17), 1511–1575.

- (38) Palmqvist, A. E. C. *Curr. Opin. Colloid Interface Sci.* **2003**, 8, 145–155.
- (39) Balazs, A. C.; Emrick, T.; Russell, T. P. *Science (80-.)*. **2006**, 314 (5802), 1107–1110.
- (40) Mangal, R.; Srivastava, S.; Archer, L. A. *Nat. Commun.* **2015**, 6:7198, 1–9.
- (41) Green, D. L.; Mewis, J. *Langmuir* **2006**, 22 (18), 9546–9553.
- (42) Srivastava, S.; Agarwal, P.; Archer, L. A. *Langmuir* **2012**, 28 (15), 6276–6281.
- (43) McEwan, M.; Green, D. *Soft Matter* **2009**, 5 (8), 1705–1716.
- (44) Dutta, N.; Green, D. *Langmuir* **2008**, 24 (10), 5260–5269.
- (45) Lindenblatt, G.; Schärfl, W.; Pakula, T.; Schmidt, M. *Macromolecules* **2001**, 34 (6), 1730–1736.
- (46) Oh, H.; Green, P. F. *Nat. Mater.* **2009**, 8 (2), 139–143.
- (47) Meng, D.; Kumar, S. K.; D. Lane, J. M.; Grest, G. S. *Soft Matter* **2012**, 8 (18), 5002–5010.
- (48) Ohno, K.; Morinaga, T.; Takeno, S.; Tsujii, Y.; Fukuda, T. *Macromolecules* **2007**, 40 (25), 9143–9150.
- (49) Glatter, O.; Kratky, O. *Small Angle X-ray Scattering*, United Sta.; Academic Press: New York, 1982.
- (50) Zaccarelli, E.; Mayer, C.; Asteriadi, A.; Likos, C.; Sciortino, F.; Roovers, J.; Iatrou, H.; Hadjichristidis, N.; Tartaglia, P.; Löwen, H.; Vlassopoulos, D. *Phys. Rev. Lett.* **2005**, 95 (26), 268301(1–4).
- (51) Mayer, C.; Zaccarelli, E.; Stiakakis, E.; Likos, C. N.; Sciortino, F.; Munam, a;

- Gauthier, M.; Hadjichristidis, N.; Iatrou, H.; Tartaglia, P.; Löwen, H.; Vlassopoulos, D. *Nat. Mater.* **2008**, *7* (10), 780–784.
- (52) Agrawal, A.; Yu, H.-Y.; Srivastava, S.; Choudhury, S.; Narayanan, S.; Archer, L. *A. Soft Matter* **2015**, *11*, 5224–5234.
- (53) Ashcroft, N. W.; Langreth, D. C. *Phys. Rev.* **1967**, *16* (3), 685–692.
- (54) Srivastava, S.; Shin, J. H.; Archer, L. *A. Soft Matter* **2012**, *8* (15), 4097–4108.
- (55) Yu, H.-Y.; Srivastava, S.; Archer, L. A.; Koch, D. L. *Soft Matter* **2014**, *10* (45), 9120–9135.
- (56) Choudhury, S.; Agrawal, A.; Kim, S. A.; Archer, L. A. *Langmuir* **2015**, *31*, 3222–3231.
- (57) Qu, D.; Qu, D.; Shi, H.; Shi, H. *J. Power Sources* **1998**, *74*, 99–107.
- (58) Shi, H. *Electrochim. Acta* **1996**, *41* (95), 1633–1639.
- (59) Choi, N. S.; Chen, Z.; Freunberger, S. a.; Ji, X.; Sun, Y. K.; Amine, K.; Yushin, G.; Nazar, L. F.; Cho, J.; Bruce, P. G. *Angew. Chemie - Int. Ed.* **2012**, *51* (40), 9994–10024.
- (60) Flandrois, S.; Simon, B. *Carbon N. Y.* **1999**, *37* (2), 165–180.
- (61) Shiraishi, S.; Kurihara, H.; Tsubota, H.; Oya, A.; Soneda, Y.; Yamada, Y. *Electrochem. Solid-State Lett.* **2001**, *4* (1), A5–A8.
- (62) Largeot, C.; Portet, C.; Chmiola, J.; Taberna, P. L.; Gogotsi, Y.; Simon, P. *J. Am. Chem. Soc.* **2008**, *130* (9), 2730–2731.
- (63) Lanfredi, S.; Rodrigues, A. C. M. *J. Appl. Phys.* **1999**, *86* (4), 2215–2219.

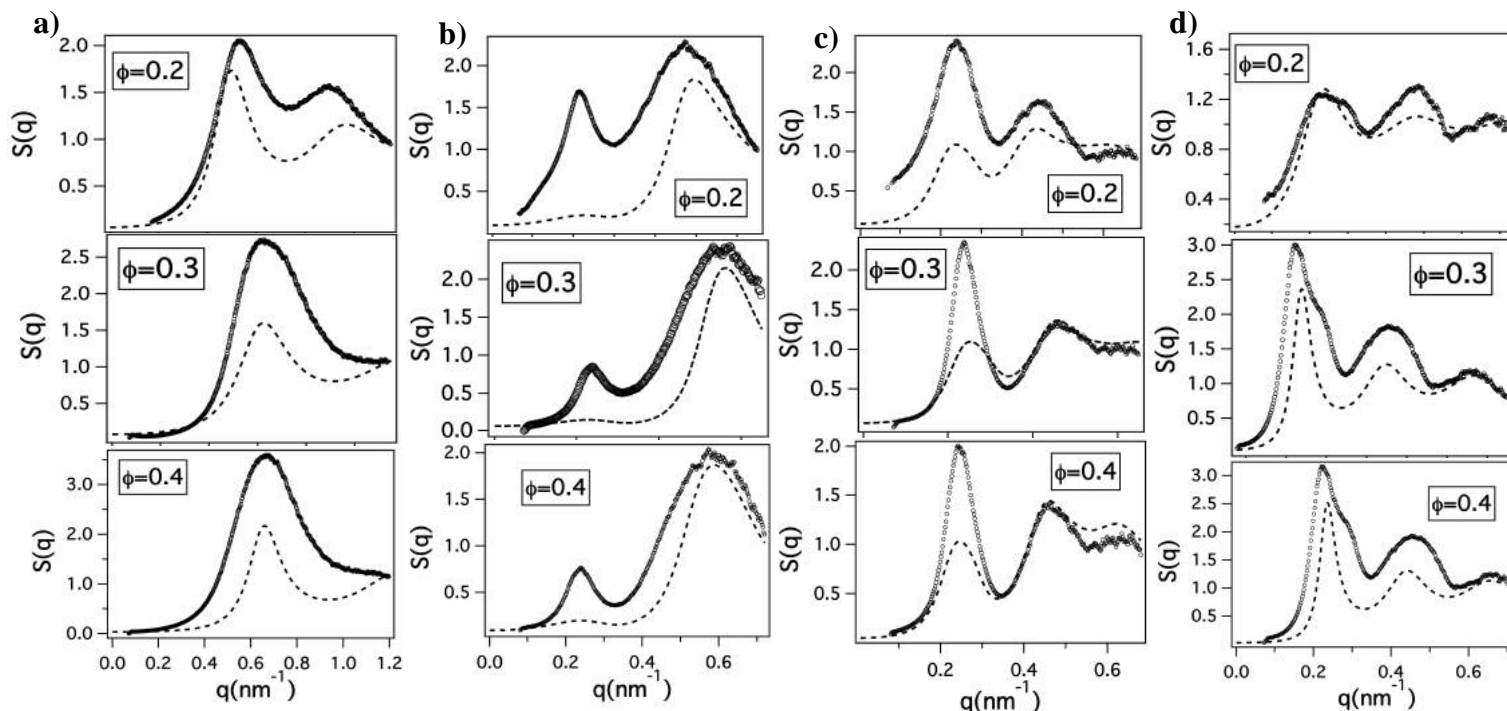
- (64) Payne, R.; Theodorou, I. E. *J. Phys. Chem.* **1972**, 76 (20), 2892–2900.
- (65) Simeral, L.; Ameyib, R. L.; Amey, L. *J. Phys. Chem.* **1970**, 74 (7), 1968–1971.
- (66) Sengwa, R. J.; Kaur, K.; Chaudhary, R. *Polym Int.* **2000**, 608 (January), 599–608.
- (67) Schneider, U.; Lunkenheimer, P.; Brand, R.; Loidl, a. *Phys. Rev. E. Stat. Phys. Plasmas. Fluids. Relat. Interdiscip. Topics* **1999**, 59 (6), 6924–6936.
- (68) Bruce, P. *Solid State Ionics* **1988**, 28-30, 918–922.
- (69) Appetecchi, G. B.; Dautzenberg, G.; Scrosati, B. *J. Electrochem. Soc.* **1996**, 143 (1), 6–12.
- (70) Jorne, J. *Nano Lett.* **2006**, 6 (12), 2973–2976.
- (71) Capuano, F.; Croce, F.; Scrosati, B. *J. Electrochem. Soc.* **2003**, 203 (7), 197–203.
- (72) Ding, F.; Xu, W.; Graff, G. L.; Zhang, J.; Sushko, M. L.; Chen, X.; Shao, Y.; Engelhard, M. H.; Nie, Z.; Xiao, J.; Liu, X.; Sushko, P. V.; Liu, J.; Zhang, J.-G. *J. Am. Chem. Soc.* **2013**, 135 (11), 4450–4456.
- (73) Jonscher, A. K. *Nature* **1977**, 267, 673–679.

1. Diffusivity and Glass Transition Variation:

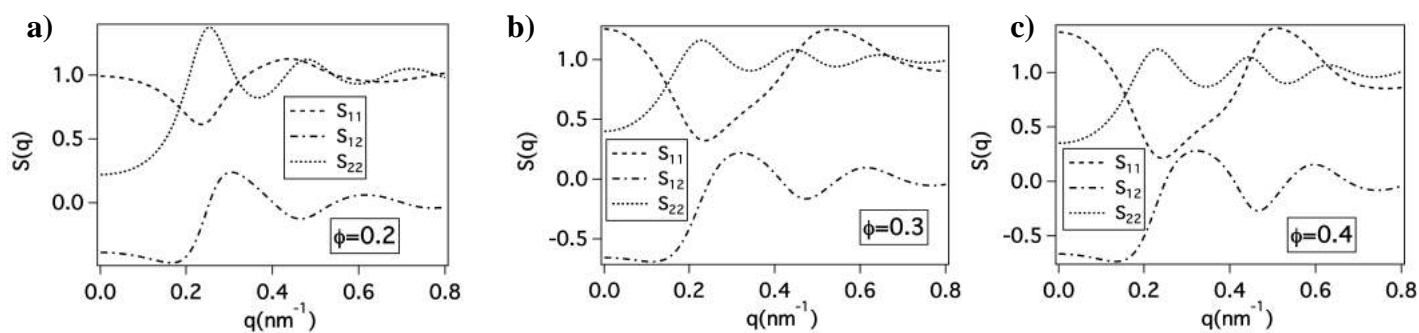


Supplementary figure 5.1 Variation of glass transition temperature (open symbols) and diffusivity (close symbols) as a function of fraction of larger particles x_L , for core volume fraction **a)** $\phi=0.2$ and **b)** $\phi=0.4$. The dashed lines are guide to eye.

2. Structure Factor Analysis:

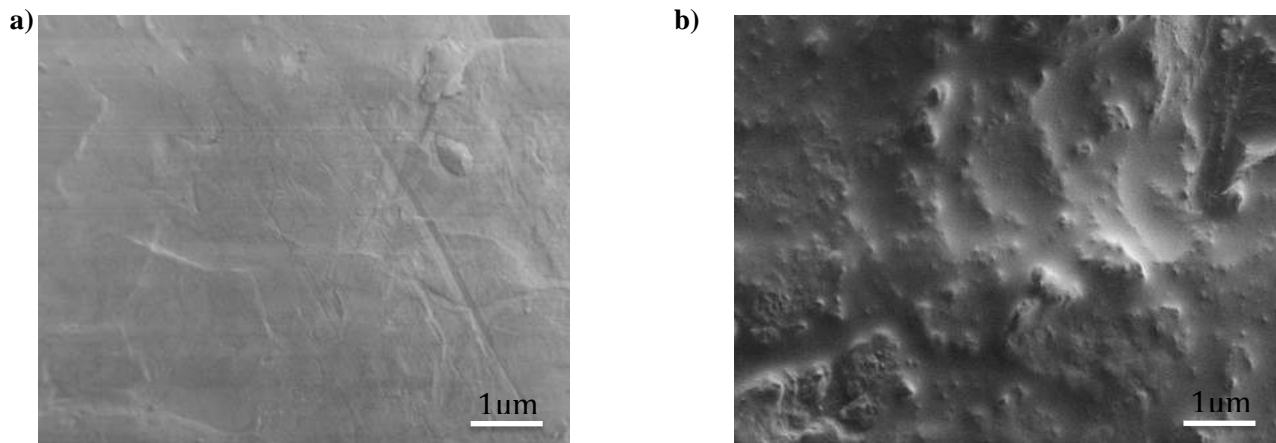


Supplementary figure 5.2 Evolution of structure factor $S(q)$ as a function of the wave vector q at volume fractions $\Phi=0.2$, 0.3 and 0.4 for **a)** $x_L=0$, **b)** $x_L=0.25$, **c)** $x_L=0.75$, and **d)** $x_L=1$. The open symbols are experimental values and the dashed lines are fit to experimental $S(q)$ using binary Hard Sphere model.



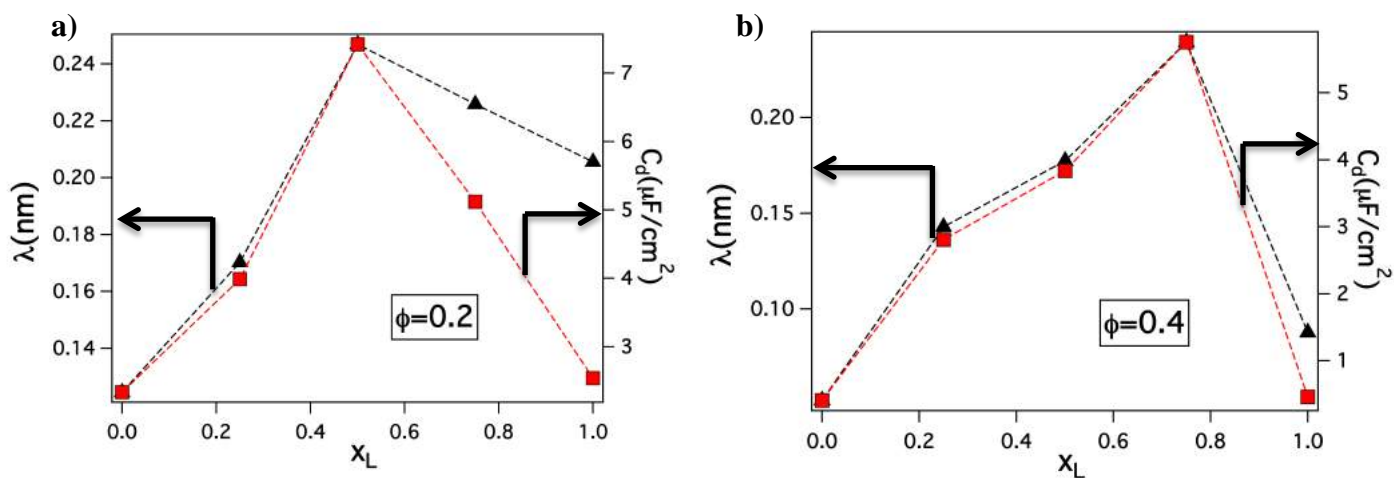
Supplementary figure 5.3 Variation in three components of structure factor viz., S_{11} , S_{12} , and S_{22} as estimated from Binary Hard Sphere model predictions. Here, 1 and 2 indicate smaller and larger particles respectively. The structure factors are shown for $x_L=0.5$ for different volume fraction **a)** $\phi=0.2$, **b)** $\phi=0.3$, and **c)** $\phi=0.4$.

3. SEM with Neat PC Electrolyte:



Supplementary figure 5.4 Scanning Electron Micrographs (SEM) of **a)** Pristine lithium electrode before cycling and **b)** after 10 cycles with neat PC electrolyte. The scale bar for both the images is 1 μm.

4. Electrical Double layer and Capacitance:



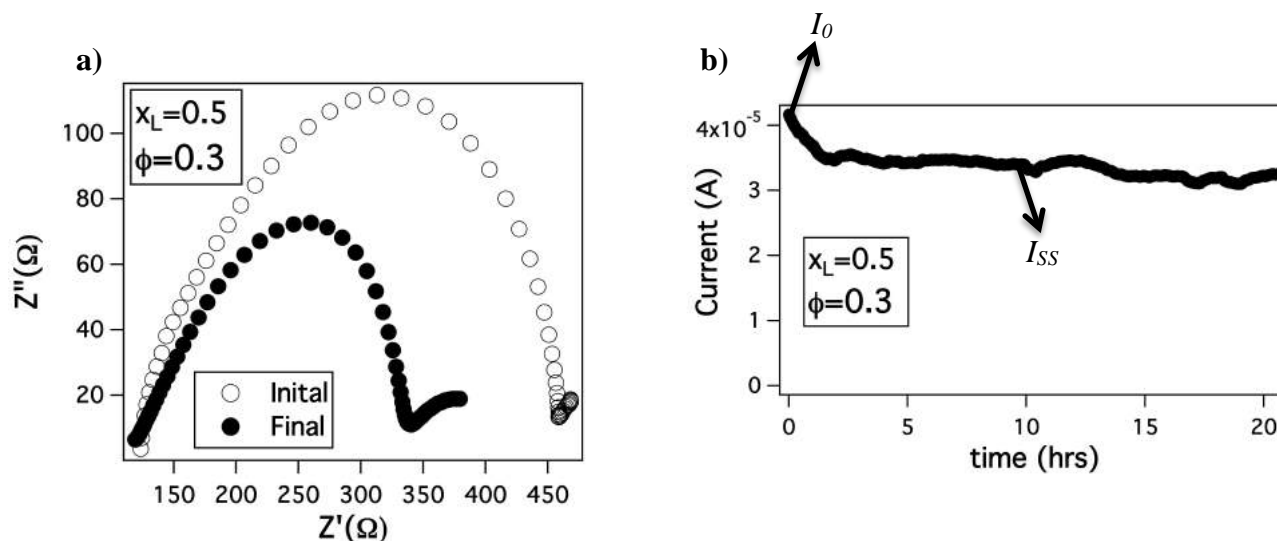
Supplementary figure 5.5 Electrical double layer (square symbols) and electrochemical capacitance (triangle symbols) for different values of x_L at **a)** $\phi=0.2$ and **b)** $\phi=0.4$

5. Lithium transference number estimation:

Lithium transference number was determined by using the method proposed by Bruce^[i] and Scrosati^[ii] using a symmetric lithium metal cell with hybrid electrolyte for $\phi=0.3$ at $x_L=0.5$. As described in the method, the transference number was determined using the following formula:

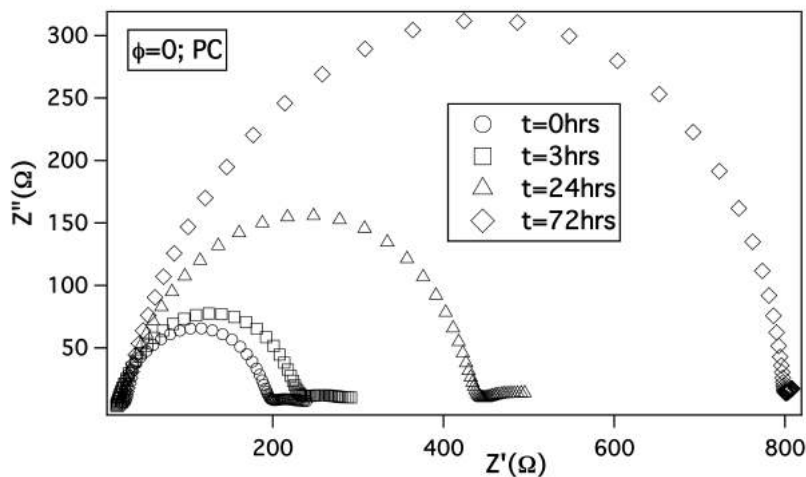
$$t_{Li}^+ = \frac{I_{SS}(\Delta V - I_0 R_0)}{I_0(\Delta V - I_{SS} R_{SS})}$$

Where, I_0 and I_{SS} are the initial and steady state current as determined for a cell undergoing polarization, and R_0 and R_{ss} are the initial and final interfacial resistances as determined from electrochemical impedance measurements. ΔV is the polarization potential, 20mV.



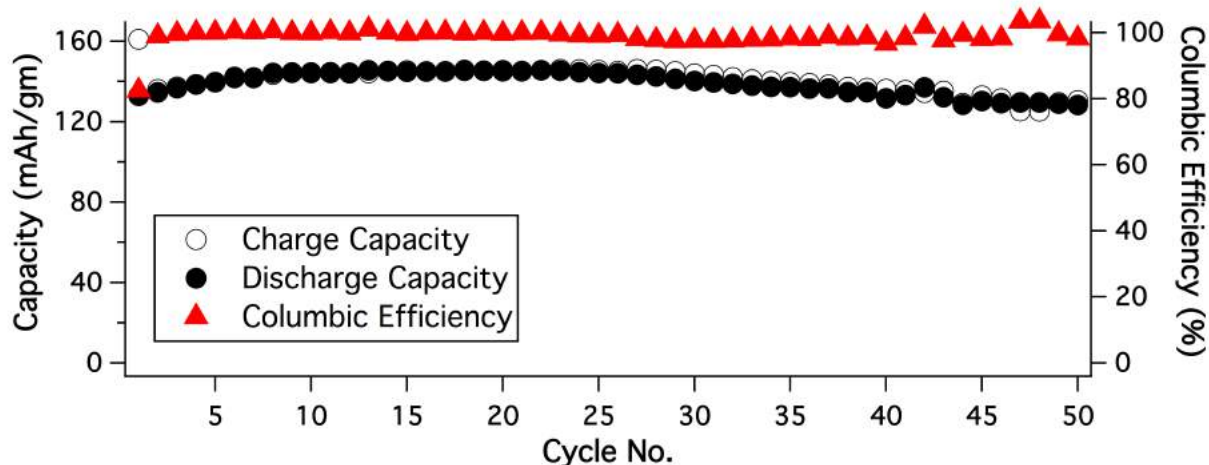
Supplementary figure 5.6 a) Electrochemical impedance measurements for a symmetric lithium cell before polarization (open symbols) and after steady state is reached (closed symbols). R_0 and R_{ss} were determined by fitting these impedances to the circuit model mentioned in the main text. b) Current decay for the cell undergoing polarization at 20mV potential. I_0 and I_{SS} were used in the calculations as observed in the plot.

6. Impedance with time for neat PC electrolyte:



Supplementary figure 5.7 Evolution of impedance spectra with time for a symmetric cell with neat PC electrolyte. It can be observed that within a span of 72 hours, the interfacial resistance increases significantly for the neat electrolyte as opposed to hybrid particle electrolyte, where the spectra remains almost the same over a time span of 1440 hours.

7. Columbic efficiency and capacity for the Li/LiFePO₄ half-cell:



Supplementary figure 5.8 Charge-Discharge capacity (black open-closed circles) and columbic efficiency (red closed triangles) for the Li/LiFePO₄ half-cell over 50 cycles.

Supplementary Information References:

- (i) Bruce, P.; Evans, J.; Vincent, C.A. Conductivity and Transference Number Measurements on Polymer Electrolytes. *Solid State Ionics* **1988**, 28-30, 918–922.
- (ii) Appetecchi, G. B.; Dautzenberg G.; Scrosati B. A New Class of Advanced Polymer Electrolytes and Their Relevance in Plastic-Like, Rechargeable Lithium Batteries. *J. Electrochem. Soc.* **1996**, 143, 6.

Chapter 6

Molecular Origins of Temperature Induced Jamming in Self-Suspended Hairy Nanoparticles

6.1 Abstract

Suspensions of solvent-less, polymer-grafted nanoparticles have previously been reported to exhibit enhanced glassy dynamics and jamming as temperature is increased. This so called thermal jamming behavior is not predicted by current models for soft glassy materials and is opposite to what is normally observed for polymer melts. Here we report results from a detailed study of structural, dynamical, and rheological transitions in solvent-less silica-polyethylene glycol methyl ether (SiO₂-PEGME) hybrid particles aimed at understanding the molecular origins of the phenomenon. We find that interdigitated PEGME corona chains enforce coupling between SiO₂ cores analogous to crosslinks in associating polymer networks leading to elastic behavior at low strains and small deformation rates. Pullout and slippage of inter-digitated corona chains leads to yielding of the materials in nonlinear shear flow and stretched exponential relaxation following small amplitude step shear. We show with the help of small-angle x-ray scattering, density functional theoretical calculations, and a constitutive model for deformation and flow of physically associating polymer networks that thermal jamming of solvent-less polymer-grafted nanoparticles originates from enhanced cross-linking of the cores produced by increased stretching and inter-digitation of particle-tethered polymer molecules as temperature increases.

6.2 Introduction

Jamming and yielding transitions in soft glassy materials such as foams, emulsions, and colloidal suspensions have been studied extensively over the past few decades, both theoretically and experimentally.¹⁻⁶ These complex, soft materials all undergo a transition to a solid-like, glassy state that is a sensitive function of concentration, shear stress, and

temperature.^{7,8} Many characteristics of this transition are captured well in the “jamming phase diagram” proposed by Liu and Nagel, which among other features shows that a decrease in temperature at constant density induces a solid-like material response.⁸ Recent experimental results for a specific class of complex materials, including multi-arm star polymers^{9,10}, block copolymer micelles¹¹, and solvent-less polymer tethered nanoparticles¹²⁻¹⁴— all formed by tethering polymer arms to a common core or branch point — show that in some cases temperature can have an effect opposite to that imagined in the Liu-Nagel diagram. Instead of exhibiting more fluid-like rheological response upon heating, materials in this group appear to become more solid-like/jammed when temperature rises, leading to the terminology *thermal jamming* to describe the enhanced elasticity observed upon increasing temperature. For multi-arm star polymers, thermal jamming has been attributed to reduced solvent quality upon heating and to the formation of clusters, which manifest as a partially dynamically arrested phase.^{9,11,15} Small-angle x-ray scattering (SAXS) experiments in solvent-less SiO₂-polymer particles in contrast show no noticeable changes with increased temperature, and the structure factor $S(q)$ deduced from these experiments exhibit very little sensitivity to temperature,^{12,13} indicating that thermal jamming in such materials occurs in the absence of any obvious structural changes. The absence of structural transformation in solvent-less SiO₂-polymer particles upon increasing temperature is nevertheless intuitive to an extent - the absence of a suspending medium in such materials means that polymer chains tethered to particles are subject to a “space-filling” constraint, which suppresses long-wavelength density fluctuations.¹⁶ However, the fact that thermal jamming in the

materials occurs without a change in morphology or structure means that the phenomena has its origins on smaller length scales than probed by SAXS.

Several previous reports have discussed the structure and rheology of solvent-less SiO₂-polymer suspensions and shed light on how the space-filling requirement on tethered polymer chains (corona) may simultaneously improve phase stability of the materials and lead to glassy solid-like rheology.¹⁷⁻¹⁹ These studies have also motivated theoretical work, which shows that short polymer chains densely grafted to small particles are effective at stabilizing these particles in the solvent-free state because the tethered polymers provide strong steric stabilization that prevents close approach of the cores.^{20,21} Additionally, because the absence of solvent space filling requires that the corona chains uniformly fill the inter-particle space, long wavelength density fluctuations are completely suppressed in the monodisperse case, which drives hyperuniformity of the particle cores and prevents formation of phase separated morphologies.^{16,20,21} Density functional theory and simulation studies in fact show that the materials are analogous to incompressible molecular fluids, wherein each nanoparticle core carries a share of fluid with itself, excluding exactly one neighboring particle.^{16,23-25} This feature also make the materials analogous to a model single component fluid, which allows one to study the role of temperature on interaction, structure and dynamics of the two components without the complications arising from temperature-dependent enthalpic interactions between the solvent and particles.^{12,23,26}

Previous dynamical and mechanical rheological studies on solvent-less SiO₂-polymer materials have shown that the core size²⁷, corona molecular weight^{14,28} and the grafting density of corona chains^{13,14,29} play synergistic roles in influencing their jamming and

yielding behaviors. It has been observed for example that at higher corona polymer grafting densities and molecular weights, the materials are more fluid-like and exhibit no or weakly elastic behavior. Under these conditions the influence of the cores is less important and corona chains can easily meet the space filling constraint while maintaining random-coil, melt-like chain configurations. In contrast, a more sparsely grafted corona comprised of short chains (in comparison to the inter-particle distance) must stretch to fill space, which produces a more solid-like material response to deformation. It is thought that these differences also affect the extent to which corona chains on neighboring cores inter-penetrate, meaning that the enhanced elasticity observed when the materials jam is analogous to what might be observed in an associating polymer.³⁰⁻³² This perspective is supported by recent experimental work on solvent-less SiO₂-polymer particles comprised of a bi-disperse distribution of cores. These studies clearly show that at the same overall concentration of SiO₂ cores, differences in curvature of the cores produced by large differences in sizes of the small and large particles in the distribution can by itself completely unjam an otherwise jammed material by reducing the degree of corona inter-penetration.²⁷

In this article we examine the effect of temperature on corona-corona inter-penetration at the molecular level and subsequently study its effect on the jamming behavior of solvent-less SiO₂-polymer particles. We focus on a single system comprised of silica nanoparticles (SiO₂) grafted with polyethylene glycol methyl ether (PEGME) chains and employ small-angle x-ray scattering, oscillatory shear and steady-shear startup rheology measurements to characterize thermal behaviors. Comparison of the experimentally measured structure factors with predictions from DFT analysis show that the tethered

PEG chains adopt more extended conformations at elevated temperature. On the basis of shear start-up experiments, we identify an analogy between the physical behaviors of interacting corona chains in SiO₂-PEGME and those of network strands in physically associating cross-linked polymer gels.³⁰ Specifically, we show that the soft-glassy rheology of solvent-less SiO₂-PEGME materials can be attributed to physical linkages between corona chains on adjacent particles as the chains stretch to uniformly fill space, which arrest long-range dynamics of the corona and core in an analogous fashion to cross-links in a rubbery polymer network. We take the analogy several steps further to show how the experimental stress-strain rheological response, including its dependence on temperature can be qualitatively captured by existing constitutive models for physically cross-linked gels.³⁰

6.3 Experimental Methods

6.3.1 Synthesis

Silica nanoparticles with diameter 10±2nm (Ludox SM-30, Sigma Aldrich) were grafted by covalent attachment of silane terminated Polyethylene glycol methyl ether (PEGME, MW~5000g/mol, Laysan Bio), using a previously described synthesis procedure.¹³ Following the synthesis, the hairy SiO₂-PEGME nanoparticles were purified by repeated centrifugation at 8500rpm for 12min using chloroform (solvent)-hexane (non-solvent) mixtures to ensure removal of unattached PEGME chains.^{19,33} The purified particles were subsequently dried in a convection oven at 60°C overnight and annealed in vacuum for 48 hours to ensure complete evaporation of solvent and to remove any residual strain in the materials. The grafting density of PEGME chains on the SiO₂ nanoparticle cores was

determined from analysis of the residual inorganic content determined by thermal gravimetric analysis (TGA, TA instruments Q500). It was found to be $\Sigma \approx 1.03$ chains/nm², such that the overall SiO₂ core volume fraction of the materials is maintained at $\phi=0.20$.

6.3.2 Small Angle X-ray Scattering (SAXS) measurements

Small Angle X-ray Scattering (SAXS) measurements were performed on the solvent-less SiO₂-PEGME nanoparticles at sector 12-ID-B of Argonne National Laboratory, using a point collimated x-ray beam. The sample was smeared on a thermal cell and the measurements were performed at different temperatures, all above melting point of PEG. The x-ray scattered intensity ($I(q,\phi,D)$) was measured as a function of the wave vector q , and can be related to the particle form factor $P(q,D)$ and structure factor $S(q,\phi,D)$ using the following expressions,³⁴

$$I(q,\phi,D) = \phi \Delta\rho_e V P(q,D) S(q,\phi,D) \quad (1)$$

Here, V and $\Delta\rho_e$ are the volume of a single particle core, and electron density contrast between the particle and the surrounding medium, respectively; ϕ and D are the core volume fraction and particle diameter. In the limit of infinite dilution, $S(q,\phi \rightarrow 0,D) \sim 1$ and the form factor can be obtained under this condition. SAXS measurements on a diluted aqueous solution of charge stabilized silica nanoparticles were performed to obtain the form factor used for this analysis.³⁵ The structure factor for the self-suspended SiO₂-PEGME hairy nanoparticles was obtained by dividing the measured $I(q,\phi,D)$ with the measured $P(q,D)$ from the diluted suspensions.

6.3.3 Rheology measurements

Oscillatory shear rheology measurements were performed at different temperatures ranging from 70°C to 120°C using a Physica MCR501 rheometer (Anton Paar) outfitted with a cone and plate geometry (10mm diameter, 2° cone angle). To study the linear and non-linear viscoelastic properties of the materials, variable strain amplitude measurements at a fixed angular frequency of $\omega=10$ rad/s as well as variable frequency measurements at a fixed strain amplitude $\gamma=0.5\%$, were employed. These measurements were used in conjunction with temperature-dependent small-amplitude step strain measurements to completely characterize the relaxation dynamics of the SiO₂-PEGME material. Step strain measurements were performed at a fixed strain of $\gamma=2\%$, which was confirmed to be well within the linear viscoelastic regime for the materials at all temperatures studied, and the stress relaxation was tracked over a time period of 10⁴ seconds. Prior to each measurement, material samples were pre-sheared using large-amplitude oscillatory shear deformations at shear strains above the yield strain at each temperature, and the deformations repeated until the strain-dependent storage and loss moduli data deduced from multiple back-to-back experiments were the same. Shear startup and flow cessation measurements were performed using a strain controlled ARES-LS rheometer (Rheometric Scientific) outfitted with cone and plate geometry (10mm diameter, 4° cone angle). The shear-startup experiments were carried out at a shear rate of 0.01s⁻¹ at every temperature. Prior to each measurement, samples were pre-sheared using the large amplitude oscillatory shear procedure described earlier.

6.4 Results and Discussion

Linear and Non-linear Temperature-Dependent Viscoelastic Behavior-

When subjected to oscillatory shear flow, the self-suspended SiO₂-PEGME nanoparticles exhibit rheological response characteristic of soft glassy materials. As can be observed from the inset of Figure 1a), for low shear strain values both the storage (G') and the loss modulus (G'') are independent of strain, and this regime corresponds to the linear viscoelastic regime of the material. Upon further increase in strain, a telltale maximum in G'' is observed, after which the material enters into a strain softening regime, and G'' becomes larger than G' . The maximum in G'' at intermediate strain is a feature of soft glassy materials such as foams, emulsions, star polymers and also of physically associating gels.^{19,36-41} In soft glasses, the maximum is thought to reflect the onset of cage breakage that facilitate relaxation of dynamically arrested particles. In physically associating gels, it is attributed to the pulling out of cross-linked chains or “bridges” from the aggregates to which they are connected.³¹ For materials in either class, the height of the loss maximum in G'' normalized by its linear response value is an indication of the amount of energy dissipated on release of the arrested materials.

It can be observed from Figure 6.1a) that the relative size of the loss maximum i.e. $G''/G''_{\gamma \rightarrow 0}$ increases with temperature, and the strain at which the maximum occurs reduces with the increase in temperature. This implies that with the increase in temperature the material becomes more jammed. A similar behavior has been reported earlier for self-suspended hairy nanoparticles with different corona chemistries, molecular weights and grafting densities.¹²⁻¹⁴ In previous studies, this temperature dependent behavior was found to be completely reversible.¹² To further quantify this effect, one can estimate the amount of energy dissipated per unit volume, U_d in this yielding event at each

temperature. Using a previously defined procedure^{27,42}, the loss maximum is fitted to a lognormal functional form and the amount of energy dissipated estimated as-

$$U_d \sim \int G''(\gamma) \gamma d\gamma \quad (2)$$

The dissipated energy U_d is reported in Figure 6.1b) and is seen to increase with temperature. This implies that a larger amount of energy is dissipated when the materials yield at higher temperatures, suggesting that the hairy nanoparticles are more strongly arrested/jammed as the temperature is increased. This *thermal jamming* behavior is also observed in the linear elastic regime where it manifests as an increase in the rubber-like shear modulus, G_e , of the materials in the low strain rheology (inset of Figure 6.1c)). Here G_e is estimated from the linear viscoelastic regime, observed in the frequency dependent oscillatory shear measurements (Supplementary figure 6.1). The increase in G' with temperature is also accompanied by a decrease in the loss tangent $\tan\delta = G''/G'$ of the materials in the linear regime (Supplementary figure 6.2). These observations again agree with previous reports that solvent-less SiO₂-polymer composites become more solid-like with increase in temperature. The thermal jamming phenomenon observed here bears resemblance to reversible thermal vitrification observed in star polymers. In case of star polymers it is found that an increase in temperature improves the solvent quality, as a result of which the polymer chains tend to swell and in order to maintain the incompressibility of the material the polymer chains begin to overlap more with an increase in temperature. This leads to formation of clusters and vitrification of the star polymers, which eventually leads to a jammed state.^{11,15} In the presently studied self-suspended hairy nanoparticles, the absence of a solvent imposes a constraint on the corona chains to uniformly fill the space as a result of which we do not observe the

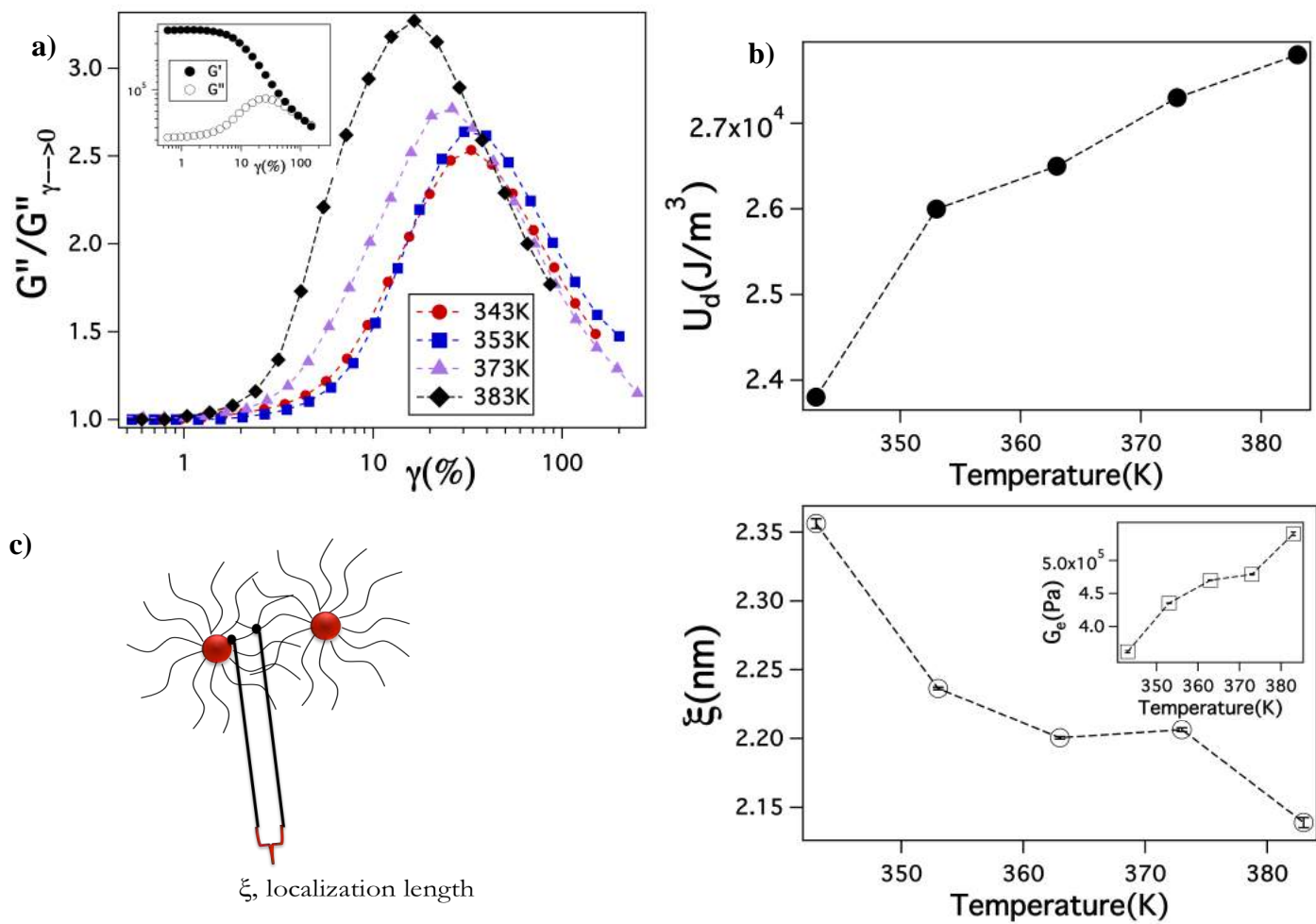


Figure 6.1 a) The maximum in normalized loss modulus, $G''/G''_{\gamma \rightarrow 0}$ (closed symbols) increases with increase in temperature. The dashed lines are lognormal fits to the modulus. Inset shows a typical oscillatory shear amplitude sweep response for the self-suspended hairy nanoparticles at $\omega=10$ rad/s. b) Energy dissipated per unit volume, U_d , in yielding the material, as calculated from area under the loss modulus peak. U_d is seen to increase with increase in temperature, indicating jamming of the material with temperature c) Illustration of localization length, ξ between two interacting hairy nanoparticles. ξ is shown to decrease with an increase in temperature. Inset shows the variation in plateau storage modulus, G_e with temperature, which is used to obtain ξ .

formation of any inhomogeneities or clusters, as shown further in SAXS measurements and in previous studies.^{12,14,43} Furthermore, since the suspending medium and the suspending phase are the same in the present case, this excludes the possibility of formation of any enthalpic driven cluster formation.

Previous studies on solvent-less hairy nanoparticles have speculated that a stronger loss maximum peak or higher values of plateau modulus are related to an enhanced degree of inter-digitation of the corona chains.^{12,13} As illustrated in Figure 6.1c), this mechanism bears analogies to reinforcing processes in physically cross-linked networks, where the points of inter-digitation of the corona chains can be thought of as physical net points that cross-link the elements in the material. We take this insight forward and estimate an effective “localization length”, $\xi = (k_B T / G_e)^{1/3}$, for these physical cross-links of corona chains.^{32,44} Results in Figure 6.1c) shows that ξ decreases as the temperature is increased. We will show later that SAXS measurements reveal no analogous change in the particle surface-to surface distance, which implies that temperature must produce greater interpenetration of the corona which results from enhanced stretching of the particle-tethered polymer chains. As the corona chains stretch and interpenetrate more, the net points between particles move closer to the particle surface (as illustrated in Figure 6.2e)), leading to a decrease in ξ . Analogous to an associating polymer network, where the yield strain is found to decrease as the cross-linked strands assume a higher degree of stretching³¹, we also find that the SiO₂-PEGME particles exhibit a progressively lower yield strain with increasing temperature.

Structural Characteristics

To explore the effect of temperature on interactions of the SiO₂ cores, we performed SAXS measurements to investigate the temperature dependent structure factor and inter-particle spacing. Supplementary figure 6.3 shows the intensity $I(q)$ at different temperatures, and it can be observed that for all the temperatures studied, $I(q)$ remains independent of the wave vector, in the low q regime. This indicates that the particles remain well-dispersed and un-aggregated.^{33,34} Figure 6.2a) shows the experimental structure factor $S(q)$, obtained at different temperatures as a function of wave vector scaled with the particle radius a . It can be observed that irrespective of temperature, the first peak position of $S(q)$ remains fixed at $qa \sim 2.02$, which corresponds to a fixed inter-particle spacing of approximately 15.7nm. This indicates that the spacing between the particles is insensitive to the change in temperature within the experimental temperature range considered, suggesting that thermal jamming seen in the rheology measurements originates from the grafted corona chains.

The experimental $S(q)$ can be compared further with the density-functional theory (DFT) for self-suspended hairy particles.¹⁶ In order to capture the effect of temperature on the equilibrium structure of the SiO₂ cores, we employ the DFT presented in [24], where the particles are modeled as hard spheres and the polymer chains as bead-linear-spring oligomers tethered to the centers of the cores with the monomer-monomer interaction being described by the Lennard-Jones (LJ) pair potential. The DFT analysis is valid in the asymptotic limit of $R_g/a \gg 1$, where R_g is the radius of gyration of polymer, and the predicted radial distribution function for particles separated by a distance \mathbf{r} is expressed in the superposition form, $g(\mathbf{r}) = g_{\text{HS}}(\mathbf{r}) + h_f(\mathbf{r})$, where g_{HS} is the radial distribution function of the reference hard sphere system and h_f is the contribution from the weak-

field oligomeric fluid. The static structure factor is obtained by $S(q) = 1 + \rho_c \int [g(r)-1]e^{-iq \cdot r} dr$ with ρ_c being the core particle number density. To bring out the stronger effect due to oligomers in the experimental systems with $R_g/a = 0.54$, we apply the modification invoked in [20] by enforcing the excluded volume constraint and rescaling the oligomer contribution outside the hard core. Meanwhile, as shown in reference [20] we also assume that the first 2 monomers may be treated as the immobile part of the tethered oligomer brush that contributes to the effective hard core, which yields an effective core volume fraction, $\phi_{c,eff}=0.264$, which is about 30% higher than the value determined from TGA analysis discussed earlier. The modification and assumption have shown to be satisfactory and allow more direct comparisons with both molecular dynamics simulations and experiments.²⁰ The incompressibility condition of the oligomeric fluid is achieved when the dimensionless temperature $T^* = k_B T / \epsilon_{LJ} = 1$ [24], where ϵ_{LJ} is the LJ potential well, k_B is the Boltzmann constant, and T is temperature. We use the same basis by assuming that $T^*=1$ when $T=343K$ in experiment. Therefore, the temperature range studied roughly corresponds to $T^*=1 \sim 1.15$. Since the oligomer grafting density and R_g/a used in the experiment are similar to those considered in [24], we choose the same coarse-grained description and equilibrium properties of the oligomeric fluid as in reference [24] at $T^*=1$, which give $N_m=10$, $f=25$, and $\rho_b=0.774$, where N_m , f , and ρ_b are the number of monomers per chain, number of chains per core, and monomer fluid number density in the model. Motivated by the SAXS results, in the theoretical analysis we assume a fixed core volume fraction at the temperature range studied ($T^*=1 \sim 1.15$).

Figure 6.2b) presents the predicted structure factor for both self-suspended particles and hard spheres. Similar to the transitions seen in the experimental data, the first peak position remains fixed at $qa \sim 2.7$ at all the temperatures, indicating that the average inter-core distance remains the same. On Comparing Figure 6.2a) and b), it is also noteworthy, that both the DFT prediction and the experimental data show a higher first peak of $S(q)$ and a much lower $S(0)$ than the reference hard sphere suspension. These differences are now understood to be a fundamental consequence of the absence of a solvent in the self-suspended material, which imposes a space filling constraint on the tethered polymer chains. This constraint results in a strong corona chain mediated correlation between the particles as well as significantly suppresses large-scale particle density fluctuations compared with hard spheres.^{20,45} We note that the densely-grafted corona chains in these self-suspended nanoparticles yield much enhanced peaks in $S(q)$ while the systems still remain in a disordered phase, in contrast to single-component Lennard-Jones liquids which crystallize as $S > 2.85$.⁴⁶

Since the first peak height of the structure factor is a measure of the degree of inter-particle correlation, in experiment, an increase in peak height with temperature (Figure 6.2c)) indicates that the correlation amongst the core is stronger, which is consistent with the hypothesis of enhanced inter-penetration of corona chains at elevated temperature. As seen from Figure 6.2d), this behavior is qualitatively supported by theory, where $S(q_{\text{peak}})$, increases very modestly with increase in temperature. Moreover, the predicted root mean-square distance between the chain center of mass and the core center, $\langle R_{\text{cc}}^2 \rangle^{1/2}$ also

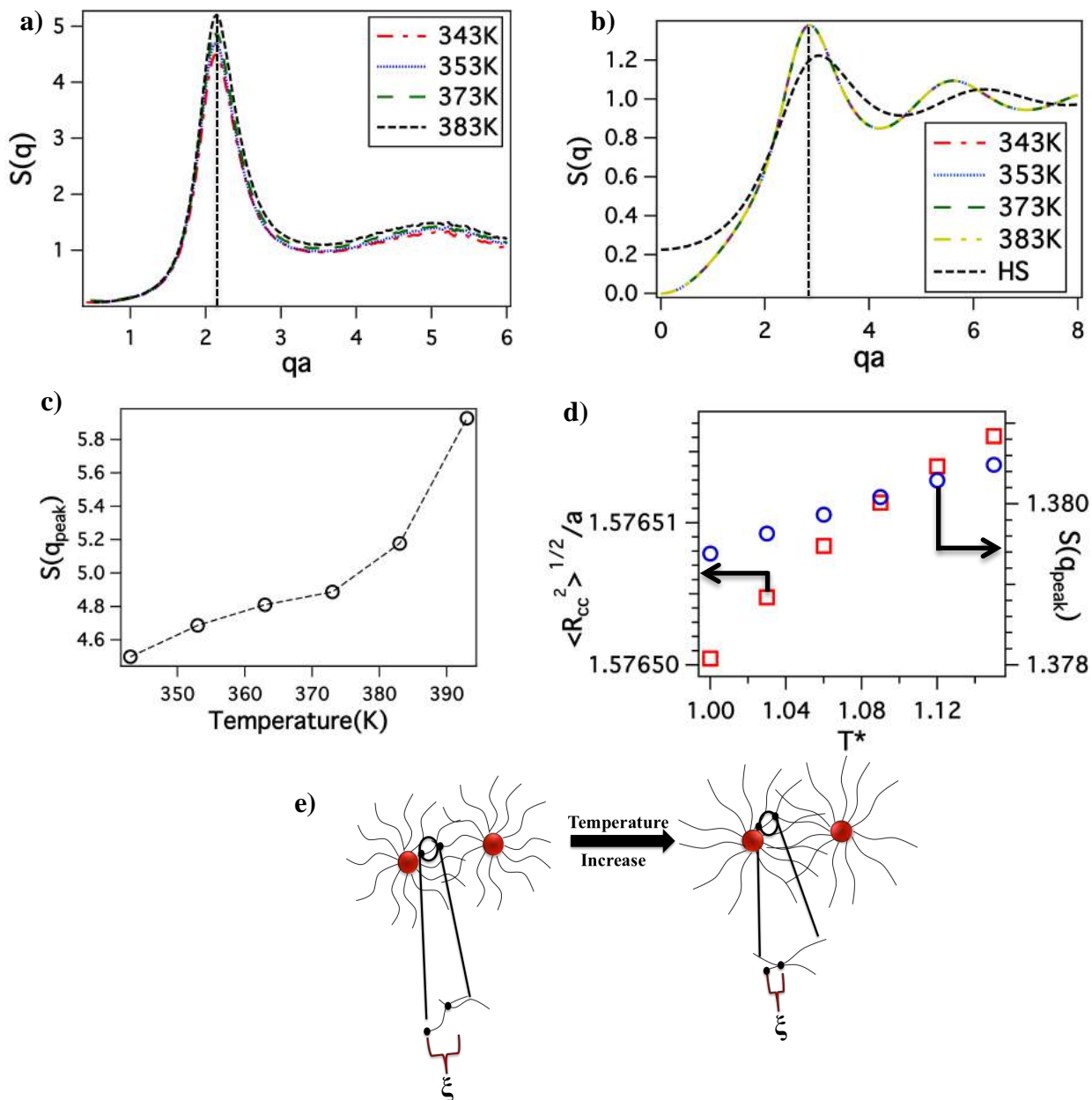


Figure 6.2 **a)** Evolution of structure factor $S(q)$ as a function of the wave vector, q at different temperatures. Irrespective of the temperature, the position of the first peak of $S(q)$ remains fixed. **b)** $S(q)$ as obtained from the prediction of DFT theory (colored lines), assuming a Lennard-Jones potential interaction between the corona chains, is compared with the result from HS theory (black dashed line). **c)** The peak height of the first peak in structure factor, $S(q_{\text{peak}})$ is seen to increase significantly with an increase in temperature. **d)** Comparisons of $S(q_{\text{peak}})$ (open circles) and root mean-square distance between the chain center of mass and the core, $\langle R_{\text{cc}}^2 \rangle^{1/2}$ (open squares), with scaled temperature T^* . **e)** Illustration showing the effect on the corona chains with temperature. The chains stretch more as the temperature increases, resulting in a higher degree of corona interpenetration.

increases modestly with an increase in temperature. Therefore, it could be argued that upon increasing temperature, the weakened monomer-monomer interactions relative to the thermal energy allow the polymers to explore more conformational space, thus making the polymer chains to extend more with temperature. This result also agrees with the trends observed in the localization length presented in Figure 6.1c) given a fixed core volume fraction (or fixed average inter-particle spacing). It should be noted that this thermal expansion mechanism would be different from typical star polymers in a solvent or from model self-suspended nanoparticles at very high temperatures considered in [24], where the chains expand due to an improved solvent condition which is absent in the presently examined self-suspended materials. The strong effects observed in experiments are however not captured by theory, and hence the increase seen in $S(q_{\text{peak}})$ and $\langle R_{\text{cc}}^2 \rangle^{1/2}$ are more modest than the measured values. We attribute these differences to two sources. First, in the current DFT for self-suspended SiO_2 -polymer particles, two monomer beads are assumed to be the part of the core at all temperatures. Depending on the actual temperature-dependent chain configurations, we anticipate that this number may change as the temperature is increased, since in general higher temperatures would lead to more stretched chain configurations. Second, although the polydispersity in grafting density and molecular weight of the corona chains is already known to play a significant role in corona-corona interaction of neighboring particles,²⁰ this effect is not considered in the present DFT analysis.

Temperature-dependent material relaxation behavior

To investigate the effect of temperature on the dynamics of SiO_2 -PEGME nanoparticles, we performed small amplitude step-strain relaxation experiments in the linear regime.

The relaxation modulus, $G(t)$, was measured at a fixed shear strain $\gamma=2\%$, as a function of time at different temperatures. Figure 6.3a) shows that the experimental $G(t)$ at all temperatures studied can be fitted with a stretched exponential functional form similar to what has been used to capture relaxation dynamics of strongly interacting materials, such as polymer networks and gels³⁰, triblock copolymer melts⁴⁷, and physically associated networks:⁴⁸

$$G(t) = G_0 \exp\left(-\left(\frac{t}{\tau}\right)^\beta\right) \quad 0 < \beta < 1 \quad (3)$$

Here, G_0 corresponds to the relaxation modulus at $t = 0$, τ is the characteristic material relaxation time and β is the stretching exponent, which describes the width of the relaxation time distribution. Supplementary table 6.1 reports the value of all parameters deduced from the fits, and it can be observed that with the increase in temperature, the characteristic relaxation time increases, but the distribution remains virtually unchanged, with $\beta \sim 0.32-0.30$ at all temperatures. It is noteworthy that the values of β are not only insensitive to temperature, but are nearly identical to those reported previously from similar analysis of step-shear dynamics of physically associating gels⁴⁹, crosslinked polymers and networks.⁵⁰ Figure 6.3b) summarizes the effect of temperature on τ . It is seen that the overall material relaxation slows down measurably. The dashed lines are Vogel-Fulcher-Tamman (VFT) fits given as,

$$\ln(\tau) = A - \frac{E_a}{R(T-T_{ref})} \quad (4)$$

where, A is a pre-factor, E_a is the activation energy in J/mol, R is the gas constant and T_{ref} is the reference temperature.⁵¹⁻⁵³ The value of T_{ref} is close to the melting temperature

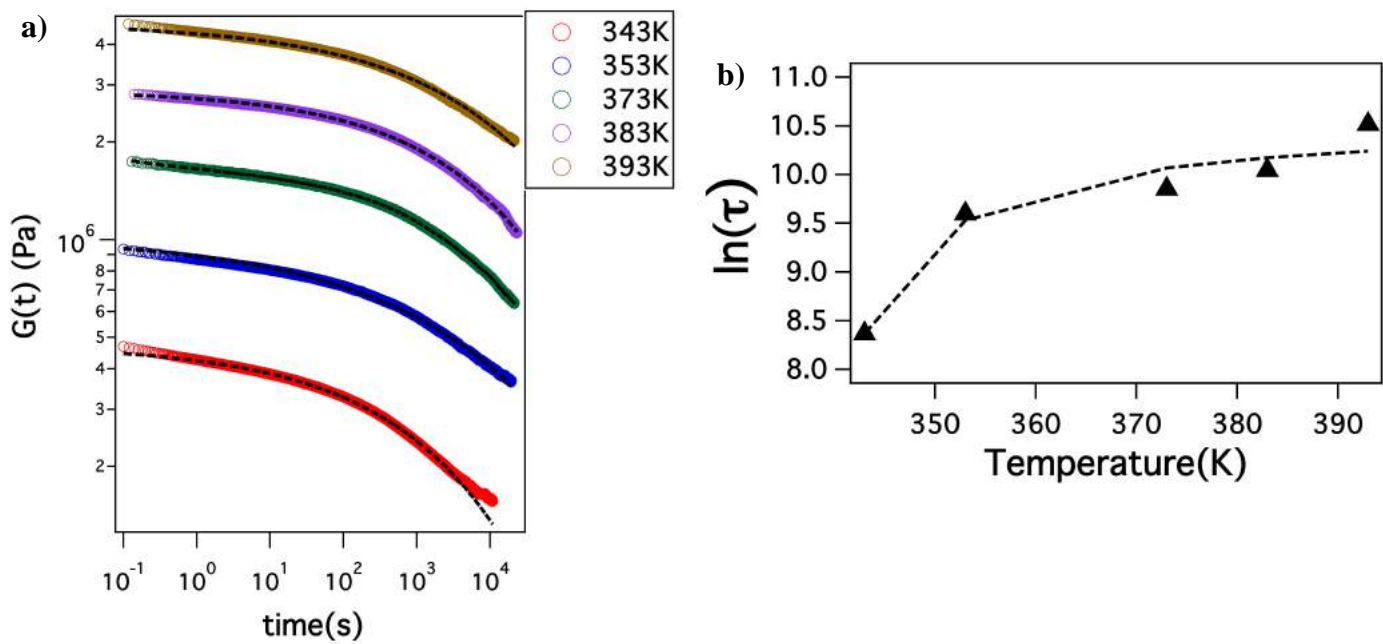


Figure 6.3 a) Relaxation modulus, $G(t)$ measured as a function of time for different temperatures, ranging from 343K to 393K. The curves are shifted for clarity. The black dashed lines are stretched exponential fits to $G(t)$. b) The material relaxation time, τ as obtained from the stretched exponential fits to $G(t)$ is seen to increase with an increase in temperature. The dashed line is VFT fit to $\ln(\tau)$.

of PEG, implying the corona chains may play a decisive role in the material relaxation behaviors observed.

The relaxation time reported from the step strain experiment has contributions from both the dynamics of the nano-cores and the corona chains. In order to obtain more specific details about the dynamics of the polymer chains, material response in a specialized interrupted shear startup-cessation measurement protocol were performed. In particular, a procedure described decades ago by Stratton *et al.*⁵⁴ in which a material is subjected to sequential shear startup measurements with variable delay time between successive measurements, investigates how shear-induced structural changes that produce stress overshoots relax (see Figure 6.4a)).⁵⁵ Stratton et al attributed the stress overshoot in shear start up to disentanglement of entangled polymer chains and related the relaxation time deduced from the overshoot recovery experiment to the polymer re-entanglement time, τ_e . For the SiO₂-PEGME system studied here, the shear strain at which the stress overshoot is observed is at least one order of magnitude lower than where it would be expected for a bulk entangled polymer. The processes (cage break-up or network segment pull-out) thought to produce the overshoot are hence different and the characteristic time required to restore the overshoot between successive experiment is related to the time required to re-establish net points that arrest the material. Mathematically, this characteristic time is estimated as the waiting time required between successive start-up experiments for the magnitude of the stress overshoot to reach $(1-e^{-1})$ of its value, σ_∞ , after an infinitely long waiting time. Figure 6.4b) and 6.4c) show the variation in the peak stress value with the delay time. The stress overshoot is observed to decrease with delay time, until a steady state value is reached. The dashed lines are exponential fits to σ_{peak} , which are then used

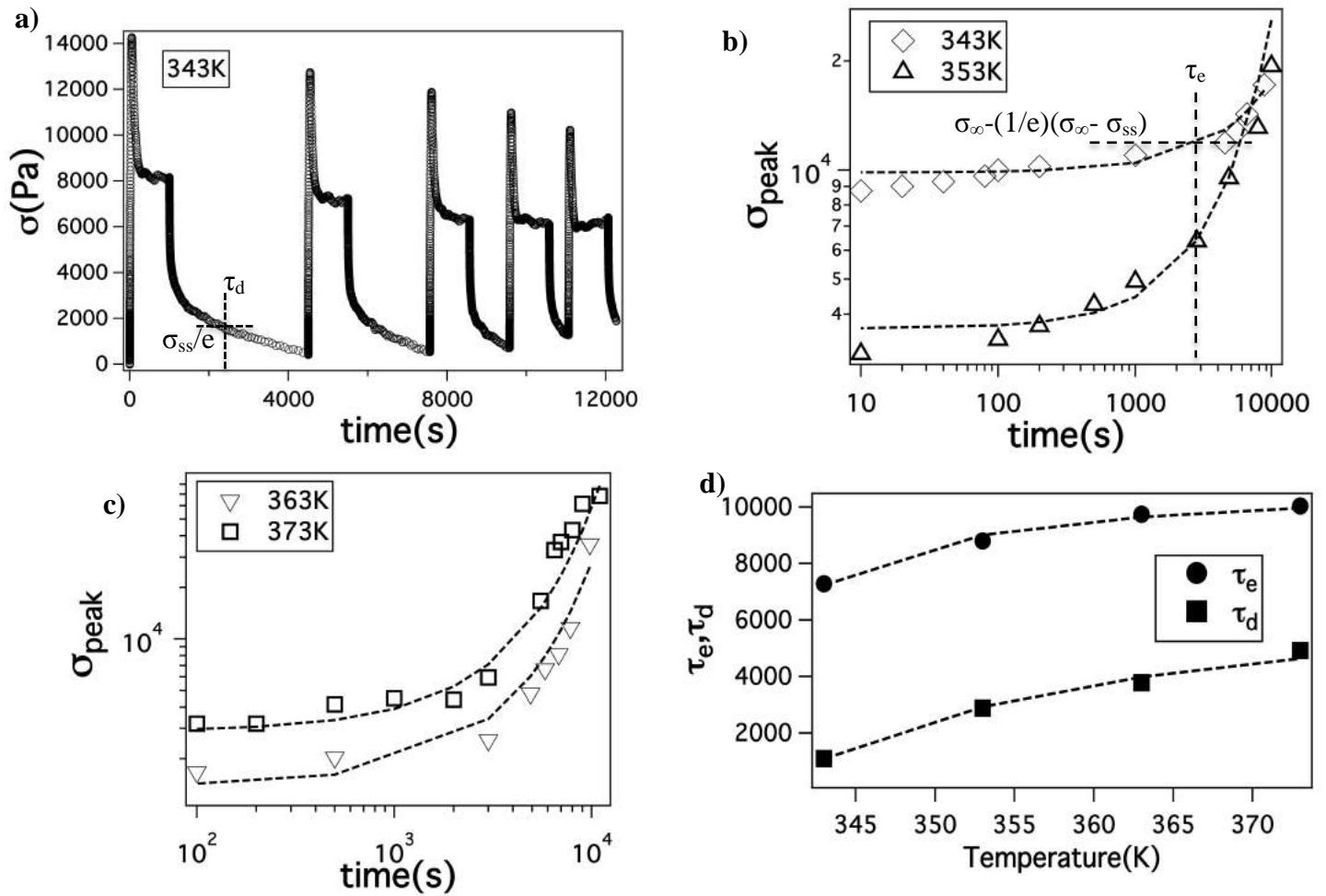


Figure 6.4 a) Characteristic overshoot recovery experiment, which measures the variation in the peak of stress overshoot, σ_{peak} with different delay times between successive measurements. Variation in σ_{peak} as a function of delay time for **b)** 343K & 353K, and **c)** 363K & 373K. The dashed lines are exponential fits, which are subsequently used to obtain τ_e . **d)** The network strand dis-entanglement time, τ_e and the stress relaxation time of the material, τ_d , increase with temperature. The dashed lines are VFT fit to the time scales.

Table 6.1. VFT fit parameters for different relaxation time scales

Relaxation time (s)	A	E_a(J/mol)	T_{ref}(K)
$\tau_{\text{step-strain}}$	10.58	165.32	333.8
τ_{d}	9.87	141.35	334
τ_{e}	9.30	31.13	334

to estimate τ_e . Figure 6.4d) reports the effect of the measurement temperature on τ_e . Another stress relaxation time τ_d can be defined from the experiments, which is the characteristic time for the shear stress to reach 1/e of its steady state value. Both of these time scales are seen to increase with temperature, corroborating the results from step-strain measurements that the material dynamics slow down with an increase in temperature. The dashed lines are VFT fits to the respective time scales and the associated parameters are reported in Table 6.1. The activation energy corresponding to τ_e is about 5 times smaller than that associated with τ_d , which is similar to that obtained from step-strain measurements. This leads us to infer that τ_e reflects the relaxation associated with dis-engagement/re-engagement of the corona chains from neighboring particles, while τ_d and $\tau_{\text{step-strain}}$ includes contribution from both the corona chains as well as the nano-core relaxation.

Microscopic origins of startup rheology response

In order to take the analogy between the corona chain inter-digitation and network processes in physically cross-linked polymers further, we next compare our experimental observations with theoretical predictions based on a constitutive model developed by Erk and Shull³⁰ for such networks,

$$\frac{\sigma}{G_0} = \frac{1}{f_0} \int_0^\gamma \Phi_b(\gamma, \gamma_b) \gamma_b \exp\left(\frac{\gamma_b}{\gamma^*}\right)^2 d\gamma_b \quad (5)$$

Here the macroscopic bulk shear stress σ is related to the local shear strain γ_b via a strain distribution function $\Phi_b(\gamma, \gamma_b)$, and at the strain γ^* where the stress diverges. f_0 is the

fraction of chains that form cross-links at equilibrium, which can be obtained from the rubbery elastic modulus,

$$G_0 = k_B T f_0 v \quad (6)$$

where v is the overall polymer strand concentration. In physically associating networks, strain can cause network rupture and apparent yielding, which in the model of Erk and Shull is captured in a network bond survival probability,

$$p_b(\gamma_b) = \exp \left[- \left(\frac{\pi^{1/2}}{\dot{\gamma} \tau} \gamma_f \operatorname{erfi} \left(\frac{\gamma_b}{\gamma_f} \right) \right)^\beta \right] \quad (7)$$

where, τ is the characteristic relaxation time of the network strand, γ_f is the shear strain at which a network bond breaks, β is a stretching exponent and $\dot{\gamma}$ is the applied bulk shear rate.

A numerical procedure described in reference [30] was used to analyze the measured stress-strain behaviors of our SiO₂-PEGME materials in the framework of equations (5) - (7). Table 6.2 reports the values of the parameters used to fit the experimental results. To constrain the parameters, the bond fracture strain γ_f was obtained from the position of maximum in loss modulus; the chain dis-engagement time τ_e was used as the characteristic relaxation time of the polymer chains in equation (7); and γ^* was obtained by fitting the initial slope of experimental stress-strain plot with the following constitutive equation (see Supplementary figure 6.4), used to describe the strain stiffening behavior of physically associating networks^{56,57}:

$$\sigma = G_0 \gamma \exp \left[\left(\frac{\gamma}{\gamma^*} \right)^2 \right] \quad (8)$$

Figure 6.5 compares the evolution of normalized stress as a function of strain for different temperatures. It is seen that the magnitude of the predicted stress overshoot increases, and the overshoot becomes narrower as temperature increases, in qualitative agreement with what is observed experimentally. For physically cross-linked networks, it has also been reported that the magnitude of stress overshoot increases and becomes narrower as the network becomes stiffer with an increase in the number of cross-linked strands or bridges.³⁰ That similar features are seen for the SiO₂-PEGME materials when the temperature rises lends support to our hypothesis that corona chains are more stretched and inter-digitated with their neighbors at higher temperature. This inference can also be seen quantitatively in terms of f_0 (Table 6.2), which increases with temperature in accordance with what would be expected if the degree of physical cross-linking between corona chains rises. Previous studies on self-suspended hairy nanoparticles have attempted to explain the origins of stress overshoot within the framework of Soft Glassy Rheology (SGR) model.¹² However, the value of yield strains obtained from SGR model predictions is significantly higher, about 100 times than the experimental observations. The present analysis using cross-linked network predicts similar values of yield strains as observed in experiments, which provides stronger support to the hypothesis that the thermal jamming observed in self-suspended hairy nanoparticles arises due to enhanced corona inter-penetration, and subsequently the yielding in startup experiments is governed by the pull-out of these corona chains from their neighbors. We close by noting that the magnitudes of the normalized stress overshoot observed experimentally are significantly smaller than predicted from

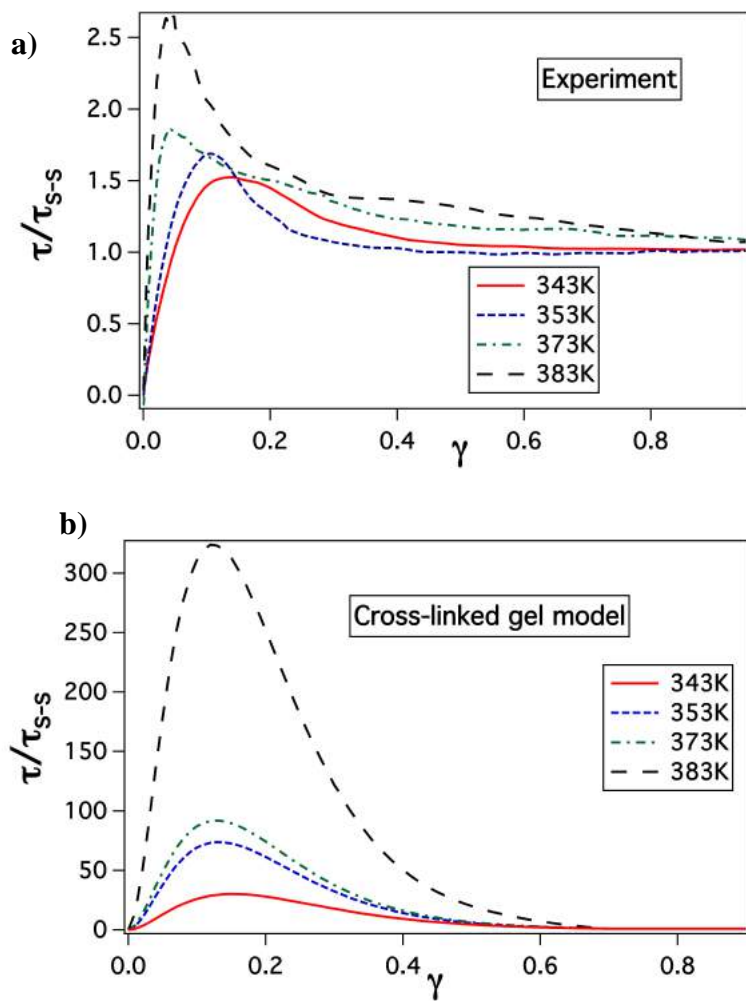


Figure 6.5 a) Normalized shear stress vs strain values obtained experimentally at shear rate= 0.01s^{-1} . The stress overshoot is seen to increase with an increase in temperature. **b)** Simulation results from prediction of the constitutive model on physically associating crosslinked gels, exhibiting qualitatively similar features as experiments.

Table 6.2 Fit parameters for the crosslinked gel constitutive model

Temperature (K)	γ_f	f_0	γ^*
343	0.33	0.160	2.65
353	0.29	0.182	2.65
373	0.21	0.195	2.65
383	0.17	0.215	2.65

equations (5). Additionally, we note that while the theoretically predicted strain at which the overshoot is observed matches fairly well with the experiments, the progressive shift of the overshoot to lower shear strains observed experimentally is not captured in the theory. These discrepancies likely arise from the assumption that stresses in the materials are purely elastic and their strain response arises solely from the dynamics of network strands. This obviously ignores the important contribution particles make to the residual viscous stresses after network yield, which leads to a higher value of the steady state stress measured experimentally, as well as a dependence of stress on shear rate not captured in the constitutive model for associative networks.

6.5 Conclusions

We have studied the effect of temperature on mechanical and dynamical properties of solvent-less polymer tethered silica nanoparticles. It is found that an increase in temperature leads to an apparent enhancement in glassy/jammed rheological behaviors in both linear and non-linear shear rheology measurements. Upon increasing strain the materials yield and flow, which manifests as asymmetric maxima in the time-dependent stress during start-up of steady shear at a constant shear rate or as pronounced maxima in G'' versus shear strain in oscillatory shear flow measurements. Both the energy dissipated upon yielding and the elastic modulus in the low-strain, linear regime increase with temperature; leading to the designation of the materials as thermally jammed. The molecular origins of this *thermal jamming* behavior is explained using an analogy to physically associating polymer networks where stress overshoots and yielding are observed experimentally and predicted theoretically to originate from chain pull-out and rupture of network segments. In particular, similar to an associating polymer network,

yielding is hypothesized to originate from pull-out and slippage of inter-digitated polymer chains tethered to adjacent nanoparticles. If this analogy holds true, it means that the soft glassy rheological properties of self-suspended SiO₂-polymer particles previously attributed to jamming by cage-like constraints particles exert on each other, in fact arises from network formation by interpenetration of tethered polymer chains.

By means of SAXS measurements and DFT analysis, we find that the position of the nano-cores remain fixed with changes in temperature, while the tethered polymer strands assume more stretched conformation at elevated temperature. These results are consistent with the above hypothesis of higher degree of corona inter-penetration, and thus creation of a stronger particle network with increase in temperature. Qualitative similarities are also found between the linear rheological response of solvent-less SiO₂-polymer particles and associating polymer networks. In small-amplitude step shear, materials in both classes undergo slow, time-dependent relaxation that is well described by a stretched exponential function. However, whereas relaxation times of solvent-less SiO₂-polymer particles deduced from step-shear and stress relaxation experiments increase with increasing temperature, those of associating networks exhibit polymer-like characteristics and decrease with increasing temperature. It is also found that the re-engagement time following stress overshoot measurements in the SiO₂-polymer hybrid materials increases with temperature, consistent with the hypothesis that an increase in temperature leads to greater degree of corona inter-digitation, thus slowing down re-engagement dynamics with neighboring chains.

Finally, we compare the stress profiles measured during startup shear measurements on SiO₂-polymer hybrids with a constitutive model developed for understanding the stress

overshoot in associating polymer networks. The model correctly captures the rise in the overshoot amplitude with temperature observed experimentally and also predicts the observed narrowing of the stress overshoot with increased temperature. More in-depth analysis reveals that the rise is associated with an increase in the fraction of chains that form cross-links. The model however predicts much larger stress overshoots than observed experimentally and predicts that the critical strain at the overshoot changes little with temperature, which disagrees with experimental observations showing that the critical strain becomes smaller as temperature increases.

Acknowledgements

This work was supported by the National Science Foundation, Award No. DMR 1609125. Use of the Advanced Photon Source, operated by Argonne National Laboratory, was supported by the U.S. DOE under Contract No. DE-AC02-06CH11357. We thank Dr. Anubhab Roy for his insights and ideas about the constitutive mode

REFERENCES

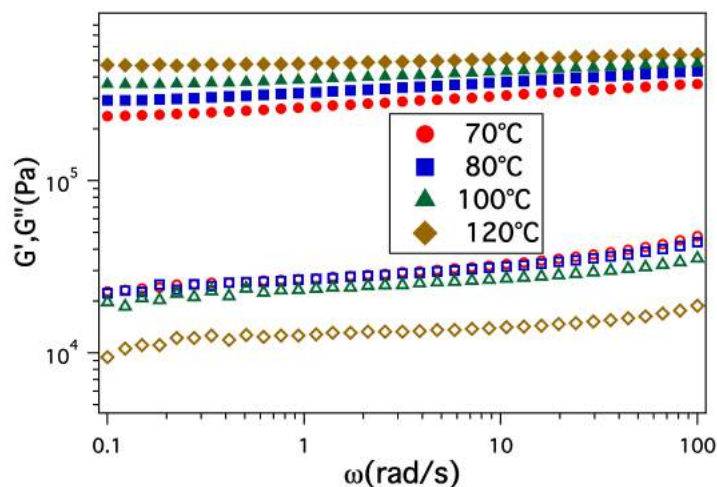
- (1) Cates, M. E.; Wittmer, J.; Bouchaud, J.-P. P.; Claudin, P. *Phys. Rev. Lett.* **1998**, *81* (9), 1841–1844.
- (2) Puertas, A. M.; Fuchs, M.; Cates, M. E. *Phys. Rev. Lett.* **2002**, *88* (9), 098301.
- (3) Fuchs, M.; Cates, M. E. *Phys. Rev. Lett.* **2002**, *89* (24), 248304.
- (4) Princen, H. M. *J. Colloid Interface Sci.* **1986**, *112* (2), 427–437.
- (5) Princen, H. M. *J. Colloid Interface Sci.* **1983**, *91* (1), 160–175.
- (6) Princen, H. M.; Kiss, A. D. *J. Colloids Interface Sci.* **1989**, *128* (1).
- (7) Trappe, V.; Prasad, V.; Cipelletti, L.; Segre, P. N.; Weitz, D. A. *Nature* **2001**, *411* (6839), 772–775.
- (8) Liu, A. J.; Nagel, S. R. *Nature* **1998**, *396* (November), 21–22.
- (9) Loppinet, B.; Stiakakis, E.; Vlassopoulos, D.; Fytas, G.; Roovers, J. **2001**, No. about 270, 8216–8223.
- (10) Stiakakis, E.; Vlassopoulos, D.; Roovers, J. *Langmuir* **2003**, *19* (8), 6645–6649.
- (11) Kapnistos, M.; Vlassopoulos, D.; Fytas, G.; Mortensen, K.; Fleischer, G.; Roovers, J. *Phys. Rev. Lett.* **2000**, *85* (19), 4072–4075.
- (12) Agarwal, P.; Srivastava, S.; Archer, L. A. *Phys. Rev. Lett.* **2011**, *107* (26), 268302–1 – 5.
- (13) Choudhury, S.; Agrawal, A.; Kim, S. A.; Archer, L. A. *Langmuir* **2015**, *31*, 3222–3231.
- (14) Kim, S. A.; Mangal, R.; Archer, L. A. *Macromolecules* **2015**, *48* (17), 6280–6293.

- (15) Rissanou, A. N.; Vlassopoulos, D.; Bitsanis, I. A. *Phys. Rev. E - Stat. Nonlinear, Soft Matter Phys.* **2005**, *71* (1), 1–12.
- (16) Yu, H.-Y.; Koch, D. L. *Langmuir* **2010**, *26* (22), 16801–16811.
- (17) Bourlinos, A. B.; Herrera, R.; Chalkias, N.; Jiang, D. D.; Zhang, Q.; Archer, L. A.; Giannelis, E. P. *Adv. Mater.* **2005**, *17* (2), 234–237.
- (18) Rodriguez, R.; Herrera, R.; Archer, L. A.; Giannelis, E. P. *Adv. Mater.* **2008**, *20* (22), 4353–4358.
- (19) Agarwal, P.; Qi, H.; Archer, L. A. *Nano Lett.* **2010**, *10* (1), 111–115.
- (20) Yu, H.-Y.; Srivastava, S.; Archer, L. A.; Koch, D. L. *Soft Matter* **2014**, *10* (45), 9120–9135.
- (21) Chremos, A.; Panagiotopoulos, A. Z. *Phys. Rev. Lett.* **2011**, *107* (10), 1–5.
- (22) Yu, H. Y.; Koch, D. L. *Langmuir* **2013**, *29* (26), 8197–8202.
- (23) Goyal, S.; Escobedo, F. A. *J. Chem. Phys.* **2011**, *135* (18), 184902.
- (24) Chremos, A.; Panagiotopoulos, A. Z.; Yu, H.-Y.; Koch, D. L. *J. Chem. Phys.* **2011**, *135* (11), 114901.
- (25) Chremos, A.; Panagiotopoulos, A. Z.; Koch, D. L. *J. Chem. Phys.* **2012**, *136* (4), 044902.
- (26) Fernandes, N. J.; Koerner, H.; Giannelis, E. P.; Vaia, R. a. *MRS Commun.* **2013**, *3* (01), 13–29.
- (27) Agrawal, A.; Yu, H.-Y.; Srivastava, S.; Choudhury, S.; Narayanan, S.; Archer, L. A. *Soft Matter* **2015**, *11*, 5224–5234.
- (28) Agarwal, P.; Kim, S. A.; Archer, L. A. *Phys. Rev. Lett.* **2012**, *109* (25), 258301–1–4.

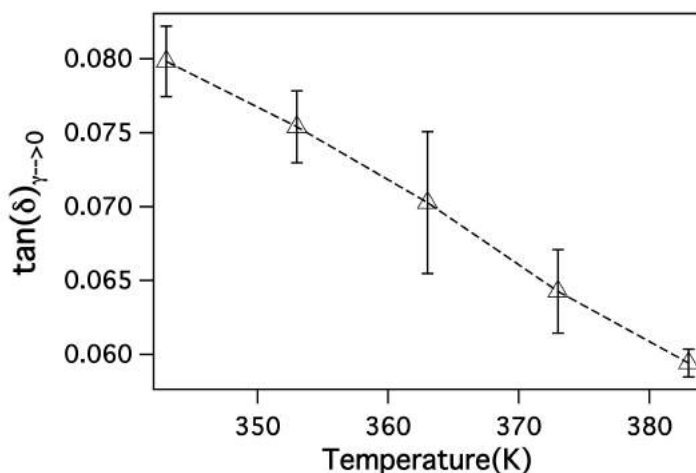
- (29) Kim, S. A.; Archer, L. A. *Macromolecules* **2014**, *47*, 687–694.
- (30) Erk, K. A.; Shull, K. R. *Macromolecules* **2011**, *44* (4), 932–939.
- (31) Tsitsilianis, C.; Iliopoulos, I. *Macromolecules* **2002**, *35* (9), 3662–3667.
- (32) Erk, K. A.; Martin, J. D.; Hu, Y. T.; Shull, K. R. *Langmuir* **2012**, *28* (9), 4472–4478.
- (33) Srivastava, S.; Agarwal, P.; Archer, L. A. *Langmuir* **2012**, *28* (15), 6276–6281.
- (34) Glatter, O.; Kratky, O. *Small Angle X-ray Scattering*, United Sta.; Academic Press: New York, 1982.
- (35) Srivastava, S.; Shin, J. H.; Archer, L. A. *Soft Matter* **2012**, *8* (15), 4097–4108.
- (36) Mason, T. G.; Weitz, D. A. *Phys. Rev. Lett.* **1995**, *75* (14), 2770–2773.
- (37) Pham, K. N.; Petekidis, G.; Vlassopoulos, D.; Egelhaaf, S. U.; Pusey, P. N.; Poon, W. C. K. *Europhys. Lett.* **2006**, *75* (4), 624–630.
- (38) Pham, K. N.; Petekidis, G.; Vlassopoulos, D.; Egelhaaf, S. U.; Poon, W. C. K.; Pusey, P. N. *J. Rheol. (N. Y. N. Y.)* **2008**, *52* (2), 649–676.
- (39) Helgeson, M. E.; Wagner, N. J.; Vlassopoulos, D. *J. Rheol. (N. Y. N. Y.)* **2007**, *51* (2), 297–316.
- (40) Agarwal, P.; Archer, L. A. *Phys. Rev. E* **2011**, *83* (4), 041402–1 – 5.
- (41) Koumakis, N.; Pamvouxoglou, A.; Poulos, A. S.; Petekidis, G. *Soft Matter* **2012**, *8* (15), 4271–4284.
- (42) Ganeriwala, S. N.; Rotz, C. A. *Polym. Eng. Sci.* **1987**, *27* (2), 165–178.
- (43) Srivastava, S.; Agarwal, P.; Mangal, R.; Koch, D. L.; Narayanan, S.; Archer, L. A. *ACS Macro Lett.* **2015**, *4* (10), 1149–1153.

- (44) Seitz, M. E.; Burghardt, W. R.; Faber, K. T.; Shull, K. R. *Macromolecules* **2007**, *40* (4), 1218–1226.
- (45) Srivastava, S.; Archer, L. A.; Narayanan, S. *Phys. Rev. Lett.* **2013**, *110* (14), 148302–1 – 5.
- (46) Hansen, J. P.; Verlet, L. *Phys. Rev.* **1969**, *184* (1), 151–161.
- (47) Hotta, A.; Clarke, S. M.; Terentjev, E. M. *Macromolecules* **2002**, *35* (1), 271–277.
- (48) Séréro, Y.; Jacobsen, V.; Berret, J. F.; May, R. *Macromolecules* **2000**, *33* (5), 1841–1847.
- (49) Stukalin, E. B.; Douglas, J. F.; Freed, K. F. *J. Chem. Phys.* **2008**, *129* (9).
- (50) Gurtovenko, A. A.; Gotlib, Y. Y. *J. Chem. Phys.* **2001**, *115* (14), 6785–6793.
- (51) Vogel, H. *Phys.Z* **1921**, *22*, 645–646.
- (52) Fulcher, G. S. *J. Am. Ceram. Soc* **1925**, *8*, 789–794.
- (53) Tammann, G. *Soc.Glass Technol.* **1925**, *9*, 166–185.
- (54) Stratton, R. A.; Butcher, A. F. *J. Polym. Sci.* **1973**, *11*, 1747–1758.
- (55) Sanchez-Reyes, J.; Archer, L. A. *Macromolecules* **2002**, *35* (13), 5194–5202.
- (56) Erk, K. A.; Henderson, K. J.; Shull, K. R. *Biomacromolecules* **2010**, *11* (5), 1358–1363.
- (57) Storm, C.; Pastore, J. J.; MacKintosh, F.; Lubensky, T.; Jamney, P. A. *Nature* **2005**, *435* (May), 191–194.

1. Oscillatory shear measurements

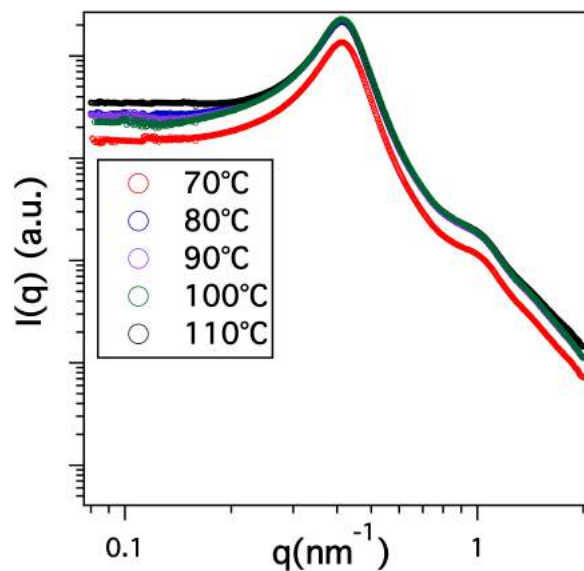


Supplementary figure 6.1 Frequency sweep measurements performed at $\gamma=0.5\%$ at different temperatures. The closed symbols correspond to the storage modulus, G' and the open symbols to the loss modulus, G'' .



Supplementary figure 6.2 Loss tangent, $\tan(\delta)=G''/G'$, at shear strain $\gamma \rightarrow 0$, as decreases with increase in temperature. This indicates that the material exhibits a more solid-like flow response as the temperature is increased.

2. Structural Analysis:



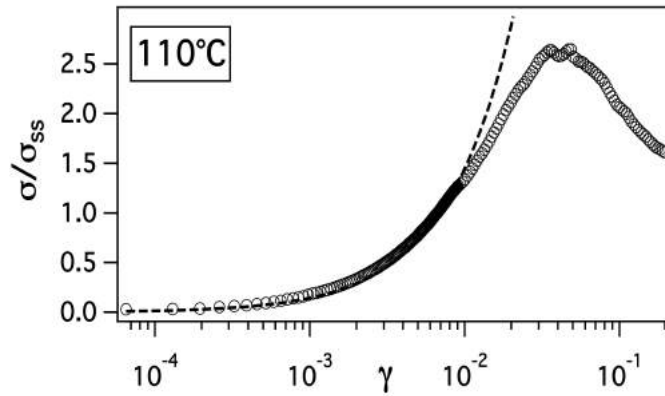
Supplementary figure 6.3 X-ray scattered intensity $I(q)$ measured from SAXS experiments as a function of the wave vector q , measured at different temperatures.

3. Parameters estimated from fits to relaxation modulus

Supplementary table 6. 1. Stretched exponential fit parameters for relaxation modulus as a function of temperature for step strain measurements

T(K)	G(0) (Pa)	β	τ(s)
343	4.42E+05	0.32	4.31E+03
353	4.65E+05	0.28	1.47E+04
373	4.74E+05	0.30	1.90E+04
383	4.81E+05	0.31	2.31E+04
393	5.12E+05	0.32	3.69E+04

4. Estimation of divergence strain



Supplementary figure 6.4 Normalized shear stress as a function of strain fitted with constitutive equation describing the strain stiffening behavior of networks (equation (10) in the text) as dashed line

Chapter 7

Interactions, Structure and Dynamics of Polymer-Tethered Nanoparticle Blends

7.1 Abstract

We report on self-suspended solvent-less suspensions of silica nanoparticles grafted with polyethylene glycol (PEG) and polymethyl methacrylate (PMMA). Favorable enthalpic attraction between PEG and PMMA chains along with the space-filling constraint imposed on them in the absence of a solvent, results in strong mechanical and structural responses in these materials. The energy dissipated to yield the material and the plateau modulus, as observed from non-linear and linear oscillatory rheology measurements, follow a non-monotonic dependence when the fraction of PMMA grafted nanoparticles added to the blend is varied. A comparison of the Small Angle X-ray Scattering (SAXS) measurements with theoretical analysis from Density Functional Theory (DFT) reveals that addition of PMMA initially leads to a higher degree of stretching of the corona chains, which is responsible for stronger inter-digitation of the polymer chains and thus leads to a higher mechanical strength. A quantitative analysis used to obtain the heat of mixing released upon blending the polymer chains when both tethered and un-tethered ,reveals a similar non-monotonic dependence with the fraction of PMMA, which shows that the volume fraction corresponding to strongest mechanical response coincides with the composition where the blend is most thermodynamically stable. Strong enthalpic attraction between the grafted polymer chains along with an “entropic attraction” between them creates a uniformly dispersed and a stabilized suspension of silica nanoparticles, where the enthalpic attraction can be tuned to alter the rheological and structural response of the material.

7.2 Introduction

Inorganic nanoparticles dispersed in polymer hosts have attracted sustained attention for more than four decades from researchers in academia and industry. These nanocomposite materials offer property profiles that cannot be obtained in the individual components and have emerged as important materials in multiple areas of technology, including electronics, medicine, data storage, sustainable energy and environment, defense etc.¹⁻¹⁰

A critical requirement for nanocomposites in all of these areas is that the dispersion state of the nanoparticles in the polymer host must be controlled such that they do not aggregate.^{1,4,6,7,11} The combination of strong long range van Der Waals attractive forces between nano-sized particles and polymer mediated depletion interactions have with rare exceptions proven insurmountable barriers to the creation of nanocomposites in which particles are uniformly dispersed at equilibrium.¹¹⁻¹⁵

A popular misconception in the field is that this situation can be remedied by sterically stabilizing the nanoparticles by grafting short polymer chains on their surface.¹⁶⁻¹⁹ Multiple recent studies of model hairy nanoparticles in high molecular weight polymer hosts have shown that above a relatively small grafting density and a large host polymer molecular weight, the host de-wets the particles, making them unstable when the ratio of degree of polymerization of host polymer chains (P) becomes greater than that of the nanoparticle-grafted polymer chain (N) by a factor of around 5.²⁰⁻²⁵ This critical P/N ratio is substantially larger than the value of unity predicted for the dewetting transition of a planar-brush/polymer interface, which has been explained in terms of greater interpenetration (wetting) of the corona and host polymer chains due to the strong curvature of

small particles used in the experimental studies.^{22,26} More remarkable, however, are the recently reported observations that even a weak enthalpic interaction between nanoparticle-tethered poly(ethylene glycol) (PEG) corona chains and high molecular poly(methyl methacrylate) (PMMA) host polymer is sufficient to increase the critical value of P/N by one or more orders of magnitude.²⁷⁻²⁹ Although this effect may again be rationalized in terms of the combined effects of the small negative Flory-Huggins χ interaction parameter between PEG and PMMA, which favors wetting, and curvature induced interpenetration of tethered PEG and their host PMMA chains, which also favors wetting, little is known fundamentally about the nature of the interactions between chemically dissimilar polymers when one is attached to curved interfaces. Such curvature could amplify the effect of the small χ to produce the large enhancements in nanoparticle dispersion observed experimentally.

We've previously reported on self-suspended, solvent-less homopolymer grafted hairy nanoparticles, which exhibit stable particle dispersion in the absence of any solvent. The phase stability in such systems has been shown by means of density functional calculations to originate from a "space-filling" constraint on the grafted corona chains,^{30,31} which leads to an effective "entropic attraction" between the particles mediated by the tethered chains, which may be crudely thought of as an entropic contribution that makes the Flory-Huggins χ parameter larger and more negative.^{31,32} Several experimental and theoretical works on these solvent-less hairy nanoparticles have surmised that the densely grafted polymer chains not only provide steric stabilization to the particles, but due to the absence of a solvent the incompressible nature of the grafted

polymer drives uniform dispersion of the nanoparticles with a suppression of long wavelength density fluctuations; consistent with the existence of such an entropic attraction force.³⁰⁻³² The mechanical, dynamical and structural properties of these self-suspended solvent-less hairy nanoparticles have been shown to be sensitive to the constraints on the corona imposed by space filling and efforts so far to understand how variables such as the core particle size³³, corona molecular weight^{34,35}, corona grafting density^{34,36,37} and the temperature^{37,38} affect physical properties of these materials, have underscored the importance of the space filling constraint.

Herein we report for the first time how interactions across interfaces formed between chemically distinct polymers influence structure, physical properties, and dynamics of hairy nanoparticles. In particular we consider how interactions between PEG and PMMA chains tethered to SiO₂ nanocores in the form of self-suspended PEG-SiO₂-PEG/SiO₂-PMMA hairy particle blends influence structure and properties of the materials. An important benefit of using such self-suspended nanoparticle materials for the study is that because no solvent is present, the polymer component in the bulk materials is entirely interfacial. It means that any bulk measurement of thermal, dynamic, or rheological transitions will report on details of such interfaces with higher signal-to-noise than previously possible. We are specifically interested in using these measurements to understand how favorable attractions between PEG and PMMA chains^{39,40} tethered to curved interfaces may be augmented by entropic attraction arising from space filling. We also manipulate the degree of attraction between the PEG and PMMA chains by varying the composition of PMMA-SiO₂ or PEG-SiO₂ nanoparticles in the blends and

experimentally study its influence on mechanical, structural, and dynamic properties. The experimental work is augmented with a simple theoretical analysis that allows us to estimate the heat of mixing of the polymer grafted nanoparticle blends.

7.3 Experimental Methods

7.3.1 Synthesis

Blends of silica nanoparticles of size $25\pm 3\text{nm}$ (Ludox TM-50, Sigma Aldrich) covalently grafted with silane terminated polyethylene glycol (PEG, $M_w\sim 5500\text{ g/mol}$, PDI ~ 1.1 , Polymer Source) and silane terminated Polymethyl methacrylate (PMMA, $M_w\sim 13000\text{ g/mol}$, PDI ~ 1.4) were prepared. Amine terminated PMMA was synthesized using Atom Transfer Radical Polymerization (ATRP)^{41,42} (see Supplementary Information) with molecular weight $M_w\approx 13000\text{ g/mol}$ and PDI of 1.4 as shown in Supplementary figure 7.1. The specific molecular weights of PMMA and PEG used in the study were chosen such that the overall degree of polymerization N of tethered PMMA and PEG polymers are approximately the same, around 130. The amine terminated PMMA was coupled to a silane using a urethane linking procedure reported previously.³⁷ The silane terminated PMMA was grafted to silica nanoparticles using a procedure reported previously for grafting the silane terminated PEG chains on SiO_2 at high coverages.³² The procedure was manipulated to create PMMA- SiO_2 or PEG- SiO_2 nanoparticles with grafting densities of 0.40 chains/nm^2 and 0.97 chains/nm^2 , respectively, such that the overall volume fraction of silica nanoparticles was approximately the same in the single-component materials and their blends. Following the synthesis, the materials were rigorously purified by repeated centrifugation in a mixture of fresh chloroform (solvent)

and hexane (non-solvent) at 8500rpm for 10min, to remove any excess PEG or PMMA chains. The resultant particles were subsequently dried in a convection oven overnight at 60°C and then under vacuum for 48 hours to remove any traces of solvent. The grafting densities of the respective materials were estimated from the residual inorganic content deduced from Thermogravimetric Analysis (TGA). The total core volume fraction, ϕ of silica nanoparticles for both types of chemistries was found to be around 0.36.³³ Blends of PEG and PMMA grafted silica nanoparticles were prepared by first dissolving the respective hairy particles in chloroform to form solutions of known concentration and then mixing the solutions together in appropriate amounts to create materials in which the volume fraction of PMMA is varied. The parameter $\phi_{PMMA} = V_{PMMA}/(V_{PMMA} + V_{PEG})$, where V_{PMMA} is the volume of PMMA and V_{PEG} is the volume of PEG in the blend, will be used throughout to characterize the compositions in the blends. We note that a blend with $\phi_{PMMA}=0$ corresponds to the pure self-suspended SiO₂-PEG particles whereas with $\phi_{PMMA}=1$ refer to the pure, self-suspended SiO₂-PMMA nanoparticles.

7.3.2 Rheology Measurements

Oscillatory shear rheology experiments were performed at discrete temperatures ranging from 70°C to 120°C, all chosen to lie above the glass transition or melting temperature (whichever is larger) of the nanoparticle blends. The measurements were performed on a strain controlled ARES-LS rheometer (Rheometric Scientific) outfitted with a cone and plate geometry (6mm diameter, 2° cone angle). Prior to data collection, all blends were pre-sheared using large amplitude oscillatory shear deformations with shear strains above the yield strain and each blend was deformed repeatedly until the data obtained from successive measurements were the same. Linear and non-linear viscoelastic properties were studied by performing variable strain amplitude measurements at a fixed angular

frequency of $\omega=10$ rad/s, and variable frequency measurements at a fixed strain of $\gamma=0.5\%$.

7.3.3 Small Angle X-ray Scattering

Small Angle X-ray Scattering (SAXS) measurements were performed on the self-suspended PEG-SiO₂ and PMMA-SiO₂ nanoparticles and their blends at station D1 of Cornell High Energy Synchrotron Source (CHESS) using a point collimated x-ray beam. Each sample was smeared on a temperature controlled sample cell and all measurements were performed above the glass transition or melting temperature of the materials. The x-ray scattered intensity $I(q,\phi,D)$ was measured as a function of the wave vector q and is known to be directly related to the product of the form factor $P(q,D)$ and the structure factor $S(q,\phi,D)$.^{43,44} Here ϕ and D are the core volume fraction and particle diameter respectively. Since, in the limit of infinite dilution $S(q,\phi,D) \sim 1$, the form factor is the measured x-ray intensity, thus, SAXS measurements on a dilute solution of the charge stabilized silica nanoparticles were performed to obtain the form factor.^{31,43} Thereafter, the respective structure factors for the materials were obtained by dividing the measured x-ray intensity with the particle form factor.

7.3.4 Differential Scanning Calorimetry (DSC) and Dielectric Spectroscopy

The melting and glass transition temperatures of the un-tethered and SiO₂-tethered polymer chains were studied using a DSC Q2000 (TA instruments). Each sample was first heated to 200°C and then cooled to -100°C at a scan rate of 5°C/min, and finally heated again to 200°C at the same scan rate. The cycle was repeated twice and the melting or the glass transition temperature was recorded from data obtained in the second cycle.

Frequency dependent dielectric relaxation measurements were performed using a Novocontrol broadband dielectric spectrometer with Quatro temperature control. All the measurements were performed at a frequency range of 10^7 Hz to 10^{-2} Hz over a wide range of temperatures, all above the melting and glass transition temperatures of the materials.

7.4 Results and Discussion

Non-linear viscoelastic measurements

Blends of PEG-SiO₂ and PMMA-SiO₂ particles and the individual polymer grafted particles were evaluated in oscillatory shear and found to exhibit typical soft glassy rheology behavior at high shear strains (Supplementary figure 7.2).^{38,45-48} Consistent with the previous reports for self suspended hairy nanoparticles, we observe three distinct flow regimes. At low shear strains, both the storage modulus G' and the loss modulus G'' are independent of strain with $G' > G''$. At higher strain a distinct maximum is observed in the loss modulus. At yet higher strains a third strain softening regime is seen wherein the storage modulus is a stronger decreasing function of strain than the loss modulus, leading to the result $G' < G''$. Such rheological behaviors have been observed in numerous soft glasses such as foams, emulsions, star polymers, associating gels etc.^{46,49-51} In a recent study, we showed that the occurrence of a maximum in loss modulus in self-suspended hairy nanoparticles arises from a fundamentally similar source to the maximum in physically associating polymer network.^{52,51} In a transient cross-linked polymer network the occurrence of loss maximum is attributed to pulling out of the cross-linked polymer chains from their junctions.^{53,54} We showed experimentally and theoretically that the

tethered corona chains in these hairy nanoparticles act as transient crosslinks for each other, where the net-points of inter-digitation of the corona chains from neighboring particles act as physical crosslink junctions.

Figure 7.1a) and b) show the variation in the relative height of normalized loss maximum values i.e. $G''/G''_{\gamma \rightarrow 0}$ at 120°C, as the fraction of PMMA is varied in the blends. It can be seen that with the addition of PMMA the relative height of the loss maximum increase up to $\phi_{PMMA}=0.47$, after which it begins to decrease. This implies that addition of PMMA first leads to an enhanced jammed/cross-linked state for the materials, in comparison to the pure SiO₂-PEG particles. Thereafter, addition of PMMA progressively reduces the amount of jamming, with a significant reduction in the height of the loss maximum occurring between $\phi_{PMMA}=0.57$ and $\phi_{PMMA}=0.8$. This effect can be quantitatively explained by first evaluating the amount of energy dissipated in yielding the materials. As reported previously, the loss maximum can be fitted to a lognormal functional form and the amount of energy dissipated per unit volume estimated from the area under the curve as^{33,55} -

$$U_d \sim \int G''(\gamma) \gamma d\gamma \quad (1)$$

Figure 7.1c) reports the dissipated energy U_d as a function of ϕ_{PMMA} for measurements performed at different temperature. It is apparent that the maximum dissipation occurs around $\phi_{PMMA} \approx 0.5$ and that while the position of the maximum changes little with temperature, the height is a strong increasing function of temperature. The last of these phenomena known as *thermal jamming* has been reported previously in solvent-less nanoparticles grafted with homopolymer with a range of chemistries and grafting

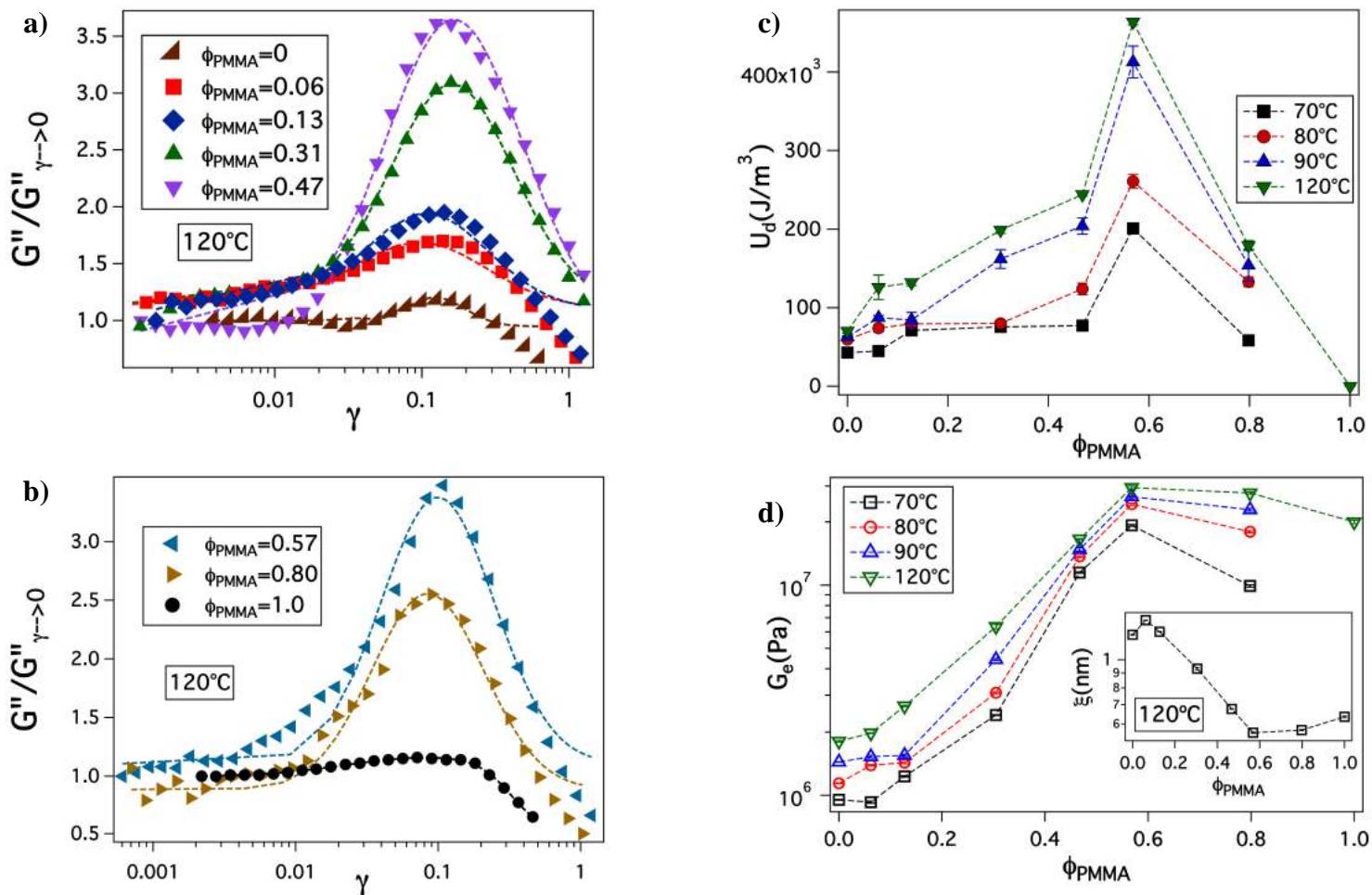


Figure 7.1 Evolution of the loss maximum normalized with the zero strain value i.e. $G''/G''_{\gamma \rightarrow 0}$ as a function of the imposed oscillatory strain for **a)** $\phi_{PMMA}=0$ to 0.47 and **b)** $\phi_{PMMA} =0.57$ to 1. It can be seen that the loss maximum initially increases with increase in ϕ_{PMMA} upto 0.47 and thereafter it decreases with increase in the concentration of PMMA. The dashed lines are lognormal fits to the loss maximum values. **c)** Energy dissipated per unit volume, U_d in yielding the hybrid particles as a function of ϕ_{PMMA} at different temperatures. **d)** The plateau modulus, G_e as obtained from the zero shear strain values of storage modulus from oscillatory shear measurements as a function of ϕ_{PMMA} . Both the dissipated energy U_d and the plateau modulus G_e are seen to increase with temperature and exhibit a non-monotonic variation with ϕ_{PMMA} . The dashed lines are a guide to the eye and the error bars are deviations in multiple measurements.

densities, and has been attributed to increased inter-penetration of tethered polymer chains with an increase in temperature.^{34,37,38,52,56} Since the extent of jamming in these materials is determined by the degree of inter-digitation/cross-linking of the grafted polymer chains we attribute the maximum in $U_d(\phi_{PMMA})$ to enhanced inter-penetration of the two kinds of grafted polymer chains at $\phi_{PMMA} \approx 0.5$. Specifically, we propose that initially addition of PMMA leads to an enhanced interpenetration/cross-linking between the grafted PEG and PMMA chains, which leads to an increase in U_d after which further addition of PMMA reduces this inter-penetration/cross-linking leading to a weakened jammed state for the material. This behavior is seen not only in non-linear regime but is also replicated in the linear viscoelastic rheology. Figure 7.1d) shows the evolution of plateau storage modulus obtained from the frequency sweep measurements in the linear regime (Supplementary figure 7.3) with changes in the fraction of PMMA. Similar to the loss maximum and U_d , the plateau modulus is also seen to follow a non-monotonic variation with ϕ_{PMMA} . It is possible to quantify these effects in terms of an effective “localization length” $\xi=(k_B T/G_e)^{1/3}$ which is related to the physical distance between net-points formed by interpenetrated corona chains and the core surface.^{57,58} As can be observed from the inset of Figure 7.1d), ξ decreases initially with an increase in the fraction of PMMA and then begins to increase, which is consistent with the idea that addition of PMMA-SiO₂ to PEG-SiO₂ produces greater tethered chain interpenetration and stronger particle-particle interfaces.

Structural analysis

To further explore the interactions in PMMA-SiO₂/PEG-SiO₂ blends, we performed SAXS measurements on the materials to obtain information about the structural arrangements of the particles and combined this with results from DFT analysis to shed light on interactions. Supplementary figure 7.4 shows the variation in the x-ray scattered intensity $I(q)$ with the wave-vector q for different fractions of PMMA. For all values of ϕ_{PMMA} , $I(q)$ shows little if any dependence on q in the low q regime, which means that the long range structure is indifferent to the specific chemistry of the corona chains.^{22,43} Figure 7.2 a) reports the structure factor $S(q)$ as a function of q normalized with the particle radius a , for different values of ϕ_{PMMA} at 120°C. The experimental $S(q)$ are compared with predictions of the density functional theory (DFT) for self-suspended hairy nanoparticles. Similar to the procedure described in [31], the particle core is modeled as a hard sphere with the polymer chains as bead-linear spring oligomers grafted to the center of the core. A polydispersity of 20% is considered in the core size and the polydispersity of the grafting density is kept fixed at around 10% for all values of ϕ_{PMMA} . While a 20% polydispersity in the core size has been measured experimentally³³, a polydispersity of 10% in grafting density is chosen as it gives the best fits to the experimental data. Furthermore, as explained in [31], a certain number of monomers, n_m closer to the core act as immobilized part of the polymer brush such that they are effectively a part of the core. As illustrated in Figure 7.2b), this leads to an effectively bigger core size, $a_{\text{eff}}=a+n_m l_m \cos(\theta/2)$. Here a is the original particle radius, l_m is the length of the monomer brush, and θ is the bond tetrahedral angle. n_m is varied for all values of ϕ_{PMMA} such that the theoretical values gives best fits to the experimental data, as evaluated from least square regression method. As can be seen from Figure 7.2a), while

the first peak height of the predicted structure factor are not in quantitative agreement with the experimental values, the peak positions agree well with the experimental data for all ϕ_{PMMA} . Since the first peak height of the structure factor is a reflection of degree of coherence between the nearest neighbors, the larger discrepancy between the experimental and predicted peak heights apparent at intermediate ϕ_{PMMA} are associated with greater interactions between the grafted PMMA and PEG chains, which is consistent with the idea that interactions between the tethered PMMA and PEG chains drive enhanced interpenetration and hence coupling of the nanoparticle cores.

The distance between the nearest neighbors can be evaluated from the position of the first $S(q)$ maximum, such that $d_{p-p}=2\pi/q$. It can be observed from Figure 7.2b) that the d_{p-p} values evaluated from the experiments are in good agreement with theory, where a slight but noticeable decrease in the inter-particle distance is observed with an increase in ϕ_{PMMA} initially, followed by an increase in d_{p-p} with an increase in ϕ_{PMMA} . This effect can be better explained by considering the effective surface to surface distance between the cores, shown in Figure 2c). The surface-to-surface distance, $h=d_{p-p}-2a_{eff}$, is seen to follow a strong non-monotonic variation with ϕ_{PMMA} , where its value decreases significantly, ultimately becoming negative, with an increase in ϕ_{PMMA} . This regime is followed by a substantial increase to positive values at even higher ϕ_{PMMA} . A negative value of h implies overlap between the tethered immobilized oligomer brushes, and more negative the value of h , more is the inter-penetration of the oligomer chains. As illustrated in Figure 7.2c), up till a value of $\phi_{PMMA}=0.47$, h becomes increasingly negative, consistent with a stronger inter-digitation of the tethered corona chains; after which the h values become positive

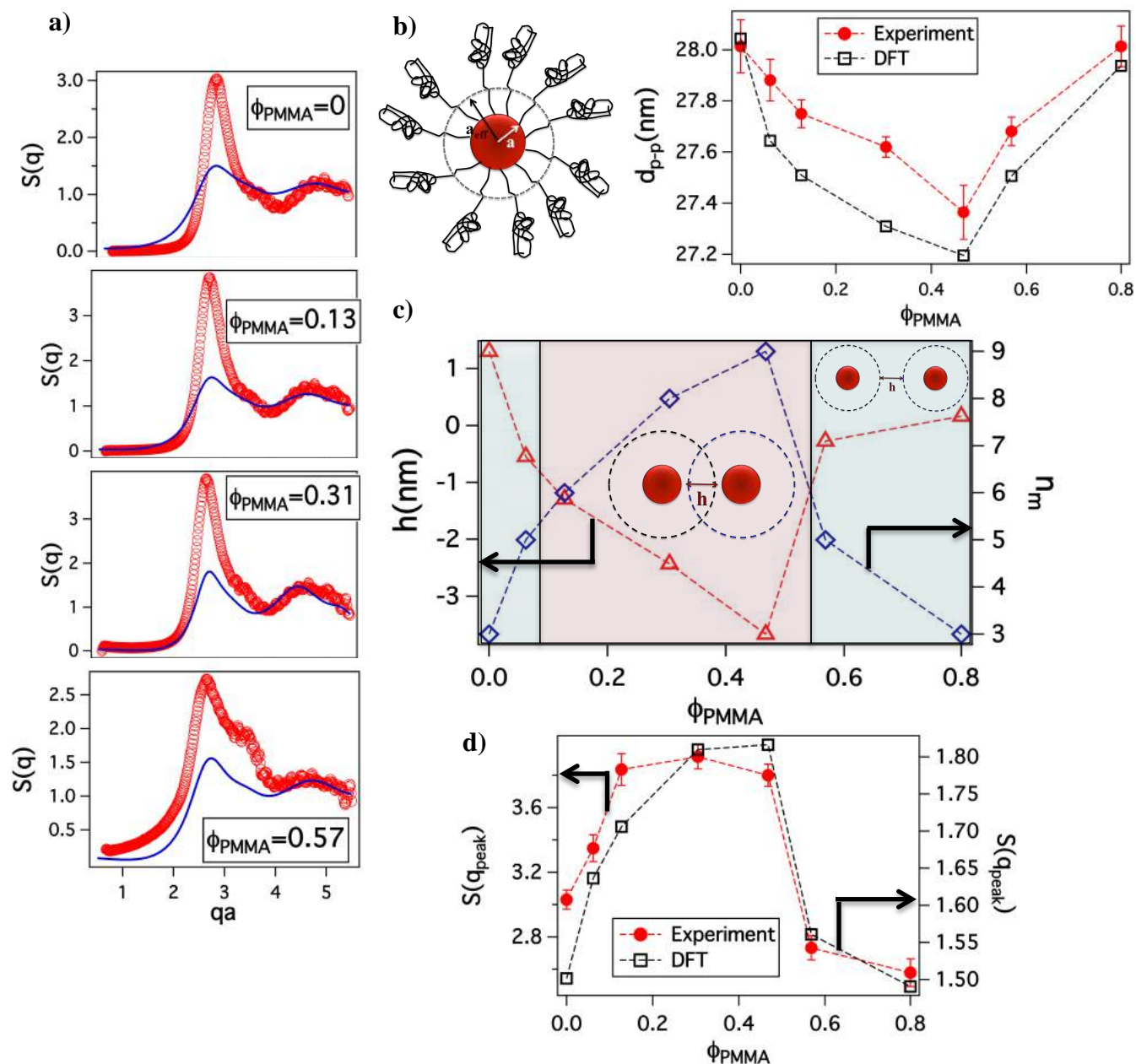


Figure 7.2 a) Experimental structure factor $S(q)$ (red circles) as obtained from SAXS measurements for different compositions at 120°C , fitted with theoretical predictions from DFT analysis (blue line). The wave vector q is scaled with the particle radius a . **b)** Illustration shows the effective core radius taken for DFT calculations, where a certain number of monomers are assumed to be immobilized such that they act as a part of the core. Comparison of experimental inter-particle distance d_{p-p} (red closed circles) with theoretical d_{p-p} (black open squares) as obtained from DFT analysis. The error bars in experimental values are deviation from multiple measurements. **c)** Variation in the surface-to-surface distance h (open red triangles) and the number of monomers assumed to be a part of the core, n_m (open blue diamonds), as a function of ϕ_{PMMA} . The negative values of h coincide with large values in n_m which suggests a stronger inter-digitation of the corona chains, as shown in the illustration. **d)** The first peak height in $S(q)$ given as $S(q_{peak})$ follows a non-monotonic variation with ϕ_{PMMA} , which is consistent with the observations made from surface-to-surface distance. The dashed lines in **b)**, **c)** and **d)** are a guide to the eye.

due to a decrease in the corona chain inter-penetration. As argued on the basis of the rheological measurements, the enhanced inter-penetration of the corona chains occurs as a result of higher degree of stretching of the chains, the variations in n_m with ϕ_{PMMA} supports this fact. The number of monomers assumed to be immobilized, is found to increase up to $\phi_{PMMA}=0.47$, after which it decreases. This implies that initially an increase in PMMA concentration leads to a higher degree of stretching of all corona chains, resulting in their increased inter-penetration. Similar trends are also observed in the variations of the first peak height of $S(q)$ (Figure 7.2d)), which confirms the hypothesis of higher degree of inter-penetration of the corona chains in PMMA-SiO₂/PEG-SiO₂ blends at intermediate ϕ_{PMMA} .

Enthalpic contributions to polymer interaction

The results from rheological and structural analysis suggest that at intermediate ϕ_{PMMA} , PMMA and PEG chains grafted on silica nanoparticles tend to inter-penetrate more as a consequence of greater degree of stretching of tethered polymer chains. We propose that this effect arises from favorable enthalpic interactions between the grafted PMMA and PEG chains that augments entropic attraction of tethered chains produced by space filling. There have been numerous studies in the literature that have shown that PMMA and PEG form a miscible blend with a negative flory-huggins parameter, χ .^{27,40,59} In order to examine how the miscibility of the presently studied PEG-PMMA blend varies with the fraction of the PMMA we first obtain the χ parameter for both the tethered and the un-tethered polymer chains.

DSC measurements performed in blends with a range of ϕ_{PMMA} to evaluate the equilibrium melting temperatures for all the blends using the Hoffman-Weeks plot (Supplementary figure 7.5).^{60,61} The experimentally estimated T_m values were used in the Nishi-Wang equation⁶² to estimate the value of χ_{12} for the untethered blend of PMMA-PEG, where 1 corresponds to PMMA and 2 corresponds to PEG-

$$\frac{1}{T_m} - \frac{1}{T_m^0} = -\frac{BV_{2u}}{\Delta H_{2u}} \frac{\phi_{PMMA}^2}{T_m} \quad (2)$$

Here, $T_m^0=349$ K is the melting temperature for pure crystalline PEG⁶³⁻⁶⁵, $V_{2u}= 38.9$ cm³/mol is the molar volume of the repeating unit of PEG⁶⁶, $\Delta H_{2u}=10080$ J/mol is the heat of fusion of fully crystalline PEG.⁶⁷ The flory-huggins parameter χ_{12} can be then obtained

from $B = \frac{RT\chi_{12}}{V_{1u}}$; where $R=8.314$ J K⁻¹ mol⁻¹ is the ideal gas constant, T is the

temperature, $V_{1u}= 86.5$ cm³/mol is the molar volume of the repeating unit of PMMA.⁶⁶

Figure 7.3a) shows a plot of $\frac{1}{T_m} - \frac{1}{T_m^0}$ vs $\frac{\phi_{PMMA}^2}{T_m}$, which consistent with Eq. 2 can be fitted

to a straight line. The slope of the line can be used to evaluate $B \approx -6.633$ J/cm³ and consequently $\chi_{12}= -0.17$ at 120°C, which is consistent with values obtained in previous

studies for PMMA-PEG blends using the melting point depression method.^{39,68} The

estimated value of χ_{12} suggests a strong enthalpic attraction between the PEG and PMMA

chains. To quantify the extent of mixing of the PEG and PMMA chains, we evaluate the

heat of mixing released upon blending the two components. The enthalpy of mixing can

be given by a van Laar relationship as^{69,70}

$$\Delta H_m(T) = \chi_{12}RT\phi_{PMMA}\phi_{PEG} \quad (3)$$

Figure 7.3b) shows the variation in ΔH_m with ϕ_{PMMA} in the PMMA/PEG blends comprised of untethered chains. It is observed that heat of mixing follows a non-monotonic dependence on ϕ_{PMMA} , with the most negative ΔH_m seen at $\phi_{PMMA} \approx 0.5$. Figures 7.3c) and 7.3d) show that the trends in enthalpy of mixing for the untethered polymer blends are reflected in the interaction parameter and heat of mixing for PMMA-SiO₂/PEG-SiO₂ blends. Ginzburg⁷¹ has outlined a procedure for determining the spinodal curve for a polymer nanocomposite. In their calculation reported in [71], one polymer is assumed to be grafted to the particle surface and the other acts as a host. This is different in the present study where both polymer chains are grafted to particles. The total free energy per unit volume for such a material can be computed in an analogous manner to reference [71] by including contributions from three types of interactions: polymer-polymer, particle-particle and polymer-particle interactions. The polymer-polymer interaction term can be written

$$F_{pol} = \frac{(1-\phi)\phi_{PMMA}}{N} \ln \left[\frac{(1-\phi)\phi_{PMMA}}{N} \right] + \frac{(1-\phi)(1-\phi_{PMMA})}{N} \ln \left[\frac{(1-\phi)(1-\phi_{PMMA})}{N} \right] \quad (4a)$$

$$+ \chi(1-\phi)^2 \phi_{PMMA}(1-\phi_{PMMA})$$

where, ϕ is the volume fraction of the particle and N is the number of monomers. The form of F_{pol} is simply the Flory-Huggins equation for a binary blend.^{72,73} The particle-particle contribution which is purely entropic can be given as-

$$F_{part} = \frac{\phi}{v_p} \left[\ln \phi + p \left(\frac{a}{r_0} \right) \frac{4\phi - 3\phi^2}{(1-\phi)^2} \right] \quad (4b)$$

where, $v_p = (4/3)\pi a^3$ is the volume of spherical nanoparticle, r_0 is the monomer radius ≈ 0.35 nm for both PEG and PMMA, and $p(x)$ is the ‘‘interpolating factor’’ that appears in Carnahan-Starling equation of state used for approximating free energy of hard spheres

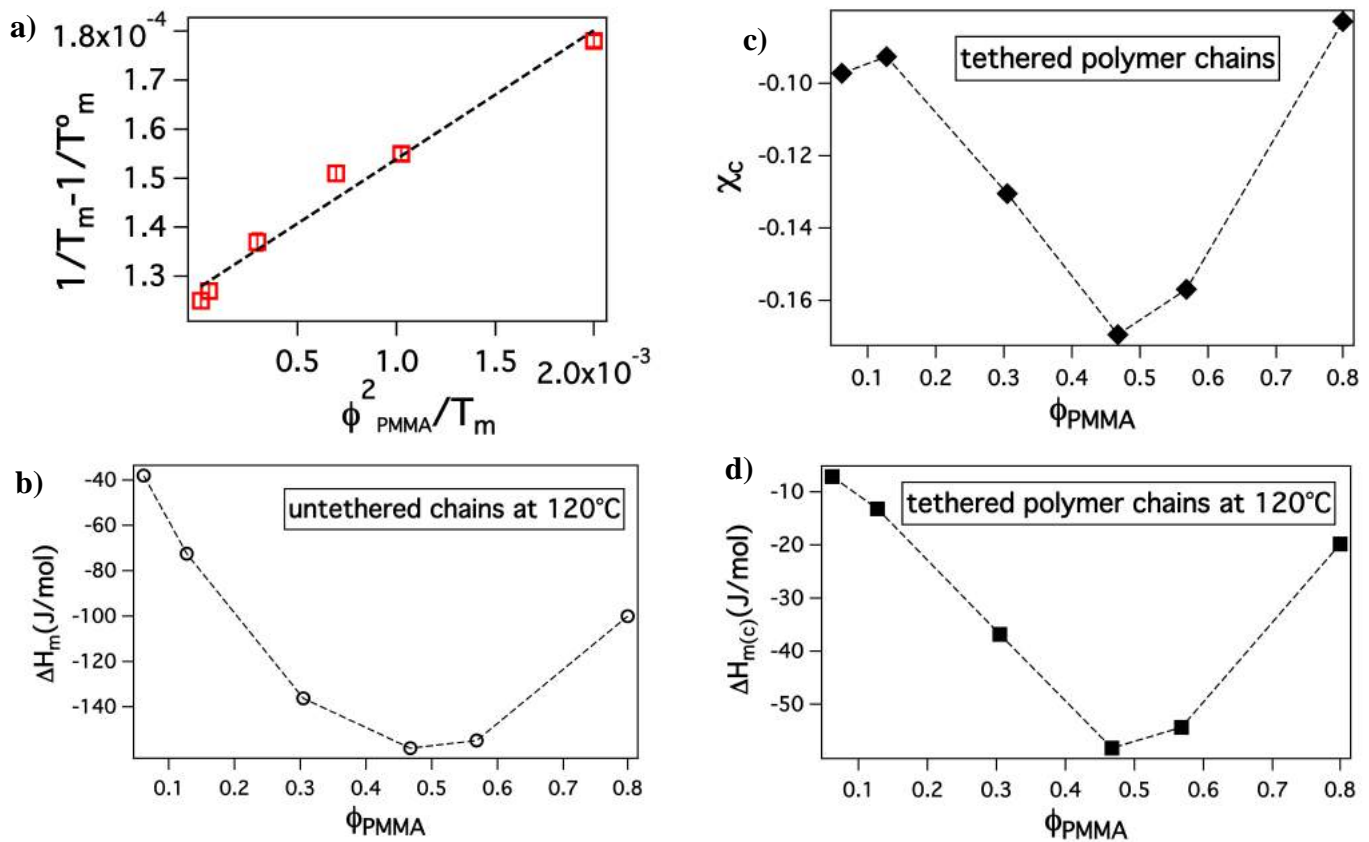


Figure 7.3 a) Variation in $1/T_m - 1/T_m^0$ as a function of ϕ_{PMMA}^2 / T_m for untethered polymer chains. The experimental values (red squares) are fitted with a straight line (black dashed line) to obtain the value of interaction parameter χ_{12} as given by the Nishi-Wang equation (2). Error bars are from multiple DSC measurements b) Heating of mixing ΔH_m obtained as a function of ϕ_{PMMA} at 120°C c) Critical interaction parameter χ as obtained from equations 5a), 5b) and 5c) for the grafted polymer chains. d) Critical heat of mixing $\Delta H_{m(c)}$ as a function of ϕ_{PMMA} at 120°C, obtained for polymer chains grafted to particles. The dashed lines in b), c) and d) are a guide to the eye.

and is chosen to be $p(x) = \max(\tanh(x-1), 0)$. Finally, for the presently studied materials the particle-polymer interaction is assumed to be entropic and to result due to the stretching of polymer chains in the vicinity of a particle. The enthalpic contribution from interactions of the host polymer with the bare particle is neglected here since both polymer chains are densely grafted on particles. Thus, the polymer-particle interaction is written as-

$$F_{\text{int}} = \frac{\phi}{v_p} (1-\phi) P \left(\frac{a}{r_0} \right) \frac{3a^2}{2Nr_0^2} \quad (4c)$$

The stability limits of free energy, $F = F_{\text{pol}} + F_{\text{part}} + F_{\text{int}}$ is then determined by satisfying the following three criteria-

$$\frac{\partial^2 F}{\partial \phi^2} > 0 \quad (5a)$$

$$\frac{\partial^2 F}{\partial \phi_{\text{PMMA}}^2} > 0 \quad (5b)$$

$$\left[\frac{\partial^2 F}{\partial \phi} \right] \left[\frac{\partial^2 F}{\partial \phi_{\text{PMMA}}^2} \right] - \left[\frac{\partial^2 F}{\partial \phi \partial \phi_{\text{PMMA}}} \right]^2 > 0 \quad (5c)$$

The critical value of the interaction parameter χ_c thus obtained is given in Figure 7.3c) as a function of polymer composition. Further, from χ_c a critical enthalpy of mixing, $\Delta H_{\text{m(c)}}$ is obtained which determines the amount of heat released for grafted polymer chains when blended for the corresponding critical interaction parameter (Figure 7.3d)). That the trends are similar to those observed for untethered polymer chains, provides strong confirmation of our hypothesis that the grafted PEG-PMMA chains inter-penetrate more as a result of higher degree of polymer stretching, which arises due to an enhanced enthalpic attraction between tethered molecules. It is also noteworthy that the value of

$\Delta H_{m(c)}$ for grafted chains is less negative than the corresponding values for untethered polymers, which may arise due to the more limited conformations of the polymer chains upon grafting.^{34,35}

Polymer segmental dynamics-

Enhanced interpenetration and stretching of polymer chains tethered to nanoparticles should also have an effect on segmental dynamics. We performed frequency dependent dielectric spectroscopy measurements at different temperatures to characterize these dynamics. Previous works have investigated dielectric relaxation of PMMA and reported that below the glass transition, a β relaxation is observed which corresponds to the rotation of $-\text{COOCH}_3$ side groups around the main chain. While above the glass transition, this β process merges with an α relaxation process which corresponds to the micro-Brownian segmental motion of the backbone; resulting in the occurrence of an $\alpha\beta$ relaxation process.⁷⁴⁻⁷⁶ In the present study, the dielectric spectroscopy was performed above the glass transition of, meaning that the observed dynamics are primarily reflective of cooperative segmental relaxation of the PMMA chains, which is influenced both by rotation of side groups and small-scale motions of the PMMA backbone.

The presence of PEG in the blends at such large volume fractions results in high values of permittivity at low frequencies, which obscure the dielectric loss (ϵ'') spectra. To circumvent this problem, we analyzed the electric loss modulus, M'' which showed clear and distinct loss maxima at different compositions. In addition to minimizing the unwanted effects of conductivity at low frequencies, an advantage of these measurements

is that they eliminate difficulties associated with electrode contact, space charge injection and fluctuations arising from adsorbed impurities.^{77,78} Figure 7.4a) and b) show the electric loss modulus, M'' spectra for the untethered and tethered polymer chains for different composition at 120°C. It can be observed that for both the untethered and tethered chains, addition of PMMA shifts the maximum in M'' to lower frequencies, suggesting that the PMMA relaxation dynamics slows down on progressing towards higher ϕ_{PMMA} . The experimentally measured M'' spectra can be fitted in the region near the loss maxima with the generalized Havriliak-Negami (H-N)⁷⁷ model as follows,

$$M'' = M_{\infty} M_s \frac{[(M_{\infty} - M_s) \sin \lambda \phi] A^{\lambda}}{M_s^2 A^{2\lambda} + 2A^{\lambda} (M_{\infty} - M_s) M_s \cos \lambda \phi + (M_{\infty} - M_s)^2} \quad (6)$$

Where,

$$A = \left[1 + 2(\omega\tau)^{1-\alpha} \sin \frac{\pi\alpha}{2} + (\omega\tau)^{2(1-\alpha)} \right]^{1/2} \quad (7)$$

And,

$$\phi = \tan^{-1} \left[\frac{(\omega\tau)^{1-\alpha} \cos \frac{\alpha\pi}{2}}{1 + (\omega\tau)^{1-\alpha} \sin \frac{\alpha\pi}{2}} \right] \quad (8)$$

M_s and M_{∞} are the values of the electric storage modulus M' , when $\omega \rightarrow 0$ and $\omega \rightarrow \infty$, respectively; τ is the relaxation time, α and λ are exponents that describe the symmetric or asymmetric distribution of relaxation times. τ values obtained from the H-N fits for untethered PMMA/PEG blends, as well as for PMMA-SiO₂/PEG-SiO₂ blends are shown in Figures 7.4d) and c) as a function of temperature for different ϕ_{PMMA} . Three distinct observations can be made from these results. First, the relaxation dynamics of the tethered chains are much slower than those of their untethered counterparts, irrespective

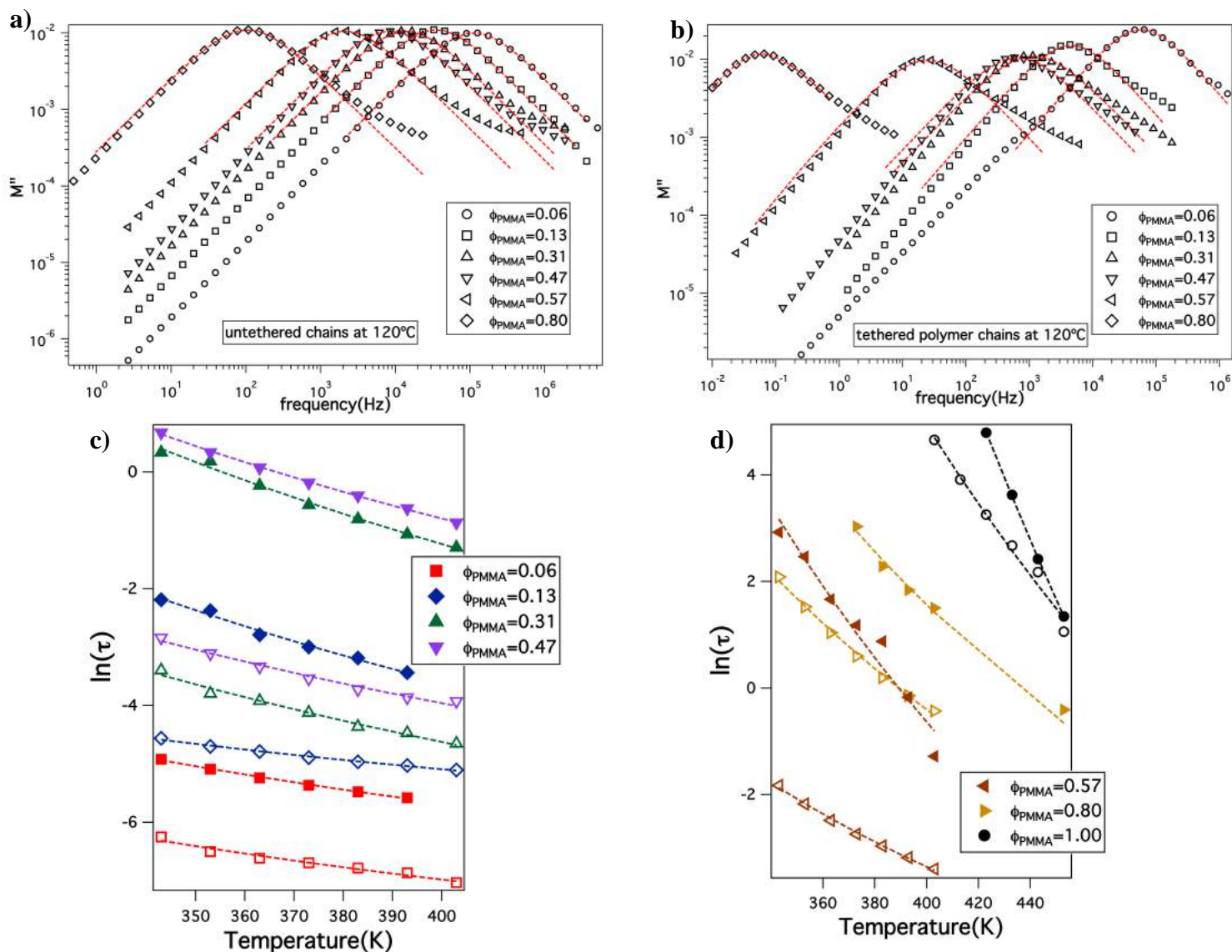


Figure 7.4 Dielectric spectra of the loss modulus as a function of frequency at 120°C for **a)** untethered polymer chains, and **b)** tethered polymer chains for different compositions. The experimental values (open symbols) are fitted with the H-N function (red dashed lines). Variation in $\ln(\tau)$ as obtained from H-N fitting as a function of temperature for **c)** $\phi_{PMMA}=0.06$ to 0.47, and **d)** $\phi_{PMMA}=0.57$ to 1. The open symbols correspond to untethered polymer chains and the closed symbols are for tethered chains. It can be observed that the relaxation times for the grafted chains is 2-3 orders of magnitude higher than for the untethered chains. The dashed lines are Arrhenius fit to the relaxation times.

of ϕ_{PMMA} . As shown in a previous study, particle tethered polymer chains in self-suspended materials are more sluggish because they are more confined by their neighbors on a crowded particle surface and because they are stretched by the requirement that chains fill space in a self-suspended material.³⁴ Dynamic slow-down of 2-4 orders of magnitude, relative to untethered polymer chains, have been reported for the normal mode relaxation.^{34,35} Secondly, as the fraction of PMMA is increased, the value of τ increases, which is consistent with the observations made previously from the dielectric relaxation of PMMA/PEG blends.⁷⁵ PMMA has the slowest dynamics and as the concentration of PEG is increased, it acts as a plasticizer for PMMA, which leads to an increase in its mobility. Third, and perhaps most remarkable is the fact that at any given fixed temperature distance from the melting or glass transition, the degree of slow-down produced by tethering, as measured for example by the ratio of τ values for the tethered and untethered polymer (see Figure 7.5a)), changes in a non-monotonic fashion with ϕ_{PMMA} , exhibiting a maximum around $\phi_{PMMA} \approx 0.5$. This last result confirm that the enhanced interpenetration of tethered chains reported previously on the basis of rheology and SAXS measurements leads to dynamic arrest of the motions of tethered chains down to segmental levels. It validates our argument that the interpenetrated chains act as effective cross-links between the particles.

The values of α and λ used for the fits are reported in Supplementary figure 7.6. It is seen that λ is close to one at all compositions and temperatures for the untethered polymer chains (see Supplementary figure 7.6a)), which is known to occur when the H-N fit becomes equivalent to a Cole-Cole function, and symmetric relaxation spectra are

observed.^{77,79,80} This observation is in accordance with previous dielectric relaxation for PMMA/PEG blends⁷⁵, and the symmetric relaxation in the untethered polymer chains indicates a homogenous environment for the PMMA chains, which is consistent with good miscibility of polymer components in the blends at all compositions. In contrast, Supplementary figure 7.6b) shows that for the tethered polymer chains λ deviates from unity with increasing ϕ_{PMMA} , which is suggestive of a heterogeneous relaxation environment for the PMMA, which is likely a reflection of the presence of the silica nanoparticles that lead to a more coupled and thus retarded relaxation of the PMMA chains.

The temperature dependent τ values can be fitted to an Arrhenius-like form to estimate the activation energy for the relaxation process-

$$\tau = A \exp(-E_a / RT) \quad (9)$$

Here, A is a pre-factor, E_a is the activation energy in kJ/mol and R is the gas constant. Figure 7.5b) shows the effect of ϕ_{PMMA} for both the PMMA/PEG and PMMA-SiO₂/PEG-SiO₂ blends. The activation energy for untethered pure PMMA is around 102kJ/mol, which is similar to the value reported in previous studies.^{75,81} For both the tethered and untethered polymers, E_a is a monotonic increasing function of ϕ_{PMMA} , implying that the barriers to segmental scale motions are dominated by the well-known plasticizing effect of PEG and PMMA. In contrast, the dielectric strength, $\Delta\epsilon = \epsilon_s - \epsilon_\infty = (1/M_s) - (1/M_\infty)$, follows a similar non-monotonic trend with ϕ_{PMMA} as shown in Figure 7.5c). The dielectric strength for an $\alpha\beta$ process can be understood in the framework of cooperativity of the surrounding chains and is directly dependent on the square of dipole moment, $\mu^{2,80}$. This

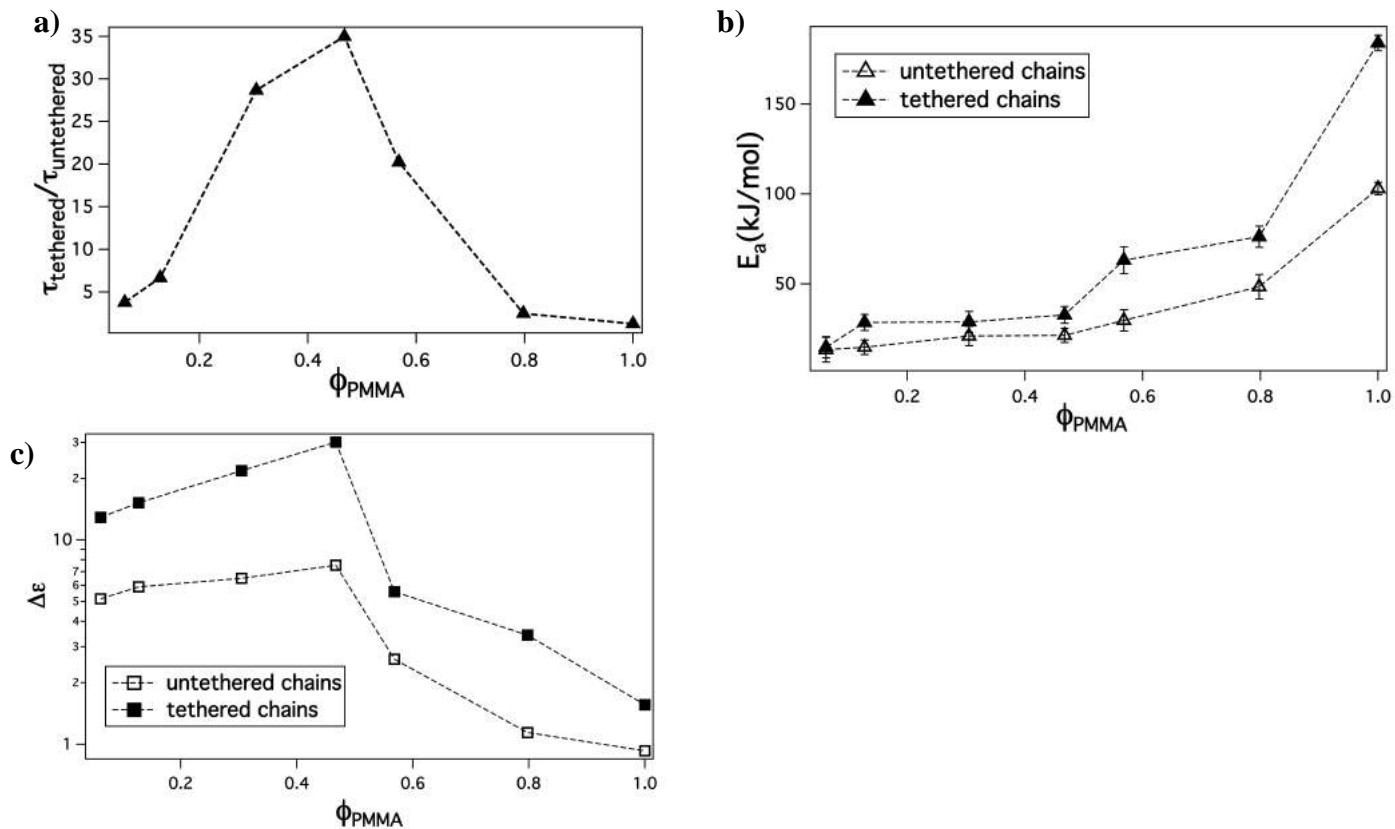


Figure 7.5 a) Ratio of relaxation time of tethered to untethered polymer chains as a function of ϕ_{PMMA} follows similar trend as expected from SAXS and heat of mixing estimations. The reported time scales are at a temperature 50°C above the melting transition for each composition and glass transition for $\phi_{PMMA}=1$. b) Activation energy E_a as obtained from the Arrhenius fit to relaxation times increases with an increase in the fraction of PMMA for both the tethered (closed symbols) and untethered (open symbols) chains. c) The dielectric strength $\Delta\epsilon$ however, follows a non-monotonic variation with ϕ_{PMMA} for both the tethered and untethered polymer chains. The dashed lines are guide to the eye.

dipole moment is influenced by cross-correlation factors arising from the surrounding chains, and thus an increase in the dielectric strength can be understood as an increase in the cooperativity from the surrounding chains. This result is in accordance with the observations made earlier about an enhancement in interpenetration of PEG and PMMA chains upon initial addition of PMMA to the blends.

7.5 Conclusion

We have studied a model system comprising of solvent-free polymer grafted silica nanoparticles, where the chemistry of the grafted polymers is changed such that the two different kinds of polymers form a thermodynamically stable blend. Silica nanoparticles grafted with PEG and PMMA chains were blended in different ratios and the effect of compositions on the mechanical and structural properties of the self-suspended suspensions of silica nanoparticles is analyzed. We observed that all rheological properties follow a non-monotonic trend with the composition of PMMA added to the blend such that both the dissipated energy and the plateau modulus first increase with the fraction of PMMA and then decrease. We attribute this behavior to a higher degree of inter-penetration of the PMMA chains with the PEG chains from the neighboring particles. From the calculated “localization length” we find that indeed the grafted chains stretch more with initially an increase in the PMMA content which leads to higher inter-digitation of the grafted chains, and thus it results in stronger mechanical response from the material. We propose that the favorable enthalpic interactions between the PEG and PMMA chains augment the space-filling constraint imposed on the tethered chains to fill the interstitial space between the cores, which subsequently leads to higher inter-digitation of the polymer chains.

The experimental findings from SAXS measurements, when fitted with DFT predictions reveal similar trends with the composition. We find that the number of monomers in the chains which become highly stretched, such that they act as a part of core, increases with an increase in the fraction of PMMA, which supports the above hypothesis of higher inter-penetration of the grafted corona chains. In order to understand the reason behind this observed behavior, we estimated the interaction parameter χ_{12} for both the untethered and the tethered polymer chains. The heat of mixing obtained from the interaction parameter suggests that the volume fraction of PMMA corresponding to strongest mechanical response as seen in the rheological measurements, or the least surface-to-surface distance as obtained from SAXS measurements coincides with the fraction where maximum amount of heat of mixing is released. This implies that in the regime where PEG and PMMA form the most thermodynamically stable blend due to strong enthalpic interaction, the mechanical and the structural responses are strongest there.

The dielectric analysis on the dynamics of the polymer chains does show that grafting slows down the relaxation time of the PMMA chains, which occurs due to the confinement of the grafted polymer chains. While the pure PMMA has the slowest relaxation time, addition of PEG increases the relaxation dynamics as it acts as a plasticizer for the PMMA chains due to its strong enthalpic interaction with the PMMA polymer chains. Furthermore, a non-monotonic variation is observed in the relaxation times of the tethered polymer chains scaled with the untethered chains and the dielectric strength of the PMMA chains, which corroborate the results obtained from rheology and

SAXS measurements. This is in accordance with the hypothesis of enhanced interpenetration of the corona chains and shows that the bulk measurements made from rheology can translate down to the segmental motion of tethered polymer chains and influence the polymer chain dynamics in a similar way. We have thus created a model system, which utilizes and tunes the enthalpic interaction between the PEG and PMMA polymer chains such that the material becomes more mechanically strong with a stable uniform dispersion. This study can open up avenues for creating a stable, uniformly dispersed nanocomposite where the grafted polymer chains might even be immiscible, by utilizing the strong interaction between the polymer chains due to space-filling constraint imposed on them.

Acknowledgements

This work was supported by the National Science Foundation, Award No. DMR 1609125. Use of the Cornell High Energy Synchrotron Source (CHESS), was also supported NSF Award No. DMR-1006323.

REFERENCES

- (1) Balazs, A. C.; Emrick, T.; Russell, T. P. *Science* (80-.). **2006**, *314* (5802), 1107–1110.
- (2) Chapman, R.; Mulvaney, P. *Chem. Phys. Lett.* **2001**, *349* (5-6), 358–362.
- (3) Evans, L. *Annu. Rev. Mater. Res.* **2001**, *32*, 347–375.
- (4) Hussain, F. J. *Compos. Mater.* **2006**, *40* (17), 1511–1575.
- (5) Yoon, P. J.; Fornes, T. D.; Paul, D. R. *Polymer (Guildf)*. **2002**, *43* (25), 6727–6741.
- (6) Schaefer, J. L.; Moganty, S. S.; Yanga, D. A.; Archer, L. A. *J. Mater. Chem.* **2011**, *21* (27), 10094–10102.
- (7) Nugent, J. L.; Moganty, S. S.; Archer, L. A. *Adv. Mater.* **2010**, *22* (33), 3677–3680.
- (8) Choudhury, S.; Mangal, R.; Agrawal, A.; Archer, L. A. *Nat. Commun.* **2015**, *6*:10101, 1–9.
- (9) Agrawal, A.; Choudhury, S.; Archer, L. A. *RSC Adv.* **2015**, *5*, 20800–20809.
- (10) Choudhury, S.; Agrawal, A.; Wei, S.; Jeng, E.; Archer, L. A. *Chem. Mater.* **2016**, *28*, 2147–2157.
- (11) Zhang, Q.; Archer, L. A. *Langmuir* **2002**, *18* (26), 10435–10442.
- (12) Hooper, J. B.; Schweizer, K. S. *Macromolecules* **2005**, *38* (21), 8858–8869.
- (13) Hooper, J. B.; Schweizer, K. S. *Macromolecules* **2006**, *39* (15), 5133–5142.
- (14) Napper, D. H. *Ind. Eng. Chem. Prod. Res. Dev.* **1970**, *9* (4), 467–477.
- (15) Feigin, R. I.; Napper, D. H. *J. Colloid Interface Sci.* **1980**, *75* (2), 525–541.

- (16) Napper, D. H. *Polymeric stabilization of colloidal dispersions*; Academic Press: London, 1984.
- (17) Napper, D. H.; Netschey, A. *J. Colloid Interface Sci.* **1971**, *37* (3), 528–535.
- (18) Vincent, B. *Adv. Colloid Interface Sci.* **1974**, *4* (2-3), 193–277.
- (19) Sunday, D.; Ilavsky, J.; Green, D. L. *Macromolecules* **2012**, *45* (9), 4007–4011.
- (20) Chevigny, C.; Jestin, J.; Gigmes, D.; Schweins, R.; Di-Cola, E.; Dalmas, F.; Bertin, D.; Boué, F. *Macromolecules* **2010**, *43* (11), 4833–4837.
- (21) Chevigny, C.; Dalmas, F.; Di Cola, E.; Gigmes, D.; Bertin, D.; Boué, F.; Jestin, J. *Macromolecules* **2011**, *44* (1), 122–133.
- (22) Srivastava, S.; Agarwal, P.; Archer, L. A. *Langmuir* **2012**, *28* (15), 6276–6281.
- (23) Green, D. L.; Mewis, J. *Langmuir* **2006**, *22* (18), 9546–9553.
- (24) Dutta, N.; Green, D. *Langmuir* **2008**, *24* (10), 5260–5269.
- (25) Matsen, M. W.; Gardiner, J. M. *J. Chem. Phys.* **2001**, *115* (6), 2794–2804.
- (26) Green, P. F. *Soft Matter* **2011**, *7* (18), 7914.
- (27) Mangal, R.; Srivastava, S.; Archer, L. A. *Nat. Commun.* **2015**, *6*:7198, 1–9.
- (28) Borukhov, I.; Leibler, L. *Macromolecules* **2002**, *35* (13), 5171–5182.
- (29) Borukhov, I.; Leibler, L. *Phys. Rev. E* **2000**, *62* (1), 41–44.
- (30) Yu, H.-Y.; Koch, D. L. *Langmuir* **2010**, *26* (22), 16801–16811.
- (31) Yu, H.-Y.; Srivastava, S.; Archer, L. A.; Koch, D. L. *Soft Matter* **2014**, *10* (45), 9120–9135.
- (32) Agarwal, P.; Qi, H.; Archer, L. A. *Nano Lett.* **2010**, *10* (1), 111–115.
- (33) Agrawal, A.; Yu, H.-Y.; Srivastava, S.; Choudhury, S.; Narayanan, S.; Archer, L. A. *Soft Matter* **2015**, *11*, 5224–5234.

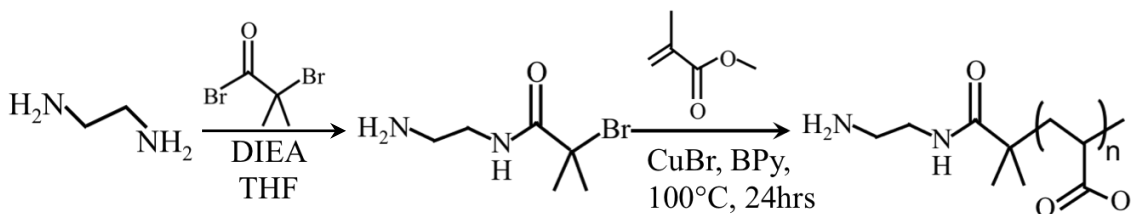
- (34) Kim, S. A.; Mangal, R.; Archer, L. A. *Macromolecules* **2015**, *48* (17), 6280–6293.
- (35) Agarwal, P.; Kim, S. A.; Archer, L. A. *Phys. Rev. Lett.* **2012**, *109* (25), 258301–1–4.
- (36) Kim, S. A.; Archer, L. A. *Macromolecules* **2014**, *47*, 687–694.
- (37) Choudhury, S.; Agrawal, A.; Kim, S. A.; Archer, L. A. *Langmuir* **2015**, *31*, 3222–3231.
- (38) Agarwal, P.; Srivastava, S.; Archer, L. A. *Phys. Rev. Lett.* **2011**, *107* (26), 268302–1 – 5.
- (39) Liberman, S. A.; Gomes, A. D. E. S. *J. Polym. Sci. Chem.* **1984**, *22*, 2809–2815.
- (40) Ito, H.; Russell, T. P.; Wignall, G. D. *Macromolecules* **1987**, *20*, 2213–2220.
- (41) Matyjaszewski, K.; Xia, J. *Chem. Rev.* **2001**, *101*, 2921–2990.
- (42) Wang, J.-S.; Matyjaszewski, K. *Macromolecules* **1995**, *28* (23), 7901–7910.
- (43) Glatter, O.; Kratky, O. *Small Angle X-ray Scattering*, United Sta.; Academic Press: New York, 1982.
- (44) Srivastava, S.; Shin, J. H.; Archer, L. A. *Soft Matter* **2012**, *8* (15), 4097–4108.
- (45) Mason, T. G.; Weitz, D. A. *Phys. Rev. Lett.* **1995**, *75* (14), 2770–2773.
- (46) Pham, K. N.; Petekidis, G.; Vlassopoulos, D.; Egelhaaf, S. U.; Pusey, P. N.; Poon, W. C. K. *Europhys. Lett.* **2006**, *75* (4), 624–630.
- (47) Helgeson, M. E.; Wagner, N. J.; Vlassopoulos, D. *J. Rheol. (N. Y. N. Y.)* **2007**, *51* (2), 297–316.
- (48) Koumakis, N.; Pamvouxoglou, A.; Poulos, A. S.; Petekidis, G. *Soft Matter* **2012**, *8* (15), 4271–4284.

- (49) Petekidis, G.; Vlassopoulos, D.; Pusey, P. N. *J. Phys. Condens. Matter* **2004**, *16* (38), S3955–S3963.
- (50) Loppinet, B.; Stiakakis, E.; Vlassopoulos, D.; Fytas, G.; Roovers, J. **2001**, No. about 270, 8216–8223.
- (51) Tsitsilianis, C.; Iliopoulos, I. *Macromolecules* **2002**, *35* (9), 3662–3667.
- (52) Agrawal, A.; Yu, H.-Y.; Sagar, A.; Choudhury, S.; Archer, L. A. *submitted* **2016**.
- (53) Tanaka, F.; Edwards, S. F. **2002**, *25* (May), 1516–1523.
- (54) Erk, K. A.; Shull, K. R. *Macromolecules* **2011**, *44* (4), 932–939.
- (55) Ganeriwala, S. N.; Rotz, C. A. *Polym. Eng. Sci.* **1987**, *27* (2), 165–178.
- (56) Chremos, A.; Panagiotopoulos, A. Z.; Yu, H.-Y.; Koch, D. L. *J. Chem. Phys.* **2011**, *135* (11), 114901.
- (57) Erk, K. A.; Martin, J. D.; Hu, Y. T.; Shull, K. R. *Langmuir* **2012**, *28* (9), 4472–4478.
- (58) Seitz, M. E.; Burghardt, W. R.; Faber, K. T.; Shull, K. R. *Macromolecules* **2007**, *40* (4), 1218–1226.
- (59) Zawada, J. A.; Ylitalo, C. M.; Fuller, G. F. *Macromolecules* **1992**, *25*, 2896–2902.
- (60) Hoffman, J. D.; Weeks, J. J. *J. Res. Natl. Bur. Stand. Sect. A Phys. Chem.* **1962**, *66A* (1), 13–28.
- (61) Ho, W.; Kwon, Y. K.; Kwon, I. H. **1991**, 4708–4712.
- (62) Nishi, T.; Wang, T. T. *Macromolecules* **1975**, *8* (6), 909–915.
- (63) Letters, P. Beech, D.R. Booth, C. **1970**, *8*, 731–734.
- (64) Hay, J. N.; Sabir, M.; Steven, R. L. T. *Polymer (Guildf)*. **1969**, *10* (3), 187–202.
- (65) Alfonso, G. C.; Russell, T. P. *Macromolecules* **1986**, *19*, 1143–1152.

- (66) Van Krevelen, D. W. *Properties of Polymers*; Elsevier, 1972.
- (67) Martuscelli, E. *Polym. Eng. Sci.* **1984**, *24* (8), 563–586.
- (68) Krause, S. J. *Macromol. Sci. Part C Polym. Rev.* **1972**, *7* (2), 251–314.
- (69) Lu, X.; Weiss, a. *Macromolecules* **1992**, *25*, 3242–3246.
- (70) Chun, Y. S.; Lee, H. S.; Jung, H. C.; Kim, W. O. O. N. *J. Appl. Polym. Sci.* **1999**, *72*, 733–739.
- (71) Ginzburg, V. V. *Macromolecules* **2005**, *38* (6), 2362–2367.
- (72) Flory, P. J. *J. Chem. Phys.* **1942**, *10*, 51–61.
- (73) Huggins, M. L. *J. Am. Chem. Soc.* **1942**, *64* (7), 1712–1719.
- (74) Jin, X.; Zhang, S.; Runt, J. *Macromolecules* **2004**, *37*, 8110–8115.
- (75) Dionisio, M.; Fernandes, A. C.; Mano, F.; Correia, T.; Sousa, R. C. *Macromolecules* **2000**, *33*, 1002–1011.
- (76) Bistac, S.; Schultz, J. *Int. J. Adhes. Adhes.* **1997**, *17* (3), 197–201.
- (77) Tsangaris, G. M.; Psarras, G. C.; Kouloumbi, N. *J. Mater. Sci.* **1998**, *33* (8), 2027–2037.
- (78) Starkweather Jr., H. W.; Avakian, P. J. *Polym. Sci. B Polym. Physcis* **1992**, *30*, 637–641.
- (79) Cole, K. S.; Cole, R. H. *J. Chem. Phys.* **1941**, *9* (4), 341.
- (80) Runt, J. P.; Fitzgerald, J. J. *Dielectric spectroscopy of polymeric materials*; American Chemical Society: Washington, D.C.
- (81) Lockwenz, H.; Beiner, M.; Schroter, K.; Donth, E. *Macromolecules* **1996**, *29*, 247–253.

1. Synthesis of Amine terminated PMMA-

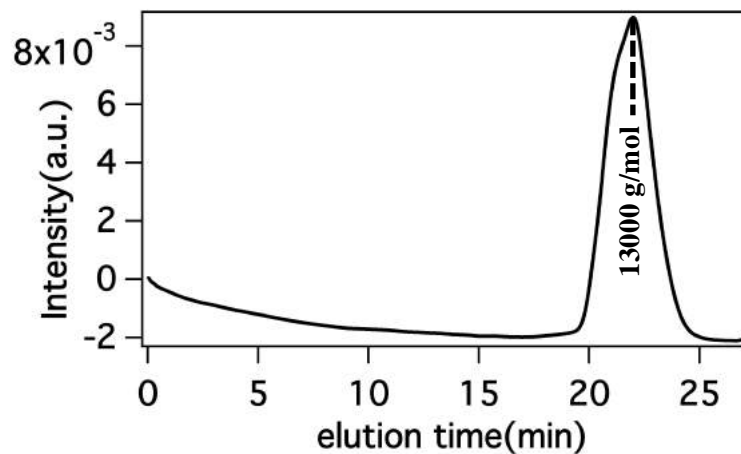
In a round bottom flask, 10 mol of ethylenediamine (Sigma Aldrich) and 100 mmol of N,N'-diisopropylethylamine (DIEA, Sigma Aldrich) were dissolved in 30 mL of tetrahydrofuran (THF) solvent under nitrogen gas. To this solution, 1 mol of α -bromoisobutyryl bromide (BIBB, Sigma Aldrich) in 15 mL of THF was added dropwise as shown in Scheme 1. The reaction was allowed to stir for 18 hours, after which the reaction solution was passed over a silica plug to remove salts. The solvent, excess ethylenediamine, and DIEA were removed *in vacuo*, and the product was obtained as a pale yellow oil.



Scheme 1: Synthesis of amine-terminated ATRP initiator followed by polymerization of

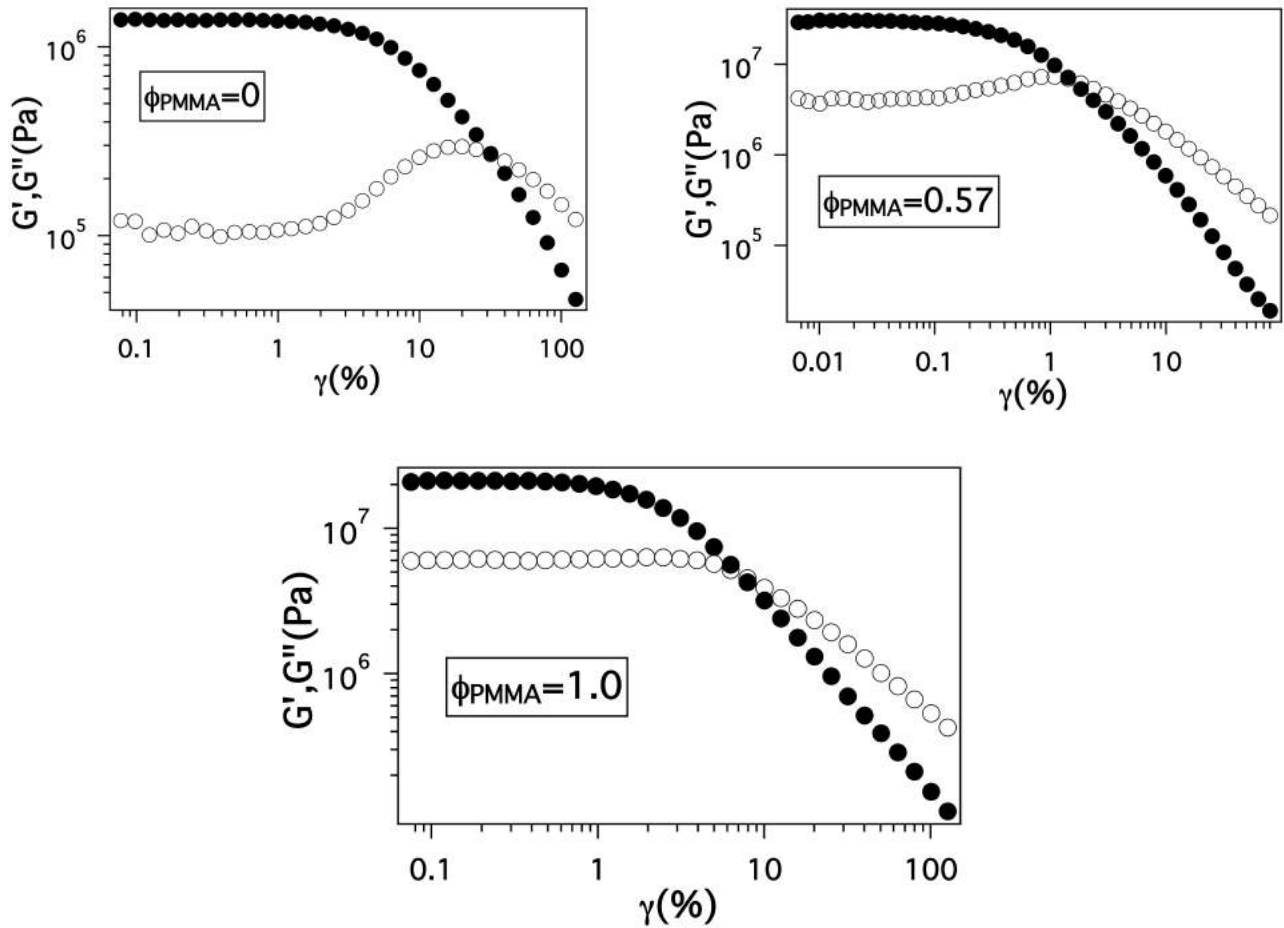
The monomer, methyl methacrylate (MMA, Sigma Aldrich) was stirred with inhibitor removers and filtered to remove inhibitors before ATRP. 30 mL of MMA was added to a Schlenk flask with 30 mL of DMF, to which 0.2 g of 2,2'-Bipyridine (BPy, Sigma Aldrich) was added, which acted as a Ligand. The solution mixture was degassed by three freeze pump thaw cycles. Under flowing nitrogen 0.57 g of purified Copper (I) bromide (CuBr, Sigma Aldrich) was added followed by an additional three freeze pump thaw cycles. The polymerization was carried out at 100°C for 24 hours under nitrogen. The polymer was obtained by precipitation in 100 L of methanol and filtration. Excess copper was removed by re-dissolving the polymer in a small amount of THF and filtering it through a plug of silica. Finally, the polymer was precipitated in excess methanol three times. The

purified polymer was characterized by GPC. As shown below in Figure S1, the synthesized PMMA has a PDI of about 1.4 with a molecular weight of 13000 g/mol

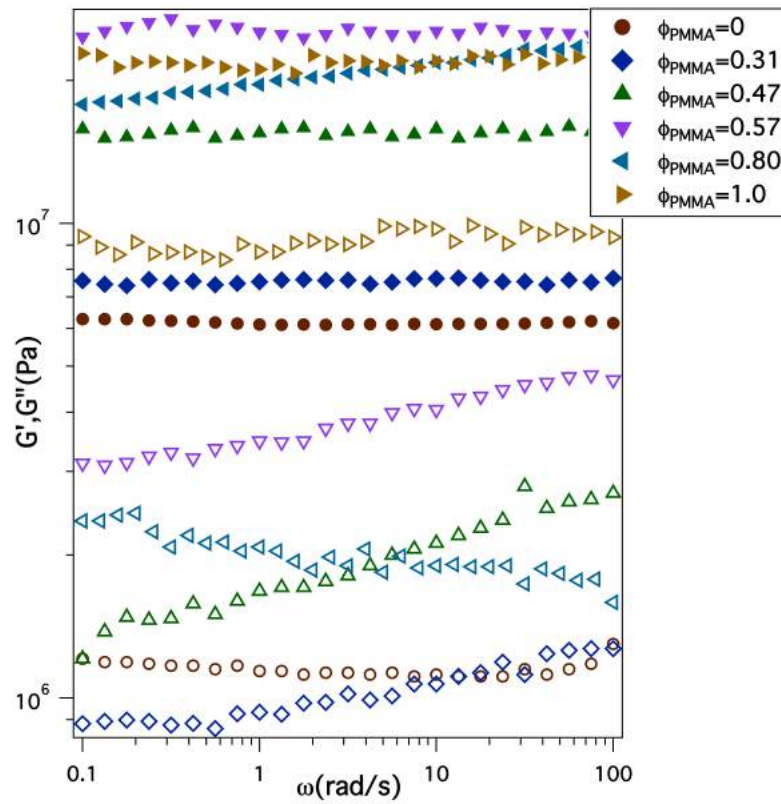


Supplementary figure 7.1 GPC curve for the synthesized PMMA polymer, with M_n

2. Oscillatory shear measurements-

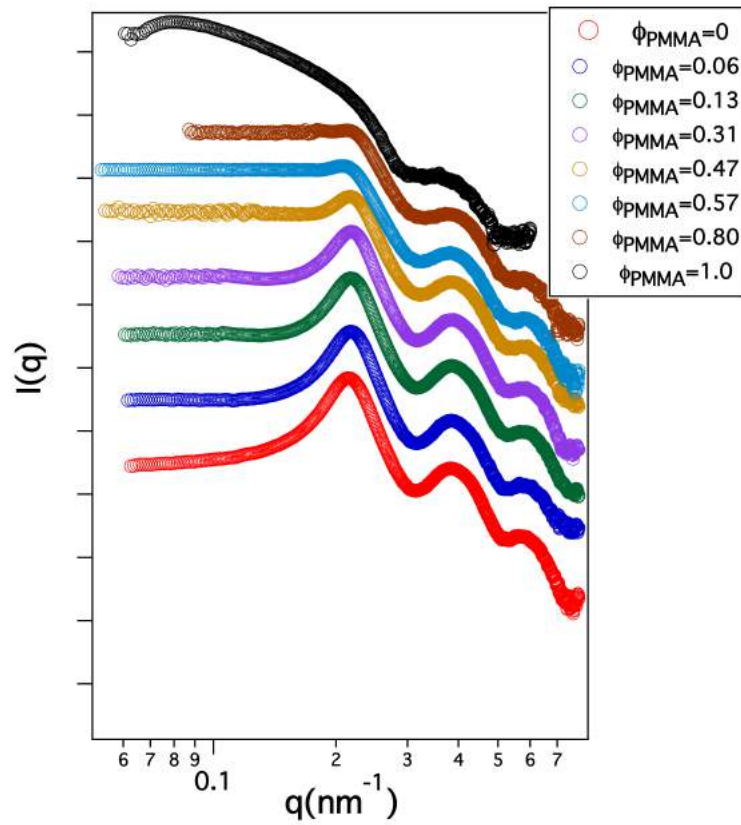


Supplementary Figure 7.2 Oscillatory shear measurements performed at an angular frequency of $\omega=10$ rad/s as a function of variable strain at a temperature of 120°C for $\phi_{PMMA}=0, 0.57$ and 1 . The closed symbols corresponds to storage modulus, G' and the open symbols to loss modulus, G'' .



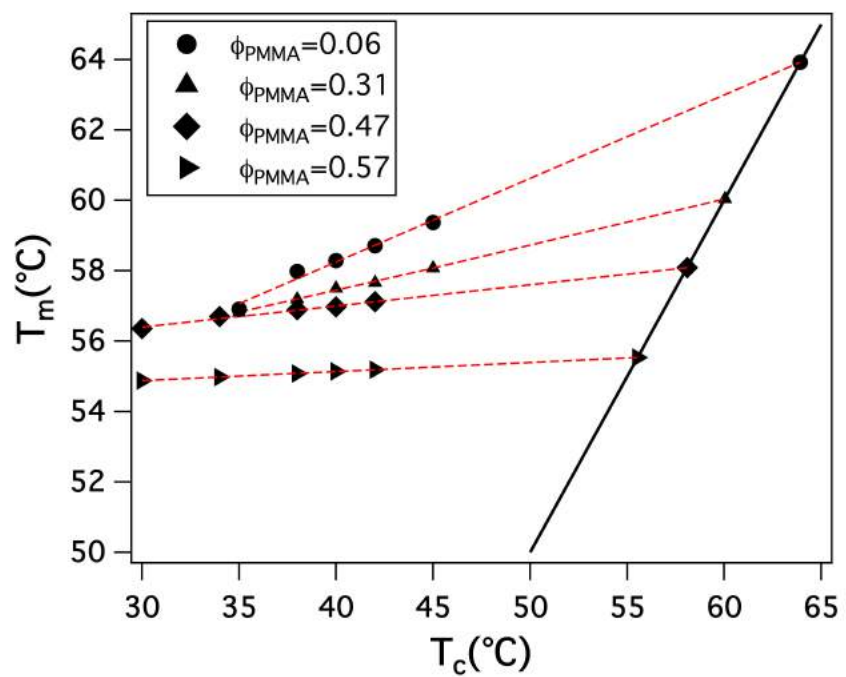
Supplementary figure 7.3 Frequency sweep oscillatory shear measurements performed at a shear strain of $\gamma=0.5\%$ at a temperature of 120°C for different volume fractions of PMMA. The closed symbols corresponds to storage modulus, G' and the open symbols to loss modulus, G'' .

3. SAXS measurements



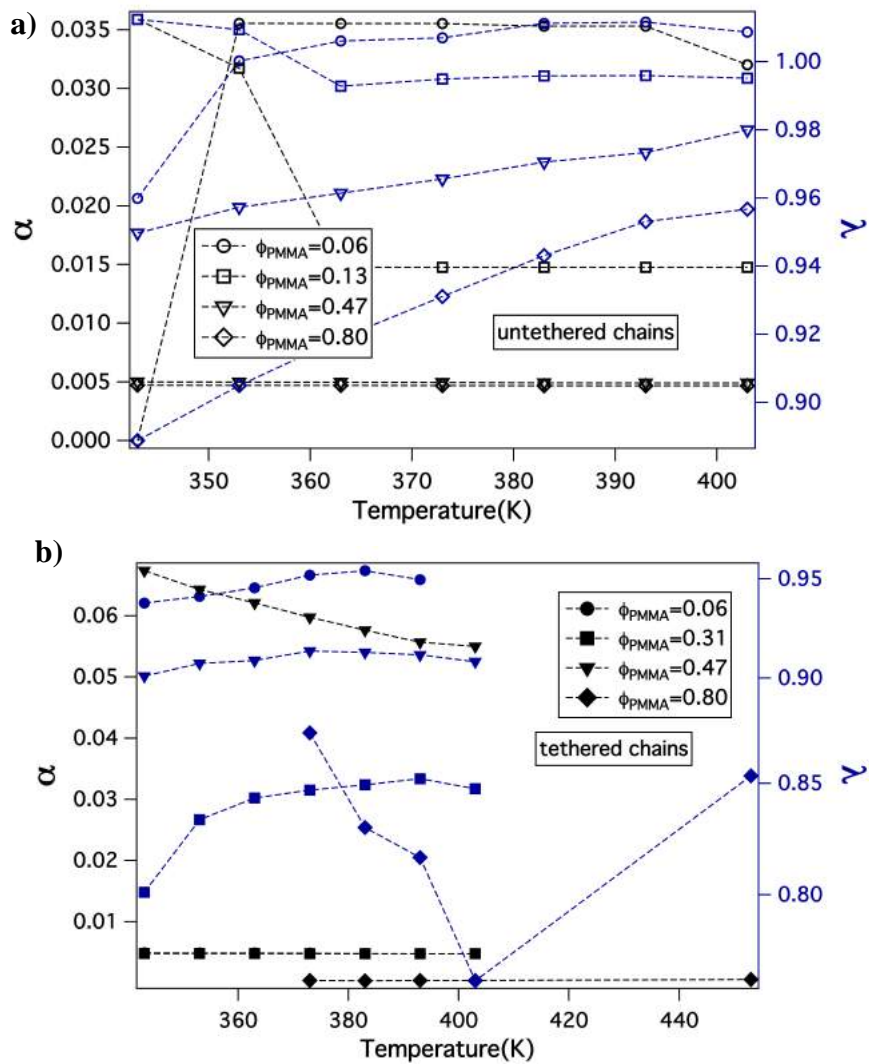
Supplementary figure 7.4 Variation of x-ray scattering intensity, $I(q)$ as measured from SAXS experiments as a function of the wave vector q at different volume fraction of PMMA.

4. DSC measurements-



Supplementary figure 7.5 Hoffman-Weeks plot for evaluating equilibrium melting temperature.

5. Dielectric spectroscopy-



Supplementary figure 7.6 Variation in the H-N fitting exponents, α and λ as a function of temperature at different compositions for **a)** untethered polymer chains, and **b)** tethered polymer chains.